THÈSE

Pour obtenir le grade de

DOCTEUR DE L'UNIVERSITÉ GRENOBLE ALPES

École doctorale : PHYS - Physique
Spécialité : Physique de la Matière Condensée et du Rayonnement
Unité de recherche : Institut Néel

Interactions paramétriques et génération d'intrication quantique dans un guide d'ondes Josephson à indice négatif

Parametric interactions and entanglement generation in a negative-index Josephson waveguide

Présentée par :

Giulio CAPPELLI

Direction de thèse :

Franck BALESTRO — Directeur de thèse
PROFESSEUR DES UNIVERSITES, UNIVERSITE GRENOBLE ALPES

Nicolas ROCH — Co-directeur de thèse
DIRECTEUR DE RECHERCHE, CNRS DELEGATION ALPES

Rapporteurs :

NICOLAS BERGEAL
PROFESSEUR, ESPCI PARIS

PHILIPPE CAMPAGNE-IBARCQ
CHARGE DE RECHERCHE HDR, CNRS DELEGATION PARIS CENTRE

Thèse soutenue publiquement le **16 décembre 2025**, devant le jury composé de :

WIEBKE GUICHARD, — Présidente
PROFESSEURE DES UNIVERSITES, UNIVERSITE GRENOBLE ALPES

NICOLAS BERGEAL, — Rapporteur
PROFESSEUR, ESPCI PARIS

PHILIPPE CAMPAGNE-IBARCQ, — Rapporteur
CHARGE DE RECHERCHE HDR, CNRS DELEGATION PARIS CENTRE

IACOPO CARUSOTTO, — Examinateur
DIRECTEUR DE RECHERCHE, ISTITUTO NAZIONALE DI OTTICA

LUKAS GRÜNHAUPT, — Examinateur
SCIENTIST, PHYSICALISCH-TECHNISCHE BUNDESANSTALT

PARAMETRIC INTERACTIONS AND ENTANGLEMENT GENERATION IN A NEGATIVE-INDEX JOSEPHSON WAVEGUIDE

GIULIO CAPPELLI

Giulio Cappelli: *Parametric interactions and entanglement generation in a negative-index Josephson waveguide,* © 21 October 2025

ABSTRACT

ENGLISH VERSION One-dimensional Josephson waveguides have generated significant interest in the fields of quantum technology and superconducting quantum information because they allow complete control over wave dispersion and nonlinear interactions. A variety of Josephson waveguides have been proposed and realized in the recent years, with applications ranging from near quantum-limited broadband amplification to multi-mode entanglement generation and non-reciprocal signals transmission.

This thesis explores parametric interactions and entanglement generation in a novel architecture of Josephson waveguide. The latter consists of a high-pass microwave network and realizes an artificial material showing left-handed wave dispersion (or equivalently negative refractive index). The left-handed dispersion, combined with the Josephson nonlinearity, enables for various parametric processes, ranging from self-phase-matched broadband amplification of co-propagating modes to amplification and mixing of waves propagating in opposite directions. The realization of such Josephson waveguide opens new avenues within the framework of Josephson traveling wave parametric amplifiers and converters.

Beyond these classical nonlinear optical processes, negative index Josephson waveguide are also powerful tools to generate nonclassical states of light such as broadband two-mode vacuum squeezed states and spatially separated entangled photon pairs. Here, we report about the measurements of such quantum states with this novel Josephson waveguide architecture, opening new perspectives for quantum sensing and quantum radar and illumination protocols, and more generally for microwave applications requiring the routing of entangled photons in different directions.

FRENCH VERSION Les guides d'onde de Josephson unidimensionnels ont suscité un intérêt considérable dans les domaines des technologies quantiques et de l'information quantique à base de circuits supraconducteurs, car ils permettent un contrôle complet de la dispersion des ondes et des interactions non linéaires. Une variété de guides d'onde à base de jonctions Josephson a été proposée, et certains réalisés au cours des dernières années, avec des applications allant de l'amplification large bande proche de la limite quantique à la génération de paires de photons intriqués et à la transmission non réciproque de signaux.

Cette thèse explore les interactions paramétriques et la génération d'intrication dans une nouvelle architecture de guide d'onde à base de jonction Josephson. Basé sur un agencement des composants micro-onde micro-fabriqués en configuration passe-haut, celui-ci implémente un matériau artificiel présentant une dispersion d'ondes qui correspond à un indice de réfraction négatif. Cette dispersion, combinée à la non-linéarité des jonctions Josephson, permet divers processus paramétriques allant de l'amplification à large bande auto-adaptée en phase de modes co-propageants, à l'amplification et au mélange d'ondes se propageant dans des directions opposées. La réalisation d'un tel guide d'onde ouvre de nouvelles perspectives dans le cadre des amplificateurs et convertisseurs paramétriques à ondes progressives à base de jonctions Josephson.

Au-delà de ces processus optiques non linéaires classiques, ce guide d'onde permet également de générer des états non classiques de la lumière, tels que des états du vide comprimés à deux modes à large bande, et des paires de photons intriqués spatialement séparés. Nous présentons ici les mesures de tels états quantiques obtenues avec cette architecture novatrice de guide d'onde à indice négatif, ouvrant de nouvelles perspectives pour la détection quantique, les protocoles de radar et d'illumination quantique, et plus généralement pour les applications micro-ondes nécessitant des photons intriqués se propageant dans différentes directions.

CONTENTS

1 INTRODUCTION AND SUMMARY 1
1.1 Engineering artificial materials . . . 2
1.1.1 Right- and Left-Handed materials . . . 3
1.1.2 Nonlinear metamaterials . . . 3
1.2 Josephson junction . . . 4
1.2.1 The Josephson effect . . . 4
1.2.2 Circuit representation . . . 5
1.3 Parametric interactions . . . 6
1.3.1 Parametric amplification . . . 7
1.3.2 Frequency conversion . . . 7
1.3.3 Cavities and waveguides . . . 7
1.4 Nonclassical states of light . . . 9
1.4.1 Hamiltonian of a Josephson junction . . . 9
1.4.2 Squeezing: a brief introduction . . . 10
1.5 Summary . . . 11
1.5.1 Thesis overview . . . 11
2 JOSEPHSON WAVEGUIDES 13
2.1 Transmission lines . . . 13
2.1.1 Right-Handed topology . . . 15
2.1.2 Left-Handed topology . . . 17
2.1.3 Composite topology . . . 18
2.2 Josephson transmission lines . . . 20
2.2.1 Dispersion relation . . . 20
2.2.2 Equation of motion . . . 24
2.3 Amplification . . . 28
2.3.1 Coupled mode equations . . . 29
2.3.2 Phase-matching . . . 34
2.3.3 Gain . . . 40
2.4 Frequency conversion . . . 47
2.4.1 Coupled mode equations . . . 48
2.4.2 Phase-matching . . . 52
2.4.3 Attenuation . . . 53
2.5 Conclusions . . . 56
3 EXPERIMENTAL SETUP 59
3.1 Extending the measurements bandwidth . . . 59
3.1.1 General requirements . . . 60
3.1.2 High-frequency output line . . . 60
3.2 Calibration . . . 61
3.2.1 Transmission . . . 63
3.2.2 Gain and noise . . . 63
3.3 Full setup . . . 65
3.3.1 Continuous wave measurements . . . 65

3.3.2 Quadratures measurements 68
4 CIRCUIT DESIGN AND FABRICATION 73
4.1 Josephson junctions fabrication 73
4.1.1 The overlap junction technic 75
4.1.2 Room temperature DC measurements 77
4.2 Parallel plate capacitors fabrication 78
4.2.1 Dielectric deposition 79
4.2.2 Dielectric characterization 81
4.2.3 Lumped-element resonators 83
4.3 Assembling things together 86
4.3.1 Josephson waveguides fabrication 87
4.3.2 Full recipe 88
5 JOSEPHSON WAVEGUIDE WITH NEGATIVE REFRACTIVE INDEX 95
5.1 The device 95
5.1.1 Description of the sample 96
5.1.2 Sample's parameters 97
5.2 Linear spectroscopy 98
5.2.1 Electrical length 98
5.2.2 Attenuation 100
5.3 Nonlinear spectroscopy 101
5.3.1 Amplification 103
5.3.2 Frequency conversion 112
5.4 Conclusions 117
5.4.1 Key results 117
5.4.2 Perspectives and open questions 118
6 ENTANGLED PHOTON PAIRS GENERATION 121
6.1 Quantum optics with Josephson waveguides 121
6.1.1 Two-mode squeezing with a parametric amplifier 123
6.1.2 Quantifying quantum correlations 125
6.2 Measuring two-mode vacuum squeezing 127
6.2.1 Experimental setup 127
6.2.2 Quadratures measurements and calibration . . 129
6.3 Entanglement generation in a negative index Josephson waveguide 131
6.3.1 Entanglement between two counter-propagating traveling modes 132
6.3.2 Co-propagating modes entanglement generation 136
6.4 Conclusions 139
6.4.1 Key results 139
6.4.2 Perspectives and open questions 140
7 CONCLUSIONS AND PERSPECTIVES 141
7.1 Conclusions 141
7.1.1 Summary of the results 142
7.2 Perspectives 148
7.2.1 Open questions 148
7.2.2 Future possibilities 151

BIBLIOGRAPHY 155

LIST OF FIGURES

Figure 1.1 Permittivity - permeability diagram 2
Figure 1.2 Right- and Left-Handed materials 3
Figure 1.3 Schematic representation of a Josephson junction 5
Figure 1.4 Schematic representation of nonlinear cavities and waveguides 8
Figure 2.1 Transmission line definition 14
Figure 2.2 Circuit diagram of right- and left-handed networks, and of a composite one 16
Figure 2.3 Dispersion relation of right- and left-handed transmission lines and of a composite one . . . 17
Figure 2.4 Characteristic impedance of a composite right-left-handed transmission line 19
Figure 2.5 Circuit diagram of Josephson junctions based right- and left-handed networks 21
Figure 2.6 Dispersion relation and characteristic impedance of right- and left-handed Josephson transmission lines 23
Figure 2.7 Finite size effects on the dispersion relations of right- and left-handed Josephson transmission lines 24
Figure 2.8 Circuit diagram with unit cells zoom of Josephson right- and left-handed transmission lines . 25
Figure 2.9 Phase-mismatch in a bare Josephson right-handed transmission line 35
Figure 2.10 Dispersion-engineered phase-matching in a Josephson right-handed transmission line 36
Figure 2.11 Reversed-Kerr phase-matching in a Josephson right-handed transmission line 37
Figure 2.12 Self-phase-matching in a Josephson left-handed transmission line. 38
Figure 2.13 Phase-matching of counter-propagating modes in a Josephson left-handed transmission line . 40
Figure 2.14 Signal gain comparison between different Josephson transmission line 42
Figure 2.15 Counter-propagating signal and idler modes gains in a left-handed Josephson transmission line 45
Figure 2.16 Signal gain dependence on the device's length for the counter-propagating process 46

Figure 2.17 Phase-matching of frequency conversion processes in a Josephson left-handed transmission line . . . 53
Figure 2.18 Total phase-mismatch of the frequency conversion processes in a Josephson left-handed transmission line . . . 54
Figure 2.19 Signal attenuation in a left-handed Josephson transmission line . . . 54
Figure 2.20 Signal attenuation dependence on the device's length . . . 56
Figure 2.21 Signal attenuation dependence on the pump frequency . . . 56
Figure 3.1 Schematic of the high-frequency output line . 61
Figure 3.2 Simplified schematic of the experimental setup used for the calibration . . . 62
Figure 3.3 Illustration of the Y-factor calibration method 64
Figure 3.4 Experimental setup for continuous wave measurements . . . 66
Figure 3.5 Input and output lines calibration . . . 67
Figure 3.6 Experimental setup for the quadratures measurements of counter-propagating modes . . . 69
Figure 3.7 Experimental setup for the quadratures measurements of co-propagating modes . . . 71
Figure 4.1 Illustration of the overlap junction technic . . . 76
Figure 4.2 Homogeneity maps of the junctions critical current density j_c . . . 78
Figure 4.3 Illustration of the oxide multilayer deposition 80
Figure 4.4 AFM characterization of the AlO_x thickness . . 81
Figure 4.5 TEM images of an $Al/AlO_x/Al$ capacitor . . . 82
Figure 4.6 Lumped-element resonators illustration 84
Figure 4.7 Lumped-element resonators simulations 85
Figure 4.8 Lumped-element resonators measurements . . 86
Figure 4.9 Illustration of the fabrication process of Josephson waveguides . . . 87
Figure 5.1 The negative index Josephson waveguide . . . 96
Figure 5.2 Simplified schematic of the experimental setup used for the linear spectroscopy . . . 99
Figure 5.3 Normalized S_{21} parameter of a left-handed transmission line . . . 100
Figure 5.4 S_{21} and S_{12} nonlinear parameters of a negative index Josephson waveguide . . . 102
Figure 5.5 Phase-matching conditions for the amplification processes in a negative index Josephson waveguide . . . 104

Figure 5.6 Simplified schematic of the experimental setup used for the nonlinear spectroscopy of the amplification processes . . . 105
Figure 5.7 Normalized gain of a negative index Josephson waveguide . . . 106
Figure 5.8 Gain profiles of the counter-propagating amplification process . . . 108
Figure 5.9 Pump power dependent gain of a negative index Josephson waveguide . . . 110
Figure 5.10 Pump frequency dependent gain of a negative index Josephson waveguide . . . 111
Figure 5.11 Phase-matching conditions for the amplification processes in a negative index Josephson waveguide . . . 113
Figure 5.12 Simplified schematic of the experimental setup used for the nonlinear spectroscopy of the frequency conversion processes . . . 114
Figure 5.13 Pump frequency dependent isolation of a negative index Josephson waveguide . . . 115
Figure 5.14 Pump power dependent isolation of a negative index Josephson waveguide . . . 116
Figure 6.1 Schematic of the generation and detection process for the counter-propagating two-mode vacuum squeezing experiment . . . 128
Figure 6.2 Quadratures phase space distribution of two counter-propagating modes . . . 130
Figure 6.3 Covariance matrix of two counter-propagating modes . . . 131
Figure 6.4 Pump power dependence of counter-propagating squeezing and logarithmic negativity . . . 134
Figure 6.5 Pump phase dependence of squeezing and logarithmic negativity . . . 135
Figure 6.6 Logarithmic negativity dependence on the emission bandwidth . . . 136
Figure 6.7 Pump power dependence of squeezing and logarithmic negativity . . . 138
Figure 7.1 Co-propagating gain comparison between different Josephson waveguide . . . 142
Figure 7.2 Signal gain comparison between co- and counter-propagating amplification in a Left-Handed Josephson waveguide . . . 143
Figure 7.3 Signal attenuation comparison between co- and counter-propagating attenuation in a Left-Handed Josephson waveguide . . . 144
Figure 7.4 Schematic of the high-frequency output line . 144
Figure 7.5 Illustration of the fabrication process . . . 145

Figure 7.6 Normalized S_{21} parameter of a left-handed transmission line . . . 146
Figure 7.7 S_{21} and S_{12} nonlinear parameters of a negative index Josephson waveguide . . . 147
Figure 7.8 Pump phase dependence of squeezing and logarithmic negativity . . . 148
Figure 7.9 Normalized gain of a negative index Josephson waveguide . . . 149
Figure 7.10 Pump power dependence of squeezing and logarithmic negativity . . . 150
Figure 7.11 Right-Handed Josephson waveguide with dispersion engineering . . . 152

LIST OF TABLES

Table 2.1 Coefficients in the coupled mode equations of Josephson transmission lines . . . 30
Table 2.2 Coefficients in the coupled mode equations of Josephson transmission lines . . . 31
Table 2.3 Parameters of the Josephson transmission lines used to simulate the gain profiles . . . 41
Table 2.4 Parameters of the left-handed Josephson transmission lines used to simulate the attenuation profiles . . . 55
Table 3.1 Components of the high-frequency output line 61
Table 4.1 Ground plane fabrication recipe . . . 89
Table 4.2 First layer fabrication recipe . . . 90
Table 4.3 Second layer junctions fabrication recipe . . . 91
Table 4.4 Second layer capacitors fabrication recipe . . . 92
Table 4.5 Dicing fabrication recipe . . . 93
Table 5.1 Main parameters of the Left-Handed sample . 97
Table 5.2 Comparison between designed and measured sample's parameters . . . 101
Table 6.1 Scattering coefficients of the amplification processes . . . 124
Table 6.2 Pump, signal and idler frequencies, measurement efficiencies and system noise temperatures for the counter-propagating squeezing measurements . . . 133

Table 6.3 Pump, signal and idler frequencies, measurement efficiencies and system noise temperatures for the co-propagating squeezing measurements 137

ACRONYMS

cQED circuit Quantum ElectroDynamic

JJ Josephson Junction

SIS Superconductor-Insulator-Superconductor

SNAIL Superconducting Nonlinear Asymmetric Inductive eLement

rf-SQUID Radio Frequency Superconducting Quantum Interference Device

4WM Four-Wave Mixing

3WM Three-Wave Mixing

RWA Rotating-Wave-Approximation

1D one-dimensional

TL Transmission Line

LH Left-Handed

LHTL Left-Handed Transmission Line

RH Right-Handed

RHTL Right-Handed Transmission Line

JTL Josephson Transmission Line

TWPA Traveling Wave Parametric Amplifier

TWPC Traveling Wave Parametric Converter

DE Dispersion-Engineered

RK Reversed-Kerr

RPM Resonant Phase-Matching

JPA Josephson Parametric Amplifier

CMEs Coupled Mode Equations

VNA Vector Network Analyzer

FPGA Field Programmable Gate Array

LO Local Oscillator
ADC Analog to Digital Converter
DAC Digital to Analog Converters
SNR Signal to Noise Ratio
HEMT High-Electron-Mobility-Transistor
DUT Device Under Test
SOLT Short-Open-Load-Thru
SOLR Short-Open-Load-Reciprocal
TRL Thru-Reflect-Line
SA Spectrum Analyzer
MWS Microwave Source
IDR Inverted Dilution Refrigerator
SNTJ Shot Noise Tunnel Junction
VTS Variable Temperature Stage
SEM Scannig Electron Microscope
CRLH Composite Right-Left-Handed
AFM Atomic Force Microscopy
TEM Transmission Electron Microscopy
PPC Parallel-Plate Capacitor
RIE Reactive Ion Etching
ALD Atomic Layer Deposition
USB Ultrasonic Bath
e-beam electron-beam
e-gun electron-gun
RT Room Temperature

1 INTRODUCTION AND SUMMARY

Optically pumping ruby crystals led to the emission of coherent light and the consquent invention of the laser[1] [1]. Entangled photon pairs allowed to support quantum mechanics over hidden variables theories [2]. The implementation of squeezed radiation is now used to improve the sensitivity of gravitational-waves detectors [3]. These are just few examples highlighting the pivotal role of light–matter interactions in advancing both fundamental physics and technological innovation[2]. From classical electromagnetism to modern quantum optics, every discovery has opened up a new way of seeing and understanding nature.

Historically, most experiments involving the electromagnetic field explored its interactions with naturally occurring media. Exciting new possibilities emerged from the study of metamaterials [4, 5], which allow to realize artificial materials able to show electromagnetic properties that are difficult or impossible to find in naturally occurring ones, as high frequency magnetism [6] and negative refraction [7].

In most recent years, significant interest has been given to the study of microwave photons interacting with superconducting circuits and metamaterials [8–11]. They enable for unprecedented control over light-matter interactions and nonlinearities, allow to reduce thermal energy $k_B T$ below the photon energy $\hbar\omega$ associated with the electromagnetic wave of interest, present low losses, hence long coherence times, and exploit the technical tools developed for microelectronics and microwave engineering, which result in an ease of design and fabrication. These are just some motivations that make superconducting circuits among the most advanced architectures for quantum computing [12], sensing [13] and information [14] purposes.

The condition $\hbar\omega \gg k_B T$ is satisfied for superconducting circuits when operated at 20 mK in the microwave C-band; indeed $6\,GHz \times h/k_B \sim 300\,mK$

Such features, along with the latter applications, motivated many experiments on superconducting waveguides based on one-dimensional (1D) metamaterials because of their direct implications in quantum simulations [15–17], near-quantum-limited broadband amplification [18–21], multimode entanglement generation [22–25], nonreciprocal signal transmission [26–28], and nondestructive quantum photon counting [29].

These thesis places itself within such thriving field of research. It explores the properties of a novel superconducting waveguide architecture based on a negative refractive index artificial material. The main concern of this introductory chapter is to describe, although not in

1 Acronym of light amplification by stimulated emission of radiation.
2 Which, anyway, are profoundly related to each other.

detail, basic concepts which will be useful through the thesis, starting from the metamaterial one. We refer the reader to the following useful articles and thesis on the topics of this thesis [11, 21, 30–37].

1.1 ENGINEERING ARTIFICIAL MATERIALS

The unique potential of superconducting waveguides lies in the possibility of engineering them at sub-wavelength scales, allowing for complete control over wave dispersion and nonlinear interactions. Such engineering is based on the metamaterial concept.

Metamaterials are artificial materials, composed of a collection of repeated elements designed to have an effective response to applied electromagnetic fields. As long as the wavelengths of the incident radiation is much larger than the size and spacing of the elements, we can consider such collection as a homogeneous material characterized by two macroscopic electromagnetic parameters: an effective electric permittivity, ε, and an effective magnetic permeability, μ.

Metamaterials allow to realize structures, with tailored values of ε and μ, at least in some frequency ranges. Depending on their relative signs, the response of the material to electromagnetic radiation changes. However, not all the combinations $(\pm\varepsilon, \pm\mu)$ can be easily found in nature, as shown in Figure 1.1 [39]. For example, dielectric materials, like glass, show positive values for both ε and μ. Others, such as many metals in the visible spectrum, have a negative ε, which can result in the formation of collective excitations of electrons at the metal surface, known as surface plasmons [40, 41].

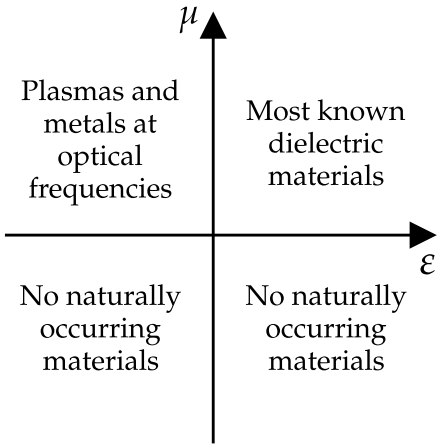

Figure 1.1: ε - μ diagram Examples of naturally occurring materials for each combination of ε and μ. Adapted from [38, 39].

On the other hand, materials with either negative μ or both negative μ and ε are quite uncommon. For each quadrant of Figure 1.1 different and interesting electromagnetic phenomena can be observed. A prominent examples of which is negative refraction [7] in artificial materials belonging to the bottom-left quadrant [38]. The latter are usually dubbed as *left-handed*, in contrast to their *right-handed* counterparts in the top-right quadrant.

1.1.1 Right- and Left-Handed materials

Thus, a simultaneous change of sign of both ε and μ, whose product is equal to the square of the material's index of refraction, has profound effects on wave propagation.

*In ordinary materials, with $\varepsilon > 0$ and $\mu > 0$, the vectors **E**, **B**, and **k** follow the "right-hand" rule*

These effects have been first addressed by Veselago [38] in 1968, who showed, starting from Maxwell's equations, that, if $\varepsilon < 0$ and $\mu < 0$, the electric **E** and magnetic **B** fields, together with the wavevector **k** of the considered monochromatic plane wave, form a left-handed set of vectors. Hence, he dubbed this kind of materials as Left-Handed (LH). As a consequence, wave propagation is reversed compared to the energy flux, given by the Poynting vector $\mathbf{S} = \mathbf{E} \times \mathbf{B}$, with phase $\mathbf{v}_\varphi$ and group $\mathbf{v}_g$ velocities which have opposite signs. The difference between

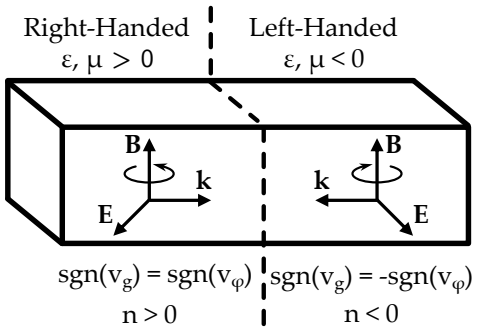

Figure 1.2: Right- and Left-Handed materials
Schematic representing the main differences between Right- and Lehft-Handed materials.

left- and right-handed materials are schematically summarized in Figure 1.2. Remarkably, the refractive index of LH materials is negative, as experimentally verified in 2001 by R. A. Shelby *et al.* [42]. For this reason they have been also dubbed as *negative-index* materials and they attracted much attention in the early 2000s [7, 39].

However, these unique materials do not naturally occur and have to be realized artificially [43]. A particularly suited approach is based on microwave Transmission Lines (TLs) [44–47]; especially within the superconducting circuits framework [48], where Left-Handed Transmission Lines (LHTLs) propose themselves as promising platforms for quantum simulation architectures [15, 49, 50] and to realize nonlinear parametric interactions [51].

1.1.2 Nonlinear metamaterials

The possibility of engineering light-matter interactions made metamaterials appealing also in the realm of nonlinear optics. First, they allow to realize desired nonlinear responses controlling both the electric and magnetic nonlinearities. Second, the magnitude of such nonlinearities can be enhanced compared to conventional nonlinear materials.

Two different strategies can been followed to realize nonlinear artificial materials [5]:

1. Insertion of nonlinear elements in the metamaterial structure, which is particularly fruitful for long-wavelengths applications[3].
2. Embedding the metamaterial in a nonlinear host medium, which is more feasible at optical frequencies.

Both strategies, however, require low values of losses. The latter can be reduced following two possible path [9]:

A. A passive one, with the replacement of metallic elements with superconducting ones [8].
B. An active one, with the insertion of active components to provide gain to overcome losses [52].

Here, we fall into both first strategies (1 and A). We make use of superconducting metamaterials, which offer both low losses and nonlinearities. The latter are brought by either the presence of Josephson Junctions (JJs) [19, 20] or exploiting high kinetic inductance superconductors [18, 53]. We deal with the former ones.

1.2 JOSEPHSON JUNCTION

One of the main building blocks of the superconducting circuit toolbox is the JJ. The latter consists of two superconducting electrodes separated by a weak-link [54]. The material realizing such link, which can be an insulator, a semiconductor or a metal, plays a crucial role in the junction behavior [55]. In our case, Superconductor-Insulator-Superconductor (SIS) junctions have been used. The most remarkable property of these devices is the Josephson effect [56].

1.2.1 The Josephson effect

In 1962 Josephson realized that a dissipationless flow of a phase-coherent current (supercurrent) could exist in a superconducting tunnel junction [57]:

$$I_j(\phi) = I_c \sin(\phi_1 - \phi_2) \tag{1.1}$$

where $\phi = \phi_1 - \phi_2$ is the difference between the phases of the superconducting condensate of each electrode, and I_c is the critical current, which gives the maximum superconducting current that can flow through the junction before its transition to a normal behavior. The

3 The addition of nonlinear components into each unit cell is easier from a technological point of view for long-wavelengths.

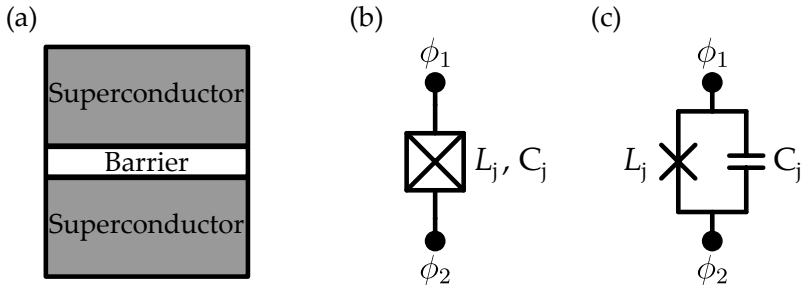

Figure 1.3: Schematic representation of a Josephson junction
(a) Schematic representing a Josephson junction as a tunnel junction with two superconducting electrodes separated by a barrier.
(b) Circuit representation of a Josephson junction embedding both the junction inductance L_j and its capacitance C_j.
(c) Circuit representation of a Josephson junction as an LC oscillator, separating the inductive and capacitive terms.

value of I_c depends on the geometry and transparency of the barrier separating the two electrodes.

The Josephson junction is also characterized by a second relation, which links the superconducting phase difference ϕ to the magnetic flux difference $\Phi(t)$ between the two electrodes:

$$\frac{d\phi(t)}{dt} = \frac{1}{\varphi_0}\frac{d\Phi(t)}{dt} \tag{1.2}$$

where $\varphi_0 = \hbar/(2e)$ is the reduced superconducting flux quantum; with e the elementary charge and $\hbar$ the reduced Planck constant.

1.2.2 Circuit representation

Therefore, combining the two previous relations the superconducting current flowing through the junction can be expressed as [33]:

$$I_j(\Phi) = I_c \sin\left(\frac{\Phi}{\varphi_0}\right), \tag{1.3}$$

which allows to model the junction as a nonlinear inductor:

$$L_j(t) = \left[\frac{\partial_t I(t)}{\partial_t \Phi(t)}\right]^{-1} = \frac{L_j}{\cos\left(\frac{\Phi(t)}{\varphi_0}\right)} = \frac{L_j}{\sqrt{1-(I(t)/I_c)^2}}, \tag{1.4}$$

where, in the last equality, we have used Equation 1.3[4], and where we have defined the Josephson inductance $L_j = \varphi_0/I_c$. The latter represents the linear inductance of the junction. Indeed, in the limit $\Phi \ll \varphi_0$, we can perform a Taylor expansion to obtain[5]:

$$I_j(t) \approx \frac{\Phi(t)}{L_j} - \frac{\Phi^3(t)}{I_c^2 L_j^3} + O(\Phi^5), \tag{1.5}$$

4 and the trigonometric identity $\sin^2(x) + \cos^2(x) = 1$.
5 Such expansion is justified as long as the current flowing through the junction I remains small compared to its critical current I_c.

with the first term corresponding to the characteristic equation of a linear inductor.

The Josephson capacitance has an important effect in building Josephson waveguides, as we will see in Chapter 2

Besides this inductive term, the capacitive effect between the two superconducting leads has to be taken into account. It can be modeled as a Parallel-Plate Capacitor (PPC) C_j. Thus, a Josephson junction is represented as a nonlinear LC electrical circuit, as shown in Figure 1.3(c), with resonant frequency $\omega_j = 1/\sqrt{L_j C_j}$.

ANALOGY WITH A NONLINEAR MEDIUM The expression of Equation 1.5, up the the leading nonlinear order, is formally equivalent to the polarization response of a nonlinear material to the electric field of an electromagnetic wave:

$$\mathbf{P}(t) \approx \varepsilon_0 \left(\chi^{(1)} \mathbf{E}(t) + \chi^{(2)} \mathbf{E}^2(t) + \chi^{(3)} \mathbf{E}^3(t) + \cdots \right), \tag{1.6}$$

where $\chi^{(n)}$ is the n-th order material's susceptibility. Note that in the case of a JJ we have only odd values of n, with the lowest nonlinear order corresponding to the $\chi^{(3)}$ nonlinearity. It is worth mentioning that, using more complex junctions composite structures [58–60], the $\chi^{(2)}$ nonlinearity can be obtained as well. In general, the $\chi^{(2)}$ and $\chi^{(3)}$ susceptibilities govern nonlinear interactions between waves at 3 or 4 distinct frequencies [61]. Therefore, JJs can be used to realize superconducting nonlinear metamaterials enabling Three-Wave Mixing (3WM) or Four-Wave Mixing (4WM) interactions, which are at the heart of parametric amplification and frequency conversion processes.

1.3 PARAMETRIC INTERACTIONS

Parametric amplification and frequency conversion are very fundamental physical processes, in which energy is transferred between different waves via the medium's nonlinear response, without net absorption of energy from the medium itself. Parametric processes have a wide range of applications and apply to mechanical, optical and electronic systems. The term parametric stands for the fact that a parameter of the system, the spring constant, the index of refraction, or the circuit reactance, in the previous cases, is modulated at a certain frequency by a strong pump field. Actually, a classical example is a child standing on a swing, who periodically modulates the system center of mass, and thus the length of the swing, raising it when approaching the peak height and lowering it when swinging away from it. This results in a periodical pumping of energy into the system at twice its rest frequency, causing the parametric amplification of the motion [32].

1.3.1 Parametric amplification

Besides the latter everyday life example, parametric amplification plays a significant role in nonlinear optics for nowadays quantum technologies, especially for superconducting quantum computing and information, as it allows to realize quantum-limited amplification. For instance, the latter is fundamental to measure, as quickly and precisely as possible, the low-power microwave fields embedding superconducting qubits state information [34].

Ultralow-noise parametric amplifiers can be realized exploiting parametric interactions in nonlinear materials, which, for superconducting applications usually consists of JJs-based circuits. Thus, by modulating the nonlinear inductance of the junctions, with an intense electromagnetic field of frequency f_p, a weak signal field, of frequency f_s, can be amplified. The mixing of the two fields, within the material, generates a sideband, usually called idler, at the frequency ω_i. The latter is equal to $f_i = f_p - f_s$, in the 3WM case, or to $f_i = 2f_p - f_s$, in the 4WM one. This mixing process transfers energy from the pump to the signal and idler fields resulting in their amplification. The signal and idler frequencies define whether one single mode is amplified, in the *degenerate* $f_s = f_i$ case, or the two of them, in the *nondegenerate* $f_s \neq f_i$ one [30, 31]. The former situation is also known as *phase-sensitive*, because only the mode quadrature in-phase with the pump is amplified while the other one is deamplified [62, 63]. On the other hand, an amplifier that transform both input quadratures represents the so-called *phase-preserving* amplifiers [64].

1.3.2 Frequency conversion

If, instead of pumping the nonlinear material at the sum of the signal and idler frequencies, we do so at their difference, a different parametric process can be obtained: frequency conversion. Now, a signal field at frequency f_s can be either up-converted at the frequency $f_u = f_s + nf_p$ or down-converted at $f_d = f_s - nf_p$, with n equal to 1 or 2, depending on the order of the nonlinearity.

Thus, this process effectively removes energy from one frequency to place it at another one, with applications related to nonreciprocal signals processing, as directional amplification and circulation [65–67].

1.3.3 Cavities and waveguides

Both previous processes occurs within the nonlinear material, thus an important feature consists in enhancing the interaction time inside it. Two main strategies, schematically shown in Figure 1.4, can be pursued to this end: embedding the nonlinear medium in a cavity, or in a waveguide.

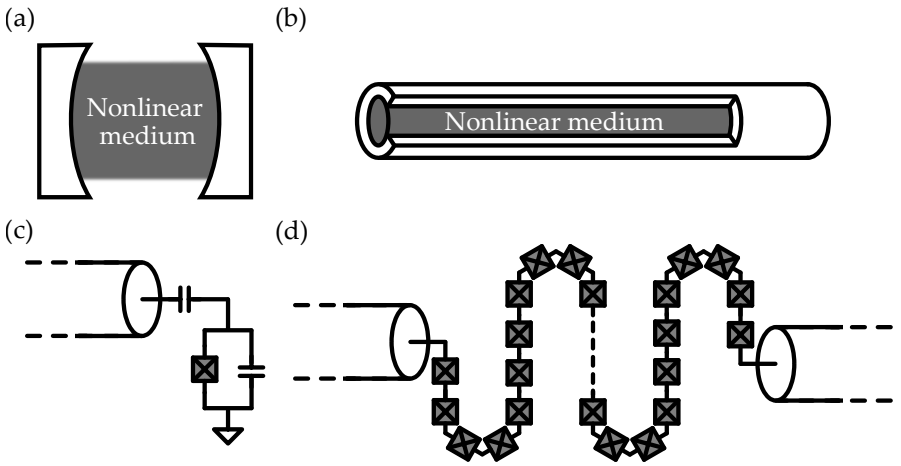

Figure 1.4: Schematic representation of nonlinear cavities and waveguides
(a) Schematic representing an optical nonlinear cavity.
(b) Schematic representation of an optical nonlinear waveguide.
(c) Schematic representing a superconducting nonlinear cavity.
(b) Schematic representation of a superconducting nonlinear waveguide.

CAVITIES Placing the nonlinear material inside a cavity, sets the interaction time between the material and the standing waves inside the cavity to the inverse of the cavity linewidth. The simplest superconducting circuit implementation consists in a parallel $L-C$ resonator, with the nonlinearity given by one junction, connected to a transmission line which allows microwave signals to propagate in and out of the circuit. Although being extremely successful [34], this approach sets a constraint on the amplification bandwidth, given the presence of a cavity in the circuit, and on the power handling of the amplifier [68].

WAVEGUIDES On the other hand, creating a nonlinear waveguide allows to increase the physical length of the medium, with the interaction time dependent on the wave velocity. This approach is realized within the superconducting circuit framework with junctions-based TLs, whose impedance is matched to the $50\,\Omega$, composed of thousands of nonlinear elements. As a consequence, these structures support traveling-waves and the bandwidth constraint is removed. Moreover, the nonlinearity is diluted over the device length, increasing the power handling and the number of supported tones. However, designing and fabricating Josephson waveguides is more challenging because of the large number of junctions. Finally, traveling-wave parametric processes requires the fulfillment of a phase-matching condition [21], resulting from the fact that waves at different frequencies travels at different effective velocities inside the nonlinear medium.

For a more detailed description of both resonant and traveling-wave nonlinear structures and of their superconducting circuits implementations, especially as parametric amplifiers, we refer the reader to [37].

1.4 NONCLASSICAL STATES OF LIGHT

Parametric processes in nonlinear materials provide also effective experimental tools to realize nonclassical states of light [61], such as squeezed radiation [69]. The latter are useful resources for a variety of applications ranging from quantum information processing [70], and quantum enhanced detection [71], and can be realized by amplification of vacuum fluctuations [32].

1.4.1 Hamiltonian of a Josephson junction

Given that we speak about nonclassical states of light, it is worth illustrating the quantum mechanical description of JJ. The latter is described as a simple anharmonic oscillator, whose total energy is given by the sum of its charging and inductive energies:

$$H_j = \frac{Q^2}{2C_j} - E_j \cos\left(\frac{\Phi}{\varphi_0}\right), \tag{1.7}$$

where we have defined the Josephson energy $E_j = \varphi_0^2/L_j$ and introduced the charge Q on the capacitor. We can pass from a classical to a quantum description by replacing the classical variables with the corresponding operators [33], satisfying the communication relation $\left[\hat{\Phi}, \hat{Q}\right] = i\hbar$.

Now, given that the junctions in Josephson Parametric Amplifiers (JPAs) are weakly nonlinear, we can expand the cosine up to the leading nonlinear order. Defining the usual bosonic annihilation and creation operators:

$$\begin{cases} \hat{\Phi} = \Phi_{zpf}\left(\hat{a} + \hat{a}^\dagger\right), \\ \hat{Q} = -iQ_{zpf}\left(\hat{a} - \hat{a}^\dagger\right), \end{cases} \tag{1.8}$$

where $\Phi_{zpf} = \sqrt{\frac{\hbar}{2\omega_j C_j}}$ and $Q_{zpf} = \sqrt{\frac{\hbar\omega_j C_j}{2}}$, gives [72]:

$$\hat{H}_j \approx \hbar\omega_j \hat{a}^\dagger\hat{a} + \frac{\hbar\chi}{6}\left(\hat{a} + \hat{a}^\dagger\right)^4. \tag{1.9}$$

where $\chi = -\frac{E_j \Phi_{zpf}^4}{4}$. Within the Rotating-Wave-Approximation (RWA), this hamiltonian is the one of a nonlinear Kerr-medium:

$$\hat{H}_K \approx \hbar(\omega_j - 2\chi)\hat{a}^\dagger\hat{a} + \frac{\hbar\chi}{6}\hat{a}^{\dagger 2}\hat{a}^2. \tag{1.10}$$

The latter can be used to realize squeezing interactions by means of resonant or traveling-wave JPAs. Such interactions, in the case of $\chi^{(3)}$, can be described by an effective Hamiltonian which, in the rotating frame, is given by:

$$\hat{H}_{Sq} = \hbar\eta \left(a_{\mathrm{p}}^2 \hat{a}_{\mathrm{s}}^\dagger \hat{a}_{\mathrm{i}}^\dagger + a_{\mathrm{p}}^{*2} \hat{a}_{\mathrm{s}} \hat{a}_{\mathrm{i}} \right) \tag{1.11}$$

where $\hat{a}_{\mathrm{m}}$, with $\mathrm{m} = \{\mathrm{s,i}\}$, represent the signal and idler modes operators, $a_{\mathrm{p}} = \left|A_{\mathrm{p}}\right| e^{i\phi_{\mathrm{p}}}$ is the coherent classical pump driving the process, and η is the 4WM nonlinear interaction strength, which depends on the details of the circuit [72, 73].

1.4.2 Squeezing: a brief introduction

One of the fundamental differences between classical and quantum mechanics lies in Heisenberg's uncertainty principle. The latter sets a limit to the precision with which conjugate variables describing a physical system, such as position $\hat{x}$ and momentum $\hat{p}$ of a massive particle, can be simultaneously known. In particular, it gives a lower bound to the product of their standard deviations:

$$\sigma_x \sigma_p \geq \frac{\hbar}{2}, \tag{1.12}$$

where $\sigma_r = \sqrt{\langle \hat{r}^2 \rangle - \langle \hat{r} \rangle^2}$ with $r = \{x, p\}$.

One of the main consequences is related to quantum fluctuations: now, position and momentum of a particle can not be simultaneously set to zero, as in classical mechanics. Thus, its ground state will always present some noise. Such situation correspond to the equality of Equation 1.12 with $\sigma_x = \sigma_p$. Luckily for us, such noise can actually be reduced, at least on one of the two quadratures, or used as a source of information, thanks to the generation of the so-called squeezed states. A state is said to be squeezed below vacuum if the variance of one of the two quadratures is lower than $\hbar/2$, resulting in $\sigma_x \neq \sigma_p$.

Here, instead of position and momentum of a massive particle, we deal with the quadratures of the electromagnetic field, which are defined as:

$$\begin{cases} \hat{x} = \frac{\hat{a}+\hat{a}^\dagger}{2}, \\ \hat{p} = \frac{\hat{a}-\hat{a}^\dagger}{2i}, \end{cases} \tag{1.13}$$

where $\hat{a}$ and $\hat{a}^\dagger$ are annihilation and creation field's mode operators, respectively, satisfying the communication relation $[\hat{a}, \hat{a}^\dagger] = 1$.

Squeezed states of light [69] are of particular interest for sensing applications [3, 71], as pointed out by Caves in 1981 [74] in the framework of interferometric detection of gravitational waves. Moreover, squeezing of two vacuum modes of the electromagnetic field is a relevant

resource for quantum information purposes by means of continuous variables [75, 76]. Indeed, the concept of squeezing the quadratures of a single-mode can be extended to multiple modes. A two-mode vacuum squeezed state presents quantum correlations between the four quadratures describing the system, which is equivalent to the generation of entanglement between the two modes.

SQUEEZING WITH JOSEPHSON PARAMETRIC AMPLIFIERS Squeezed states can be achieved within the superconducting circuits framework exploiting the nonlinearity brought by Josephson junctions in JPAs, as first demonstrated in resonant structures [77–81]. More recently, the fervent effort in developing Josephson-based Traveling Wave Parametric Amplifiers (TWPAs) allowed to observe broadband two-mode vacuum squeezing [22–24].

Of particular interest are sources of two-photons entangled states, with the photons propagating in different spatial directions. The latter provide key tools for quantum sensing and computing applications, with realizations spanning from the optical [16, 82] to the microwave [80] domain. However, a microwave traveling-wave implementation of such sources is still missing, to the best of our knowledge. The realization of the latter, exploiting a negative-index Josephson waveguides, is probably the main result of this thesis, as we will see in Chapter 6.

1.5 SUMMARY

Besides this introductory chapter, this thesis contains six others, which start from a classical description of Josephson waveguides and of the parametric processes enabled by them, and end with the measurements of quantum states of light, passing by their fabrication. A more detailed overview of the manuscript is as follows.

1.5.1 Thesis overview

In Chapter 2, we describe how to exploit different design topologies of Josephson waveguides to realize artificial materials with tailored wave dispersion and nonlinear interactions to enable the desired parametric processes. First, we give a brief introduction on linear transmission lines, focusing on describing the two design topologies of interest for this thesis. Then, we will introduce the nonlinearity adding the JJs to the networks and discuss the different parametric processes enabled by the two topologies. A particular focus will be given to the amplification ones and to the differences between the phase-matching mechanisms enabled by the Right-Handed (RH) and LH topologies. Frequency conversion processes will be described as well, especially in the context of the LH topology.

In Chapter 3 we briefly discuss the experimental setups used to measure the samples, for both continuous-wave and pulsed characterizations, and we describe calibration methods. However, particular space is given to the improvement of the measurement bandwidth, which now allows to measure from 3 GHz up to the Ku-band.

In Chapter 4 we detail the fabrication process, which have been devised to realize the samples described in this thesis. We stress the novelty and flexibility of the process in the framework of Josephson waveguides, showing how both RH and LH networks can be realized with minimal changes. Finally, we report the characterization of the parallel-plate capacitors, which are the main building blocks, together with the junctions, of the waveguides.

In Chapter 5 we describe the first realization of a negative-index Josephson waveguide showing nonlinear traveling-wave parametric interactions. First, we discuss its linear properties. Then, the focus moves to the nonlinear behavior. The Josephson junctions nonlinearity, together with the LH dispersion enables various parametric processes, ranging from broadband amplification of signal and idler modes traveling in the same direction to both frequency conversion and amplification of counter-propagating waves. We detail the measurements of all these different parametric processes. A special consideration is given to the two amplification processes.

In Chapter 6 we report about the experimental investigation of the quantum properties of a negative index material. We demonstrate the flexibility of Josephson Transmission Lines (JTLs) with LH topology as sources of entangled radiation by describing the measurements of both co- and counter-propagating signal and idler entangled modes.

In **??**, we summarize the key results reported in this thesis and outline the main perspectives enabled by this work. We focus on both ongoing efforts to better understand the nonlinear dynamics in the described devices and on possible future improvements and novel applications.

2 JOSEPHSON WAVEGUIDES

Josephson waveguides have generated significant interest in the fields of quantum technology and superconducting quantum information. A variety of Josephson waveguides have been proposed and realized in the recent years [19, 29, 51], with applications ranging from near quantum-limited amplification [20, 83, 84] to multi-mode entanglement generation [22–24] and to non-reciprocal signals transmission [26–28].

All of them are based on weakly nonlinear metamaterials, with the nonlinearity provided by a large number of JJs composing the metamaterial itself. The combination of weak nonlinearity and large spatial extent enables to obtain the desired interaction time without having to rely on the presence of a cavity. This allows for broadband interactions, but brings additional constraints: besides energy conservation, a phase-matching condition must be satisfied. The latter is rendered particularly challenging by both the curvature of the dispersion relation and the presence of the nonlinear effects themselves.

Here, we will describe how to exploit different design topologies of Josephson waveguides to realize artificial materials with tailored wave dispersion and nonlinear interactions, enabling the desired parametric processes. First, we give a brief introduction on linear transmission lines, focusing on describing the two design topologies of interest for this work. Then, we will introduce the nonlinearity adding the JJs to the networks and discuss the different parametric processes enabled by the two topologies. A particular focus will be given to the amplification ones and to the differences between the phase-matching mechanisms enabled by the RH and LH topologies. Frequency conversion processes will be described as well, especially in the context of the LH topology.

2.1 TRANSMISSION LINES

Transmission lines are distributed network, where voltages and currents can vary over their length, which allow for the controlled propagation of electromagnetic waves [85]. Implementations can be based on actual continuous strips of metals sandwiching a dielectric material, as schematically shown in Figure 2.1(a), or on a network of lumped-elements whose size a is smaller than the wavelength λ of the electromagnetic radiation, as shown in Figure 2.1(b). As long as the approximation $\lambda \gg a$ is valid, the two systems are equivalent.

Indeed, considering the lumped-element circuit of Figure 2.1(b) and applying Kirchhoff's laws we can write down for the voltages and currents at each node:

$$\begin{cases} V_{n+1} - V_n = -Z_s I_n, \\ I_n - I_{n-1} = -Y_g V_n, \end{cases} \tag{2.1}$$

where Z_s and Y_g are the series impedance and ground admittance per unit cell.

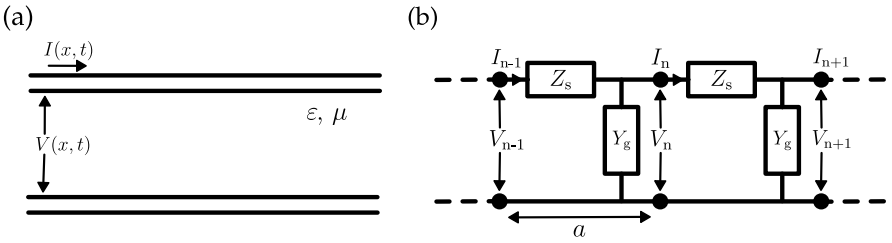

Figure 2.1: Transmission line definition
(a) Continuous transmission line composed by two conductors separated by a dielectric. The voltage $V(z,t)$ and current $I(x,t)$ are also represented.
(b) Discrete transmission line composed by a ladder of unit cells of size a with series impedance Z_s and ground admittance Y_g. Nodes' voltages V_n and currents I_n are also represented.

Now within the long wavelength approximation $\lambda \gg a$, we can take the continuous limit $a \to 0$, while keeping the ratios $z_s = Z_s/a$ and $y_g = Y_g/a$ constant, to obtain the so-called *telegrapher's equations* [85]:

$$\begin{cases} \partial_z V(x,\omega) = -z_s(\omega) I(x,\omega), \\ \partial_z I(x,\omega) = -y_g(\omega) V(x,\omega), \end{cases} \tag{2.2}$$

which can be written as:

$$\begin{cases} \partial_x^2 V(x,\omega) = \gamma^2(\omega) V(x,\omega), \\ \partial_x^2 I(x,\omega) = \gamma^2(\omega) I(x,\omega). \end{cases} \tag{2.3}$$

In general $\gamma = \alpha + i\kappa$ is a complex number, with α being the attenuation constant and κ the wavevector

by defining the propagation constant:

$$\gamma(\omega) = \sqrt{z_s(\omega) y_g(\omega)}. \tag{2.4}$$

Solutions can than be found as traveling voltage and current waves

$$\begin{cases} V(x,\omega) = V_+ e^{-\gamma x} + V_- e^{\gamma x}, \\ I(x,\omega) = I_+ e^{-\gamma x} + I_- e^{\gamma x}, \end{cases} \tag{2.5}$$

propagating in both the $+x$ and $-x$ directions. Using Equation 2.2 and Equation 2.5 allows to define the characteristic impedance $Z_c(\omega)$, that relates voltage and current of the line, as:

$$Z_c(\omega) = \sqrt{\frac{z_s(\omega)}{y_g(\omega)}} = \frac{V_+}{I_+} = \frac{-V_-}{I_-}. \tag{2.6}$$

Therefore the propagation of electromagnetic waves in a transmission line can be modelled in terms of current and voltage waves with wavelength λ and phase and group velocity, v_φ and v_g, given by:

$$\lambda(\omega) = \frac{2\pi}{|\kappa(\omega)|}, \quad v_\varphi(\omega) = \frac{\omega}{\kappa(\omega)} \quad \text{and} \quad v_g(\omega) = \frac{\partial\omega}{\partial\kappa}, \tag{2.7}$$

which are related, through Equation 2.4, to the impedance and admittance per unit length of the line.

The latter can be associated to equivalent permittivity and permeability by drawing an analogy between Equation 2.2 and *Maxwell's equations* in a linear, isotropic and homogeneous medium:

$$\begin{cases} \nabla \times \mathbf{E} = -i\omega\mu\mathbf{H}, \\ \nabla \times \mathbf{H} = i\omega\varepsilon\mathbf{E}, \end{cases} \tag{2.8}$$

which give:

$$\varepsilon(\omega) = \frac{y_g(\omega)}{i\omega}, \quad \text{and} \quad \mu(\omega) = \frac{z_s(\omega)}{i\omega}, \tag{2.9}$$

linking the material properties to the circuit parameters.

Thus, a transmission line approach can be used to realize artificial materials by choosing the appropriate series impedance and ground admittance.

In the next paragraphs we will briefly describe the three main topologies of linear transmission lines, depicted in Figure 2.2, which differentiate themselves by the arrangement of the inductance L and capacitance C in the unit cells. For simplicity, we will consider only lossless lines[1] for which $\alpha = 0$ and $\gamma = i\kappa$.

2.1.1 Right-Handed topology

Usual TL, as the one schematically shown in Figure 2.1(a), are composed of two conductors separated by a dielectric material. The equivalent circuit realizes a low-pass network, as depicted in Figure 2.2(a).

1 Losses can be taken into account considering a complex permittivity $\varepsilon = \varepsilon' - i\varepsilon''$, which gives $\gamma = i\omega\sqrt{\mu\varepsilon} = i\omega\sqrt{\mu\varepsilon'(1 - i\tan\delta)}$, where $\tan\delta = \varepsilon''/\varepsilon'$ is the loss tangent of the material. In the low-loss case we can expand the square root and obtain $\gamma \approx i\omega\sqrt{\mu\varepsilon'}\left(1 - \frac{\tan\delta}{2}\right) \approx \frac{\kappa}{2}\tan\delta + i\kappa$, with $\kappa = \omega\sqrt{\mu\varepsilon'}$ [85].

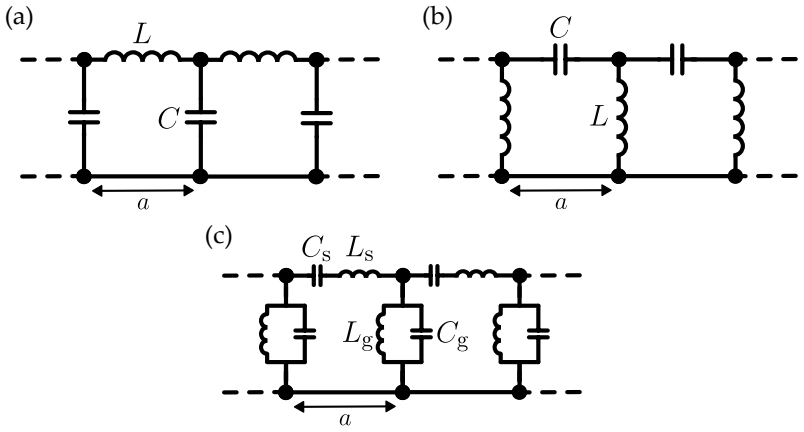

Figure 2.2: Circuit diagram of right- and left-handed networks, and of a composite one
(a) A Right-Handed Transmission Line (RHTL) with each unit cell, of size a, composed of a series inductance L and a ground capacitance C.
(b) A Left-Handed Transmission Line (LHTL) with each unit cell, of size a, composed of a series capacitance C and a ground inductance L.
(c) A composite TL with each unit cell, of size a, with series impedance Z_s composed of a series capacitance C_s and an inductance L_s, with ground admittance Y_g composed of a parallel ground capacitance C_g and an inductance L_g.

In the lossless case, the impedance and admittance composing the network are:

$$Z_s(\omega) = i\omega L \quad \text{and} \quad Y_g(\omega) = i\omega C. \tag{2.10}$$

Thus, the wavevector and the phase and group velocities of the line are:

$$\kappa(\omega) = \frac{\omega}{a\omega_0} \quad \text{and} \quad v_\varphi = a\omega_0 = v_g, \tag{2.11}$$

In the following we will omit to write "angular" when referring to ω to ease readability

where $\omega_0 = 1/\sqrt{LC}$. Therefore, the wavevector is linearly proportional to the angular frequency of the wave, as depicted in Figure 2.3, and the phase and group velocities are equal. The characteristic impedance of such line is frequency independent, and is given by:

$$Z_c = \sqrt{\frac{L}{C}}. \tag{2.12}$$

This type of TL can be used to model any homogeneous dielectric[2] by choosing appropriate values of the inductance and capacitance per

2 These distributed low-pass networks can also represent free space. In this case, the capacitance and inductance per unit length can be directly related to the free-space permittivity ε_0 and permeability μ_0, respectively, so that the characteristic impedance of the network is equal to the free-space wave impedance of 377 Ω [85].

unit length. Indeed, the latter can be directly related to equivalent permeability μ and permittivity ε, respectively.

This kind of transmission lines are usually dubbed as *right-handed*, in analogy with the RH materials introduced in Section 1.1.1 in **??**. On the other hand, the dual topology gives rise to the so called *left-handed* transmission lines.

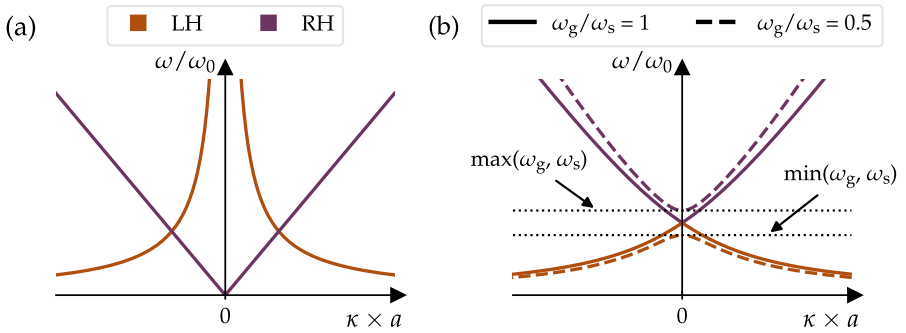

Figure 2.3: Dispersion relation of right- and left-handed transmission lines and of a composite one
(a) Dispersion relation of a LHTL, in orange, and of a RHTL in purple.
(b) Dispersion relation of a composite TL in the unbalanced case, dashed line, and balanced one, solid line. The color code refers to (a), highlighting the LH or RH behavior of each frequency band. Δ corresponds to the bandgap width at $\kappa = 0$.

2.1.2 Left-Handed topology

The dual topology of a RHTL is obtained by exchanging the inductance and capacitance arrangements. This realizes an high-pass microwave network, as depicted in Figure 2.2(b), with series impedance and ground admittance:

$$Z_s(\omega) = \frac{1}{i\omega C} \quad \text{and} \quad Y_g(\omega) = \frac{1}{i\omega L}, \tag{2.13}$$

respectively. Thus, the equivalent permittivity ε and permeability μ are given by:

$$\varepsilon(\omega) = -\frac{1}{\omega^2 La} < 0 \quad \text{and} \quad \mu(\omega) = -\frac{1}{\omega^2 Ca} < 0. \tag{2.14}$$

Therefore, this high-pass network reproduces a unique material having both negative ε and μ, which show a dispersive nature with a $1/\omega^2$ frequency dependence.

Such a material has been first postulated by Veselago [38] in 1968 and experimentally realized in 2001 by R. A. Shelby *et al.* [42]. These type of materials, show interesting electromagnetic phenomena such as backward wave propagation [86] and negative refraction [7]. For this reason they have been also dubbed as *negative-index* materials.

In the following years the idea of using TL theory to realize a LH material was introduced [44, 45] with applications ranging from the realization of perfect lenses [46] to directional couplers [47]. In more recent years the concept of LHTL attracted again attention within the superconducting circuits framework [48] as promising platforms for quantum simulation architectures [15, 49, 50] and near-quantum-limited amplification [51].

All these interest is based on the peculiar properties of such lines, indeed, the wavevector and the phase and group velocities of a LHTL are given by:

$$\kappa(\omega) = \frac{\omega_0}{a\omega} \quad \text{and} \quad v_\varphi(\omega) = \frac{a\omega^2}{\omega_0} = -v_g(\omega). \tag{2.15}$$

Thus, with respect to the RH case, the **wavevector is inversely related to the frequency**, as shown in Figure 2.3(a), and the **phase and group velocities have opposite signs**. One more significant difference lies in the frequency dependence of the wavelength. The latter, for a RHTL is inversely proportional to the frequency:

$$\lambda(\omega) = \frac{2\pi a\omega_0}{\omega}, \tag{2.16}$$

while, in the LH topology, the proportionality is linear:

$$\lambda(\omega) = \frac{2\pi a\omega}{\omega_0}. \tag{2.17}$$

Thus, **the electrical length $\theta(\omega)$ of a LHTL is higher at lower frequencies**:

$$\theta(\omega) = 2\pi\frac{l}{\lambda} = \frac{l\omega_0}{a\omega} = \frac{N_{\text{cell}}\omega_0}{\omega}, \tag{2.18}$$

where $l = aN_{\text{cell}}$ is the physical length of the network, with N_{cell} being the number of unit cells composing it. On the other hand, the characteristic impedance is the same as in the RHTL:

$$Z_c = \sqrt{\frac{L}{C}}. \tag{2.19}$$

2.1.3 Composite topology

From the previous discussion it is clear that, for a LHTL, both the frequency and the group velocity diverge as the wavevector decreases, which is unphysical. However, such behavior does not occur in any practical realization because of stray series inductances L_s and stray ground capacitances C_g [49]. Therefore, each realization of a LHTL is actually a *composite right-left-handed transmission line* [29, 47], which is depicted in Figure 2.2(c).

In this case the series impedance and ground admittance are:

$$Z_s(\omega) = i\left(\omega L_s - \frac{1}{\omega C_s}\right) \quad \text{and} \quad Y_g(\omega) = i\left(\omega C_g - \frac{1}{\omega L_g}\right), \tag{2.20}$$

which give:

$$\kappa(\omega) = \frac{1}{a}\sqrt{\left(\frac{\omega}{\omega_s}\right)^2 + \left(\frac{\omega_g}{\omega}\right)^2 - \left(\frac{L_s}{L_g} + \frac{C_g}{C_s}\right)}, \tag{2.21}$$

where $\omega_s = 1/\sqrt{L_s C_s}$ and $\omega_g = 1/\sqrt{L_g C_g}$. The latter dispersion relation presents two frequency bands, as shown in Figure 2.3(b), with a bandgap at $\kappa = 0$. The width of this bandgap is given by $\Delta = \max(\omega_s, \omega_g) - \min(\omega_s, \omega_g)$ and it closes when the transmission line is balanced, *i.e.* when $\omega_s = \omega_g$. The balanced case corresponds to the condition for which the characteristic impedance of the line is not frequency dependent:

$$Z_c = \begin{cases} \sqrt{\frac{L_s}{C_s}} = \sqrt{\frac{L_g}{C_g}} & \text{if } \omega_s = \omega_g, \\ \sqrt{\frac{L_s}{C_g}\frac{\omega^2-\omega_s^2}{\omega^2-\omega_g^2}} & \text{if } \omega_s \neq \omega_g, \end{cases} \tag{2.22}$$

as shown in Figure 2.4.

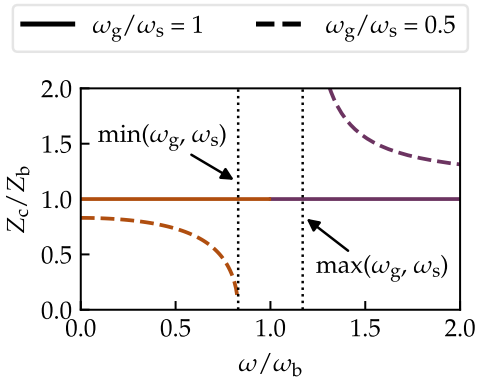

Figure 2.4: Characteristic impedance of a composite right-left-handed transmission line
Frequency dependence of the characteristic impedance of a composite TL in the unbalanced case, dashed line, and balanced one, Solid line. The color code refers to Figure 2.3(a), highlighting the LH or RH behavior of each frequency band. The impedance Z_c is normalized by the one in the balanced case Z_b, see Equation 2.22; while the frequency is normalized by the one at which the gap closes in the balanced case $\omega_b = \omega_{s,g}$. The dotted line corresponds to the bandgap width at $\kappa = 0$.

Note that in the upper frequency band, in purple in Figure 2.3(b), the metamaterial presents a RH behavior, while in the lower frequency

band, in orange in Figure 2.3(b), group and phase velocity have opposite sign, such as in a LH line.

Thus, artificial materials with tailored wave dispersion can be implemented by different transmission lines topologies. However, the strength of metamaterials lies also in the possibility of controlling nonlinear interactions. Within this framework this is done by replacing the linear inductors with JJs. Thus the next section is dedicated to the description of JTLs.

2.2 JOSEPHSON TRANSMISSION LINES

Recently, JTLs underwent a striking development because of their impact in the fields of quantum information and quantum computing. Several applications rely on these structures. Among them, there are implementations of multimode electromagnetic environments for simulations of quantum many body systems [87, 88], realizations of superinductances for qubit architectures [89] or of Josephson TWPAs [19, 20] for near-quantum-limited amplification of weak microwave signals. All these realizations are based on TLs, as the ones described in Section 2.1, with N_{cell} unit cells, in which the linear inductance is replaced by a JJ or a composite of them. A key difference between all above realizations is the characteristic impedance of the transmission line. Whenever it matches the one of the microwave environment, *i.e* $Z_0 = 50\ \Omega$, traveling-waves can be obtained. Otherwise, the TL behaves as a resonant structure. Here, we are interested in the former case which allows to realize a microwave analogue of nonlinear optical fibers.

Before discussing nonlinear processes in such structures, we shall describe how the linear dispersion relation is modified by the presence of the junctions.

2.2.1 Dispersion relation

As described in **??**, the equivalent circuit of a JJ consists of a LC circuit with inductance[3] L_j and capacitance C_j. Therefore, the exchange of the linear inductances L in Figure 2.1 with JJs leads to the circuits depicted in Figure 2.5.

By applying the equations derived in Section 2.1, we can obtain the linear properties of these structures. Note that we will consider valid the limit $\kappa \times a \ll 1$, which correspond to the long wavelength limit relative to the unit cell size. Within this approximation, and considering no losses, the dispersion relation is given by:

$$k(\omega) = -i\sqrt{Z_s(\omega)Y_g(\omega)} \quad \text{if} \quad |k| \ll 1, \tag{2.23}$$

3 For now we consider only the linear contribution.

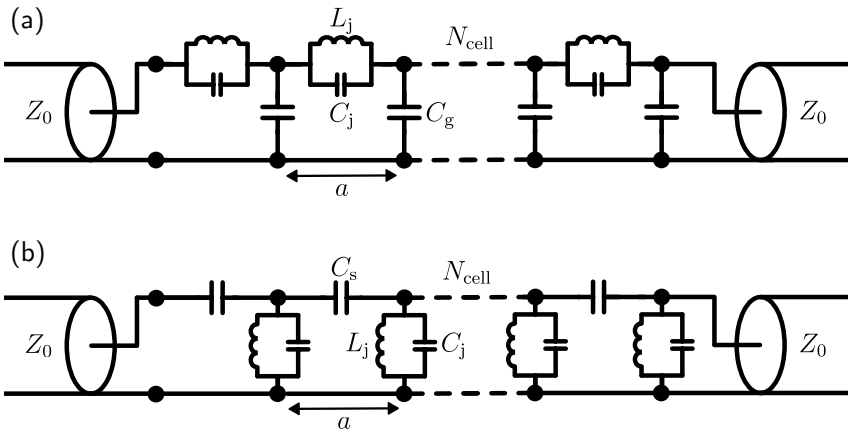

Figure 2.5: Circuit diagram of Josephson junctions based right- and left-handed networks
(a) Linearized RH JTL with unit cells, of size a, composed of a JJ, approximated here as the parallel of a linear inductance L_j and of a capacitance C_j, shunted to ground by a capacitance C_g.
(b) Linearized LH JTL with unit cells, of size a, composed of a capacitance C_s, shunted to ground by a JJ, approximated here as the parallel of a linear inductance L_j and of a capacitance C_j.

where we have defined the *dimensionless wavevector* $k = \kappa \times a$.

RIGHT-HANDED Let us start with the RH case, depicted in Figure 2.5(a). The series impedance and the ground admittance are given by:

$$Z_s(\omega) = \frac{i\omega L_j}{1 - (\omega/\omega_j)^2} \quad \text{and} \quad Y_g(\omega) = i\omega C_g, \tag{2.24}$$

where $\omega_j = 1/\sqrt{L_j C_j}$ is the plasma frequency of the junctions. Therefore, the dispersion relation and the characteristic impedance of the line are:

$$k(\omega) = \frac{\omega}{\omega_0 \sqrt{1 - (\omega/\omega_j)^2}}, \tag{2.25}$$

$$Z_c = \frac{Z_{RH}}{\sqrt{1 - (\omega/\omega_j)^2}}, \tag{2.26}$$

where $\omega_0 = 1/\sqrt{L_j C_g}$ and $Z_{RH} = \sqrt{L_j/C_g}$. At low frequencies, *i.e.* when $k \ll 1$, the behavior of the line is well approximated by the RH one described in Section 2.1.1. The dispersion relation is linear and the characteristic impedance of the chain is constant and equal to Z_{RH}, as shown by the purple lines in Figure 2.6(a) and (b), respectively. However, as the frequency increases, the dispersion relation starts to bend because of the in-line Josephson capacitance C_j and no wave propagation is allowed above the junctions plasma frequency.

Phase and group velocities are given by:

$$\begin{aligned} v_\varphi(\omega) &= a\omega_0\sqrt{1-\left(\omega/\omega_\mathrm{j}\right)^2}, \\ v_\mathrm{g}(\omega) &= a\omega_0\left[1-\left(\omega/\omega_\mathrm{j}\right)^2\right]^{3/2}, \end{aligned} \tag{2.27}$$

which are approximately equal, $v_\varphi(\omega) \approx v_\mathrm{g}(\omega)$, for $\omega \ll \omega_\mathrm{j}$, as expected from the previous discussion.

LEFT-HANDED On the other hand, in the LH case, depicted in Figure 2.5(b), the series impedance and the ground admittance are:

$$Z_\mathrm{s}(\omega) = (i\omega C_\mathrm{s})^{-1} \quad \text{and} \quad Y_\mathrm{g}(\omega) = \frac{1-\left(\omega/\omega_\mathrm{j}\right)^2}{i\omega L_\mathrm{j}}, \tag{2.28}$$

which give for the dispersion relation and the characteristic impedance [51]:

$$k(\omega) = \frac{\omega_0}{\omega}\sqrt{1-\left(\omega/\omega_\mathrm{j}\right)^2} \tag{2.29}$$

$$Z_\mathrm{c} = \frac{Z_\mathrm{LH}}{\sqrt{1-(\omega/\omega_\mathrm{j})^2}}, \tag{2.30}$$

where $\omega_0 = 1/\sqrt{L_\mathrm{j}C_\mathrm{s}}$ and $Z_\mathrm{LH} = \sqrt{L_\mathrm{j}/C_\mathrm{s}}$. Now, the limit $k \ll 1$ corresponds to high frequencies, as shown by the orange line in Figure 2.6(a). However, with respect to the LH line described in Section 2.1.2, the presence of the JJ sets a cut-off frequency above which no wave propagation is allowed preventing the unphysical divergence discussed in the previous section[4]. The characteristic impedance of the chain is equal to the RH one except for the frequency independent value Z_LH, as shown by the orange line in Figure 2.6(b).

It is worth noticing that, as well as in the LHTL case described in Section 2.1.2, **for a LH JTL phase and group velocities are antiparallel** [51]:

$$\begin{aligned} v_\varphi(\omega) &= \frac{a\omega^2}{\omega_0\sqrt{1-\left(\omega/\omega_\mathrm{j}\right)^2}}, \\ v_\mathrm{g}(\omega) &= -\frac{a\omega^2\sqrt{1-\left(\omega/\omega_\mathrm{j}\right)^2}}{\omega_0}, \end{aligned} \tag{2.31}$$

and their modulus, for $\omega \ll \omega_\mathrm{j}$, is approximately the same $|v_\varphi(\omega)| \approx a\omega^2/\omega_0 \approx |v_g(\omega)|$.

4 As already discussed at the end of Section 2.1.3, in any practical realization there will also be a stray series inductance L_s leading to a RH high-frequency band. However, it can be neglected if L_s is small enough such that $\omega_\mathrm{s} \gg \omega_\mathrm{g}$.

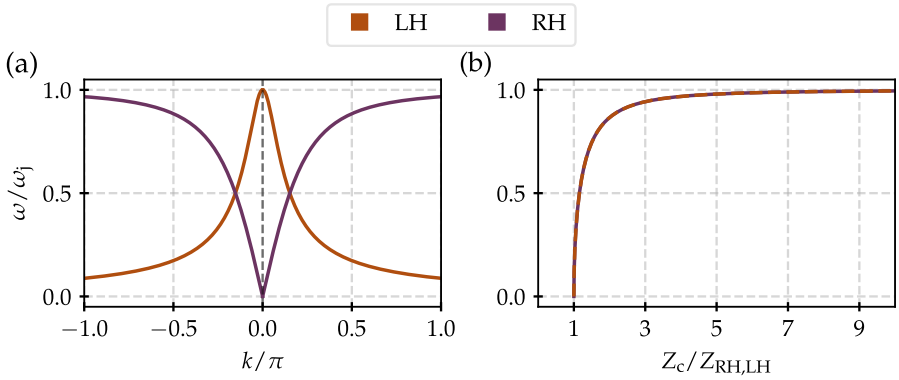

Figure 2.6: Dispersion relation and characteristic impedance of right- and left-handed Josephson transmission lines
(a) Dispersion relation of LH, in orange, and RH, in purple, JTLs.
(b) Characteristic impedance Z_c, normalized by the frequency independent value $Z_{RH,LH} = \sqrt{L_j/C_{g,s}}$, of LH, in orange, and RH, in purple, JTLs.

FINITE SIZE EFFECTS Before moving forward, we shall briefly discuss the influence of the finite dimensionality of such JTLs. If the long wavelength limit is not taken, the previous descriptions are still valid. However, because of the finite size a of the unit cell the smallest allowed wavelength corresponds to $\lambda_{min} = 2a$, which sets the largest wavevector to $\kappa_{max} = \pi/a$. This introduces a new cut-off frequency, slightly modifying the dispersion relation. The latter can be obtained from Equation 2.1 without taking the continuous limit and reads [29, 49]:

$$\cos(k) = 1 + \frac{Z_{s(\omega)} Y_{g(\omega)}}{2}. \tag{2.32}$$

Using the expression for the series impedance and ground admittance for the RH and LH lines, given in Equation 2.24 and Equation 2.28, respectively, we obtain:

Here, we also make use of the trigonometric identity $\sin^2\left(\frac{x}{2}\right) = \frac{1-\cos x}{2}$

$$\begin{aligned} \omega_{RH}(k) &= \frac{\omega_j \left|\sin\left(\frac{k}{2}\right)\right|}{\sqrt{\sin^2\left(\frac{k}{2}\right) + C_g/4C_j}}, \\ \omega_{LH}(k) &= \frac{\omega_0}{2\sqrt{\sin^2\left(\frac{k}{2}\right) + C_j/4C_s}}. \end{aligned} \tag{2.33}$$

The latter differ from the dispersion relation obtained within the long wavelength approximation as k approaches π, as shown in Figure 2.7. The frequency value at which $k = \pi$ defines therefore the real cut-off frequency of the TLs:

$$\omega_\pi^{RH} = \frac{\omega_j}{\sqrt{1 + C_g/4C_j}}, \quad \text{and} \quad \omega_\pi^{LH} = \frac{\omega_0}{2\sqrt{1 + C_j/4C_s}}. \tag{2.34}$$

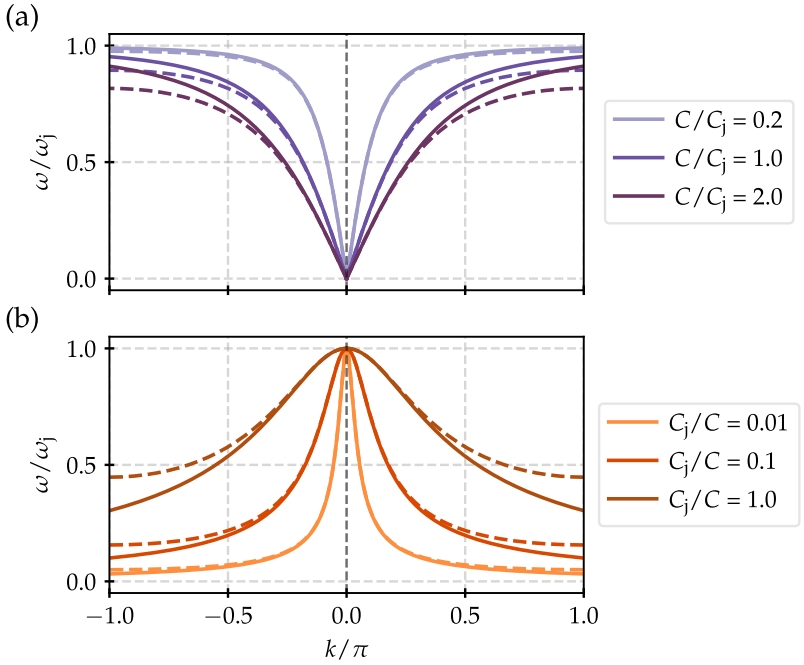

Figure 2.7: Finite size effects on the dispersion relations of right- and left-handed Josephson transmission lines
Dispersion relations of RH JTLs (a) and of a LH JTLs (b). The solid lines correspond to the dispersion relation within the long wavelength limit and given in Equation 2.25 and in Equation 2.29, while the dashed lines represent the ones given in Equation 2.33, obtained taking into the finite size of the unit cell. The different shades of the respective colors correspond to different values of the to-ground and in-line capacitances ratio; the darker the color, the higher the ratio.

The discrepancy between taking the continuous limit or not strongly depends on the ratio between the to-ground and in-line capacitances: it increases as the ratio increases. As far as we are concerned, we will always work with small ratios. Therefore, in the following we will consider the continuous limit as valid.

Before moving forward to study nonlinear interactions in these Josephson waveguides, it is worth mentioning that changing the to-ground and in-line capacitances ratio allows to tailor the curvature of the dispersion relation, allowing full control on it, which is quite important when dealing with parametric processes in the traveling-wave regime, as it will become clear in the next sections.

2.2.2 Equation of motion

We will now derive the nonlinear equation of motion which describes wave propagation and interactions in JTLs. To do so, we will also consider the leading nonlinear order term in the expansion of the Joseph-

son current-phase relation, given in Section 1.2 in **??**, and parametrize the circuits as depicted in Figure 2.8.

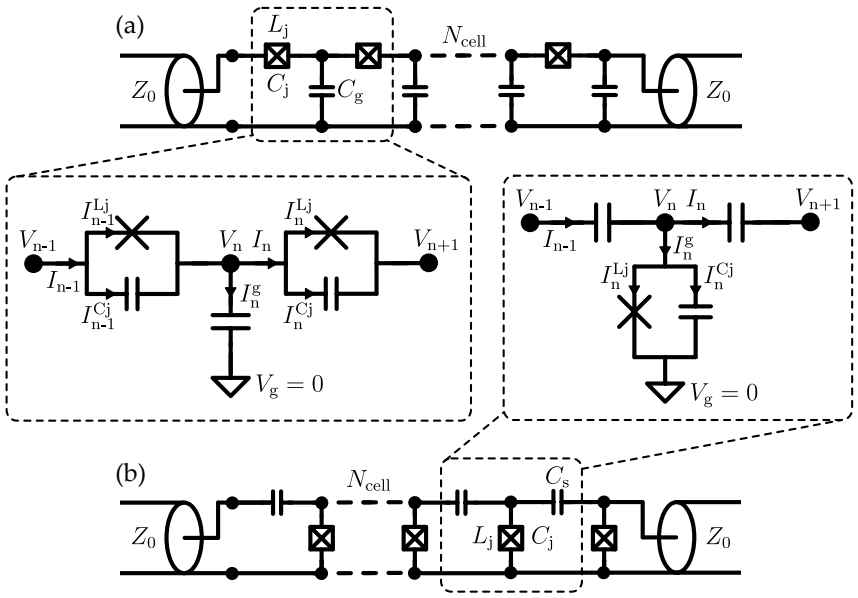

Figure 2.8: Circuit diagram with unit cells zoom of Josephson right- and left-handed transmission lines
RH (a) and LH (b) JTLs, with a focus on their respective unit cells, highlighting the voltage V_n at the n-th node, the current I_n flowing from node n to node n+1 and the current I^g_n flowing from node n to ground. The currents through the inductive part I^{Lj}_n and through the capacitive part I^{Cj}_n of the junctions are also represented.

Following the standard approach [90] to write down the nonlinear wave equation in Josephson waveguides we start by writing Kirchhoff's current conservation law:

$$I_{n-1}(t) = I_n(t) + I^g_n(t), \tag{2.35}$$

which relates the current flowing from node n-1 to node n, I_{n-1}, to the one flowing from node n to node n+1, I_n, and to the one flowing from node n to the ground, I^g_n.

Now, those currents can be directly expressed in terms of the generalized flux $\Phi_n(t)$ at the n-th node. The latter is related to the voltage at that same node by:

$$V_n(t) = \frac{d\Phi_n(t)}{dt} = \dot{\Phi}_n(t), \tag{2.36}$$

where we wrote the time derivative $\frac{d}{dt}$ as $\dot{_}$ for shortening the notation. Depending on the topology of the line, the expressions of those currents will be different.

In the following we will drop the time arguments to simplify the notation

LEFT-HANDED Let us start with the LH line [51], shown in Figure 2.8(b). Here, the current flowing from node n-1 to node n is the one through the n-th series capacitor, while the one flowing to ground goes through the junction:

$$I_n = I_n^{Cs} \quad \text{and} \quad I_n^g = I_n^{Lj} + I_n^{Cj}. \tag{2.37}$$

The latter are give by:

$$I_n^{Cs} = C_s \left(\ddot{\Phi}_n - \ddot{\Phi}_{n+1}\right), \tag{2.38}$$

$$I_n^{Lj} = I_c \sin\left(\frac{\Phi_n}{\varphi_0}\right) \approx \frac{\Phi_n}{L_j} - \frac{\Phi_n^3}{6I_c^2 L_j^3}, \tag{2.39}$$

$$I_n^{Cj} = C_j \ddot{\Phi}_n. \tag{2.40}$$

Now, by replacing the former expressions in Equation 2.35 we obtain the discrete system of equations describing the nonlinear dynamics of the generalized magnetic flux in a LH JTL[5]:

$$\frac{1}{\omega_j^2}\ddot{\Phi}_n - \frac{a^2}{\omega_0^2}\left(\ddot{\Phi}_{n+1} - 2\ddot{\Phi}_n + \ddot{\Phi}_{n-1}\right) + \Phi_n - \frac{\Phi_n^3}{6I_c^2 L_j^2} = 0. \tag{2.41}$$

Within the long wavelength limit $a/\lambda \ll 1$, the discrete variable n indexing the nodes is replaced by the continuous position coordinate x along the chain and the discrete flux differences in Equation 2.41 become (up to the second order in a/λ):

$$\begin{aligned} \Phi_{n+1} - \Phi_n &\approx a\partial_x\Phi + \frac{a^2}{2}\partial_x^2\Phi \\ \Phi_n - \Phi_{n-1} &\approx a\partial_x\Phi - \frac{a^2}{2}\partial_x^2\Phi, \end{aligned} \tag{2.42}$$

which give:

$$\Phi_{n+1} - 2\Phi_n + \Phi_{n-1} \approx a^2\partial_x^2\Phi \tag{2.43}$$

Setting the latter in Equation 2.41 we obtain the nonlinear wave equation for the propagating field amplitude, described in terms of the position dependent flux variable $\Phi(x,t)$, in a LH JTL:

$$\frac{1}{\omega_j^2}\partial_t^2\Phi - \frac{a^2}{\omega_0^2}\partial_x^2\partial_t^2\Phi + \Phi - \frac{\Phi^3}{6I_c^2 L_j^2} = 0. \tag{2.44}$$

Here, the first three terms describe the linear propagation in a dispersive medium, while the fourth term represents the nonlinearity of the system. The latter appears directly in the flux amplitude, *i.e.* in the potential energy, while in the RH case it is related to the kinetic one as we will see next.

5 Note that solving the linearized form of this equation, without the cubic nonlinear term, with the ansatz $\Phi_n = A_n e^{i(\omega t - kn)}$ gives the dispersion relation in Equation 2.33.

RIGHT-HANDED Following the same procedure [37, 90], the wave equation of a RH JTL, shown in Figure 2.8(a), can be derived. The main difference is that now the current flowing from node n-1 to node n is the one through the n-th junction, while the one flowing to ground goes through the capacitor:

$$I_n = I_n^{Lj} + I_n^{Cj} \quad \text{and} \quad I_n^g = I_n^{Cg}. \tag{2.45}$$

The latter are given by:

$$I_n^{Cg} = C_g \ddot{\Phi}_n, \tag{2.46}$$

$$I_n^{Lj} = I_c \sin\left(\frac{\Phi_n - \Phi_{n+1}}{\varphi_0}\right) \approx \frac{\Phi_n - \Phi_{n+1}}{L_j} - \frac{(\Phi_n - \Phi_{n+1})^3}{6 I_c^2 L_j^3}, \tag{2.47}$$

$$I_n^{Cj} = C_j \left(\ddot{\Phi}_n - \ddot{\Phi}_{n+1}\right). \tag{2.48}$$

As before, inserting these expressions in Equation 2.35 and taking the continuous limit[6] yields to the nonlinear wave equation for the generalized flux in a RH JTL:

$$\frac{1}{\omega_0^2}\partial_t^2\Phi - \frac{a^2}{\omega_j^2}\partial_x^2\partial_t^2\Phi - a^2\partial_x^2\Phi - \frac{a^4}{2I_c^2L_j^2}\left(\partial_x^2\Phi\right)\left(\partial_x\Phi\right)^2 = 0. \tag{2.49}$$

Again, the first three terms describe linear propagation in a dispersive medium, while the fourth term represents the cubic nonlinear wave mixing which now appears in the kinetic energy term.

INCLUDING LOSSES Until now we have considered our systems lossless, however, the requirement for impedance matching the arrays to 50 Ω implies the use of quite high capacitances[7]. The realization of such capacitors is based on lossy dielectrics. Thus, losses should be taken into account. To do so, we can add to the ground and series capacitors $C_{g,s}$ of the RH and LH lines, respectively, a parallel resistance $R_{g,s}$[8]. Thus Equation 2.46 and Equation 2.38 become:

$$I_n^{Cg} = C_g \ddot{\Phi}_n + \frac{1}{R_g}\Phi_n, \tag{2.50}$$

$$I_n^{Cs} = C_s \left(\ddot{\Phi}_n - \ddot{\Phi}_{n+1}\right) + \frac{1}{R_s}\left(\dot{\Phi}_n - \dot{\Phi}_{n+1}\right), \tag{2.51}$$

6 Now we also need to use $(\Phi_{n+1} - \Phi_n)^3 - (\Phi_n - \Phi_{n-1})^3 \approx 3a^4\left(\partial_x^2\Phi\right)(\partial\Phi)^2$ at the lowest order in a/λ.

7 Considering Josephson inductances of the order of 500 pH gives for the matching capacitance $C = L/50^2 = 200$ fF.

8 Which is equivalent to consider losses through a complex dielectric constant. Indeed, the values of R and C are related to the material loss tangent by $\tan\delta = 1/\omega RC$.

respectively. Following the same steps as before the wave equations of the RH and LH JTLs, within the long wavelength limit, become:

$$\frac{L_j}{R}\partial_t\Phi + \frac{1}{\omega_0^2}\partial_t^2\Phi - \frac{a^2}{\omega_j^2}\partial_x^2\partial_t^2\Phi - a^2\partial_x^2\Phi - \frac{a^4}{2I_c^2L_j^2}\left(\partial_x^2\Phi\right)\left(\partial_x\Phi\right)^2 = 0, \tag{2.52}$$

$$a^2\frac{L_j}{R}\partial_x^2\partial_t\Phi + \frac{1}{\omega_j^2}\partial_t^2\Phi - \frac{a^2}{\omega_0^2}\partial_x^2\partial_t^2\Phi + \Phi - \frac{\Phi^3}{6I_c^2L_j^2} = 0, \tag{2.53}$$

respectively. The first terms account for dissipation. In the RH case it correspond to a damping term which will just reduce the amplitude along propagation; while, in the LH case it will also bring a frequency shift because the considered resistance couples different sites.

Now we are able to study nonlinear interactions in JTLs through these wave equations. However, we will need to choose the processes we are interested in and the corresponding waves involved in it.

In the following sections we will describe the two parametric processes introduced in Section 1.3 in **??**: amplification and frequency conversion. For simplicity we will use the dimensionless coordinate $x = x/a$.

2.3 AMPLIFICATION

Let us start by considering the 4WM amplification process in which a signal of interest, with frequency ω_s, propagates along the nonlinear transmission line, in presence of a strong pump wave, with frequency ω_p. Thanks to the $\chi^{(3)}$ nonlinearity, two photons from the pump tone can be converted to a pair of signal and idler photons. The latter is co-generated by the amplification process at the frequency $\omega_i = 2\omega_p - \omega_s$, to satisfy energy conservation. Thus the nonlinear wave equations derived in previous section can be solved introducing a plane wave ansatz of the form:

$$\Phi_{ans}(x,t) = \frac{1}{2}\sum_{m\in\{p,s,i\}}\left(A_m(x)e^{i(k_m x-\omega_m t)} + c.c\right), \tag{2.54}$$

In the following we will drop the position argument of all $A_m(x)$ to shorten the notation

where $A_m(x)$ is the position dependent slow varying flux amplitude of the mode m; p,s,i respectively denote the pump, signal and idler modes, with ω_m and k_m their associated angular frequencies and dimensionless wavevectors, which are given by either Equation 2.25 or Equation 2.29, depending on the TL topology.

Thus, inserting Equation 2.54 into the wave equations Equation 2.52 or Equation 2.53 three coupled differential equations for the pump, signal and idler modes can be obtained.

2.3.1 Coupled mode equations

To write down such Coupled Mode Equations (CMEs), two main approximation can be performed:

1. Slowly varying envelope approximation by neglecting the second spatial derivative of the amplitude A_m, *i.e.* $\left|\partial_x^2 A_m\right| \ll |k_m \partial_x A_m|$[9].
2. Rotating-wave approximation by retaining only the terms that rotate at the frequencies of interest ω_p, ω_s and ω_i.

Therefore, substitution of $\Phi_{ans}(x,t)$ in Equation 2.52 or in Equation 2.53 gives us the following propagation equations for the pump, signal and idler flux amplitudes:

$$\begin{cases} \partial_x A_p = -\Gamma_p A_p + i\alpha_{pp}\left|A_p\right|^2 A_p + i\alpha_{ps}\left|A_s\right|^2 A_p \\ \qquad\qquad + i\alpha_{pi}\left|A_i\right|^2 A_p + i\beta_p A_s A_i A_p^* e^{-i\Delta k x}, \\ \partial_x A_s = -\Gamma_s A_s + i\alpha_{ss}\left|A_s\right|^2 A_s + i\alpha_{sp}\left|A_p\right|^2 A_s \\ \qquad\qquad + i\alpha_{si}\left|A_i\right|^2 A_s + i\beta_s A_p^2 A_i^* e^{i\Delta k x}, \\ \partial_x A_i = -\Gamma_i A_i + i\alpha_{ii}\left|A_i\right|^2 A_i + i\alpha_{ip}\left|A_p\right|^2 A_i \\ \qquad\qquad + i\alpha_{is}\left|A_s\right|^2 A_i + i\beta_i A_p^2 A_s^* e^{i\Delta k x}, \end{cases} \tag{2.55}$$

where $\Delta k = 2k_p - k_s - k_i$ is the dimensionless linear phase mismatch. These equations are identical in either the RH and LH cases, with the first terms on the right hand side which models the effect of dissipation, the second terms represent self-Kerr interactions, while the third and fourth ones are due to cross-Kerr interactions between the signal, idler and pump modes, and finally, the last term is the one ruling the energy exchange between the different waves. Now, the coefficients in front of each of these terms are quite different between the RH and LH lines, and are listed in Table 2.1. The main difference lies in the **negative sign present in the LH nonlinear coefficients**, which is thus opposite with respect to the sign of the respective wavevectors. This has profound effects on the dynamics of the amplification processes, as discussed in Section 2.3.2.

Such CMEs can be solved numerically [91], however, one more approximation can be performed in order to simplify them:

3. Strong pump approximation by considering the pump amplitude A_p much higher than the signal and idler ones, *i.e.* $A_p \gg A_{s,i}$[10].

9 For the RH case it also implies neglecting the first spatial derivative of the amplitude A_m in the nonlinear term of Equation 2.52, *i.e.* $|\partial_x A_m| \ll |k_m A_m|$.

10 Note that, in general, whenever a nonlinear system is driven by a strong wave, such as the pump, it will exhibit complicated dynamics with higher harmonics generation, which are not taken into account in this model.

COEFFICIENT	RH	LH	DEFINITION
Γ_m	$\frac{k_m \tan\delta}{2}$	$\frac{1}{1-i2\tan\delta}\frac{k_m \tan\delta}{2}$	Loss per-unit-length
α_{mm}	$\frac{\omega_0^2 k_m^5}{16 I_c^2 L_j^2 \omega_m^2}$	$-\frac{\omega_0^2}{16 I_c^2 L_j^2 \omega_m^2 k_m}$	Self-Kerr
α_{mn}	$\frac{\omega_0^2 k_m^3 k_n^2}{8 I_c^2 L_j^2 \omega_m^2}$	$-\frac{\omega_0^2}{8 I_c^2 L_j^2 \omega_m^2 k_m}$	Cross-Kerr
$\beta_{s,i}$	$\frac{\omega_0^2 k_p^2 k_s k_i \left(2k_p - k_{i,s}\right)}{16 I_c^2 L_j^2 \omega_{s,i}^2}$	$-\frac{\omega_0^2}{16 I_c^2 L_j^2 \omega_{s,i}^2 k_{s,i}}$	Nonlinear coupling
β_p	$\frac{\omega_0^2 k_p^2 k_s k_i \left(k_s + k_i - k_p\right)}{8 I_c^2 L_j^2 \omega_m^2}$	$-\frac{\omega_0^2}{8 I_c^2 L_j^2 \omega_p^2 k_p}$	Nonlinear coupling

Table 2.1: Coefficients in the coupled mode equations of Josephson transmission lines
Definition of the coefficients in the CMEs, given in Equation 2.55, for both RH and LH JTLs. The subscripts m, n $\in$ {p,s,i} index the pump, signal and idler modes considered.

As a consequence, in the equation for the pump amplitude only the first two terms survive. The propagation of the pump wave is not affected by the signal and idler ones anymore; it acts as an infinite reservoir of energy for the amplification process. While, on the signal and idler side all terms which are quadratic in their amplitudes can be neglected, leading to the following CMEs:

$$\begin{cases} \partial_x A_p = -\Gamma_p A_p + i\alpha_{pp} \left|A_p\right|^2 A_p, \\ \partial_x A_s = -\Gamma_s A_s + i\alpha_{sp} \left|A_p\right|^2 A_s + i\beta_s A_p^2 A_i^* e^{i\Delta k_L x}, \\ \partial_x A_i = -\Gamma_i A_i + i\alpha_{ip} \left|A_p\right|^2 A_i + i\beta_i A_p^2 A_s^* e^{i\Delta k_L x}, \end{cases} \tag{2.56}$$

The latter equations are the most suited ones to predict the behavior of the JTL, however, they do not help us in grasping the basic mechanisms behind the amplification process.

LOSSLESS CASE Thus, in the spirit of simplicity, we can also set the loss coefficients to zero and solve for the pump propagation:

$$A_p(x) = A_p(0) e^{i\tilde{\alpha}_p x}, \tag{2.57}$$

which can be replaced in the signal and idler equations, together with the definition $A_{s,i} = a_{s,i} e^{i\tilde{\alpha}_{s,i} x}$, to obtain:

$$\begin{cases} \partial_x a_s = i\tilde{\beta}_s a_i^* e^{i\Delta\tilde{k} x}, \\ \partial_x a_i = i\tilde{\beta}_i a_s^* e^{i\Delta\tilde{k} x}, \end{cases} \tag{2.58}$$

where $\Delta\tilde{k}$ is the total phase mismatch and the new coefficients $\tilde{\alpha}_{mn}$ and $\tilde{\beta}_m$, which now include the pump amplitude $A_p(0)$, are given in Table 2.2. Note that the amplitude of the pump tone can be expressed

COEFFICIENT	RH	LH
$\tilde{\alpha}_m$	$(2-\delta_{m,p})\frac{\omega_0^2 k_m^3 k_p^2}{\omega_m^2}\rho$	$-(2-\delta_{m,p})\frac{\omega_0^2}{\omega_m^2 k_m}\rho$
$\tilde{\beta}_{s,i}$	$\frac{\omega_0^2 k_p^2 k_s k_i (2k_p - k_{i,s})}{\omega_{s,i}^2}\rho$	$-\frac{\omega_0^2}{\omega_{s,i}^2 k_{s,i}}\rho$

Table 2.2: Coefficients in the coupled mode equations of Josephson transmission lines
Definition of the coefficients in the CMEs, obtained after the stiff pump approximation and neglecting losses, and given in Equation 2.56, for both RH and LH JTLs. The subscript $m \in \{p,s,i\}$ indexes the pump, signal and idler modes. Respect to the previously defined coefficients, reported in Table 2.1, now the pump amplitude is included in ρ, which is given in Equation 2.59.

in terms of the characteristic impedance and of the pump current as $A_p(0) = I_p Z_c/\omega_p$, from which it is possible to define a nonlinear mixing coefficient depending only on the pump parameters [51]:

$$\rho = \left(\frac{I_p}{I_c}\frac{\omega_o}{4\omega_p}\right)^2. \tag{2.59}$$

The total phase-mismatch $\Delta\tilde{k}$ has both a dispersive component, caused by the chromatic dispersion relation being not perfectly linear, and a nonlinear component, arising from the self-Kerr and cross-Kerr couplings. It reads:

$$\Delta\tilde{k} = \Delta k + \Delta\tilde{\alpha} \quad \text{with} \quad \begin{cases} \Delta k = 2k_p - k_s - k_i, \\ \Delta\tilde{\alpha} = 2\tilde{\alpha}_p - \tilde{\alpha}_s - \tilde{\alpha}_i, \end{cases} \tag{2.60}$$

and it limits the efficiency of the amplification process, as it will become clear in the following sections.

Now, depending on the propagation direction of signal and idler modes, the solution of Equation 2.58 is quite different.

CO-PROPAGATING SIGNAL AND IDLER MODES Let us start by considering the more standard case where all three modes involved in the amplification process propagate in the same direction. Thus, the initial conditions to solve the CMEs derived in the previous section must be given at the initial position $x = 0$: $a_{s,i,in} = a_{s,i}(0)$, which lead to the following scattering relations for the signal and idler modes:

$$\begin{aligned} a_{s,i}(x) = \Bigg\{ &\left[\cosh(gx) - i\frac{\Delta\tilde{k}}{2g}\sinh(gx)\right] a_{s,i}(0) \\ &+ i\frac{\tilde{\beta}_{s,i}}{g}\sinh(gx)\, a_{i,s}^*(0)\Bigg\} e^{i\frac{\Delta\tilde{k}}{2}x}, \end{aligned} \tag{2.61}$$

where

$$g = \sqrt{\tilde{\beta}_s \tilde{\beta}_i^* - \left(\frac{\Delta\tilde{k}}{2}\right)^2}, \tag{2.62}$$

is the per-unit-length parametric gain coefficient. Despite all the approximations that have been made, these expressions for the signal and idler amplitudes as a function of the position x can be particularly insightful. First of all, it is now clearer the need to keep the phase-mismatch as close as possible to zero, such that g is a real number and it keeps being one as the pump power increases[11]. This will results in an exponential dependence of the gain with respect to the distance x. Indeed, the signal and idler power gains at $x = \ell \equiv N_{\text{cell}}$, when considering no idler at the input, *i.e.* $a_i(0) = 0$, are given by:

Note that we are working with the dimensionless coordinate $x = \mathrm{x}/a$

$$\begin{cases} G_s(\ell) = \left|\frac{a_s(\ell)}{a_s(0)}\right|^2 = \left|\cosh(g\ell) - i\frac{\Delta\tilde{k}}{2g}\sinh(g\ell)\right|^2, \\ G_i(\ell) = \left|\frac{a_i(\ell)}{a_s(0)}\right|^2 = \left|i\frac{\tilde{\beta}_i}{g}\sinh(g\ell)\right|^2. \end{cases} \tag{2.63}$$

Hence, the necessity to keep the phase-mismatch as low as possible. In the ideal case of perfect phase-matching, *i.e.* $\Delta\tilde{k} = 0$, the gain coefficient g is maximum and the signal gain becomes:

$$G_s(\ell) = \left|\cosh\left(\sqrt{\tilde{\beta}_s\tilde{\beta}_i^*}\,\ell\right)\right|^2 \approx \frac{e^{2\sqrt{\tilde{\beta}_s\tilde{\beta}_i^*}\,\ell}}{4}, \tag{2.64}$$

which gives an exponential growth with respect to the amplification length $\sqrt{\tilde{\beta}_s\tilde{\beta}_i^*}\,\ell$, in the asymptotic limit.

Therefore, an important work has to be done to reduce the phase-mismatch has much as possible to ensure large gain with a reasonable device length.

COUNTER-PROPAGATING SIGNAL AND IDLER MODES Before describing the different approaches that can be implemented to solve the phase-matching problem in Josephson TWPAs, we discuss the situation in which the signal and idler modes travel in opposite directions. The latter realizes a novel regime of traveling-wave parametric amplification with superconducting circuits, which is of particular interest when quantum effects, such as entanglement generation, are considered.

Let us consider the case in which the signal and pump modes propagate in the same direction, while the idler travels in the opposite one. This changes the initial conditions to solve Equation 2.58. Now,

11 Note that both $\tilde{\beta}_{s,i}$ and $\Delta\tilde{k}$ depend on the amplitude of the pump tone.

$a_{\mathrm{s,in}} = a_{\mathrm{s}}(0)$, while $a_{\mathrm{i,in}} = a_{\mathrm{i}}(\ell)$, leading to the following scattering relations for the counter-propagating signal and idler modes:

$$\begin{aligned} a_{\mathrm{s}}(x) = \Bigg\{ & \frac{\cosh\left[g(\ell-x)\right] - i\frac{\Delta\tilde{k}}{2g}\sinh\left[g(\ell-x)\right]}{\cosh(g\ell) - i\frac{\Delta\tilde{k}}{2g}\sinh(g\ell)} a_{\mathrm{s}}(0) \\ & + i\frac{\tilde{\beta}_{\mathrm{s}}}{g}\frac{\sinh(gx)}{\cosh(g\ell) - i\frac{\Delta\tilde{k}}{2g}\sinh(g\ell)} e^{i\frac{\Delta\tilde{k}\ell}{2}+g(\ell-x)} a_{\mathrm{i}}^{*}(\ell) \Bigg\} e^{i\frac{\Delta\tilde{k}x}{2}}, \end{aligned} \tag{2.65}$$

and

$$\begin{aligned} a_{\mathrm{i}}(x) = \Bigg\{ & \frac{\cosh(gx) + i\frac{\Delta\tilde{k}}{2g}\sinh(gx)}{\cosh(g\ell) + i\frac{\Delta\tilde{k}}{2g}\sinh(g\ell)} e^{-i\frac{\Delta\tilde{k}L}{2}} a_{\mathrm{i}}(\ell) \\ & - i\frac{\tilde{\beta}_{\mathrm{i}}}{g}\frac{\sinh\left[g(\ell-x)\right]}{\cosh(g\ell) + i\frac{\Delta\tilde{k}}{2g}\sinh(g\ell)} a_{\mathrm{s}}^{*}(0) \Bigg\} e^{i\frac{\Delta\tilde{k}x}{2}}, \end{aligned} \tag{2.66}$$

where

$$g = \sqrt{\tilde{\beta}_{\mathrm{s}}\tilde{\beta}_{\mathrm{i}}^{*} - \left(\frac{\Delta\tilde{k}}{2}\right)^{2}}, \tag{2.67}$$

is the same as before, with the important exception that $\tilde{\beta}_{\mathrm{i}}$ has changed its sign because of the direction of propagation of the idler mode. Thus, if the product $\tilde{\beta}_{\mathrm{s}}\tilde{\beta}_{\mathrm{i}}^{*}$ is negative, g is purely imaginary and the gain is not anymore a monotonically increasing function of the position, but a periodic one.

Therefore, because the signal and idler modes propagate in opposite directions, instead of exponential amplification the resulting process is an oscillatory amplification. The exchange between the two modes and the pump continues back and forth with a periodic pattern, whose period depends on the amplification length $|g|\,\ell$.

The signal and idler power gains, when considering no idler at the end of the device, *i.e.* $a_{\mathrm{i}}(\ell) = 0$, are now given by:

$$\begin{cases} G_{\mathrm{s}}(\ell) = \left|\frac{a_{\mathrm{s}}(\ell)}{a_{\mathrm{s}}(0)}\right|^{2} = \left|\frac{1}{\cos(|g|\ell) + i\frac{\Delta\tilde{k}}{2g}\sin(|g|\ell)}\right|^{2}, \\ G_{\mathrm{i}}(0) = \left|\frac{a_{\mathrm{i}}(0)}{a_{\mathrm{s}}(0)}\right|^{2} = \left|i\frac{\tilde{\beta}_{\mathrm{i}}}{g}\frac{\sin(|g|\ell)}{\cos(|g|\ell) + i\frac{\Delta\tilde{k}}{2g}\sin(|g|\ell)}\right|^{2}. \end{cases} \tag{2.68}$$

Now, it is not only necessary to keep the phase-mismatch as low as possible, but also to finely tune the pump amplitude, for a given length, so that full amplification happens at the end of the nonlinear medium. Indeed, in the ideal case of perfect phase-matching, *i.e.* $\Delta\tilde{k} = 0$, the signal gain becomes:

$$G_{\mathrm{s}}(\ell) = \left|\left[\cos\left(\sqrt{|\tilde{\beta}_{\mathrm{s}}\tilde{\beta}_{\mathrm{i}}^{*}|}\,\ell\right)\right]^{-1}\right|^{2}, \tag{2.69}$$

which is maximum whenever $\sqrt{|\tilde{\beta}_s \tilde{\beta}_i^*|}\ell = \left(n + \frac{1}{2}\right)\pi$ with $n \in \mathbb{N}$.

Thus, engineering a metamaterial to realize amplification of counter-propagating signal and idler modes requires three main ingredients:

1. Energy must be conserved between the three modes, *i. e.* $2\omega_p = \omega_s + \omega_i$.
2. Momentum must be conserved, *i. e.* the phase-matching condition $\Delta\tilde{k} = 0$ has to be satisfied.
3. The product of the nonlinear couplings $\tilde{\beta}_{s,i}$, has to be negative.

Satisfying all three conditions requires quite a lot of engineering work, especially in a JTL with a RH topology. Indeed, if we just think about the third condition, the sign of the nonlinear couplings, in a RH JTL, strongly depends on its particular dispersion relation because $\tilde{\beta}_{s,i} \propto k_s k_i (2k_p - k_{i,s})$, as shown in Table 2.2. While, in a LH JTL, such product will always be negative, for counter-propagating signal and idler modes, because $\tilde{\beta}_{s,i} \propto k_{s,i}^{-1}$. Moreover, satisfying the frequency- and phase-matching conditions, for this process, is also easier in a JTL with a LH topology, as explained in the following section.

2.3.2 Phase-matching

As shown in the two previous sections, satisfying the phase-matching condition is of primarily importance for the dynamic of parametric amplification with traveling-waves. Thus, we shall describe the different strategies that have been implemented to ensure:

$$\Delta\tilde{k} = 2\tilde{k}_p - \tilde{k}_s - \tilde{k}_i = 0, \tag{2.70}$$

in Josephson TWPAs. Here, $\tilde{k}_m = k_m + \tilde{\alpha}_m$ are the effective wavevectors of each mode $m \in \{p,s,i\}$.

The natural approach consists in playing with either the linear or nonlinear components of each $\tilde{k}_m$ to correct for the phase of each wave, such that the three points $(\tilde{k}_m, \omega_m)$, for $m \in \{p,s,i\}$ are aligned. From Figure 2.9(a), it is clear that this is not the case for a bare RH JTL. This can be realized by adjusting the relative sign of Δk and $\Delta\tilde{\alpha}$, such that they compensate for each other. Note that for a bare RH JTL, both contributions are negative, as shown in Figure 2.9(b). Such idea is the core of the Dispersion-Engineered (DE) [92] and Reversed-Kerr (RK) [84] phase-matching technics in RH Josephson TWPAs, and of the self-phase-matched technic in LH ones [51], which are briefly described in the following paragraphs.

DISPERSION-ENGINEERED PHASE-MATCHING The first approach used to tackle the phase matching problem was based on opening a stop-band in the dispersion relation [18–20] aiming at slowing down

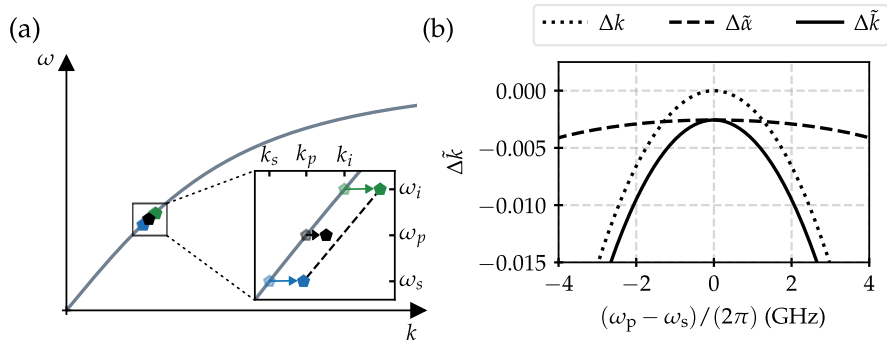

Figure 2.9: Phase-mismatch in a bare Josephson right-handed transmission line
(a) The dispersion relation, in grey, of a RH JTL highlighting the phase-mismatch between the pump, signal and idler modes. The latter are represented by the black, blue and green pentagons, respectively. Each of them is shifted from their position on the dispersion relation, represented by the shaded pentagons, by the arrows corresponding to the self- and cross-Kerr contributions $\tilde{\alpha}_m$, reported in Table 2.2. The different magnitudes of the latter, together with the initial curvature of the dispersion relation, cause the misalignment of the final effective wavevectors $\tilde{k}_m$.
(b) The total phase-mismatch, solid line, together with the linear, dotted line, and nonlinear, dashed line, contributions, as a function of the signal frequency ω_s, for a given pump frequency ω_p. The, already negative linear part is shifted down by the nonlinear one, resulting in $\Delta\tilde{k} < 0$.

the pump wave and align its phase with the one of the signal and idler modes, as shown in Figure 2.10(a).

Such dispersive feature has been realized in RH JTL by adding a capacitively coupled shut LC resonator every few unit cells [92], dubbed Resonant Phase-Matching (RPM) technic, or by following a photonic crystal approach [83], through the periodic modulation of the JTL's impedance. Note that the latter is equivalent to the periodic loading pattern firstly done in kinetic inductance TWPAs [18].

The RPM technic probably allows better control on the position of the stop-band, because it depends only on the resonant frequency of the linear LC resonators, however it presents an increased fabrication complexity. The photonic crystal approach, on the other hand, simplifies the fabrication, at the cost of a pump power dependent frequency position of the dispersive feature [37].

In both cases, the idea is to take advantage of the curvature of the dispersion relation close to the dispersive feature to slow down the pump tone, and thus increase its wavevector, and change the sign of the linear phase mismatch, such that:

$$\begin{cases} 2k_p > k_s + k_i, \\ 2\tilde{\alpha}_p < \tilde{\alpha}_s + \tilde{\alpha}_i, \end{cases} \Rightarrow \begin{cases} \Delta k > 0, \\ \Delta\tilde{\alpha} < 0, \end{cases} \Rightarrow \quad \Delta\tilde{k} = 0, \tag{2.71}$$

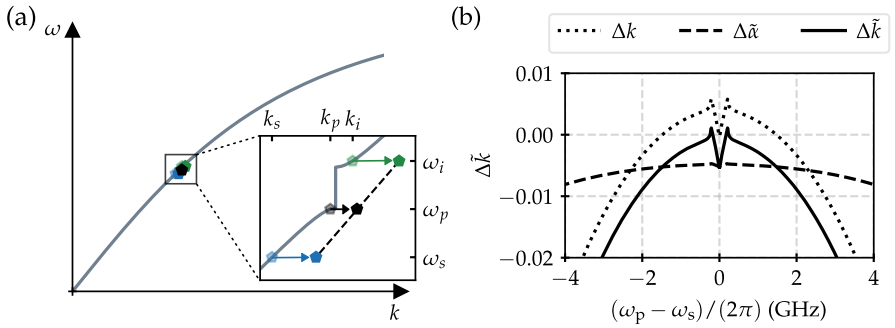

Figure 2.10: Dispersion-engineered phase-matching in a Josephson right-handed transmission line
(a) The dispersion relation, in grey, of a dispersion-engineered RH JTL highlighting the phase-matching condition between the pump, signal and idler modes. The latter are represented by the black, blue and green pentagons, respectively. Each of them is shifted from their position on the dispersion relation, represented by the shaded pentagons, by the arrows corresponding to the self- and cross-Kerr contributions $\tilde{\alpha}_m$, reported in Table 2.2. The presence of the dispersive feature increases the pump wavevector compensating for the different magnitudes of the $\tilde{\alpha}_m$, thus, aligning the final effective wavevectors $\tilde{k}_m$.
(b) The total phase-mismatch, solid line, together with the linear, dotted line, and nonlinear, dashed line, contributions, as a function of the signal frequency ω_s, for the pump frequency ω_p, close to the edge of the dispersive feature. Now, the linear part is positive for signal frequencies around the pump frequency. Thus, the sum of the two contributions results in $\Delta\tilde{k}$ crossing zero.

as shown in Figure 2.10(b).

Although, this solution to the phase-matching problem has been quite successful to realize broadband near quantum-limited amplifiers, it does have some disadvantages. Main one being that the dispersion feature is design dependent, limiting the in-situ tunability of the amplification band. A second drawback results from the poor impedance matching close to the stop-band, which leads to significant gain ripples, making it difficult to obtain flat gain profiles. However, the latter problem has been recently mitigated by implementing a window function on top of the periodic modulation [93].

REVERSED-KERR PHASE-MATCHING The dispersion engineering approach affects the linear contribution Δk of the total phase mismatch $\Delta\tilde{k}$. An alternative solution, relies on modifying the nonlinear contribution $\Delta\tilde{\alpha}$, by reversing the sign of the Kerr-nonlinearity [84, 94]. This will accordingly shift the wavevectors k_m of each mode to lower values satisfying the phase-matching condition, as shown in Figure 2.11(a).

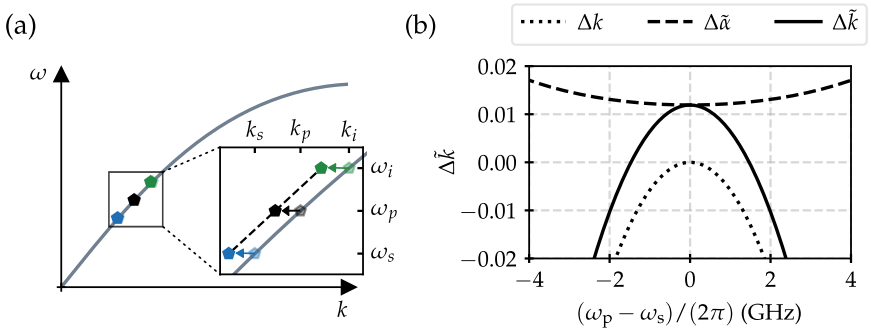

Figure 2.11: Reversed-Kerr phase-matching in a Josephson right-handed transmission line
(a) The dispersion relation, in grey, of a Reversed-Kerr RH JTL highlighting the phase-matching condition between the pump, signal and idler modes. The latter are represented by the black, blue and green pentagons, respectively. Each of them is shifted from their position on the dispersion relation, represented by the shaded pentagons, by the arrows corresponding to the self- and cross-Kerr contributions $\tilde{\alpha}_m$. Now, the sign of the latter is flipped thanks to the presence of JJs composites, biased at a specific flux. This negative shifts, together with the natural curvature of the dispersion relation, results in the alignment of the final effective wavevectors $\tilde{k}_m$.
(b) The total phase-mismatch, solid line, together with the linear, dotted line, and nonlinear, dashed line, contributions, as a function of the signal frequency ω_s, for a pump frequency ω_p. Now, the nonlinear part is positive and it shifts the linear one upwards. Thus, the sum of the two contributions results in $\Delta\tilde{k}$ crossing zero at two symmetric signal frequencies.

Therefore, with this approach, given a pump frequency ω_p, there will be two frequencies around it, for which:

$$\begin{cases} 2k_p < k_s + k_i, \\ 2\tilde{\alpha}_p > \tilde{\alpha}_s + \tilde{\alpha}_i, \end{cases} \Rightarrow \begin{cases} \Delta k < 0, \\ \Delta\tilde{\alpha} > 0, \end{cases} \Rightarrow \quad \Delta\tilde{k} = 0, \tag{2.72}$$

as shown in Figure 2.11(b).

Such nonlinear engineering can been implemented in RH JTL by replacing single JJs with more complex junctions' composites, such as Superconducting Nonlinear Asymmetric Inductive eLements (SNAILs) [60] or Radio Frequency Superconducting Quantum Interference Devices (rf-SQUIDs) [95], which allow full control of the metamaterial's nonlinearities [96] by applying an external magnetic flux to the devices[12].

Actually, such elements has been first thought for the realization of 3WM nonlinear devices

12 When this type of JTL is biased at the specific flux for which the second-order nonlinearity is zero and the third-order one in negative, waves propagation and interactions can be modeled as in the previous sections by introducing a normalization factor in front of the nonlinear coefficients [91, 96], given in Table 2.2, which changes their sign.

Since this solution does not rely on any designed dispersive feature, it offers the advantage of gain tunability at the cost of increased fabrication complexity and sensitivity to the external magnetic environment. The latter renders this approach less suitable for applications requireing an high-magnetic field. However, it is worth mentioning that careful magnetic shielding of the device can be implemented to preserve device's performances in such environments [97].

SELF-PHASE-MATCHING The potential of LH JTL appears now clearly: the sign of the nonlinear coefficients $\tilde{\alpha}_m$ in Table 2.2 is opposite compared to the linear wavevectors k_m. Thus, the phase of each wave is naturally corrected such that Equation 2.70 holds, as shown in Figure 2.12(a).

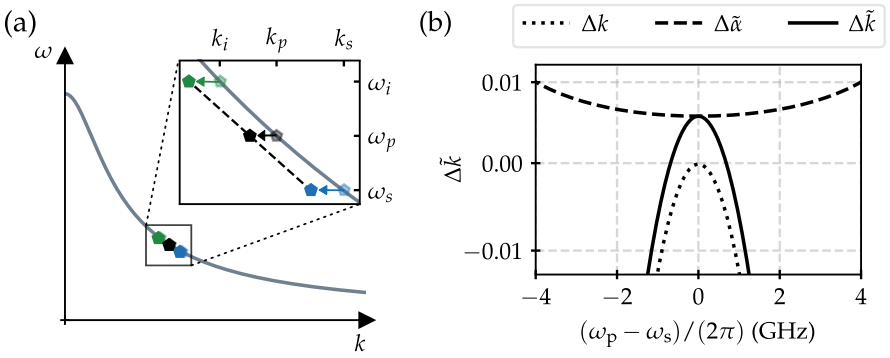

Figure 2.12: Self-phase-matching in a Josephson left-handed transmission line.
(a) The dispersion relation, in grey, of a LH JTL highlighting the self-phase-matching condition between the pump, signal and idler modes. The latter are represented by the black, blue and green pentagons, respectively. Each of them is shifted from their position on the dispersion relation, represented by the shaded pentagons, by the arrows corresponding to the self- and cross-Kerr contributions $\tilde{\alpha}_m$, reported in Table 2.2. Now, the sign of the latter is already negative. This shifts to lower wavevectors, together with the natural curvature of the dispersion relation, results in the alignment of the final effective wavevectors $\tilde{k}_m$.
(b) The total phase-mismatch, solid line, together with the linear, dotted line, and nonlinear, dashed line, contributions, as a function of the signal frequency ω_s, for a pump frequency ω_p. Now, the nonlinear part is positive and it shifts the linear one upwards. Thus, the sum of the two contributions results in $\Delta\tilde{k}$ crossing zero at two symmetric signal frequencies.

Therefore a JTL with LH topology presents native phase-matching [51] and, given a pump frequency ω_p, there will be two frequencies around it, for which:

$$\begin{cases} 2k_p < k_s + k_i, \\ 2\tilde{\alpha}_p > \tilde{\alpha}_s + \tilde{\alpha}_i, \end{cases} \Rightarrow \begin{cases} \Delta k < 0, \\ \Delta\tilde{\alpha} > 0, \end{cases} \Rightarrow \quad \Delta\tilde{k} = 0, \tag{2.73}$$

as shown in Figure 2.12(b).

This approach to satisfy the phase-matching condition presents two main advantages compared to the previous solutions. It neither relies on any dispersion feature, nor needs an external flux biasing to satisfy the phase-matching condition, with the result of a tunable amplification band and of a simplified TL design. However, LH devices present the fabrication challenge of realizing a chain of thousands of low-loss series capacitors.

PHASE-MATCHING OF COUNTER-PROPAGATING WAVES We shall now discuss about phase matching the amplification between counter-propagating signal and idler modes.

Considering signal and idler modes propagating in opposite directions results in a sign change of the backward propagating modes effective wavevectors. Thus, if the signal and pump modes propagate in the positive direction, while the idler one is generated in the opposite one, its wavevector gets a minus sign $k_i \mapsto -k_i$. As a consequence both $\tilde{\alpha}_i$ and $\tilde{k}_i$ change sign.

Thus, the phase-matching condition becomes $\Delta\tilde{k} = 2\tilde{k}_p - \tilde{k}_s + \left|\tilde{k}_i\right| = 0$, which is satisfied only when the signal wavevector compensate for the sum of the pump and idler ones, as shown in Figure 2.13(b). Therefore, phase-matching amplification between counter-propagating modes requires waves with significantly different effective wavevectors, *i.e.* different velocities. The latter condition is easily fulfilled in a LH line topology exploiting its low frequency cut-off, as shown in Figure 2.13(a); while, it is more challenging to achieve in a RH one, whose cut-off is at high frequency[13].

This phase-matching condition can be satisfied at any given signal frequency, by adjusting the pump one, as long as signal and idler fall within the bandwidth of the device. At a given pump frequency, both contributions to the total phase-mismatch cross zero at one signal frequency, which is far detuned from the pump one, as shown in Figure 2.13(c). Moreover, the main contribution to $\Delta\tilde{k}$ is the linear one, whose gradient close to zero sets the bandwidth of the process, while the nonlinear contribution $\Delta\tilde{\alpha}$ causes a small shift of the frequency at which the process is matched.

It is worth mentioning that traveling-wave amplification of counter-propagating signal and idler modes could be realized with a RH topology coupling two Josephson waveguides in which light travels at different velocities, as it has been done in [28] to phase-match frequency conversion processes.

13 Thus, an idea could be to devise a RH JTL with low cut-off frequency and tailored dispersion relation, such that the three conditions given in the previous section are satisfied. However, this is quite a design challenge compared to the native phase-matching of the process in a LH line.

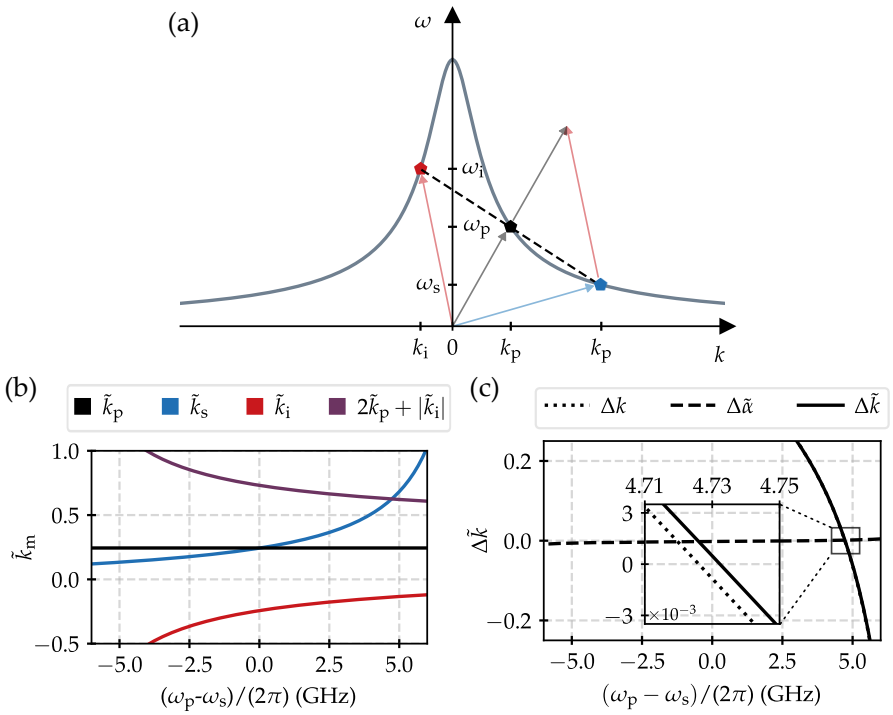

Figure 2.13: Phase-matching of counter-propagating modes in a Josephson left-handed transmission line

(a) The dispersion relation, in grey, for both positive and negative wavevectors, of a LH JTL, highlighting the phase-matching condition between the pump, and the counter-propagating signal and idler modes. The latter are represented by the black, blue and red pentagons, respectively. The position of each of them is highlighted by the vectors $(\tilde{k}_{p,s,i}, \omega_{p,s,i})$. Now, the idler lies on the negative branch of the dispersion relation. Thus, the three points are naturally aligned and the process is matched when the sum of the two input pump vectors is equal to the sum of the two output signal and idler ones. The shifts caused by the self- and cross-Kerr contributions $\tilde{\alpha}_m$, given in Table 2.2, are barely visible on this scale.

(b) Effective wavevectors of the pump, in black, signal, in blue, and idler, in red, as function of the signal frequency. The counter-propagating amplification process is matched when $\tilde{k}_s$ crosses $2\tilde{k}_p + |\tilde{k}_i|$, represented by the purple line.

(c) The total phase-mismatch, solid line, together with the linear, dotted line, and nonlinear, dashed line, contributions, as a function of the signal frequency ω_s, for a pump frequency ω_p. Now, all contributions cross zero at only one signal frequency. The effect of the nonlinear part on the linear one is to slightly shift the phase-matching frequency, as shown in the inset.

2.3.3 Gain

Now, all the ingredients have been prepared to discuss the amplification performances of the different JTL topologies. To do so, we

PARAMETER	RH	DE	RK	LH	UNIT
Number of cells N_{cell}	2000	2000	500	1000	#
Josephson inductance L_j	150	150	832	1800	pH
Josephson capacitance C_j	400	400	31	21	fF
Matching capacitance $C_{g,s}$	60	60	333	720	fF
Critical current I_c	2.2	2.2	1.4	0.18	μA
Critical current ratio r	-	-	0.06	-	#
Plasma frequency $\omega_j/(2\pi)$	20.6	20.6	31.3	26.0	GHz
Cut-off frequency $\omega_o/(2\pi)$	53.0	53.0	9.6	4.4	GHz
Gap frequency $\omega_g/(2\pi)$	-	6.1	-	-	GHz

Table 2.3: Parameters of the Josephson transmission lines used to simulate the gain profiles
Definition of the parameters used to simulate the gain profiles in Figure 2.14, for both RH and LH JTLs, with reference to Figure 2.8. In the RK case we are considering a JTL made out of SNAILs, the given critical current is the one of the large JJ and the values of the Josephson inductance and capacitance refer to the unit-cell equivalent ones at half-flux (see [84, 91, 96], for more details). In the DE case we considered a photonic-crystal approach to implement the dispersive feature, using a sinusoidal modulation with a period of $N_p = 26$ unit-cells and a 3% amplitude (see [37, 83] for more details).

will make the distinction between the case of co-propagating signal and idler modes and the counter-propagating one. Indeed, they serve different purposes, the former realizes broadband amplification with applications such as multiplexed qubit readout, while the latter has the potential to generate spatially and frequency separated entangled states.

CO-PROPAGATING MODES Let us start with the co-propagating case. The gain profile of a JTL can be computed from the analytical formulas given in Equation 2.63. Note that it will strongly depend on the topology of the line and, in particular, on the phase-matching mechanisms. Each approach requires different parameters of the line's components. Thus, to perform this comparison we choose parameters, which are given in Table 2.3, close to the one reported in the literature [51, 83, 84], which have demonstrated state-of-the-art performances.

The resulting gain profiles, obtained using a pump frequency of 6 GHz and a pump to critical currents ratio of 0.4, are shown in Figure 2.14(a). First of all, it is clear the difference between phase-

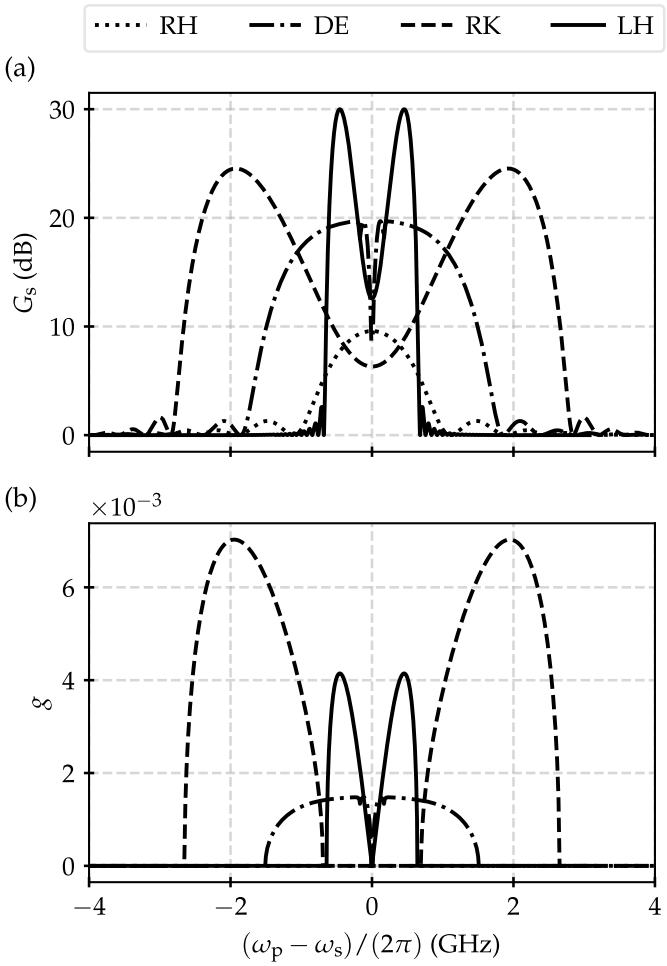

Figure 2.14: Signal gain comparison between different Josephson transmission line

(a) Signal gain G_s and (b) gain coefficient g of the co-propagating amplification process for the RH, dotted line, DE, dashed-dotted line, RK, dashed line and LH, solid line, JTLs. The gain profiles have been obtained with a pump tone with frequency $\omega_p = 6$ GHz and a pump to critical currents ratio of 0.4. The parameters of each JTL are given in Table 2.3.

matching the process or not. The gain of the bare RH JTL is about 10 dB lower than the corresponding DE one. The differences in the magnitudes between the other typologies are a consequence of the different number of cells composing each of them[14]. Anyway, the obtained magnitudes are an optimistic estimation, given the simplifications of the modeling, which are discussed at the end of the section. A length-independent comparison of the amplifiers' performances is given by the per-unit-length gain coefficient g (see Equation 2.62), whose real part is shown in Figure 2.14(b). The RK TWPA has the higher value, has expected given the high gain obtained with just 500 unit-cells.

14 We choose different number of cells to obtain realistic results.

A second insightful information given by this comparison is related to the amplification bandwidth. The latter is related to the slope of total phase-mismatch $\Delta\tilde{k}$ around the points where it crosses zero. The smaller the slope, the broader the amplification bandwidth. Indeed, comparing the values of $\Delta\tilde{k}$ for the RK and LH cases, shown in Figure 2.11(a) and Figure 2.12(a), respectively, we can easily understand the differences in the two gain profiles.

Before moving forward to the counter-propagating case, it is worth mentioning that this comparison gives just an idea of the differences between the considered Josephson TWPAs, and it does not want to be exhaustive. For example, the recent improvements brought by Floquet engineering [98] and modulation windowing [93] in DE TWPAs has not been discussed, despite their impact on the performances. Moreover, we did not touch the realm of 3WM Josephson TWPAs [23, 99–101], which have in the large detuning between the pump frequency and the amplification band, their main advantage.

Finally, comparing the two different topologies at the same pump frequency is not completely fair. Indeed, RH JTLs show higher gain as the pump frequency increases [84] and can be thought as "high-frequency" amplifiers, in contrast to the dual LH topology, which shows better performances at lower pump frequencies [51]. In both cases gain increases as the operating frequencies approach the cut-off of the line. This is expected because it implies smaller velocities, thus effectively longer lines, or equivalently, longer interaction times. Note that it also implies higher losses, which will lower the effective gain and, most importantly, degrade the noise performances of the amplifier.

MOVING TOWARDS HIGHER FREQUENCIES The previous discussion gives us the opportunity to open a brief digression on what would be the best choice to increase the operating frequencies of Josephson TWPAs. The main drives to do so, come from both the particle physics and superconducting qubit communities. Indeed, searches for dark matter and axion-like particles in the Ku and K frequency bands [102, 103] and high-frequency qubit readout [104], would greatly benefit from broadband near-quantum limited amplification chains.

Hence, according to the previous discussion, the natural choice to implement a Josephson TWPA working above 10 GHz would be a JTL with a RH topology. However, such goal presents three main challenges:

A. Higher frequencies implies higher losses, thus lower effective gain and worst noise performances. Therefore, quite some work has to be done on the fabrication of the ground capacitors to minimize their loss tangent.

B. As the operating frequency increases the dispersion relation becomes less linear, as discussed in Section 2.1.1. Thus, phase-matching is more challenging.

C. Finally, finite size effect, described at the end of Section 2.2.1, might start to matter. Hence, the line parameters, such as the junctions plasma frequency and the ratio between the to-ground and in-line capacitances, need to be carefully designed.

Therefore, between the RK and the DE approaches to phase-match amplification, the latter is the most suited one. Indeed, it implies, usually, lower values of C_g, as can be seen from Table 2.3, making the last two points of the previous list easier to solve. Moreover, as demonstrated in [93, 98], losses can be quite low with this approach.

COUNTER-PROPAGATING MODES Now that the more standard gain performances of Josephson TWPAs has been discussed, we can focus our attention on the amplification process of counter-propagating signal and idler modes. As discussed at the end of the previous section, we consider this process only for the LH topology.

Using the same parameters as in Table 2.3 it is possible to compute the signal gain G_s and the idler conversion gain[15] G_i from the analytical formulas given in Equation 2.68. The resulting gain profiles are shown in Figure 2.15 for a pump frequency of 12 GHz and six different pump to critical currents ratios. The two amplified modes are now far detuned from each other, more than 10 GHz and, compared to the co-propagating case, the amplification bandwidth is orders of magnitudes narrower. Moreover, the maximum gain does not monotonically increase with the pump current. This is caused by the $1/\cos^2(|g|\ell)$ scaling of the gain at the phase-matching frequency, which has been discussed in paragraph 2.3.1.

For the same device length, the periodicity of the cosine, as a function of the pump current, changes, causing a non-monotonous behavior. This can be better understood looking at the gain as a function of the number of cells, shown in Figure 2.16(a). Of course, for each pump current, the gain is maximum when $gN_{cell} = (n + 1/2)\pi$ with $n \in \mathbb{N}$, as depicted in Figure 2.16(b).

Thus, a LH JTL can be used to phase-match the amplification process between two modes propagating in opposite directions with gain as high as the product gN_{cell} gets close to $\pi/2$. Of course, losses, which are not taken into account here, will limit the maximum value. Besides the spatial separation, this process results in a high frequency detuning between the modes. This is a significant advantage because is allows to easily filter out the high-power pump tone. Cancelling the latter,

15 We recall here that G_i is given by the ratio between the amplitude amplitude at the signal frequency and the output amplitude at the idler one, which is also called *trans*-gain.

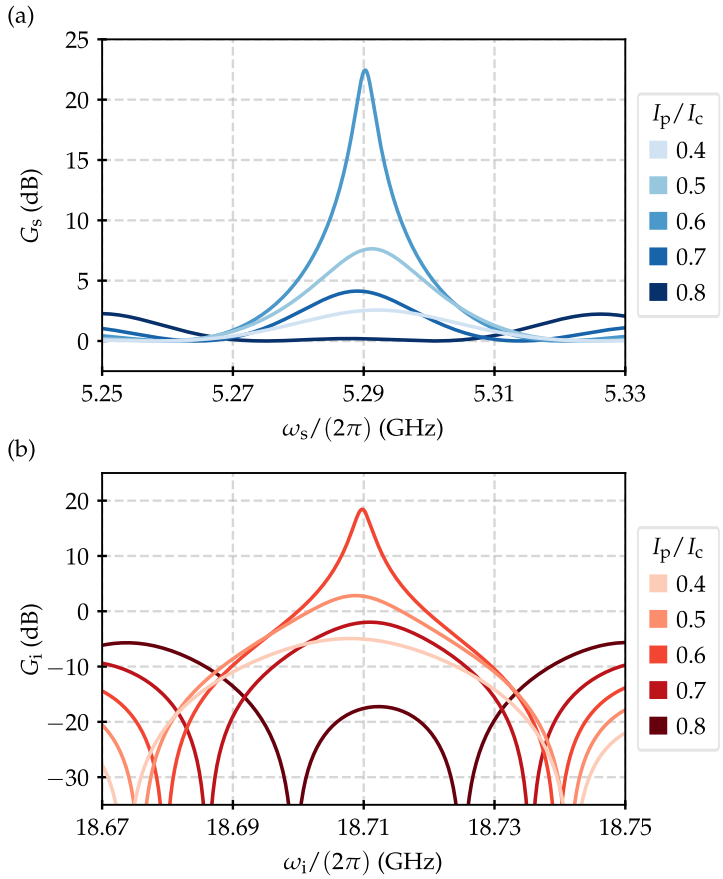

Figure 2.15: Counter-propagating signal and idler modes gains in a left-handed Josephson transmission line
(a) Signal gain G_s, as a function of the signal frequency $\omega_s/(2\pi)$, and (b) idler gain G_i, as a function of the idler frequency $\omega_i/(2\pi) = (2\omega_p - \omega_s)/(2\pi)$, for the counter-propagating amplification process, obtained from Equation 2.68, for a LH JTL. The gain profiles have been obtained with a pump tone with frequency $\omega_p/(2/pi) = 12$ GHz. Each shade of color corresponds to a different pump to critical currents ratio, as shown in the legends. The parameters of each JTL are given in Table 2.3.

is one of the main technical challenges when performing quantum optics experiments with 4WM-based Josephson TWPAs [22].

However, this high detuning can also be a problem. Indeed, the idler frequency is outside the usual bandwidth of most conventional circuit Quantum ElectroDynamic (cQED) experiment[16]. Note that there are ways to reduce both the idler frequency and the detuning between the two modes. First, the pump frequency allows a certain degree of control over them. Then, at the design level, by increasing the ratio

16 The majority of the low temperature components, such as circulators, have bandwidth as large as 4 to 12 GHz. More details on how we overcame this technical limitation are given in Section 3.1 in Chapter 3.

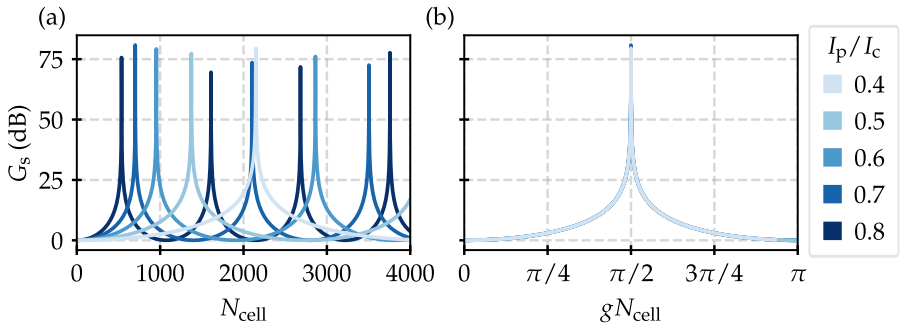

Figure 2.16: Signal gain dependence on the device's length for the counter-propagating process
Signal gain G_s at the signal frequency for which $\Delta\tilde{k} = 0$ as a function of (a) the number of cells and (b) the amplification length gN_{cell}. The curves have been obtained with a pump tone with frequency $\omega_p/(2/pi) = 12$ GHz. Each shade of color corresponds to a different pump to critical currents ratio as shown in the legends. The parameters of each JTL are given in Table 2.3.

between the to-ground and in-line capacitances, as shown in Figure 2.7, is possible to both lower the device cut-off and reduce its bandwidth.

INCREASING THE DYNAMIC RANGE Before concluding this section we shall discuss about the dynamic range of a LH JTL. From the two previous sections we have seen that the design of such a structure operating in the usual bandwidth of cQED experiments requires ground inductances on the order of the nH, as shown in Table 2.3. The latter implies critical currents in the hundreds of the nA scale. Now, this will limit the total amount of power the line can handle. All we have described in the previous sections was based on the initial assumption of low currents flowing through the JJs compared to their critical one, thus low critical current results in low power handling capabilities.

A solution commonly used to overcome this issue is based on implementing the required inductance with an array of N_j junctions with N_j times higher critical current [37, 105]. Thus, wave dynamic in the modified LH line can be described with the same equations as in the previous sections by performing the substitutions $L_j \mapsto N_j L_j$ and $I_c \mapsto N_j I_c$. It is worth pointing out that this is true under the assumption that the phase-drop across the array is equally divided across each junction. The latter is a valid assumption if the charging energy $E_c = e^2/2C_j$ of the superconducting islands connecting each of them can be ignored compared to the junctions Josephson energy $E_j = \varphi_0 I_c$. If we consider using JJs with an inductance of about 150 pH and a capacitance of about 250 fF, the aforementioned condition $E_j \gg E_c$ is easily satisfied, thus the previous discussions on the amplification properties still holds.

THEORETICAL MODELING LIMITATIONS Although this theoretical model helped us explaining the basic mechanisms behind the amplification processes in Josephson TWPAs, it will not help us in exactly predicting the gain produced by a real device. Indeed, several simplifications has been made:

A. We did not take into account for losses. Their effect will be to reduce the amount of gain, and can be modeled with Equation 2.56. Note that it is quite important to include them to obtain quantitative results [96].

B. We considered valid the strong pump approximation. Breaking such approximation helps when a quantitative modeling of pump depletion and of the 1-dB compression point is needed [91]. This can be done solving the entire system dynamics given by Equation 2.55.

C. We considered only the three modes of interest, but the presence of a high power tone in a nonlinear medium usually leads to more complex dynamics with generation of higher harmonics and intermodulation products. If justified, the inclusion of some of these other modes can be done, although the calculation will quickly become cumbersome. To efficiently model these more complex dynamics X-PARAMETER [106] or WRSPICE simulations can be performed.

D. We set the limit for the maximum pump current that can enter the JTL at the critical current I_c of the single JJ, although the value of the switching current[17] I_s is usually lower than I_c. Thus, taking I_c as upper bound for the pump current I_p is probably not the most realistic limit. However, we can not do better than using I_c and being aware of it.

Understanding the quantum dynamics of a strongly driven array of JJs is still an open problem

These comments will also apply to the modeling of frequency conversion processes in JTLs, which is the subject of the next section.

2.4 FREQUENCY CONVERSION

Besides amplification, JTLs can realize frequency conversion. This kind of parametric process has been recently leveraged to demonstrate Josephson TWPAs showing both broadband forward amplification and backward isolation within the same bandwidth [26, 27], and JTLs that can be configured both as an isolator or as a tunable coupler [28]. All of these realizations are based on waveguides with a RH topology, with the latter being the only one exploiting solely the $\chi^{(3)}$ nonlinearity. Doing so required coupling two JTLs with very different wave

17 The current at which the transmission through the JTL decreases by orders of magnitude.

velocities of propagation: by significantly lowering the pump wave velocity, phase-matching of conversion processes involving counter-propagating modes has been possible. Thinking about the previous discussions on the counter-propagating amplification we can already imagine how similar 4WM conversion processes could be obtained in a JTL with LH topology. Thus, in the following, we will focus on the latter.

Let us consider a process where a photon from the signal of interest, with frequency ω_s, gets combined with two photons from the strong pump wave, with frequency ω_p, and converted to a photon at the sum frequency $\omega_u = 2\omega_p + \omega_s$. Thus, this process leads to depletion of the signal wave, *i. e.* to its attenuation. Note that the down-conversion process in which a high frequency signal photon gets converted to a photon at the difference frequency $\omega_d = \omega_s - 2\omega_p$, together with the generation of the two pump photons, is possible.

We can solve the nonlinear wave equation derived in Section 2.2.2 by considering a plane wave ansatz, with the pump, signal and sum modes involved:

$$\Phi_{ans}(x,t) = \frac{1}{2} \sum_{m \in \{p,s,u\}} \left(A_m(x) e^{i(k_m x - \omega_m t)} + c.c \right), \tag{2.74}$$

In the following we will drop again the position argument of all $A_m(x)$ to shorten the notation

where $A_m(x)$ is the position dependent slow varying flux amplitude of the mode m; p,s,u respectively denote the pump, signal and sum modes with k_m and ω_m their associated dimensionless wavevectors and angular frequencies. As before, the $\pm$ sign in front of k_m represents the direction of propagation of the wave.

2.4.1 Coupled mode equations

Thus, by plugging Equation 2.74 into the wave equations Equation 2.53 three coupled differential equations for the pump, signal and sum modes can be obtained.

The same slowly varying envelope and rotating wave approximations, described in Section 2.3.1, can be performed. With the difference that now we will retaining only the terms that rotate at ω_p, ω_s and ω_u.

The following propagation equations for the pump, signal and sum waves are obtained:

$$\begin{cases} \partial_x A_\mathrm{p} = -\Gamma_\mathrm{p} A_\mathrm{p} + i\alpha_\mathrm{pp} \left|A_\mathrm{p}\right|^2 A_\mathrm{p} + i\alpha_\mathrm{ps} \left|A_\mathrm{s}\right|^2 A_\mathrm{p} \\ \qquad\qquad + i\alpha_\mathrm{pu} \left|A_\mathrm{u}\right|^2 A_\mathrm{p} + i\beta_\mathrm{p} A_\mathrm{u} A_\mathrm{s}^* A_\mathrm{p}^* e^{-i\Delta k x}, \\ \partial_x A_\mathrm{s} = -\Gamma_\mathrm{s} A_\mathrm{s} + i\alpha_\mathrm{ss} \left|A_\mathrm{s}\right|^2 A_\mathrm{s} + i\alpha_\mathrm{sp} \left|A_\mathrm{p}\right|^2 A_\mathrm{s} \\ \qquad\qquad + i\alpha_\mathrm{su} \left|A_\mathrm{u}\right|^2 A_\mathrm{s} + i\beta_\mathrm{s} A_\mathrm{p}^{*2} A_\mathrm{u} e^{-i\Delta k x}, \\ \partial_x A_\mathrm{u} = -\Gamma_\mathrm{u} A_\mathrm{u} + i\alpha_\mathrm{uu} \left|A_\mathrm{u}\right|^2 A_\mathrm{u} + i\alpha_\mathrm{up} \left|A_\mathrm{p}\right|^2 A_\mathrm{u} \\ \qquad\qquad + i\alpha_\mathrm{us} \left|A_\mathrm{s}\right|^2 A_\mathrm{u} + i\beta_\mathrm{u} A_\mathrm{p}^2 A_\mathrm{s} e^{i\Delta k x}, \end{cases} \tag{2.75}$$

where $\Delta k = 2k_\mathrm{p} + k_\mathrm{s} - k_\mathrm{u}$ is the dimensionless linear phase mismatch for the frequency sum process. The main difference between this equations and the ones for amplification, given in Equation 2.55, lies in these last terms, which will result in attenuation of the signal wave and generation of the sum one. The coefficients in front of each of these terms are the same as the ones listed in Table 2.1, with the change of the index i into u.

Such CMEs can be solved numerically [91], however, we can again perform the strong pump approximation to simplify them. As a consequence, in the equation for the pump amplitude we only keep the first two terms and the propagation of the pump wave is not affected by the signal and sum ones anymore. While, on the signal and sum side all terms which are quadratic in their amplitudes can be neglected, leading to the following CMEs:

$$\begin{cases} \partial_x A_\mathrm{p} = -\Gamma_\mathrm{p} A_\mathrm{p} + i\alpha_\mathrm{pp} \left|A_\mathrm{p}\right|^2 A_\mathrm{p}, \\ \partial_x A_\mathrm{s} = -\Gamma_\mathrm{s} A_\mathrm{s} + i\alpha_\mathrm{sp} \left|A_\mathrm{p}\right|^2 A_\mathrm{s} + i\beta_\mathrm{s} A_\mathrm{p}^{*2} A_\mathrm{u} e^{-i\Delta k_\mathrm{L} x}, \\ \partial_x A_\mathrm{u} = -\Gamma_\mathrm{u} A_\mathrm{u} + i\alpha_\mathrm{up} \left|A_\mathrm{p}\right|^2 A_\mathrm{u} + i\beta_\mathrm{u} A_\mathrm{p}^2 A_\mathrm{s} e^{i\Delta k_\mathrm{L} x}, \end{cases} \tag{2.76}$$

LOSSLESS CASE As for the amplification case, in the same spirit of simplicity, we can set the loss coefficients to zero and solve for the pump propagation:

$$A_\mathrm{p}(x) = A_\mathrm{p}(0) e^{i\tilde{\alpha}_\mathrm{p} x}, \tag{2.77}$$

which can be replaced in the signal and sum equations, together with the definition $A_\mathrm{s,u} = a_\mathrm{s,u} e^{i\tilde{\alpha}_\mathrm{s,u} x}$, to obtain:

$$\begin{cases} \partial_x a_\mathrm{s} = \quad i\tilde{\beta}_\mathrm{s} a_\mathrm{u} e^{-i\Delta\tilde{k} x}, \\ \partial_x a_\mathrm{u} = \quad i\tilde{\beta}_\mathrm{u} a_\mathrm{s} e^{i\Delta\tilde{k} x}, \end{cases} \tag{2.78}$$

where $\Delta\tilde{k}$ is the total phase mismatch, which reads:

$$\Delta\tilde{k} = \Delta k + \Delta\tilde{\alpha} \quad \text{with} \quad \begin{cases} \Delta k = 2k_\mathrm{p} + k_\mathrm{s} - k_\mathrm{u}, \\ \Delta\tilde{\alpha} = 2\tilde{\alpha}_\mathrm{p} + \tilde{\alpha}_\mathrm{s} - \tilde{\alpha}_\mathrm{u}, \end{cases} \tag{2.79}$$

and the coefficients $\tilde{\alpha}_m$ and $\tilde{\beta}_m$ are the same as in the amplification case, given in Table 2.2. As before, the phase-mismatch $\Delta\tilde{k}$ has both a dispersive component and a nonlinear one and it limits the efficiency of the process.

Again, depending on the propagation direction of signal and sum modes, the solution of Equation 2.58 is quite different.

CO-PROPAGATING SIGNAL AND SUM MODES Let us start also for the frequency conversion process by considering the signal and sum modes propagating in the same direction. Thus, the initial conditions to solve the CMEs derived in the previous section must be given at the initial position $x = 0$: $a_{s,u,in} = a_{s,u}(0)$, which lead to the following scattering relations:

$$a_{s,u}(x) = \left\{ \left[\cos(gx) \pm i\frac{\Delta\tilde{k}}{2g} \sin(gx) \right] a_{s,u}(0) + i\frac{\tilde{\beta}_{s,u}}{g} \sin(gx) a_{u,s}(0) \right\} e^{\mp i\frac{\Delta\tilde{k}x}{2}}, \tag{2.80}$$

where

$$g = \sqrt{\tilde{\beta}_s\tilde{\beta}_u + \left(\frac{\Delta\tilde{k}}{2}\right)^2}, \tag{2.81}$$

is the per-unit-length parametric conversion coefficient. Now, the exchange between the signal and sum modes is ruled by sinusoidal functions. Thus, it continues back and forth along the line with a period depending on the value of g. Indeed, the attenuation and the frequency conversion gain at $x = \ell \equiv N_{cell}$, when the input at the sum frequency is vacuum, *i.e.* $a_u(0) = 0$, are given by:

$$\begin{cases} A_s(\ell) = \left|\frac{a_s(\ell)}{a_s(0)}\right|^2 = \left|\cos(g\ell) + i\frac{\Delta\tilde{k}}{2g}\sin(g\ell)\right|^2, \\ G_u(\ell) = \left|\frac{a_u(\ell)}{a_s(0)}\right|^2 = \left|i\frac{\tilde{\beta}_u}{g}\sin(g\ell)\right|^2, \end{cases} \tag{2.82}$$

which, in the ideal case of perfect phase-matching, *i. e.* $\Delta\tilde{k} = 0$, become:

$$\begin{cases} A_s(\ell) = \left|\cos\left(\sqrt{\tilde{\beta}_s\tilde{\beta}_u}\ell\right)\right|^2, \\ G_u(\ell) = \left|i\sqrt{\frac{\tilde{\beta}_u}{\tilde{\beta}_s}}\sin\left(\sqrt{\tilde{\beta}_s\tilde{\beta}_u}\ell\right)\right|^2, \end{cases} \tag{2.83}$$

Therefore, to achieve full conversion, one needs to carefully tune the power of pump tone, *i. e.* the values of the nonlinear coupling coefficients such that $\sqrt{\tilde{\beta}_s\tilde{\beta}_i^*}\ell = \left(n + \frac{1}{2}\right)\pi$ with $n \in \mathbb{N}$.

COUNTER-PROPAGATING SIGNAL AND SUM MODES Now, we will describe the other situation in which the signal and sum modes travel in opposite directions. The latter, is similar to what has been realized in [28].

Let us consider the case in which the signal modes propagate in the positive direction, thus with a positive wavevector, while the sum is generated in the opposite one. This changes the initial conditions to solve Equation 2.78. Now, $a_{s,0} = a_s(0)$, while $a_{u,0} = a_u(\ell)$, leading to the following scattering relations:

$$\begin{aligned} a_s(x) = \Bigg\{ & \frac{\cos\left[g(\ell - x)\right] - i\frac{\Delta\tilde{k}}{2g}\sin\left[g(\ell - x)\right]}{\cos(g\ell) - i\frac{\Delta\tilde{k}}{2g}\sin(g\ell)} a_s(0) \\ & + i\frac{\tilde{\beta}_s}{g}\frac{\sin(gx)}{\cos(g\ell) + i\frac{\Delta\tilde{k}}{2g}\sin(g\ell)} e^{-i\frac{\Delta\tilde{k}\ell}{2}} a_u(\ell) \Bigg\} e^{-i\frac{\Delta\tilde{k}x}{2}}, \end{aligned} \tag{2.84}$$

and

$$\begin{aligned} a_u(x) = \Bigg\{ & \frac{\cos(gx) - i\frac{\Delta\tilde{k}}{2g}\sin(gx)}{\cos(g\ell) - i\frac{\Delta\tilde{k}}{2g}\sin(g\ell)} e^{-i\frac{\Delta\tilde{k}L}{2}} a_u(\ell) \\ & - i\frac{\tilde{\beta}_u}{g}\frac{\sin\left[g(\ell - x)\right]}{\cos(g\ell) + i\frac{\Delta\tilde{k}}{2g}\sin(g\ell)} a_s(0) \Bigg\} e^{i\frac{\Delta\tilde{k}x}{2}}, \end{aligned} \tag{2.85}$$

where

$$g = \sqrt{\tilde{\beta}_s\tilde{\beta}_u + \left(\frac{\Delta\tilde{k}}{2}\right)^2}, \tag{2.86}$$

is the same as before, with the important exception that $\tilde{\beta}_u$ has changed its sign because of the direction of propagation of the sum mode. Again, we can write down the signal attenuation and frequency conversion gain:

$$\begin{cases} A_s(\ell) = \left|\frac{a_s(\ell)}{a_s(0)}\right|^2 = \left|\frac{1}{\cos(g\ell) - i\frac{\Delta\tilde{k}}{2g}\sin(g\ell)}\right|^2, \\ G_u(0) = \left|\frac{a_u(0)}{a_s(0)}\right|^2 = \left|i\frac{\tilde{\beta}_u}{g}\frac{\sin(g\ell)}{\cos(g\ell) + i\frac{\Delta\tilde{k}}{2g}\sin(g\ell)}\right|^2, \end{cases} \tag{2.87}$$

which, in the ideal case of perfect phase-matching, *i. e.* $\Delta\tilde{k} = 0$, become:

$$\begin{cases} A_s(\ell) = \left|\left[\cos\left(\sqrt{\tilde{\beta}_s\tilde{\beta}_u}\ell\right)\right]^{-1}\right|^2, \\ G_u(0) = \left|\sqrt{\frac{\tilde{\beta}_u}{\tilde{\beta}_s}}\tan\left(\sqrt{\tilde{\beta}_s\tilde{\beta}_u}\ell\right)\right|^2. \end{cases} \tag{2.88}$$

Now, given that the signal and sum modes propagate in opposite directions and that $\tilde{\beta}_{s,u} \propto k_{s,u}^{-1}$, for a LH JTL, the product $\tilde{\beta}_s\tilde{\beta}_u$ is negative. Thus, the signal attenuation can be written as:

$$A_s(\ell) = \left| \left[\cosh\left(\sqrt{|\tilde{\beta}_s\tilde{\beta}_u|}\ell \right) \right]^{-1} \right|^2 \approx 4e^{-2\sqrt{|\tilde{\beta}_s\tilde{\beta}_u|}\ell}, \tag{2.89}$$

which gives an exponential attenuation with respect to the conversion length $\sqrt{|\tilde{\beta}_s\tilde{\beta}_u|}\ell$, in the asymptotic limit.

However, as for the amplification processes, both conversion ones are limited by the phase-matching constraint.

2.4.2 Phase-matching

In recent years, very different technics has been used to phase-match conversion processes in RH JTL, ranging from dispersion engineering [27] to dynamical phase-matching [26] and to using a two-mode JTL with different velocities [28]. The latter approach can be applied in a similar way to a LH JTL leveraging its unique dispersion relation. The idea is to use modes with very different wavevectors, *i.e.* very different velocities, such that they compensate for each other, as for the amplification of counter-propagating signal and idler modes described in Section 2.3.2.

Now, the phase-matching condition is $2\tilde{k}_p + \tilde{k}_s - \tilde{k}_u = 0$. Given the LH dispersion relation, a low frequency mode, has a larger wavevector compared to an high frequency one. Thus, to satisfy the previous condition a slow pump tone, propagating in the opposite direction with respect to the signal, such that $\tilde{k}_p \mapsto -\tilde{k}_p$, is required, as schematically shown in Figure 2.17(a). Considering the conversion process in which the up-converted mode travels backwards with respect to the signal, such that $\tilde{k}_u \mapsto -\tilde{k}_u$, the latter requirement for the pump is even more clear.

The phase-matching condition can be satisfied at any given signal frequency, by adjusting the pump one, such that $2\omega_p + \omega_s - \omega_u = 0$, as long as the up-converted tone falls within the bandwidth of the device. For a given pump frequency, the two conversion processes are phase-matched at two different signal frequencies, with the up-converted tone propagating either forward or backwards with respect to the signal, as shown in Figure 2.17(b).

In both cases, the total phase-mismatch crosses zero at one signal frequency, as shown in Figure 2.18(a) and (b), for the co- and counter-propagating cases, respectively. The main contribution to $\Delta\tilde{k}$ is given by the linear one, whose gradient close to zero sets the bandwidth of the process. Thus, we expect the counter-propagating conversion process to show a broader bandwidth.

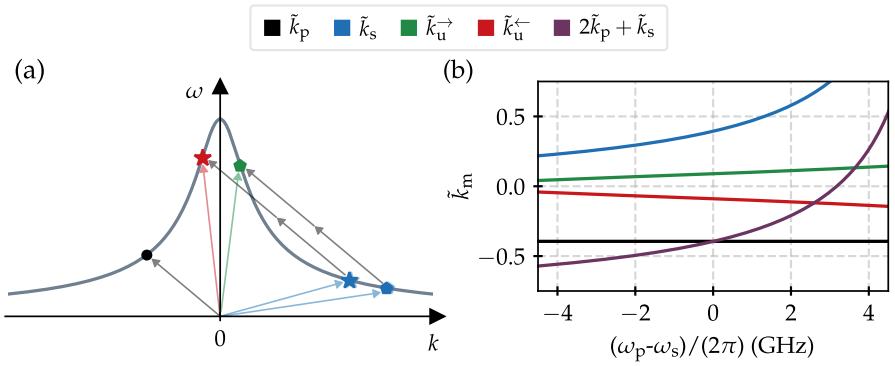

Figure 2.17: Phase-matching of frequency conversion processes in a Josephson left-handed transmission line
(a) The dispersion relation, in grey, for both positive and negative wavevectors, of a LH JTL, highlighting the phase-matching condition of the two frequency conversion processes described in the previous section, by means of a pump wave propagating with negative wavevector. The latter is represented by the black dot. For a given pump tone, there are two signal, in blue, and sum, in red and green, modes for satisfying the phase-matching and energy conservation conditions, as shown by the vectors $(\tilde{k}_{p,s,u}, \omega_{p,s,u})$, representing each mode. In one case, represented by the pentagons, the up-converted mode propagates in the same direction as the signal one; while, in the other case, represented by the stars, the up-converted mode propagates backwards.
(b) Effective wavevectors of the pump, in black, signal, in blue, forward sum, in green, and backward sum, in red, as function of the signal frequency. The co- and counter-propagating conversion processes are matched when $\tilde{k}_u$ crosses $2\tilde{k}_p + \tilde{k}_s$, represented by the purple line.

2.4.3 Attenuation

Now that we have understood how frequency conversion processes can be obtained in a JTL with LH topology, we can compare the attenuation performances of the two cases, previously discussed. This is of particular interest, because it allows to directly compare the differences between the exponential behavior and the periodic one, described in Section 2.4.1. In the following, all curves have been obtained with the parameters given in Table 2.4.

Neglecting losses, the signal attenuation profiles of the co- and counter-propagating conversion processes can be obtained from the analytical formulas given in Equation 2.82 and in Equation 2.87, respectively. The result, obtained using a pump tone with frequency $\omega_p/(2\pi) = 7$ GHz for five different values of pump to critical currents ratio, are shown in Figure 2.19.

There are two main differences between the two processes:

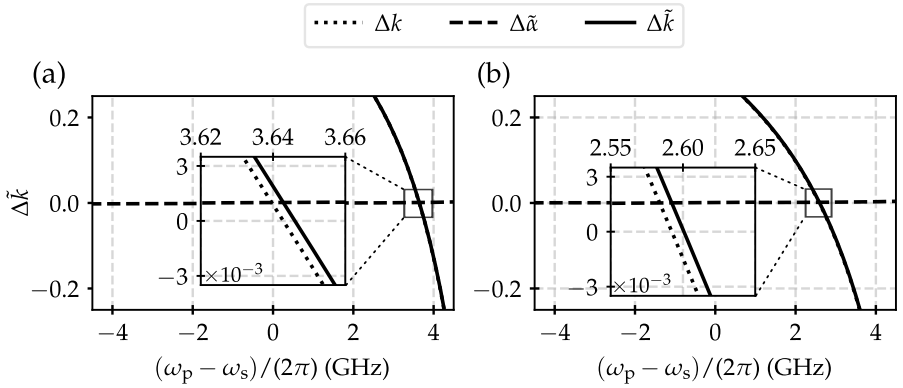

Figure 2.18: Total phase-mismatch of the frequency conversion processes in a Josephson left-handed transmission line
The total phase-mismatch, solid line, together with the linear, dotted line, and nonlinear, dashed line, contributions, as a function of the signal frequency ω_s, for a pump frequency ω_p, for (a) the co-propagating and (b) the counter-propagating conversion processes. Now, all contributions cross zero at only one signal frequency. The effect of the nonlinear part on the linear one is to slightly shift the phase-matching frequency, as shown in the inset.

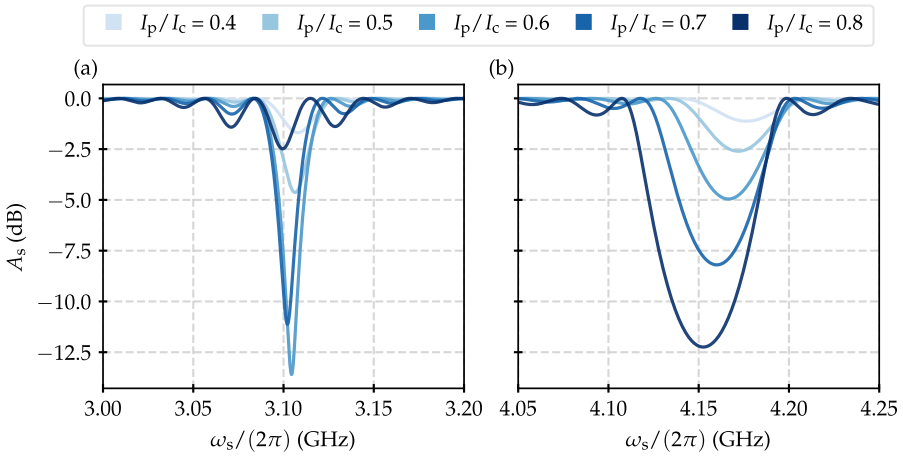

Figure 2.19: Signal attenuation in a left-handed Josephson transmission line
Signal attenuation of (a) the co-propagating conversion process, obtained from Equation 2.82, and (b) the counter-propagating conversion process, obtained from Equation 2.87. The gain profiles have been obtained with a pump tone with frequency $\omega_p = 7$ GHz for several pump to critical currents ratios, as listed in the legend. The parameters of the JTL are given in Table 2.4.

1. First, the bandwidth is quite different. The counter-propagating conversion results is a broader process, as expected by the behavior of the total phase-mismatch, shown in Figure 2.18.

PARAMETER	VALUE	UNIT
Number of cells N_{cell}	1000	#
Josephson inductance L_{j}	3	nH
Josephson capacitance C_{j}	12.5	fF
Series capacitance C_{s}	1.2	pF
Critical current I_{c}	110	nA
Plasma frequency $\omega_{\text{j}}/(2\pi)$	26.0	GHz
Cut-off frequency $\omega_{\text{o}}/(2\pi)$	2.7	GHz

Table 2.4: Parameters of the left-handed Josephson transmission lines used to simulate the attenuation profiles
Definition of the parameters used to simulate the attenuation profiles in Figure 2.19, with reference to Figure 2.8.

2. Then, the minimum magnitude for the same values of $I_{\text{p}}/I_{\text{c}}$ are different, and different is their dependence on it. The latter is again expected given the different scaling with respect to $|g|\ell$ of the attenuation, as discussed in Section 2.4.1.

For the co-propagating case the attenuation scales as $\cos^2(|g|\ell)$ at the phase-matching frequency. Therefore, it is minimum when $gN_{\text{cell}} = (n + 1/2)\pi$ with $n \in \mathbb{N}$. While, in the counter-propagating case we expect an exponential decrease of the signal power as the conversion length $|g|\ell$ increases. This difference can be better understood by looking at the attenuation as a function of the number of cells for a given value of $I_{\text{p}}/I_{\text{c}}$, as shown in Figure 2.20.

It is worth mentioning that despite the small bandwidth, the frequency at which the conversion occurs can be tuned by varying the frequency of the pump tone. Of course, this will equally change the frequency of the up-converted mode. The dependence of the two conversion processes as a function of the frequency of the signal and pump tones is shown in Figure 2.21. The frequency of both isolation gaps increases with the pump frequency until $\omega_{\text{u}} = 2\omega_{\text{p}} + \omega_{\text{s}}$ reaches the plasma frequency of the JJs, above which, no conversion is allowed.

Thus, a LH JTL can be used to phase-match conversion processes between two modes propagating either in the same or in opposite direction. Depending on the process the signal attenuation scale monotonically or not with the conversion length as high as the product $g\ell$. In either cases, the process is frequency tunable over a few GHz bandwidth, which depends only on the junctions' properties. The comments on how to increase the dynamic range of a LH JTL and on the limitations of the theoretical model, made at the end of Section 2.3.3 can be applied to the conversion case as well.

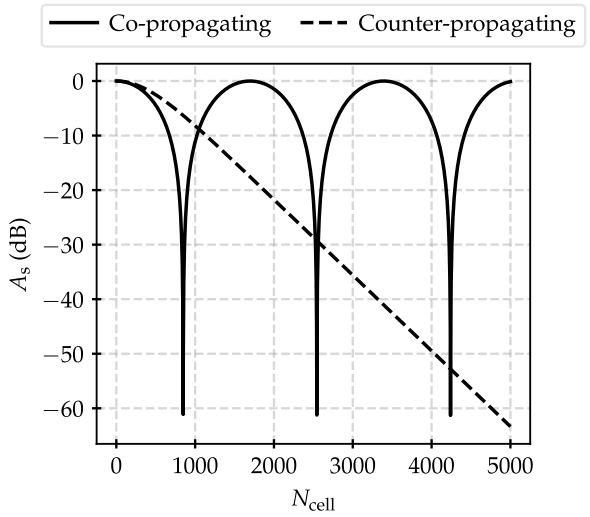

Figure 2.20: Signal attenuation dependence on the device's length
Signal attenuation at the signal frequency for which $\Delta\tilde{k} = 0$ as a function of the number of cells for the co-propagating, solid line, and counter-propagating, dashed line, conversion processes. The curves have been obtained with a pump tone with frequency $\omega_p/(2\pi) = 7$ GHz and pump to critical currents ration of 0.6.

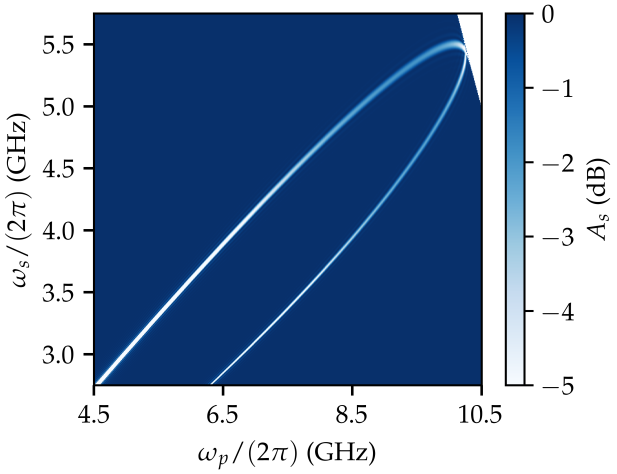

Figure 2.21: Signal attenuation dependence on the pump frequency
Signal attenuation as a function of the signal $\omega_p/(2\pi)$ and pump $\omega_p/(2\pi)$ frequencies for pump to critical currents ratio of 0.6. Note that the two process have been simulated separately and then the results added together. The rightmost gap corresponds to the co-propagating conversion process, while the other gap corresponds to the counter-propagating one.

2.5 CONCLUSIONS

This concludes our description of 4WM-mediated traveling-wave parametric interactions in Josephson waveguides. We have seen how, in the

microwave range, it is possible to artificially design materials with tailored response to the electromagnetic field. In Section 2.1, we described how wave dispersion can be controlled in TLs by varying the arrangement of its constitutive series impedances and ground admittances. In particular, a high-pass network can be used to implement materials characterized by negative permittivity and permeability, dubbed as LH. Then, in Section 2.2, Josephson junctions have been included in the lines, slightly modifying their dispersion relation, and the equation of motion describing wave dynamics inside the lines have been derived for both topologies. This way, we could finally move to describe, in Section 2.3, how parametric amplification can be modeled and phase-matched in these structures. Of special interest is the LH topology, its unique dispersion relation allows for amplification of both co- and counter-propagating signal and idler modes. The differences between the two have been also discussed. Moreover, a brief comparison of the amplification performances resulting from the different approaches to phase-matching for the broadband co-propagating case has been done. In the end, in Section 2.4, we derived the scattering relations describing frequency conversion processes in JTLs. Particular focus has been given to show how leveraging the LH dispersion relation is possible to phase-match conversion processes between two modes propagating either in the same or in opposite direction.

3 EXPERIMENTAL SETUP

Behind the advancements obtained studying light-matter interactions with superconducting circuits, there, certainly, are the fact that such systems can be characterized with conventional microwave electronics tools and that their thermal fluctuations can be reduced below the relevant energy scale of the system. Such goal is achieved by operating superconducting circuits at very low temperatures, around 20 mK, inside dilution refrigerators[1]. Indeed, the typical energy scale of superconducting circuits systems lies in the microwave C-band, spanning the 4 to 8 GHz range, which correspond to about 200 and 400 mK. Hence, the choice of such ultra-low temperatures[2].

Here, we describe the experimental setup used to perform the experiments whose results are reported in Chapter 5 and Chapter 6. Those experiments have been realized in an Inverted Dilution Refrigerator (IDR), designed and manufactured at the Institut Néel, with the samples placed at its 20 mK stage, inside a μ-metal magnetic shield. A description of the working principles of this kind of dilution refrigerators can be found in [107]. Here, we will focus on the microwave setup, starting from the description of the *high-frequency* output line, which has been devised to perform microwave measurements up to the Ku-band, spanning the 12 to 18 GHz range. Then, we discuss the measurements calibration procedure, which allows to relate the values measured by the instruments at room temperature to the ones at the input and output of the Device Under Test (DUT). Finally, the full microwave experimental setup is described.

The fridge was fully operational and working perfectly, thanks to the work of the previous PhD and postdoc, Arpit Ranadive and Martina Esposito

3.1 EXTENDING THE MEASUREMENTS BANDWIDTH

The aforementioned frequency range of superconducting circuits experiments is usually easily extended to the X-band, spanning the 8 to 12 GHz range. More recently, particle physics and superconducting qubit communities are pushing the higher limit up to the K-band, *i.e.* to the the 18 to 26.5 GHz range, in the frameworks of detection schemes for dark matter and axion-like particles searches [102] and high-frequency qubit readout [104]. The latter applications would see

1 Which are, nowadays, commercially available and user-friendly, with cooling cycle almost fully automatized.

2 The required operating temperature can be estimated by imposing the thermal photon occupation number $n(\omega, T)$, given by Bose-Einstein distribution, to be less than one [107].

major improvements from broadband near-quantum limited amplifiers. Moreover, the performances of standard TWPAs would greatly benefit from studies of intermodulation product and higher harmonics generation [108], which usually fall in the aforementioned bands. Finally, as seen in Chapter 2, the to measure the idler generated by the counter-propagating amplification process, in LH Josephson waveguides, a setup working, at least, up to 18 GHz, is needed. The same applies for the frequency conversion processes. This motivated us to devise a setup with available bandwidth until the Ku-band.

3.1.1 General requirements

When reading out low power microwave signals one needs to implement an amplification chain, in order to maximize the Signal to Noise Ratio (SNR). However, every amplifier will add some noise, while amplifying the signal [30]. The total noise N_{tot} added by an amplification chain is given by [85]:

$$N_{tot} = N_1 + \frac{N_2}{G_1} + \frac{N_3}{G_1 G_2} + \cdots , \tag{3.1}$$

This explains the importance of near-quantum limited amplifiers

where N_i and G_i are the input-referred added noise and the gain of the $i-th$ amplifier, respectively. Thus, the choice of the first amplifier is crucial. Its added noise has to be as low as possible, while the its gain has to be large enough to suppress the contributions of the following amplifiers in the chain. Thus, the first component one needs to look for, when devising a readout line, is a suitable low-noise amplifier. Besides near-quantum limited amplifiers, the most suited low-noise amplifiers are High-Electron-Mobility-Transistor (HEMT) ones, working at 4 K.

A second requirement is to decouple the DUT, anchored at at the coldest stage of the cryostat, from the thermal noise radiating from the components at higher temperatures stages. This is achieved using isolators to avoid attenuation, which would degrade the SNR. The isolation performances of such component need to cover the frequency band of interest.

3.1.2 High-frequency output line

Unfortunately, no commercially available broadband cryogenic isolators cover the all 4 to 18 GHz band we are interested in. Therefore, we decided to use of the existing output line in the cryostat, with measurement bandwidth from 4 to 12 GHz, combining it with a second line, whose bandwidth spans the 12 to 18 GHz range, using two diplexers, as schematically shown in Figure 3.1.

A first diplexer allows to split the output line at the DUT level, enabling the isolation and amplification of the two bands separately. Then, a second diplexer is used to recombine the two lines at the

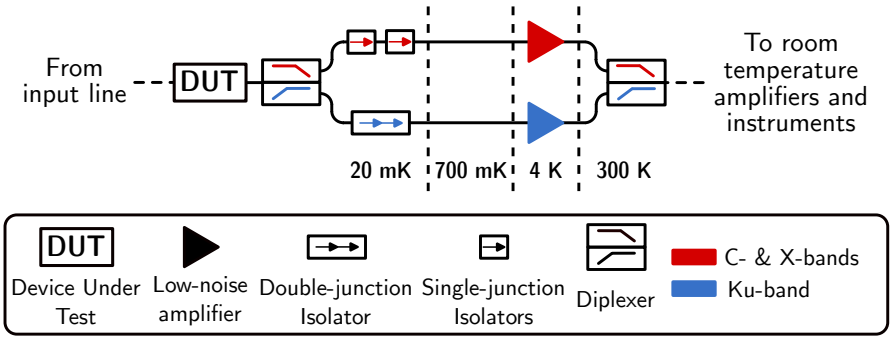

Figure 3.1: Schematic of the high-frequency output line
The extension of the measurements bandwidth to the Ku-band has been realized by splitting the line at the output of the DUT and recombining it at room temperature. Thus, the high-frequency output lines is composed of a line working in the C- & X-bands, in red, and a line working in the Ku-band, in blue. The specifics of the depicted components in each line are given in Table 3.1.

COMPONENT	REFERENCE	BANDWIDTH	LINE
Amplifier	LNF-LNC0.3_14B	0.3-14 GHz	C & X
	LNF-LNC6_20D	6-20 GHz	Ku
Isolator	QCI-G0401201AU	4-12 GHz	C & X
	QCI-G1201802AU	12-18 GHz	Ku
Diplexer	TGF-A4216-002	DC-11.4 GHz	C & X
		12.6-18.0 GHz	Ku

Table 3.1: Components of the high-frequency output line
List of the main components used in the high-frequency output line. The operating bandwidth of the line is given by the bandwidth of the isolators.

output of the fridge, allowing to measure the full 4 to 18 GHz span. A list[3] of the aforementioned three main components used in each frequency band is given in Table 3.1.

3.2 CALIBRATION

In order to characterized the devices, we need to readout the generated microwave signals, but also to address them. Thus, the DUT has to be electrically connected to the instruments at room temperatures

3 We explicitly identify the components as reference, given the novelty of the setup. However, we do not imply that the such components are necessarily the best available.

via coaxial cables. A simplified schematic of the measurement setup, including the input line, is shown in Figure 3.2.

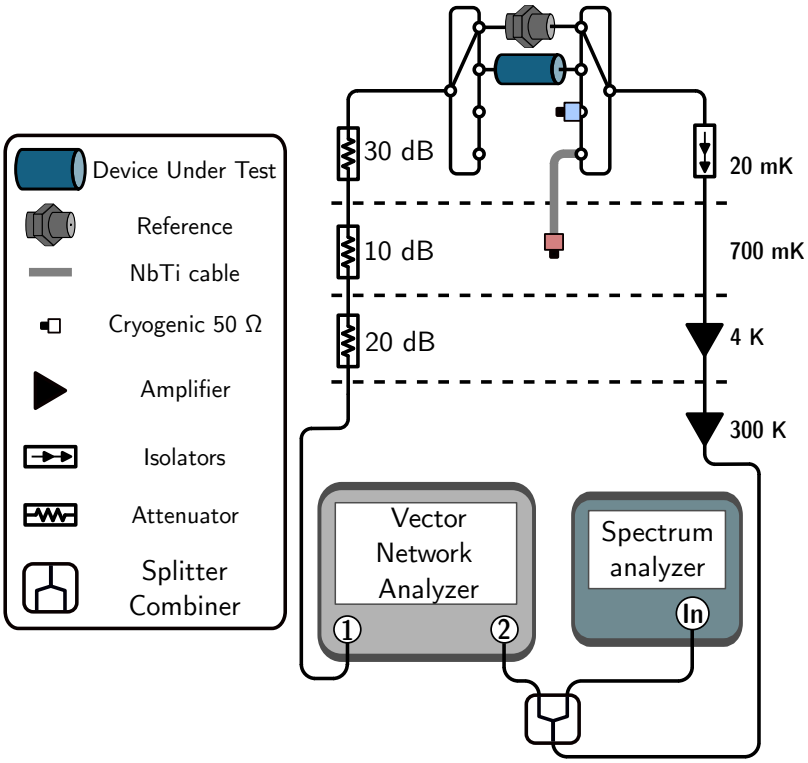

Figure 3.2: Simplified schematic of the experimental setup used for the calibration
Only the relevant components and input/output lines used for the setup calibration are shown. The sample parameters and loss can be inferred by measuring its normalized linear transmission S_{21}. To do so only one input and output lines are necessary. The normalization is performed using a cable as a reference. The system gain and noise are obtained by a Y-factor measurement thanks to the two 50 Ω loads that acts as noise sources at two different temperatures.

The DUT is usually probed with a Vector Network Analyzer (VNA), which measures the scattering matrix S of a microwave network, relating the magnitude and phase of the incident waves with the reflected and transmitted ones [85]. To accurately determine the S-matrix of the DUT a calibration scheme is needed. The latter is used to shift the reference plane of the measurements from the VNA ports to the ports of the DUT itself, de-embedding the contributions coming from all the passive and active components between the instrument and the device. Such procedure is easily performed at room temperature using commercial calibration kits, which embed the necessary standards to perform the calibration procedure[4]. When the DUT is placed at

4 Depending on the number of ports one is interested in, different calibration procedures can be performed. For two-port network three main procedures can be used

the coldest point of the dilution refrigerator at mK temperatures, as for superconducting circuits experiments, implementing an accurate microwave calibration is more challenging, but still possible [109, 110].

Here, we choose the most common solution used in the community when characterizing TWPAs [84, 111], *i.e.* an in-situ transmission normalization based on a reference device, plus a Y-factor noise figure method for the system gain calibration. To do so, the experimental setup features a pair of microwave switches at mK temperature, as shown in Figure 3.2.

3.2.1 Transmission

Thanks to the switches we can perform an in-situ transmission calibration using a female-female SMA adapter as reference. The sample and the reference are connected to the switches with cables which are nominally the same. Thus, the transmission S parameter of the DUT is obtained by comparing the one measured through the device with that measured through a reference:

$$S_{21}(\omega) = \frac{S_{21}^{\mathrm{DUT}}(\omega)}{S_{21}^{\mathrm{ref}}(\omega)}, \tag{3.2}$$

where S_{21}^{DUT} and S_{21}^{ref} are the uncalibrated S_{21} parameters measured by the VNA through the DUT and the reference, respectively. Here, we are assuming that the attenuation and electrical length of the reference are negligible with respect to the ones of the DUT. This motivates the choice of a female-female SMA adapter as reference. Indeed, it can be considered as a zero-length thru which adds no delay, no loss, no capacitance, and no inductance. A cable or a connectorized printed circuit board (PCB) would add some delay or loss, which could cause a significant error when estimating the normalized S_{21} parameter.

3.2.2 Gain and noise

The above transmission calibration gives the value of the normalized DUT S_{21} parameter, but we have no access to the power reaching its ports, because the input line attention $A_{sys}(\omega)$ and the output line gain $G_{sys}(\omega)$ are unknown. The latter can be obtained by performing a noise power calibration procedure. A common technique for such purpose is the *Y*-factor method [85], illustrated in Figure 3.3. It consists in using two matched loads at different temperatures, T_{C} and T_{H}, as noise sources, connected via a switch to the output amplification chain. We use two cryogenic 50 Ω loads placed at the 20 mK stage, together with the DUT, and at an hotter plate, together with a thermometer to

Thru-Reflect-Line (TRL), Short-Open-Load-Thru (SOLT), Short-Open-Load-Reciprocal (SOLR). For all of them several standards are required.

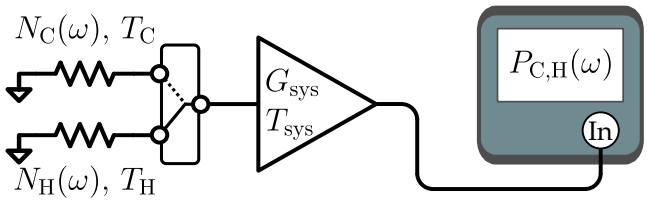

Figure 3.3: Illustration of the Y-factor calibration method
The system gain and noise are obtained by a Y-factor measurement thanks to the two 50 Ω loads that acts as noise sources at two different temperatures.

monitor its temperature, of approximately 1.2 K. The two sources are represented in Figure 3.2, in light blue and red, respectively. The hot load is connected to the switch with a superconducting coaxial cable made of NbTi which thermally isolates it from the 20 mK stage.

The two sources generates broadband thermal white noise given by:

$$N_{C,H}(\omega) = \frac{\hbar\omega}{2} \coth\left(\frac{\hbar\omega}{2k_B T_{C,H}}\right), \tag{3.3}$$

where $\hbar$ is the reduced Planck constant and k_B is the Boltzmann constant. Thus, the output noise power measured with a Spectrum Analyzer (SA) in the desired frequency band B, is given by the noise power generated by the amplification chain $N_{sys}(\omega) = G_{sys}(\omega)k_B T_{sys}(\omega)B$ plus the one emitted by of the two sources:

In the following we will drop the frequency argument to simplify the notation

$$\begin{cases} P_C = G_{sys}N_C B + G_{sys}k_B T_{sys} B, \\ P_H = G_{sys}N_H B + G_{sys}k_B T_{sys} B, \end{cases} \tag{3.4}$$

where G_{sys} and T_{sys} are the unknown output line gain and noise temperature, respectively. Defining the Y-factor as $Y = P_H/P_C$ and solving the latter system of equations gives:

$$T_{sys} = \frac{1}{k_B}\frac{N_H - YN_C}{Y-1} \quad \text{and} \quad G_{sys} = \frac{P_C}{B}\frac{Y-1}{N_H - N_C}. \tag{3.5}$$

Thus, the input line attenuation can be computed as:

$$A_{sys} = S_{21}^{ref}/G_{sys}. \tag{3.6}$$

It is worth mentioning that the chosen noise calibration method is not the only possible one [112]. First of all, the presented Y-factor method can be extended by using a Variable Temperature Stage (VTS) [84, 101], which allows to generate noise at more that two temperatures. However, a calibration cycle realized with a VTS takes several hours due to its slow thermalization. A second alternative consists in using a Shot Noise Tunnel Junction (SNTJ) [22, 53], whose output noise level

can be controlled by the voltage applied across it, as self-calibrated noise source. The latter allows for faster calibration measurements, but it requires a low noise DC line to control it, and it is more sensitive device. Hence, the choice of using the two 50 Ω loads as calibrated noise sources. They allow for fast calibration measurements and are robust against electrostatic discharges.

The calibration methods presented here have been described using the simplified setup, shown Figure 3.2. The latter allows to probe the sample only from one direction giving no access to the reflected waves. However, to fully characterized the processes enabled in a LH Josephson waveguide, described in Chapter 2, a more complete setup is necessary. The latter is described in next section.

3.3 FULL SETUP

To study the nonlinear properties of a negative index waveguide we need to drive it with a strong pump tone. Depending on the relative propagation directions of the signal and pump waves phase-matching of parametric amplification and frequency conversion processes can be obtained, as discussed in Chapter 2. Moreover, the generated idler or up-converted tones may travel in the same direction as the signal or in the opposite one. Thus, to fully characterize a a LH Josephson waveguide, we need to be able to probe it from both directions, and to measure waves propagating in the same direction of the probe and in the opposite one. In the following section we describe the full experimental setup used to perform the characterization of the aforementioned processes with continuous waves. The results of this characterization are reported in Chapter 5.

3.3.1 Continuous wave measurements

The full experimental setup used to perform the measurements presented Chapter 5 is shown in Figure 3.4. At room temperature, besides the previous mentioned VNA and SA, we have a Microwave Source (MWS), which is used to pump the device. The probe tone from the output of the VNA and the pump one, generated by the MWS, are either combined, and fed into the same input of the cryostat, or not, and fed into the two different input lines, labeled 1 and 2 in Figure 3.4. The latter present 50 dB of total discrete attenuation distributed between the various temperature stages of the cryostat to suppress the thermal noise coming from room temperature. Note that the last 20 dB are given by the coupled port of the two directional couplers. The latter allow to perform both reflection and transmission measurements, giving access to output waves traveling in the opposite direction with respect to the input ones, and enable to probe the system with signal

waves traveling in the opposite direction with respect to the pump one. Indeed, the coupled ports of the directional couplers are connected to the microwave switches, which include the DUT, the reference, and the two 50 Ω noise sources, used for the setup calibration discussed in Section 3.2. The other ports of the directional couplers are connected

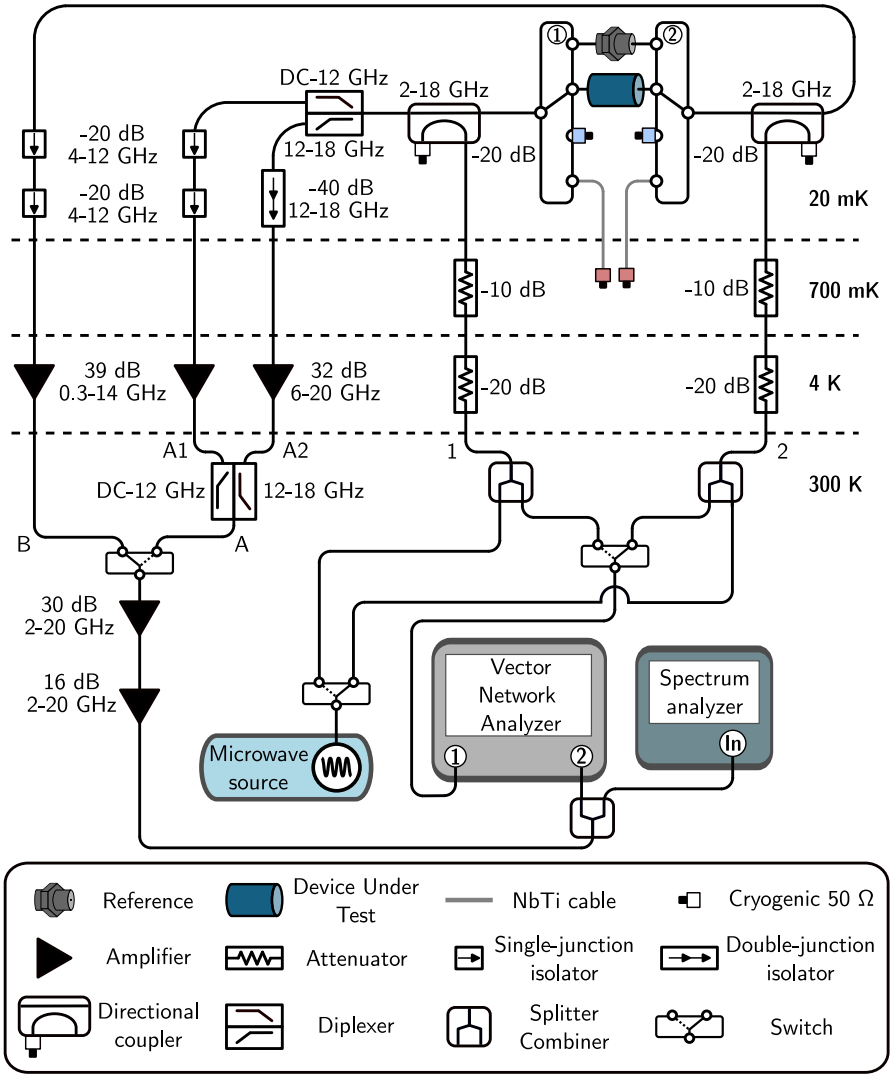

Figure 3.4: Experimental setup for continuous wave measurements
Full experimental setup used to perform the devices characterization presented Chapter 5. It features to input lines, 1 and 2, and two output lines, *A* and *B*, which allow to perform both transmission and reflection measurements, giving access to output waves traveling both in the same and in the opposite direction with respect to the input ones. Two SP6T microwave switches placed at the coldest stage of the cryostat allow for the system calibration described in Section 3.2. At room temperature, two pairs of microwave switches and combiners allow either combine or split the probe tone generated by the VNA and the pump one, generated by the MWS, and fed them either into the same or into the two different input lines of the cryostat.

to the two output lines, labeled A and B in Figure 3.4. The output line B, the most left one in Figure 3.4, features two single-junction isolators, which provide $\sim$ 40 dB of backwards isolation, within a 4 to 12 GHz bandwidth. An HEMT cryogenic amplifier, with $\sim$ 39 dB of gain and a 0.3 to 14 GHz bandwidth is then used to amplify the output signal. The output line A corresponds to the high-frequency one described in Section 3.1. At the output of the cryostat, a microwave switch is used to direct towards two room temperatures low-noise amplifiers, the signal coming from one of the two output lines. The amplified signal can then be measured with either the VNA or the SA.

System gain, noise and attenuation, corresponding to the measurements reported in Chapter 5, are shown in Figure 3.5, for all the input and output lines. The output line A, corresponding to the high-frequency one described in Section 3.1, clearly shows the effect of the diplexers, with increased noise at 12 GHz, and the differences between the two cryogenic low-noise amplifiers.

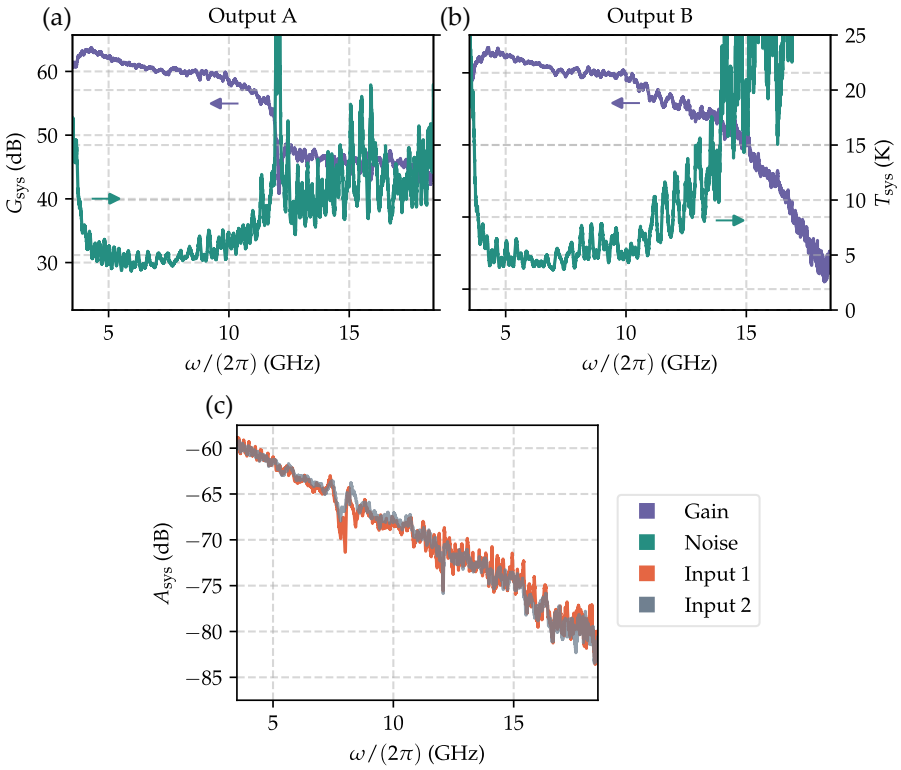

Figure 3.5: Input and output lines calibration

(a) System gain, in purple, and noise, in green, calibration of the A output line, corresponding to the high-frequency one described in Section 3.1.

(b) System gain, in purple, and noise, in green, calibration of the B output line.

(c) Input lines calibration obtained as in Equation 3.6, for the input line 1, in orange, and for the input line 2, in grey.

3.3.2 Quadratures measurements

Besides the classical parametric processes described in Chapter 2, Josephson waveguide are also powerful sources of nonclassical states of light, such as broadband two-mode vacuum squeezed states [22, 23], as briefly introduced in **??**. The latter naturally arise from the parametric amplification of input vacuum fluctuations [32], as coherent pair production of photons from a classical pump tone into the signal and idler modes. Hence, to measure such nonclassical states we need to simultaneously record two frequencies, forming the signal and idler pair while pumping the device.

Here, we describe the experimental setup used to conduct such measurements on a LH JTL, whose results are reported in Chapter 6. We recall here that in a LH Josephson waveguide, described in Chapter 5, for a given pump frequency, shows both amplification of co- and counter-propagating signal and idler modes. Thus, in the latter case the modes are spatially separated, traveling in opposite directions; while in the former they propagate along the same one. Therefore, to simultaneously measure the signal and idler pairs, two different setups are needed depending on the amplification process. The cryogenic part of the setup is the same as in the previous section. The main changes are realized at room temperature. In particular, such measurements are performed using a Field Programmable Gate Array (FPGA)-based module supported by a up- and down-conversion stage[5].

SETUP FOR COUNTER-PROPAGATING MEASUREMENTS The setup used to simultaneously record the quadratures of two modes propagating in opposite directions is shown in Figure 3.6.

At room-temperature, the input pump tone, at frequency f_p, is generated by up-conversion using an IQ mixer, whose Local Oscillator (LO) input is fed with an RF tone with frequency f_p^{LO}, while the I and Q inputs are fed with two pulses generated by the Digital to Analog Converterss (DACs) of the FPGA board at the intermediate frequency f_p^{IF}. A signal tone can also be generated to measure the gain of the device. The signal input line features 50 dB of attenuation to avoid saturation of the device and of the following readout active components. The generated tones are then send to the device by the input line 1.

On the readout side, two output lines are combined at room temperature using the diplexer. With respect to the previous configuration, now we combine the one connected to the input and the one connected to the output of the DUT, labeled A2 and B in Figure 3.6, respectively. The A2 line is used instead of the A1 because of the frequency of the backward-propagating idler mode, which is above 13 GHz, as dis-

5 We used a Quantum Machines OPX+ plus Octave system, however previous ones [22] relied on a multi-channel Xilinx RF System-on-Chip (RFSoC) acquisition board, as described in [96].

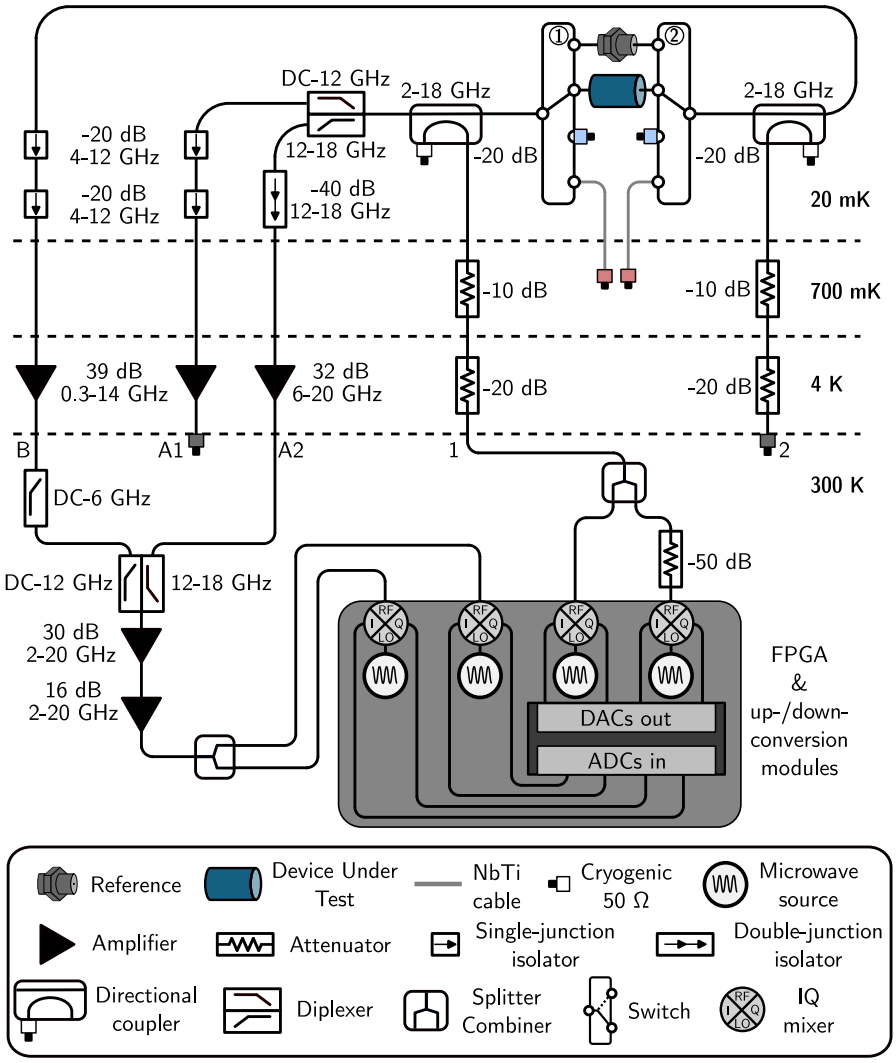

Figure 3.6: Experimental setup for the quadratures measurements of counter-propagating modes
Full experimental setup used to perform the measurements presented Chapter 5 for the counter-propagating case. The cryogenic part is equivalent to the one shown in Figure 3.4. The measurements are performed using a FPGA-based module supported by a up- and down-conversion stage, Quantum Machines OPX+ plus Octave system, respectively. To simultaneously readout signals coming from the input and output ports of the DUT we combine the output lines connected to them, A2 and B, respectively. We use the A2 line because it allows to measure in the X-band, which is where the idler frequency lies.

cussed in Chapter 6. Before combining the two lines we filter out, with a low-pass filter, the high power pump tone to prevent saturation of the down-conversions mixer and Analog to Digital Converters (ADCs)

electronics[6]. The output signal is then amplified at room temperature and split in two different path for the readout at the signal and idler frequencies of interest $f_{s,i}$. Such readout is performed using a two step demodulation procedure [35], which consists in down-converting the RF frequencies $f_{s,i}$ to the intermediate frequencies $f_{s,i}^{IF}$ using an IQ mixer, fed with an LO of frequency $f_{s,i}^{LO}$, and then digitizing them with the ADCs, before demodulation to DC on the FPGA board. We split the output in two path and perform the down-conversion with separate mixers and LOs because of the frequency difference between the phased-matched signal and idler modes of the counter-propagating amplification processes, as shown in Section 2.3.3 in **??**. It is worth stressing that we only digitize the down-converted I quadrature, to avoid distortion in the phase space of the noise distribution, which can be caused by the different gain between the I and Q lines at IF frequencies. However, when measuring the gain of the device we keep both quadratures, in case the signal is out-of-phase with the I one.

SETUP FOR CO-PROPAGATING MEASUREMENTS The setup used to simultaneously record the quadratures of two modes propagating in the same direction is shown in Figure 3.7.

The generation of the input tones is the same as the previous one. However, the readout room temperature line is quite different. First of all, for this measurements only the output line B, connected to the output port of the device, is used. Then, an interferometric cancellation of the pump tone [22] has to be performed in order to avoid saturation of the down-conversions mixer and ADCs electronics. The pump cancellation is performed combining, with a directional coupler, an additional tone, generated at the pump frequency f_p, as the pump one, with the output signal from the cryostat. Varying the amplitude and phase of this additional tone, a sweet spot for which the pump one is canceled can be found. The directional coupler is placed between two attenuators. The one before lowers the amplitude of the pump tone such that the cancellation tone's one is in an accessible range for the electronics. While, the one after mitigates saturation of the following room temperature amplifiers during the calibration of the cancellation tone parameters. Indeed, when looking for the sweet spot, the pump tone is not canceled and can even be amplified via constructive interference that can strongly saturate the following electronics and hinder a proper optimization of the cancellation tone parameters. Then, as before, the readout is performed using a two step demodulation procedure [35] using the Octave plus Quantum Machine modules. However, now the signal and idler frequencies of interest are around the pump frequency: $f_{s,i} = f_p \pm \Delta$, with Δ within

6 As we will see in the next paragraph, being able to filter out the pump tone greatly simplifies the experimental setup complexity. This is also a non-negligible advantage of the count-propagating amplification process with respect to the co-propagating 4WM amplification.

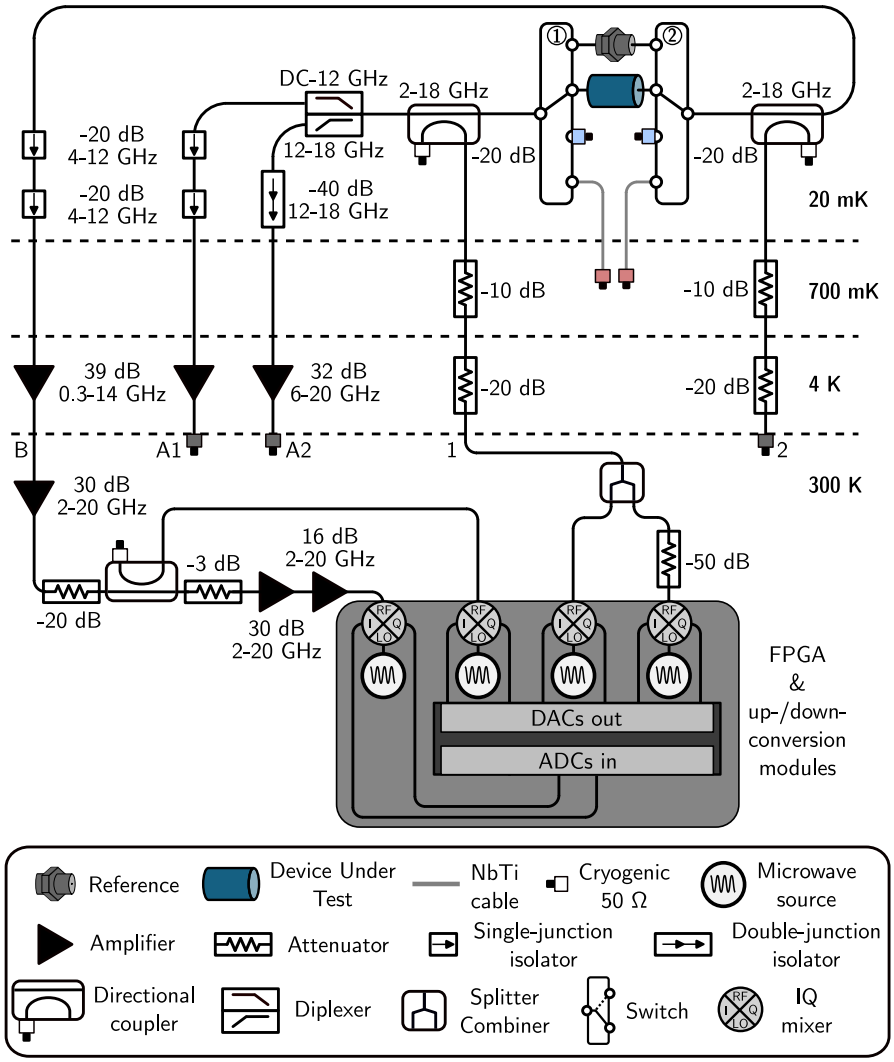

Figure 3.7: Experimental setup for the quadratures measurements of co-propagating modes
Full experimental setup used to perform the measurements presented Chapter 5 for the co-propagating case. The cryogenic part is equivalent to the one shown in Figure 3.4. The measurements are performed using a FPGA-based module supported by a up- and down-conversion stage, Quantum Machines OPX+ plus Octave system, respectively. With respect to the setup shown in Figure 3.6 we, now, use only the B output line to readout signals coming from the same output port of the DUT. Moreover, the frequencies at stake do not allow for filtering of the pump tone an interferometric pump cancellation scheme is implemented.

the 700 MHz range of a single input of the Octave. Thus, they can be down-converted with the same LO used for the pump tone generation to the intermediate frequencies $f_{s,i}^{IF} = f_p^{IF} \pm \Delta$, and fed to one single ADC of the FPGA board, which allows for demodulation and acquisition at different frequencies, within such bandwidth.

4 CIRCUIT DESIGN AND FABRICATION

The development of the fabrication process presented in this chapter would not have been possible without the help and guidelines of Alexis Coissard from Silent Waves. He had a huge impact in the successful realizition of the LH devices. So, thanks Alexis!

Superconducting circuits can be fabricated with relatively standard micro-fabrication technics on wafer scale. The desired circuits can be realized by means of either optical or electron-beam (e-beam) lithography and metal and dielectric depositions. In our case, we used e-beam lithography, while both the metal and the dielectric depositions have been performed with and electron-gun (e-gun) evaporator.

As we have seen in Chapter 2, Josephson waveguides are based on either low-pass or high-pass microwave networks, whose building blocks are Josephson junctions and capacitors. The main challenges in fabricating such structures are related to their high number of unit cells, to the inductances and capacitances needed to impedance match them to the $50\,\Omega$ microwave environment, and to keeping the losses as low as possible. Such challenges have already been addressed and solved in the context of RH JTLs [20, 83, 93, 98]. However, such implementations, although very successful, are not well suited for the realization of LH JTLs because of either their complexity or their lack of flexibility.

Here, we describe the fabrication process which has been devised to realize negative index Josephson waveguides. Beyond this clear goal, the process flexibility allows to fabricate RH JTLs as well. The devices are fabricated on 2-inch high-resistivity intrinsic Si wafers, divided into 16, 8×8 mm^2, chips in a 4×4 matrix. The process is based on an overlap fabrication technic, which is used to obtain both building blocks of the circuits. First, we present this technic for the fabrication of the junctions and their Room Temperature (RT) characterization. Then, we extend it to obtain the matching capacitors and describe the dielectric deposition method used to realize them. Finally, we give the complete fabrication recipe.

Before going into the details, it is worth mentioning that all the fabrication has been performed in the NanoFab facility at the Néel Institut.

4.1 JOSEPHSON JUNCTIONS FABRICATION

The JJ plays a crucial role in superconducting circuits. As introduced in Section 1.2 in **??**, the junctions used to realize the JTLs for the experiments reported in Chapter 5 and in Chapter 6 are SIS junctions. The two superconducting electrodes are made of aluminum, while the tunnel barrier is made of aluminum oxide, grown in a pure oxygen

atmosphere in the evaporator. The quality and microscopic details of such barrier sets the losses and properties of the junctions, which affect the performances of the final device.

Several methods have been demonstrated to realize JJs for superconducting circuits applications, among them are:

A. The *trilayer process* [113], which is based on the deposition of SIS tri-layers, followed by etching of the structures. Despite being very successful, and CMOS compatible, this process is quite involved, because of the presence of several etching and deposition steps of both metals and dielectrics.

B. The *shadow-evaporation process*, among which we can find the Manhattan, the Dolan-bridge [114], and the bridge-free [115] technics. This process consists in only one lithography step, allowing for the deposition of the two superconducting electrodes and the $in-situ$ growth of the oxide barrier, within the same step in the evaporator. The latter is made possible by a two-resist stack and by using double-angle evaporations. The two resists have a different sensitivity with respect to the electrons dose, with the bottom layer being the more sensitive one. This allows to obtain undercut or suspended bridge structures. The size of the JJs[1], and the success of their fabrication, strongly depend on the size of those structures. Hence, both the aforementioned technics suffer from dose issues and present many geometrical constraints. In particular, most problems arise when highly dense arrays of junctions or complicated circuits designs have to be realized.

C. The *overlap process* [116], which is based on two separate lithography steps and depositions of the two superconducting electrodes with zero-angle evaporation. Hence, it requires a careful cleaning of the native aluminum oxide on the first electrode, before the growth of the oxide barrier and the subsequent deposition of the second electrode. The surface treatment can be performed using an argon ion beam milling, which was shown to efficiently remove the native oxide present on aluminum thin films [117]. This technic allows to access a wide range of junctions dimensions, without any prominent geometrical constraint, easing the circuits design and fabrication.

Here, despite the fact our group has been relying for years on the shadow-evaporation process to fabricate JJs arrays[2], we decided to

1 The Manhattan and Dolan-bridge technic are usually used to realize small area junctions, less than $\sim 1\mu m^2$, while the bridge-free one is used to realize JJs with larger areas.

2 The development of this process for realizing Josephson junctions has been done in collaboration with Shivansh Bansal and Alexis Coissard from Silent Waves, and with Adam Najmi and Shelender Kumar, who are working in the qubit team in the group.

adopt the latter process for the fabrication of the junctions, given the freedom and robustness it provides. Such process has been also used to fabricate the matching PPCs, as described in Section 4.2, allowing for a fully modular fabrication[3].

4.1.1 The overlap junction technic

The overlap junction technic is a two-layer process, which enables the fabrication of junctions in both the sub-micrometer and in the micrometer scales [116, 118].

This technic consists in two lithography steps, which we perform with a commercial e-beam lithography system nB5 from Nanobeam Ltd with an 80 kV acceleration voltage[4]. The two steps allow to define the top and bottom electrodes of the junctions. The metal deposition and oxidation is performed in a commercial Plassys evaporator, featuring two chambers, a loadlock and a main evaporation one, connected by a gate valve. The loadlock enables fast loading and unloading of wafers and controlled oxidations, while maintaining an high vacuum in the main chamber containing the metal crucibles. This machine is also equipped with a Kaufman & Robinson ion beam source, allowing for ion beam etching. The latter is essential to achieve low-losses with the overlap technic.

The main fabrication steps, which have been followed to realize junctions arrays with this technic are illustrated in Figure 4.1. A more detailed recipe is given in Section 4.3.2.

The process starts by patterning the first electrode by e-beam lithography, using a resit bi-layer composed of $\sim$ 750 nm of PMMA/MAA (9%) covered by $\sim$ 250 nm of PMMA (4%), to ease the lift-off process. After development in a H_2O:IPA (1 : 3) solution, for 90 s at about 1°C followed by 60 s in H_2O as stopper, the sample is loaded in the loadlock of the evaporator, which is pumped down to a pressure lower than 1×10^{-7} mbar. Next, two surface-cleaning steps are performed with the ion beam source. First, a physical and chemical etching, with Ar and O_2, is used to remove resit and other organic residues in the developed regions. Then, a mild Ar ion beam milling is performed to remove the native oxide from the Si substrate. Next, we deposit 100 nm of Al, at a rate of 0.5 nm/s, to realize the first electrode. Before removing the sample from the evaporator we perform a passivation of the deposited metal surface in a static O_2 atmosphere at the pressure of 10 mbar for 5 minutes. A commercial NMP-based solvent heated at

3 It is worth mentioning that we started by using the already developed bridge-free technic. However, after some trials and errors caused by the dose and geometrical sensitivity of such technic, we decided to switch to the overlap one. The unsuccessful implementations of both RH and LH JTLs with the bridge-free technic are briefly described in **??**.

4 An high acceleration voltage minimizes the back-scattering of electrons in the resist, allowing for higher resolutions.

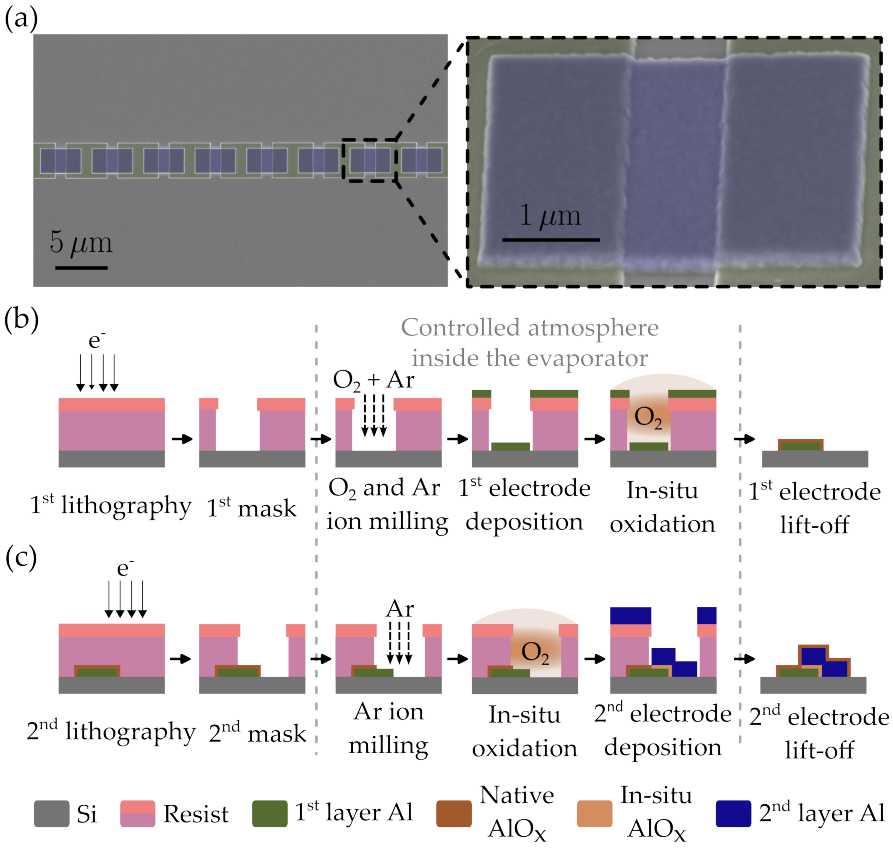

Figure 4.1: Illustration of the overlap junction technic
(a) Scannig Electron Microscope (SEM) images of a chain of 16 Josephson junctions, with the bottom electrode in green and the top one in blue.
(b) Schematic illustrating the main fabrication steps needed to realize the bottom electrode of the junctions.
(b) Schematic illustrating the main fabrication steps needed to realize the top electrode of the junctions, together with the bottom electrode surface cleaning and controlled oxidation.

about 80°C is used to lift-off the metal in excess, together with a low-power Ultrasonic Bath (USB). Then, the second electrode is patterned using the same resist stack and development process as for the first one. The sample is loaded in the loadlock of the evaporator, which is now pumped overnight to reach a pressure lower than 5×10^{-8} mbar to improve the reproducibility of the junctions parameters. Again, two surface cleaning steps are performed with the ion beam source. The same first physical and chemical etching, with Ar and O_2, is followed by a longer Ar ion beam milling to remove the native oxide from the aluminum first electrode. These surface cleaning steps are of primary importance for the precise definition of the junction's tunnel barrier. The latter is formed by controlled oxidation in static O_2 atmosphere at the pressures of either 10 or 20 mbar for 10 minutes, depending of the target junctions electrical parameters. Then, we deposit 200 nm of Al,

at a rate of 0.5 nm/s, to realize the second electrode. Before removing the sample from the evaporator we passivate again the top metal surface. Finally, the metal in excess is lifted using the aforementioned NMP-based solvent heated at about 80°C.

The junctions tunnel barrier homogeneity over the whole wafer is critical when dealing with arrays of JJs. Such homogeneity can be obtained by measuring the junctions resistance at RT on test structures placed at different positions over the whole wafer.

4.1.2 Room temperature DC measurements

The junctions can be tested at RT by measuring their resistance R_j. First of all, these measurements allow to check if the junctions are working fine, *i.e.* if they are neither shorted nor opened. Then, from the RT resistance we can infer their critical current I_c, using the Ambegaokar-Baratoff relation:

$$I_c R_N = \frac{\pi}{2}\frac{\Delta}{e} \tag{4.1}$$

where R_N is the junctions the normal state tunneling resistance, Δ is the superconducting gap of aluminum and e is the absolute value of the electron charge. To account for the temperature dependence of the junctions resistance, we map the measured RT one to R_N using a correction factor of about 30%.

The resistance of a single junction is obtained by measuring a set of arrays with varying number of junctions N_j and computing the slope of $R_{array}(N_j)$ with a linear fit.

By placing these sets of arrays in different locations on the wafer we can infer the junctions critical current homogeneity, as shown in Figure 4.2. We normalize the obtained critical currents with the area of the junctions A_j. The latter have been slightly varied, between 3 and 7.5 μm^2, from chip to chip, to ensure that it does not play a significant role. Moreover, two different oxidation pressures, 10 and 20 mbar, have been tested. In both cases, all the measured arrays were working, highlighting the good yield achievable with this process[5], and a good homogeneity has been obtained, with variances in the 1% and 2% range. However, these are just two realizations, a more detailed study is needed to claim that the process is truly reproducible for different junctions dimensions and oxidation parameters.

Finally, these measurements also allow to know the junctions inductance $L_j = \varphi_0 / I_c$, which is used to design the matching capacitors, whose fabrication and characterization is described in the next section.

5 It is worth mentioning that we measured ten arrays per chip, with number of junctions varying from 10 to 100, and 14 chips per wafer. Thus, a total number of 7700 junctions per wafer has been tested.

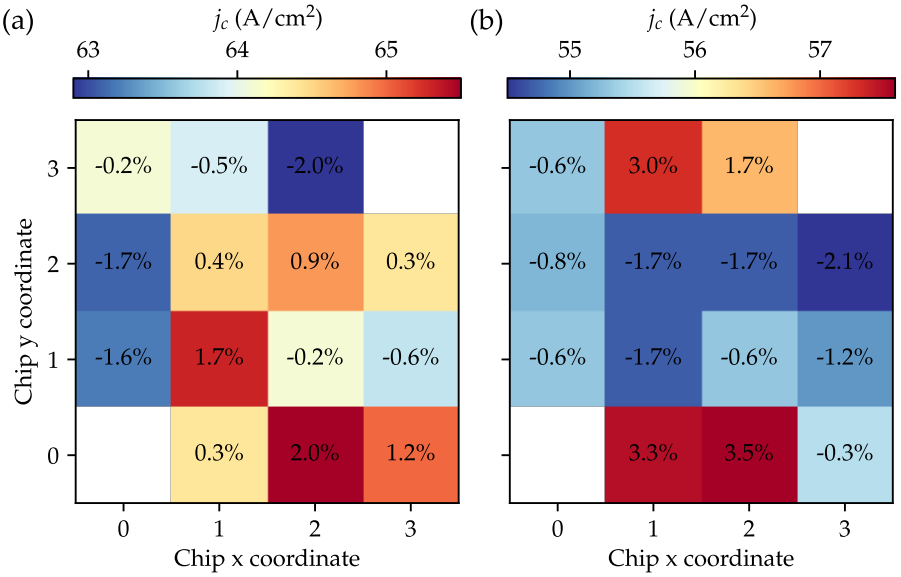

Figure 4.2: Homogeneity maps of the junctions critical current density j_c Values of the critical current density $j_c = I_c/A_j$ obtained by measuring the junctions RT resistance, as described in the main text, for two oxidation parameters: (10 mbar; 10 min) in (a) and (20 mbar; 10 min) in (b). Each square represent a chip in the wafer. Each chip has its own test structures composed of 10 arrays of junctions with varying number from 10 to 100. The numbers in each square represent the variation of the chip critical current density from the mean value of the all wafer, which is $j_c = 64.2 \pm 0.8$ A/cm^2, for (a), and $j_c = 55.7 \pm 1.1$ A/cm^2, for (b).

4.2 PARALLEL PLATE CAPACITORS FABRICATION

In order to obtain traveling-waves in the JTL, their impedance has to be matched to the 50 Ω impedance of the environment. This implies quite high values of capacitances. Indeed, considering inductances of the order of 500 pH, gives for the matching capacitance 200 fF. Actually, the latter varies by about one order of magnitude between the RH and the LH topologies, as shown in Table 2.3 in Chapter 2. Hence, the necessity to have a fabrication process which allows to realize capacitors up to the $\sim$ 1 pF scale, while keeping a relatively small footprint, such that thousands of them could be arranged in an array. A second requirement consists in minimizing the amount of dielectric losses, which mainly depend on the chosen material and deposition method. This brings us to the last constraint on the fabrication process for the matching capacitors of JTLs: it has to be compatible with the junctions themselves. The latter are usually fabricated first, such that one can infer their inductance and design the required capacitance.

Thus, for example, any dielectric deposition method involving high-temperatures has to be excluded[6].

In our group an inverted microstrip geometry, based on Al_2O_3 deposited with an Atomic Layer Deposition (ALD) system, was successfully developed by Luca Planat during his PhD [37]. However, values of loss tangent of the order of 5×10^{-3} has always been obtained with this technic [119]. More recently, Josephson TWPAs based on coplanar stubs capacitors has been realized [93, 98], showing an improvement of more than one order of magnitude in the loss tangent. Although being very successful, both technics are not well suited to realize a LH topology. Therefore, we decided to develop an oxide multilayer deposition, inspired by Zotova *et al* [120], and based on the same overlap technic previously explained for junctions.

4.2.1 Dielectric deposition

The dielectric deposition is realized in the same Plassys evaporator as the junctions. However, instead of performing just one oxidation before the evaporations of the second electrode, we realize a multilayer aluminum deposition and oxidation process, as illustrated in Figure 4.3. A detailed recipe is given in Section 4.3.2.

First, we prepare the bottom aluminum electrode as described in Section 4.1. Then, the second electrode is patterned using a single layer of PMMA (8%) resist $\sim 1\,\mu$m thick[7]. The development is again performed in a H_2O:IPA (1 : 3) solution at about 1°C. The sample is loaded in the loadlock of the evaporator, which is pumped overnight to reach a pressure of 5×10^{-8} mbar to improve the reproducibility of the capacitors parameters. The same two surface cleaning steps are performed to remove resist residues and the aluminum native oxide from the developed regions of the first electrodes. Next, a first oxidation is realized in a static oxygen atmosphere for 15 minutes at 20 mbar. Then, 6 cycles of aluminum deposition plus oxidation are performed to grow the oxide. Each cycle is composed of the deposition of a thin aluminum layer, of about 1.2 nm at a rate of 0.05 nm/s, followed by an oxidation in the same condition as before. Then, 200 nm of aluminum are deposited, at the rate of 0.5 nm/s, to realize the second electrode. Before removing the sample from the evaporator we passivate again the top metal surface and the metal in excess is lifted, as for described in Section 4.1.

6 Indeed, JJs are highly sensitive to heating. For reference, the melting point of Al is about 600°C.

7 We now use only one layer of resist to avoid the formation of long bridges between two electrodes in series, which could easily collapse and ruin the lift-off. Indeed, given the size and spacing of the capacitors required for a LH JTLs, using a resist bilayer results in complete exposure of the more sensitive bottom one, between the patterned electrodes, because of proximity effect.

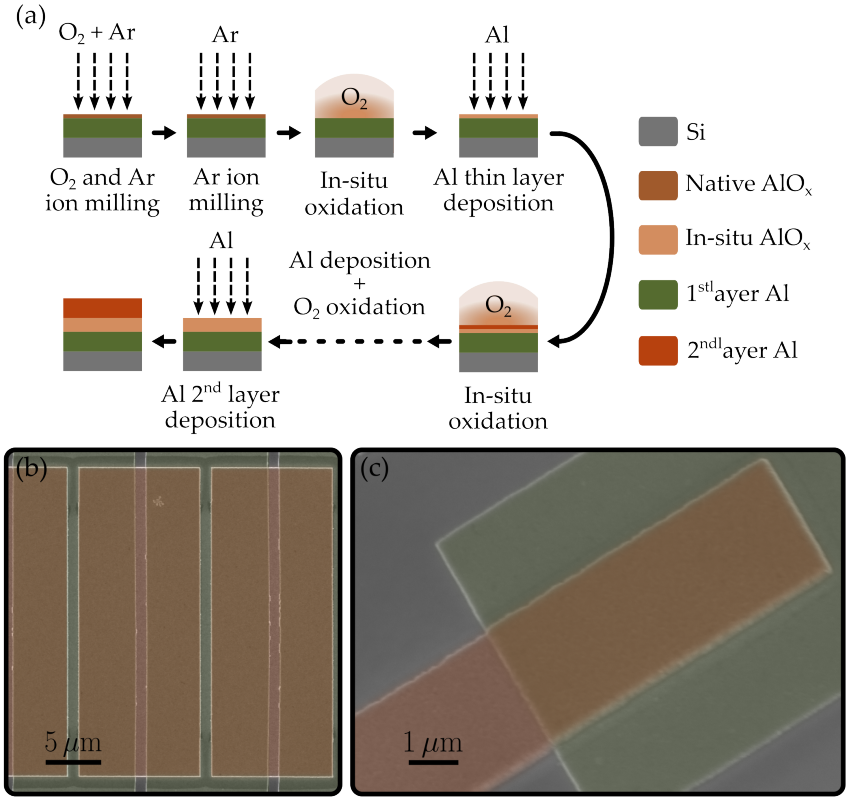

Figure 4.3: Illustration of the oxide multilayer deposition
(a) Schematic representing the main steps performed inside the evaporator to deposit the aluminum oxide and the top electrode of the capacitors.
(b) False colored SEM image of a chain of capacitors, taken from a LH JTL, with the bottom electrode in green and the top one in red.
(c) False colored SEM image of a capacitor, taken from a RH JTL, with the bottom electrode in green and the top one in red.

The number of cycles have been calibrated such that the final oxide is thick enough to suppress Cooper-pairs tunneling, which would result in a parasitic (nonlinear) inductance[8]. However, realizing compact PPCs of the order of ~ 1 pF, a thin oxide is required. Indeed, considering a target capacitor area A of $100\,\mu m^2$ and the dielectric constant of aluminum oxide $\varepsilon_r = 10$ gives an oxide thickness t of about 9 nm, using the standard PPC model for which $C = \varepsilon_0 \varepsilon_r A/t$.

The characterization of the oxide thickness has been performed in two different ways, which are described in the following section.

8 Indeed, such multilayer deposition can been used to control the critical current of Josephson junctions by changing the tunnel barrier thickness and not their area for qubits applications [121].

4.2.2 Dielectric characterization

Through the dielectric characterization we want to address three main points. First, we aim to calibrate the deposited thickness per cycle. This has been performed with both Atomic Force Microscopy (AFM) imaging, by measuring the step of some deposited oxide on top of a Si chip, and with Transmission Electron Microscopy (TEM) imaging, by looking at the cross section of a capacitor itself. Thus, the internal composition ot the latter can be accessed, to see if the deposited aluminum is fully oxidized or if some metallic inclusion are present within the oxide layer. Finally, to properly design the capacitors for the JTLs, we need to know the capacitance per-unit-area, which has been calibrated by measuring lumped-element resonators at microwave frequencies and at low temperatures.

ATOMIC FORCE MICROSCOPY Let us start by describing the deposition thickness calibration performed with the AFM.

These measurements have been performed at the Néel Institut with the help of Simon Le Denmat, who is taking care of the AFM platform, and of Alexis Coissard

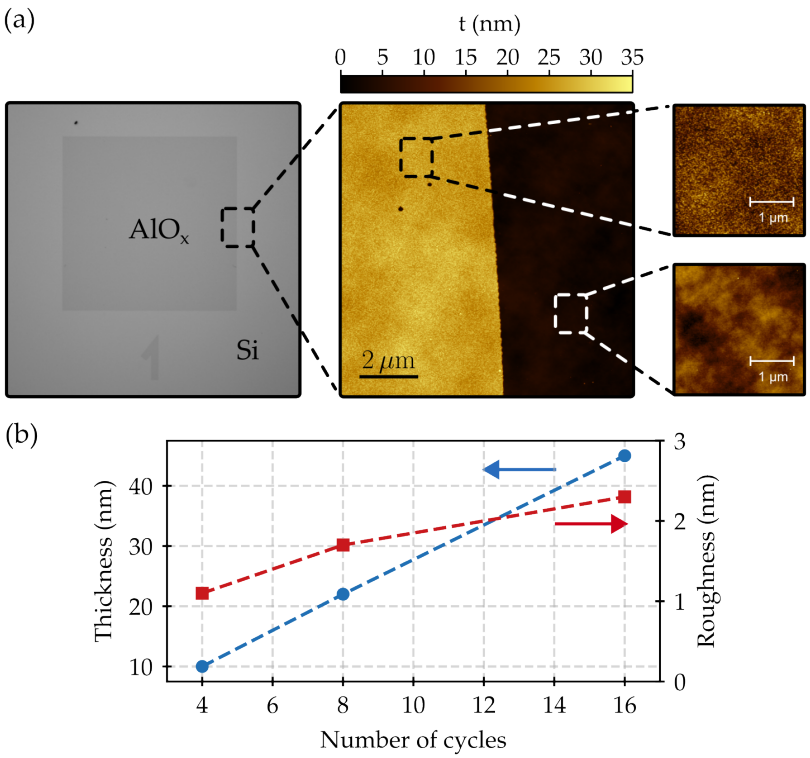

Figure 4.4: AFM characterization of the AlO_x thickness
(a) From left to right: optical image of a deposited aluminum oxide square, AFM image of the step of the deposited oxide on top of the silicon wafer, and AFM images of the oxide, above, and of the silicon wafer, below.
(b) Thickness, in blue, and RMS roughness, in red, of the deposited aluminum oxide, as characterized by AFM, for three different number of cycles.

To do so, we deposited three squares of only aluminum oxide, with different number of cycles, following the recipe described in the previous section[9]. An optical image of one of these squares is shown in Figure 4.4(a). By taking an AFM image of the step between the deposited oxide and the native silicon oxide of wafer for each square, their height could be extracted, which is shown, by the blue dots, in Figure 4.4(b), as a function of the number of cycles. From these measurements we could compute a deposition rate of about 2.8 nm/cycle.

TRANSMISSION ELECTRON MICROSCOPY Now, we move on to the description of the results of the TEM characterization. The latter has been performed in collaboration with Emanuele Enrico at INRIM, in Turin. Compared to the previous technic, the TEM allows to image the cross-section of the whole $Al/AlO_x/Al$ capacitor stack, and thus the internal structure of the dielectric layer.

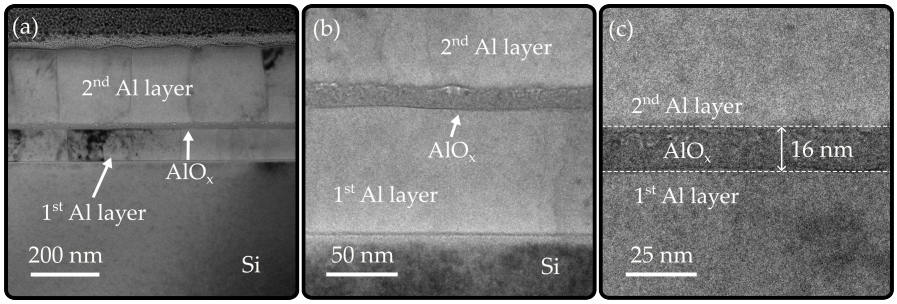

Figure 4.5: TEM images of an $Al/AlO_x/Al$ capacitor
(a) to (c) TEM images of a capacitor stack realized with the process described in Section 4.2.1 with 6 cycles. The thickness of the dielectric layer is estimated to be $t \sim 16$ nm. These images have been taken at INRIM, in Turin, with the collaboration of Emanuele Enrico.

The results are reported in Figure 4.5 for a capacitor realized with the process described in Section 4.2.1 with 6 cycles[10]. One can clearly see the two superconducting electrodes separated by the aluminum oxide. Some bright defects can also be spotted, as can be seen in Figure 4.5(b). However, determining their composition requires a more detailed imaging and analysis, using for example energy dispersive x-ray spectroscopy. Moreover, the boundaries between the aluminum layers and the oxide are spatially not uniform, resulting in an inhomogeneous oxide thickness. The latter was estimated to be ~ 16 nm, as reported in in Figure 4.5(c). Such value is in good agreement with the

9 The squared have been patterned with e-beam lithography directly on a Si chip. Then, only the oxide was deposited in the e-gun evaporator, without the final aluminum deposition, and lifted overnight in NMP at about 80°C.

10 The imaged sample was obtained from a chip coming from the same wafer of the device whose characterization is reported in Chapter 5.

indirect estimation performed with the AFM, discussed in the previous paragraph.

From the above characterization the design of some capacitors is possible. Indeed, by assuming that the deposited oxide has a dielectric constant of 10, which is a standard value for Al_2O_3, and a thickness of 16 nm, we obtain a capacitance per-unit-area $c_a = \varepsilon_0\varepsilon_r/t \sim 6$ fF/μm^2. However, a more careful calibration of the latter can be performed measuring the resonant frequencies of lumped-element resonators with different capacitors areas.

4.2.3 Lumped-element resonators

To extract the capacitance per-unit-area we designed, fabricated and measured a set of 13 lumped-element resonators, inductively coupled to a common feedline, in an hanger geometry, as schematically shown in Figure 4.6. Each resonator is composed of an inductor, a 100 nm thick and 5.9 mm long Al wire, and of a PPC. The inductor is kept the same in each resonator, while the area of the capacitors is changed to obtain different resonant frequencies. The capacitors have been realized with the process described in Section 4.2.1, except for the fact that the inductor, which serves also as their bottom electrode, is defined by wet-etching, together with the ground plane and the feedline. The fabrication process is described in the following paragraph, while a detailed recipe is given in Section 4.3.2.

FABRICATION First, we deposit 100 nm of Al at a rate of 0.5 nm/s, which is then passivated in a static oxygen atmosphere at a pressure of 10 mbar for 5 minutes. Prior to the deposition the native silicon oxide is removed with a mild argon ion beam milling. Next, the inductors of the resonators and the feedline are patterned with e-beam lithography using a 750 nm thick single layer of PMMA/MMA 9%. The development is performed in a MIBK:IPA (1 : 3) solution for 60 s, followed by 30 s in IPA as stopper. Then, the developed areas are etched using a commercial aluminum etchant type A for 5 minutes at RT. Before the metal etching, a low-power oxygen plasma in a Reactive Ion Etching (RIE) machine is performed to remove resist and organic residues from the developed regions and increase the reproducibility of the metal etching time. After the etching, the protective layer of resist on top of the ground plane is stripped in NMP at about 80°C, overnight. Finally, the capacitors are patterned, deposited, and lifted as previously described. A false colored optical image of a resonator and a SEM image of the capacitor are shown in Figure 4.6 (a) and (c), respectively. Note that with this process, two capacitors in series, of same area, are obtained. Thus, the equivalent parallel-plate capacitance C_{eq} of the resonator is given by $C_{eq} = C_{ppc}/2$, where $C_{ppc} = c_a A_{ppc}$ is the capacitance of each PPC.

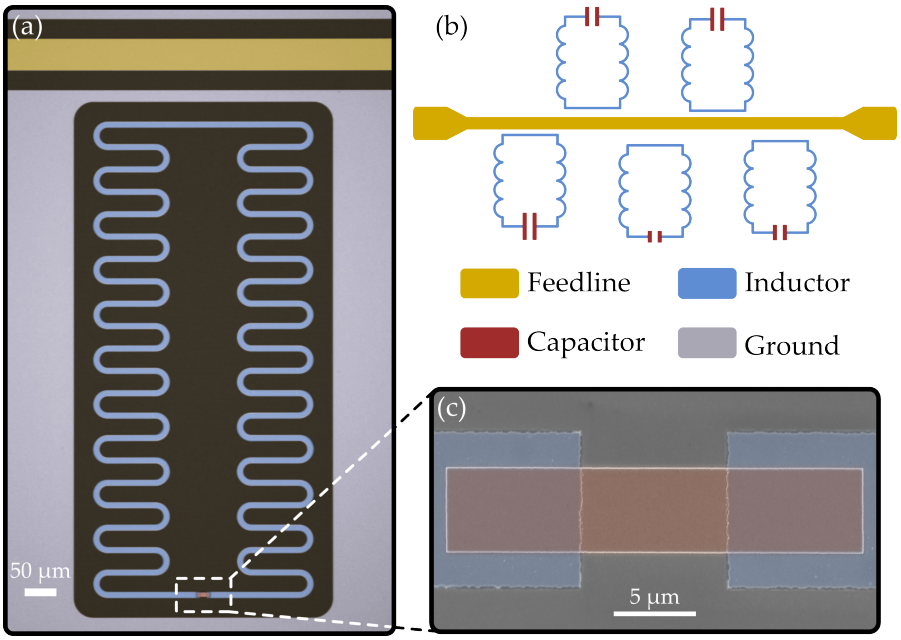

Figure 4.6: Lumped-element resonators illustration
(a) False colored optical image of a lumped-element resonator, which is composed of an inductor, in blue, and a PPC, in red, and it is inductively coupled to a feedline, in yellow.
(b) Schematic of a chip with the lumped-element resonators coupled to the same feedline. The distance of each resonator from the feedline is varied, depending on the expected resonant frequency, to target for all of them the same coupling. The actual design has 13 lumped-element resonators.
(c) False colored SEM image of the two series capacitors, which give the capacitance of the resonator.

DESIGN AND SIMULATIONS Each chip contains 13 resonators with the same inductor wire, but different capacitors areas. Thus, their resonant frequency is given by:

$$\omega_0(A_{\text{ppc}}) = \frac{1}{\sqrt{L_w \times (C_s + C_{\text{eq}}(A_{\text{ppc}}))}}, \tag{4.2}$$

where L_w is the inductance of the aluminum wire, C_s takes into account stray capacitances, and C_{eq} is the aforementioned equivalent parallel-plate capacitance, which depends on the area of the two PPCs of the resonator.

We can extract the value of the capacitance per-unit-area c_a by measuring the resonant frequency of each resonator and fitting them to Equation 4.2. However, prior to that, the value of L_w is obtained by simulating the resonators transmission scattering parameter with Sonnet. Such simulation have been performed with the actual designs, by replacing the PPCs with an ideal equivalent capacitor connected at the two ends of the aluminum wire. The resonant frequencies obtained from these simulations are shown in Figure 4.7, as a function of the

values of the aforementioned ideal equivalent capacitances C_{id}. Fitting the data to $\omega_0 = 1/\sqrt{L_w \times (C_s + C_{id})}$ we inferred the inductance of the wire and the stray capacitance to be $L_w = 2.84$ nH and $C_s = 30.8$ fF.

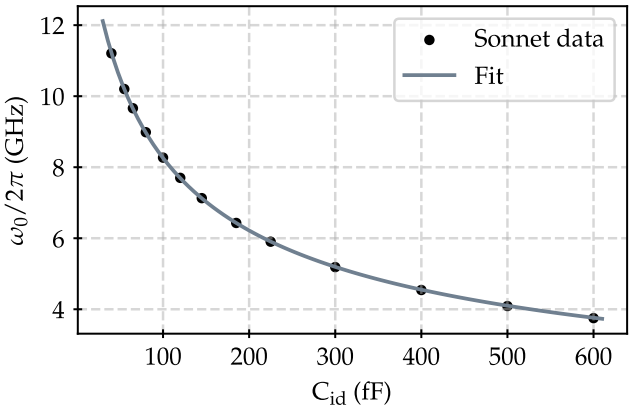

Figure 4.7: Lumped-element resonators simulations
Resonant frequency as a function of the ideal capacitance. The black dots represent the values obtained from the simulations with Sonnet, while the grey solid line represents the fit to $\omega_0 = 1/\sqrt{L_w \times (C_s + C_{id})}$, from which we extracted the inductance of the wire and the stray capacitance to be 2.84 nH and 30.8 fF, respectively.

The values of C_{id} have been optimized to have resonant frequencies in the 4 to 12 GHz range, and then use to design the areas of the PPCs of the resonators as:

$$A_{ppc} = \frac{2tC_{id}}{\varepsilon_0 \varepsilon_r}, \tag{4.3}$$

assuming $t = 16$ nm for the oxide thickness and $\varepsilon_r = 10$ for its dielectric constant.

MEASUREMENTS Once realized, the resonators have been characterized at low temperature in a setup similar to the one presented in Section 3.3.1 in Chapter 3. We can locate the resonant frequencies by measuring the transmission through the feedline using the VNA, and scanning the probe frequency over a wide band. The resulting normalized transmission is shown in **??**(a). All the 13 expected resonances are visible, as highlighted by the arrows. Two more resonances, whose width is in the order of 100 MHz, are present at about 11 GHz and just above the 13th resonance. We can assume they are not related to the lumped-element resonators, given that their width is more than one order of magnitude larger than the one of the other resonances.

From the values of the resonant frequencies as a function of the PPCs area, we can extract the capacitance per-unit-area by fitting them to Equation 4.2. The fit has been performed setting L_w to the simulated value, while leaving c_a and C_s as free parameters. The results of the fit

are 7 fF/μm^2 and 25 fF, respectively, which are consistent with what we were expecting.

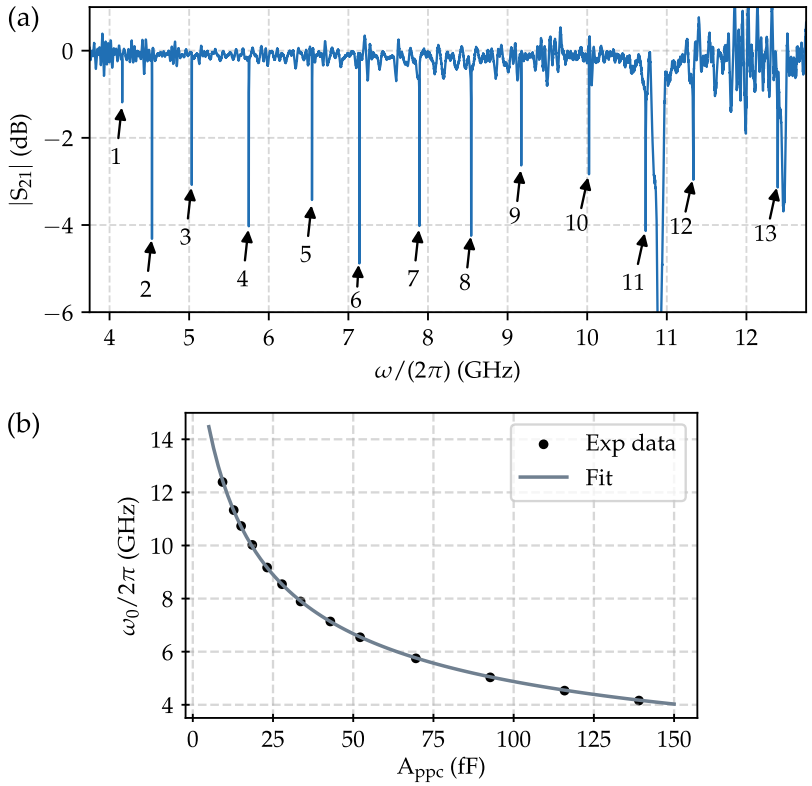

Figure 4.8: Lumped-element resonators measurements
(a) Normalized transmission, as described in Section 3.2.1 in Chapter 3, of a chip showing the resonant response of all the 13 lumped-element resonators, which are highlighted by the arrows. The input power has been inferred to be between -102 and -115 dBm, depending on the frequency of the resonator.
(b) Resonant frequency as a function of the PPCs area. The black dots represent the experimental data, while the grey solid line represents the fit to Equation 4.2, from which we inferred a capacitance per-unit-area of 7 fF/μm^2.

We used this value of c_a to design the matching capacitors of the JTLs, whose fabrication is detailed in the following section.

4.3 ASSEMBLING THINGS TOGETHER

Putting together in one workflow the fabrication processes of junctions and capacitors is now reasonably easy, except that for two matters that have to be thought of. First, the fabrication of the capacitors will affect the junctions. In particular, their resistance will change because of the resist spin coating step before the capacitors lithography, during which the wafer undergoes a baking at 180°C for 7 minutes. This change has been calibrated performing DC measurements on test structures, as

described in Section 4.1.2, before and after the baking. We observed an increase of the junctions resistance of about 30%, which has to be taken into account when designing the devices.

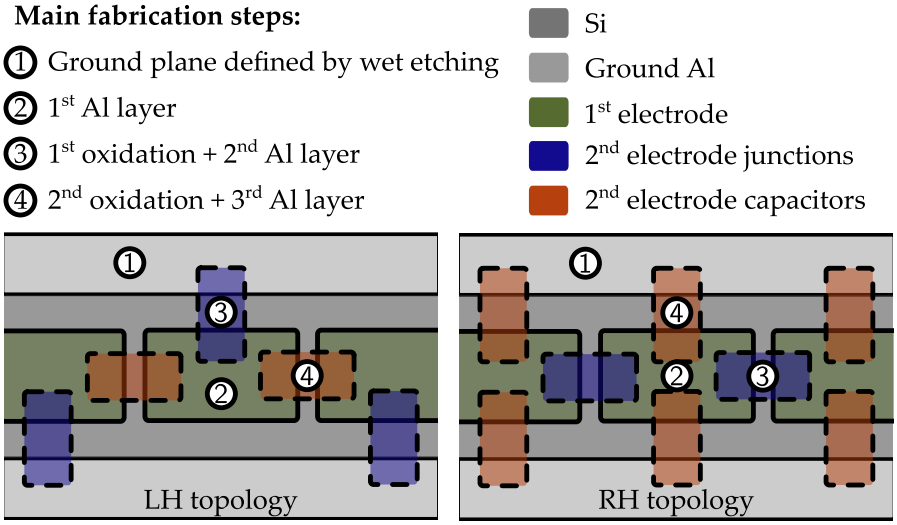

Figure 4.9: Illustration of the fabrication process of Josephson waveguides Main steps of the fabrication process used for the realization of either LH, on the bottom left, or RH, on the bottom right, JTLs topologies.

Then, we need to think about how to actually connect the junctions and the capacitors either together or to ground. We thought about two options: using the so-called bandages [117, 122], which require an additional lithography step, or having a shared bottom electrode for junctions and capacitors, and using the ground plane as bottom electrode itself to make the connections to ground. We choose the second option, which is illustrated in Figure 7.5, because it is simpler, and it is usually better to minimize the fabrication steps. However, it implies the presence of two elements (junctions or capacitors) in series per unit cell. The full process is described in the following section.

4.3.1 Josephson waveguides fabrication

Before describing all the fabrication steps, it is worth mentioning that with this fabrication, both LH and RH JTLs and the previously described lumped-element resonators, can be processed together, on different chips of the same wafer. The process is as follows:

1. It starts by depositing, patterning and etching the ground plane as described in Section 4.2.3.

2. Then, the first aluminum electrode, which is common to both junctions and capacitors is defined, as explained in Section 4.1.1.

3. Next, we realize the second electrode of the junctions by removing the native aluminum oxide with the Ar ion beam milling from the first electrodes, forming the tunnel barrier with the controlled oxidation, and depositing a second aluminum layer, as explained in Section 4.1.1.

4. At this point, the junctions of the test structures are measured at RT, as described in Section 4.1.2, to infer the obtained value of critical current, and correct the area of the capacitors for accurate impedance matching, if necessary.

5. Then, the capacitors dielectric and second electrodes are realized, as detailed in Section 4.2.1.

6. As an optional step, the junctions RT resistance can be measured again in order to check if everything is still ok and to precisely know of how much it changed because of the previous step.

7. Finally, the wafer is covered with a protective layer of thick optical resist and diced with a precise diamond saw to obtain the 16 chips. The latter, after rinsing in acetone, ethanol and isopropanol, are ready to be packaged, wire-bonded and measured.

The experimental characterization of a JTL with LH topology is the topic of the next chapter, but before that we give the full recipe with which it has been fabricated.

4.3.2 Full recipe

Besides the RT resistance measurements, the full fabrication process can be divided into five main steps, at which one needs to add the markers fabrication, which are used for the lithography steps and the dicing alignment. The markers are realized between the ground plane deposition and its patterning, following the usual scheme of writing, development, Ti plus Au deposition, and lift-off.

The recipes for each of the other five steps, ground plane, first layer, junctions second layer, capacitor second layer, and dicing, are given in the following pages.

PROCESS	STEP	PARAMETERS
Deposition	Ar milling	300 V, 14 mA, 60 V_{acc}
		7 sccm, 3 min, 5 rpm
	Ti evaporation	30 nm, 0.1 nm/s, 0°, shutter closed
	Al evaporation	100 nm, 0.5 nm/s, 0°, 5 rpm
	Passivation	static, 10 mbar, 5 min
Coating	Pre-bake	200°C, 2 min
	Resist	PMMA/MAA 9%
	Spin	3000 rpm, 3000 rpm/s, 30 s
	Bake	200°C, 10 min
Lithography	Dose	3 C/m^2
	Current	15 nA
Development	Developer	MIBK:IPA (1 : 3), 60 s
	Rinse I	IPA
	Stopper	IPA, 30 s
	Rinse II	IPA
	Dry	N_2
Wet etching	Cleaning	RIE, O_2, 10 W, 15 s
	Bath I	Al etchant type A, 5 min
	Bath II	H_2O, 30 s
	Bath III	H_2O, 1 min
	Bath IV	H_2O, 2 min
Resist stripping	Bath I	NMP, 80°C, overnight
	Rinse I	Acetone
	Rinse II	Ethanol
	Rinse III	IPA
	Dry	N_2

Table 4.1: Ground plane fabrication recipe

PROCESS	STEP	PARAMETERS
Coating	Pre-bake	180°C, 2 min
	Resist	PMMA/MAA 8%
	Spin	2000 rpm, 2000 rpm/s, 30 s
	Bake	180°C, 5 min
Lithography	Pads dose	20 C/m^2
	Pads current	30 nA
	JJ/PPC dose	16 C/m^2
	JJ/PPC current	3 nA
Development	Developer	H_2O:IPA (1 : 3), 1°C, 105 s
	Stopper	H_2O, 1°C, 60 s
	Bath	H_2O, 30 s
	Dry	N_2
Deposition	Ar + O_2 milling	250 V, 8 mA, 50 V_{acc}
		9 sccm Ar, 1 sccm O_2, 30 s, 5 rpm
	Ar milling	300 V, 14 mA, 60 V_{acc}
		7 sccm, 3 min, 5 rpm
	Ti evaporation	30 nm, 0.1 nm/s, 0°, shutter closed
	Al evaporation	100 nm, 0.5 nm/s, 0°, 5 rpm
	Passivation	static, 10 mbar, 5 min
Lift-off	Bath I	NMP, 80°C, $\sim$ 7 h
	Bath II	NMP, 1 min, 20% power USB
	Bath III	Acetone, 1 min, 20% power USB
	Rinse I	Ethanol
	Rinse II	IPA
	Dry	N_2

Table 4.2: First layer fabrication recipe

PROCESS	STEP	PARAMETERS
Coating	Pre-bake	200°C, 2 min
	Resist I	PMMA/MAA 9%
	Spin I	3000 rpm, 3000 rpm/s, 30 s
	Bake I	200°C, 10 min
	Resist II	PMMA 4%
	Spin II	4000 rpm, 4000 rpm/s, 30 s
	Bake II	180°C, 5 min
Lithography	JJ dose	16 C/m^2
	JJ current	3 nA
Development	Developer	H_2O:IPA (1 : 3), 1°C, 105 s
	Stopper	H_2O, 1°C, 60 s
	Bath	H_2O, 30 s
	Dry	N_2
Deposition	Ar + O_2 milling	250 V, 8 mA, 50 V_{acc} 9 sccm Ar, 1 sccm O_2, 30 s, 5 rpm
	Ar milling	300 V, 14 mA, 60 V_{acc} 7 sccm, 10 min, 5 rpm
	Oxidation	static, 10 mbar, 10 min
	Ti evaporation	30 nm, 0.1 nm/s, 0°, shutter closed
	Al evaporation	200 nm, 0.5 nm/s, 0°, 5 rpm
	Passivation	static, 10 mbar, 5 min
Lift-off	Bath I	NMP, 80°C, $\sim$ 7 h
	Bath II	NMP, 1 min, 20% power USB
	Bath III	Acetone, 1 min, 20% power USB
	Rinse I	Ethanol
	Rinse II	IPA
	Dry	N_2

Table 4.3: Second layer junctions fabrication recipe

PROCESS	STEP	PARAMETERS
Coating	Pre-bake	180°C, 2 min
	Resist I	PMMA/MAA 8%
	Spin I	2000 rpm, 2000 rpm/s, 30 s
	Bake I	180°C, 5 min
Lithography	PPC dose	16 C/m^2
	PPC current	3 nA
Development	Developer	H_2O:IPA (1 : 3), 1°C, 105 s
	Stopper	H_2O, 1°C, 60 s
	Bath	H_2O, 30 s
	Dry	N_2
Deposition	Ar + O_2 milling	250 V, 8 mA, 50 V_{acc}
		9 sccm Ar, 1 sccm O_2, 30 s, 5 rpm
	Ar milling	300 V, 14 mA, 60 V_{acc}
		7 sccm, 10 min, 5 rpm
	Oxidation	static, 20 mbar, 15 min
		6 cycles
	AlO_x deposition	Al, 1.2 nm, 0.05 nm/s, 0°, 5 rpm
		O_2, static, 20 mbar, 15 min
	Al evaporation	200 nm, 0.5 nm/s, 0°, 5 rpm
	Passivation	static, 20 mbar, 15 min
Lift-off	Bath I	NMP, 80°C, $\sim$ 7 h
	Bath II	NMP, 1 min, 20% power USB
	Bath III	Acetone, 1 min, 20% power USB
	Rinse I	Ethanol
	Rinse II	IPA
	Dry	N_2

Table 4.4: Second layer capacitors fabrication recipe

PROCESS	STEP	PARAMETERS
Coating	Resist I	AZ-4562
	Spin I	1000 rpm, 100 rpm/s, 40 s
	Bake I	95°C, 5 min
Dicing	Speed	3 mm/s
Resist stripping	Bath I	Acetone, 5 min per chip
	Bath I	Acetone, 5 min per chip
	Rinse I	Ethanol
	Rinse II	IPA
	Dry	N_2

Table 4.5: Dicing fabrication recipe

5 JOSEPHSON WAVEGUIDE WITH NEGATIVE REFRACTIVE INDEX

Since their initial proposal [38], materials with a negative refractive index, also dubbed as LH, have attracted significant interest because of their unusual electromagnetic properties and promising technological applications [7, 42, 47]. Recently, they have gained renewed attention in the field of cQED as potential platforms to realize multimode electromagnetic environments for quantum simulations architectures [50] or near-quantum-limited parametric amplification [51].

In Chapter 2 we have seen the main differences between Josephson waveguides based on the RH and LH topologies from both a linear and nonlinear point of view. Here, we will discuss about the first realization of a Josephson waveguide with LH dispersion showing nonlinear traveling-wave parametric interactions.

First, we will study its linear properties, such as dispersion relation and losses, and we will see how they correspond to the expectations for a LH material. Then, the focus will move to the nonlinear behavior. The Josephson junctions nonlinearity, together with the LH dispersion enables various parametric processes, ranging from broadband amplification of signal and idler modes traveling in the same direction [51] to both frequency conversion and amplification of counter-propagating waves. We will describe the measurements of all these different parametric processes and see how we can model them using the simple couple mode differential equations derived in Chapter 2. A special consideration is given to the two amplification processes, being it the main topic of this thesis. However, given the rising interest in the community on microwave on-chip isolation and frequency routing [26–28] we briefly discuss how a negative index Josephson waveguide can be used for such applications.

5.1 THE DEVICE

A metamaterial with negative refractive index in the microwave frequency range can be engineered as a high-pass network [44]. The one whose properties are discussed in this chapter[1] is illustrated in Figure 5.1 and will be now briefly described. Here, we report about the characterization of only one device, however 5 other samples, which showed a similar behavior, have been measured[2].

1

2 Actually, several others, which were fabricated with using the bridge-free evaporation technic, briefly described in Section 4.1 in Chapter 4, have been tested, but none of

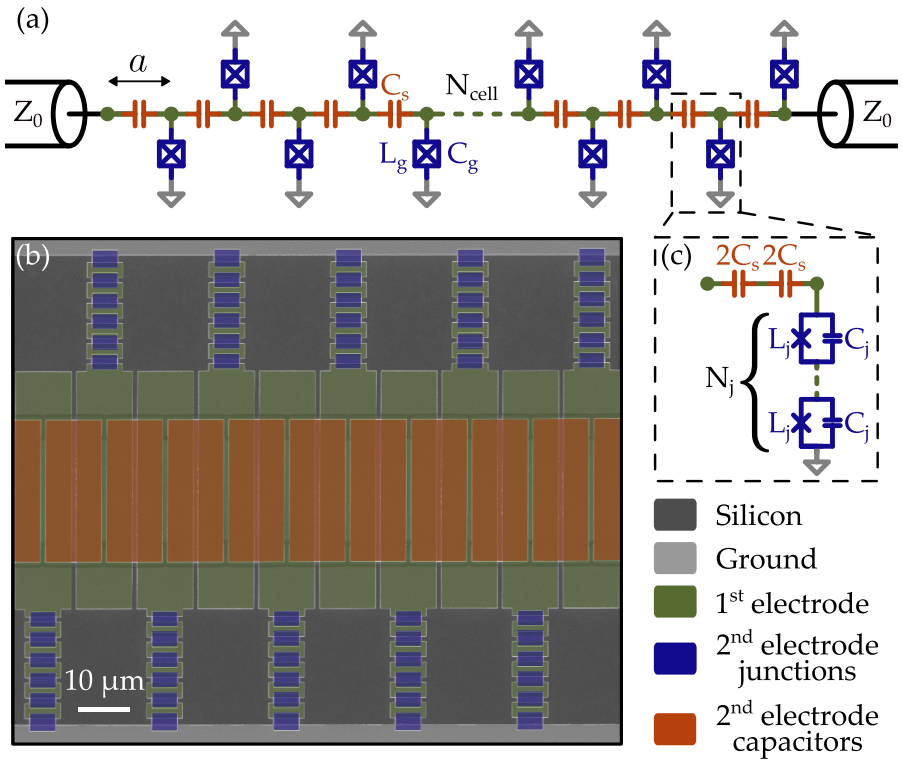

Figure 5.1: The negative index Josephson waveguide
(a) Circuit scheme of the transmission line modeled as an array of capacitors, in red, shunted to ground by Josephson junctions, in blue.
(b) False colored SEM image of a LH sample, not specifically the one whose characterization is reported here. The capacitors are formed at each overlap between the green layer and red one, while the junctions are given by the overlap between the green and the blue layers.
(c) Detailed circuit schematic of the unit cells which is composed by two series capacitors and a chain of Josephson junctions shunted to ground.

5.1.1 Description of the sample

The device consists of 600, 12 μm long, unit cells. Each unit cell contains two capacitors[3] in series that are shunted to ground by an array of 20, nominally identical[4], Josephson junctions. The latter is used to implement the required ground inductance while enhancing the dynamic range of the device [37, 68, 105]. The position of these arrays is alternated with respect to the capacitors central line: arrays of

them was working. This motivated us to move to the overlap technic, which showed a yield of 6 working devices out of 7 tested ones.

3 The number of capacitors per unit cell is set by fabrication constraints, as described in Chapter 4.

4 Up to the fabrication disorder, which, given the novelty of the fabrication process, has not been fully characterized yet.

neighboring cells are connected to the ground plane either upwards or downwards. It is worth mentioning that this configuration may lead to a distortion of the dispersion relation [49] or to the presence of slot modes [85] because of asymmetries in the grounding between the two ground planes.

5.1.2 Sample's parameters

The main parameters of the sample are given in Table 5.1. Most of them are obtained from the linear characterization of the device described in the next section.

PARAMETER	VALUE	UNIT	OBTAINED FROM
Number of unit cells N_{cell}	600	-	design
Number of Josephson junction per unit cell N_j	20	-	design
Number of capacitors per unit cell N_c	2	-	design
Unit cell size a	12	μm	design
Critical current of the junctions I_c	1.7	μA	measurements
Josephson inductance L_j	191	pH	measurements
Josephson capacitance C_j	227	fF	measurements
Inductance to ground per unit cell L_g	3.8	nH	measurements
Capacitance to ground per unit cell C_g	11.4	fF	measurements
Capacitance in series per unit cell C_s	1.1	pF	measurements
Characteristics impedance Z_c	59	Ω	measurements
Low-frequency cut-off f_o	2.4	GHz	measurements
Plasma frequency f_j	24.1	GHz	measurements
Area Josephson junctions A_j	3.75	μm^2	design
Area series capacitors A_c	308	μm^2	design

Table 5.1: Main parameters of the Left-Handed sample
Parameter of the device extracted from the characterization in the linear regime, as described in Section 5.2, and from design values.

5.2 LINEAR SPECTROSCOPY

Before delving into the more intriguing nonlinear regime shown by the device, we shall discuss its linear characterization. The latter can be obtained performing a broadband spectroscopy of the device with low enough probe powers to not activate any nonlinear interaction.

This is done by measuring the transmission scattering parameter

$$S_{ij}(\omega) = \frac{a_i^{out}(\omega)}{a_j^{in}(\omega)} \quad \text{for } i \neq j, \tag{5.1}$$

that relates the amplitudes (magnitude and phase) of the traveling waves $a_j^{in}(\omega)$ incident on and $a_i^{out}(\omega)$ transmitted from the probed microwave network [85]. Here, i and j index the two different ports of the network. Thus, measuring the $S_{ij}(\omega)$ parameter gives us information on the phase $\theta(\omega) \equiv \arg(S_{ij}(\omega))$ and the attenuation $A(\omega) \equiv |S_{ij}(\omega)|$ of a wave traveling through the sample, from which its linear parameters can be inferred.

For a fully symmetric and reciprocal system measuring S_{21} is equivalent to measuring S_{12}

In the following we will focus the discussion on the S_{21} parameter, meaning that the probe wave travels from the left to right of the device, as schematically depicted in Figure 5.2. The latter shows a simplified scheme of the setup used to perform these measurements.

Being the device under test at the coldest point of a dilution refrigerator, the measured scattering parameter needs to be normalized to remove the contributions coming from all the cables and components between the VNA and the device itself. For a detailed description of the complete setup and about the calibration we refer the reader to Chapter 3. The normalized S_{21} parameter of the device is obtained by comparing the one measured through the device, S_{21}^{DUT}, with that measured through a reference, S_{21}^{ref}:

As reference we used a microwave female to female adapter

$$\begin{aligned} |S_{21}(\omega)| &= \frac{|S_{21}^{DUT}(\omega)|}{|S_{21}^{ref}(\omega)|}, \\ \theta(\omega) &= \theta^{DUT}(\omega) - \theta^{ref}(\omega), \end{aligned} \tag{5.2}$$

where we are assuming that the attenuation and electrical length of the reference are negligible[5]. Indeed, in our metamaterial light travels about 100 times slower than in the reference. The normalized electrical length and attenuation of the device are shown in Figure 5.3.

5.2.1 Electrical length

The electrical length corresponds to the phase $\theta(\omega)$ acquired by a wave traveling through the sample. This phase is directly linked to the dispersion relation by $k(\omega) = \theta(\omega)/N_{cell}$. Thus, the linear param-

Here $k(\omega)$ is the dimensionless wavevector introduced in Chapter 2

5 Here we are also assuming that return loss of both the sample and the reference are comparable.

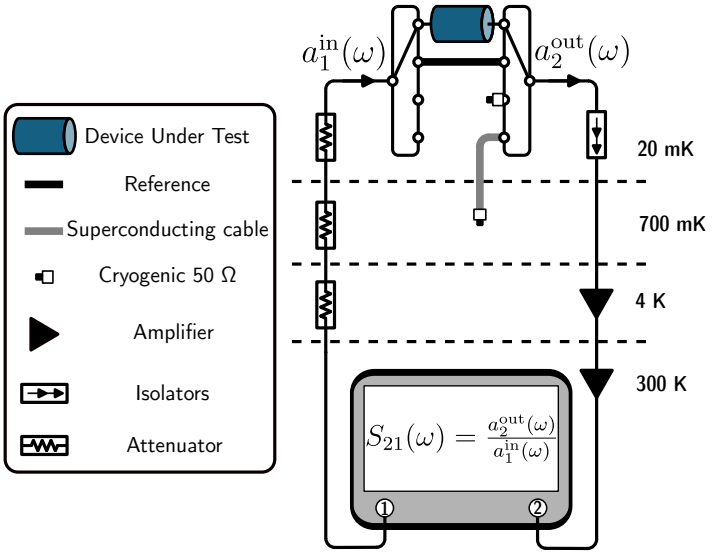

Figure 5.2: Simplified schematic of the experimental setup used for the linear spectroscopy
Only the relevant components and input/output lines used for the linear characterization of the sample are shown. The sample's parameters and loss can be inferred by measuring its normalized linear transmission S_{21}. To do so only one input and output lines are necessary. The normalization is performed using a female to female adapter as a reference. The system gain and noise are obtained by a Y-factor measurement thanks to the two 50 Ω loads that acts as noise source at two different temperatures. A detailed description of the full setup and calibration can be found in Chapter 3.

eters, reported in Table 5.1, can be obtained by fitting the frequency dependent phase evolution to the LH dispersion relation derived in Section 2.2.1 in Chapter 2:

$$\theta(\omega) = N_{\text{cell}} \frac{\omega_0}{\omega} \sqrt{1 - \frac{\omega^2}{\omega_j^2}} + \theta_0, \tag{5.3}$$

where $\omega_0 = 1/\sqrt{L_g C_s}$ and $\omega_j = 1/\sqrt{L_g C_g}$.

The experimental data and the corresponding fit are shown in Figure 5.3(a). As expected for a LH material, the electrical length is higher at lower frequencies, in contrast to the "usual" RH case, as described in Section 2.1 in Chapter 2. This results from the fact that the LH dispersion relation $k(\omega)$ is a decreasing function of the frequency: waves with lower frequency have an higher wavevector.

To perform the fit we leave as free parameters θ_0, which accounts for the uncertainty introduced by the phase wrapping, the ground and series capacitances, C_g and C_s, and the ground inductance L_g. The choice of using four free parameters is related to the novelty of the fabrication. We could have reduced such number to three by setting one of the capacitances or the inductance to its fabrication

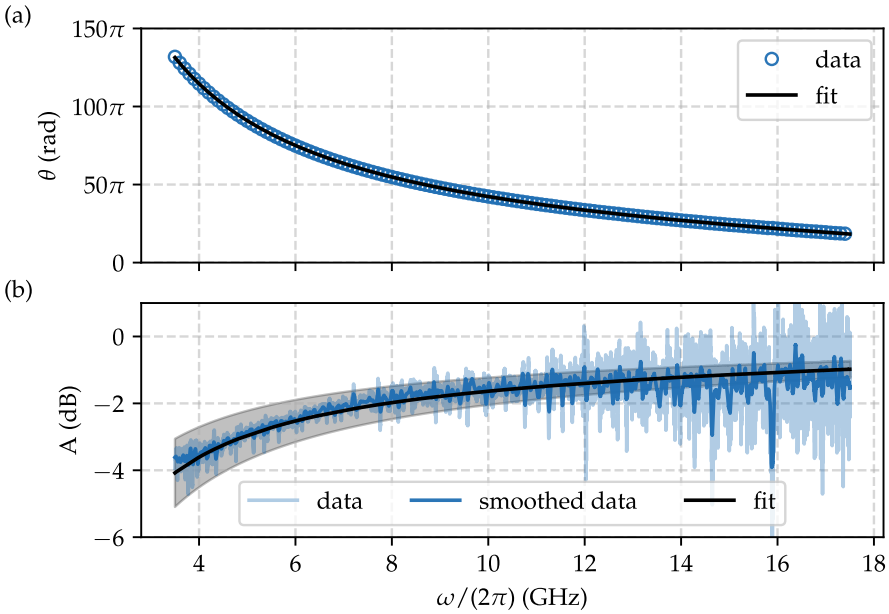

Figure 5.3: Normalized S_{21} parameter of a left-handed transmission line
(a) Normalized electrical length as a function of frequency, blue dots. The black line represents the fit to the LH phase dispersion relation given in Equation 5.3.
(b) Normalized attenuation as a function of frequency. The brighter shaded line shows the raw data while the darker blue line corresponds to the smoothed data. The black line represents the fit to Equation 5.4 from which we obtained a loss tangent of 2.0×10^{-3}. The brighter shaded region shows the attenuation calculated from Equation 5.4 with $\tan\delta = (2.0 \pm 0.5) \times 10^{-3}$.

value. However, we preferred to fit all of them and then compare the results with the values expected from the design.

This comparison is shown in Table 5.2: the measured values are consistent with the expected ones. The value that differs the most is the ground capacitance. This difference can be attributed to the presence of stray capacitances in the line. The values obtained from the fit has been used to compute all the parameters reported in Table 5.1.

5.2.2 Attenuation

The frequency dependence of the electrical length reflects on the attenuation of the material. The latter can be caused by either conductor or dielectric loss. However, the only metal used for the fabrication of this device, as describe in Chapter 4, is aluminum, which is superconducting at 20 mK. Thus, it is safe to neglect conductor loss and to assume that dielectric losses are the main cause of the measured attenuation. Such losses are mainly due to the dielectric forming the series parallel

	MEASUREMENT	DESIGN
L_g (nH)	3.83	3.81
C_g (fF)	11.37	8.44
C_s (pF)	1.12	1.08

Table 5.2: Comparison between designed and measured sample's parameters
The measured parameters are inferred from the fit of the frequency dependent electrical length shown in Figure 5.3. The designed parameters have been computed using the calibration of the fabrication process described in Chapter 3 and the designed junctions and capacitors dimensions.

plate capacitors[6]. Thus, the attenuation $A(\omega)$ of a signal at the output of the device can be modeled as [85]:

$$A(\omega, x = l) = e^{\alpha_d(\omega) l} = e^{\frac{\theta(\omega)\tan\delta}{2}}, \tag{5.4}$$

where $\alpha_d = \frac{k(\omega)\tan\delta}{2}$ is the dielectric loss attenuation constant, $l = N_{\text{cell}} a$ is the total length of the transmission line and $\tan\delta$ is the dielectric loss tangent. Therefore, the attenuation directly depends on the electrical length. The longer the device at a given frequency, the higher the attenuation. In contrast to RH transmission lines, in a LH material losses are therefore higher at low frequency, as shown in Figure 5.3(b).

By fitting the frequency dependent insertion loss we obtain a loss-tangent of 2×10^{-3} for the AlOx forming the parallel plate capacitors. Such value of loss tangent is about a factor two lower than the one obtained with the previous fabrication process used in our group [91, 119] and comparable to other JTL implementations based on such types of capacitors [20].

5.3 NONLINEAR SPECTROSCOPY

Now we will study the nonlinear properties of the negative index waveguide. 4WM interactions can occur inside this medium thanks to the presence of the Josephson junctions. As described in Chapter 2, these interactions, together with the unique LH dispersion relation, can lead to the phase-matching of various parametric processes, ranging

6 Here we are neglecting the losses at the interface between the various aluminum layers and the silicon substrate, whose contribution is usually smaller. Indeed, recent realizations of JTLs based on coplanar lumped-element capacitors showed an improvement of more than one order of magnitude in the los-tangent [93, 98] compared to previous implementations with parallel-plate capacitors [20, 83]

from amplification to frequency conversion, depending on the relative propagation directions of the signal and pump waves.

As before i and j index the two different ports of the device

Such processes can be characterized by performing a broadband nonlinear spectroscopy of the device response to a weak input signal wave $a^{\text{in}}_{i,j}(\omega_s)$ in presence of a second stronger wave, the pump, $a^{\text{in}}_{i,j}(\omega_p)$. Driving the system with a high power pump tone leads to the activation of the parametric processes described in Chapter 2.

Signal gain or attenuation, depending on the process of interest, are given by the normalized $S_{ij}(\omega_s)$ parameter, defined in Equation 5.1. It is important to note that the presence of the pump wave breaks the symmetry of the system. Now, for a given pump input the measured $S_{21}(\omega_s)$ and $S_{12}(\omega_s)$ will be quite different, as shown in Figure 5.4. Thus, the system is nonreciprocal. Sending a signal in the same or

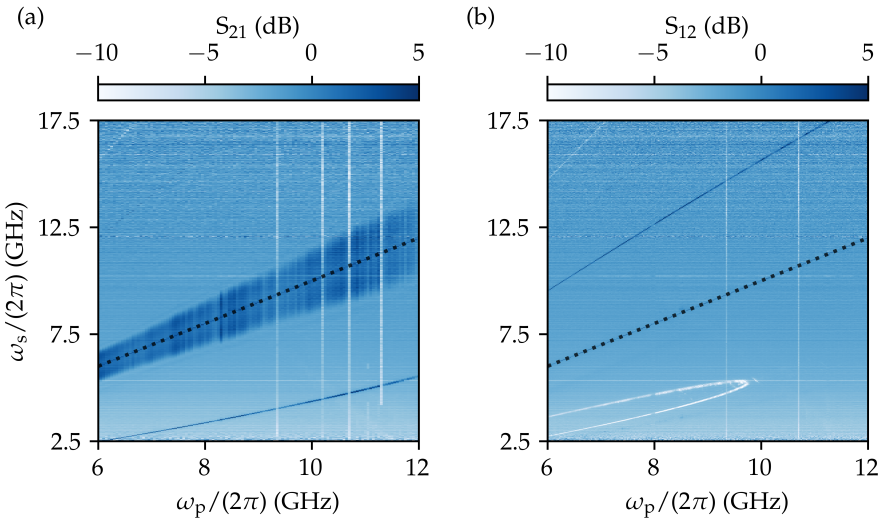

Figure 5.4: S_{21} and S_{12} nonlinear parameters of a negative index Josephson waveguide
Measured signal, S_{21} (a) and S_{12} (b), parameters as a function of the signal and pump frequencies. Note that for both measurements the pump tone, highlighted by the black dots, was sent from port 1 to port 2 of the device. The white, frequency independent lines, are cause by a pump power higher than the critical one of the array, which results in a sudden decrease in transmission.

opposite direction with respect to the pump leads to different outcomes: the signal can get amplified, attenuated or simply transmitted. Here we see all the processes described in Chapter 2. In the S_{21} measurement the broadband darker region around the pump frequency, highlighted by the black dots, corresponds to the amplification of co-propagating signal and idler modes, while the narrow band feature at low signal frequencies is the counter-propagating one. By probing the device in the opposite direction with respect to the pump, thus measuring the S_{12} parameter, the latter process is still visible, but at

high frequencies; while, at low frequencies both isolation gaps, described in Section 2.4 in Chapter 2, are clearly visible. Moreover, some other shallow features are present in the top left regions of both plots, which have not been investigated yet.

Given that these nonlinear interactions will also generate a third wave at the image frequency $2\omega_p \pm \omega_s$[7], measuring only the response of the sample at the same frequency is not enough to characterize these processes. Thus, we measure also scattering parameters between different frequencies:

$$S_{ij}^{mn} = \frac{a_i^{out}(\omega_m)}{a_j^{in}(\omega_n)}, \tag{5.5}$$

where, again, i and j index the ports of the network, while m and n index the frequencies of the input and output waves. The pump tone will always be sent from port one to port two of the network, *i.e.* from left to right, defining the directionality for the system. Thus, these inter-frequency scattering parameters give information about the non-reciprocal and nonlinear response of the material and their normalized magnitude corresponds to the frequency conversion amplitude.

To perform these measurements we used the setup described in Chapter 3 and a VNA that allows such frequency conversion measurements. As for the linear case, a careful calibration of the input line attenuation and output line amplification is necessary to relate the values measured by the VNA to the ones at the input and output of the sample. By knowing the output line gain $G^{sys}(\omega)$ and the input line attenuation $A^{sys}(\omega)$, the normalized magnitude of such inter-frequency scattering parameters can be obtained as:

$$S_{ij}^{mn} = \tilde{S}_{21}^{mn} - G_i^{sys}(\omega_m) - A_j^{sys}(\omega_n) \quad (\text{dB}), \tag{5.6}$$

where $\tilde{S}_{21}^{mn}$ is the frequency conversion scattering parameter measured by the VNA at its ports.

5.3.1 Amplification

Let us start by considering a pump wave co-propagating with the signal one. In Section 2.3 in Chapter 2 we saw that two different amplification processes can occur in this situation, depending on the frequencies of the two waves:

1. Broadband amplification of signal and idler waves propagating in the same direction.

2. Amplification of signal and idler waves propagating in opposite directions.

7 The $-$ sign corresponds to the amplification process, while the $+$ sign corresponds to frequency conversion one.

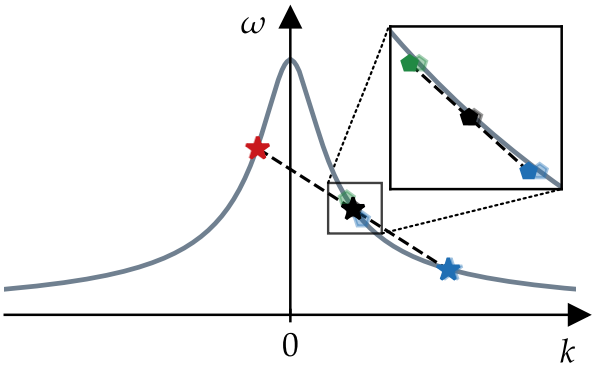

Figure 5.5: Phase-matching conditions for the amplification processes in a negative index Josephson waveguide
LH dispersion relation $\omega(k)$ for both positive and negative wavevectors. For a given pump wave, in black, with frequency ω_p and positive wavevector k_p, two amplification processes can occur depending on the frequency ω_s and wavevector k_s of the signal wave, in blue. In one case, represented by the pentagons in the inset, broadband amplification can occur with the generation of an idler, in green, with a positive wavevector k_i. For a higher detuning between the signal and the pump, a different amplification process, represented by the stars, is phase-matched. It results in the generation of an idler, in red, propagating in the opposite direction with respect to the signal and the pump. The frequency and phase-matching condition is represented by the the black dashed lines. For a detailed description of the frequency and phase-matching mechanism of both processes we refer the reader to Section 2.3.2 in Chapter 2.

We recall here the frequency and phase-matching conditions for these two processes. The latter are schematically shown on the dispersion relation $\omega(k)$ in Figure 5.5 by the green and blue pentagons and by the red and blue stars, respectively. For a detailed discussion on the frequency and phase-matching mechanism of both processes, we refer the reader to Section 2.3.2 in Chapter 2.

A simplified scheme of the setup used to characterize both amplification processes is shown in Figure 5.6. The presence of the directional coupler before the switch at the coldest stage of the cryostat allows to perform reflection measurements. The latter give us access to the reflected output waves or to the ones traveling in the opposite direction with respect to the input ones.

Therefore, such setup allows to measure the following scattering parameters:

- $S_{21}^{ss} = \frac{a_2^{out}(\omega_s)}{a_1^{in}(\omega_s)}$, corresponding to the signal gain.
- $S_{21}^{is} = \frac{a_2^{out}(\omega_i)}{a_1^{in}(\omega_s)}$, corresponding to the co-propagating idler gain.

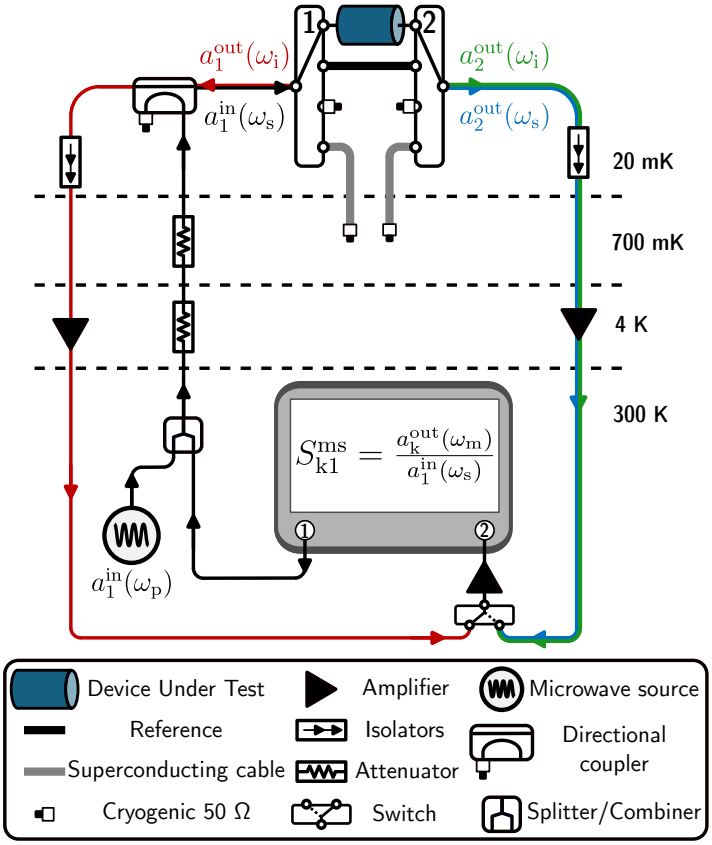

Figure 5.6: Simplified schematic of the experimental setup used for the nonlinear spectroscopy of the amplification processes
Only the relevant components and input/output lines used for the characterization of the two amplification processes are shown. A pump tone $a_1^{\text{in}}(\omega_\text{p})$ is generated with a microwave source and combined with the VNA probe tone $a_1^{\text{in}}(\omega_\text{s})$. The signal gain can be obtained by measuring the response of the sample at the same frequency ω_s through the blue output line. The VNA can also be set to perform frequency conversion measurements, *i.e.* the frequencies of its ports can be configured independently. Thus, by measuring the response of the sample, to the same input waves, at the idler frequency $\omega_\text{i} = 2\omega_\text{p} - \omega_\text{s}$ we have access to the idler conversion gain. The directional coupler allows to measure both the idler generated in the same direction of the signal and the one generated in the opposite direction through the green and red output lines, respectively. A detailed description of the full setup and calibration can be found in Chapter 3.

- $S_{11}^{\text{is}} = \frac{a_1^{\text{out}}(\omega_\text{i})}{a_1^{\text{in}}(\omega_\text{s})}$, corresponding to the counter-propagating idler gain.

where $\omega_\text{i} = 2\omega_\text{p} - \omega_\text{s}$.

The result of these measurements for a pump tone with frequency $\omega_\text{p}/(2\pi) = 10$ GHz and power $\text{P}_\text{p} = -62.0$ dBm, referenced at the input of the device, is shown in Figure 5.7.

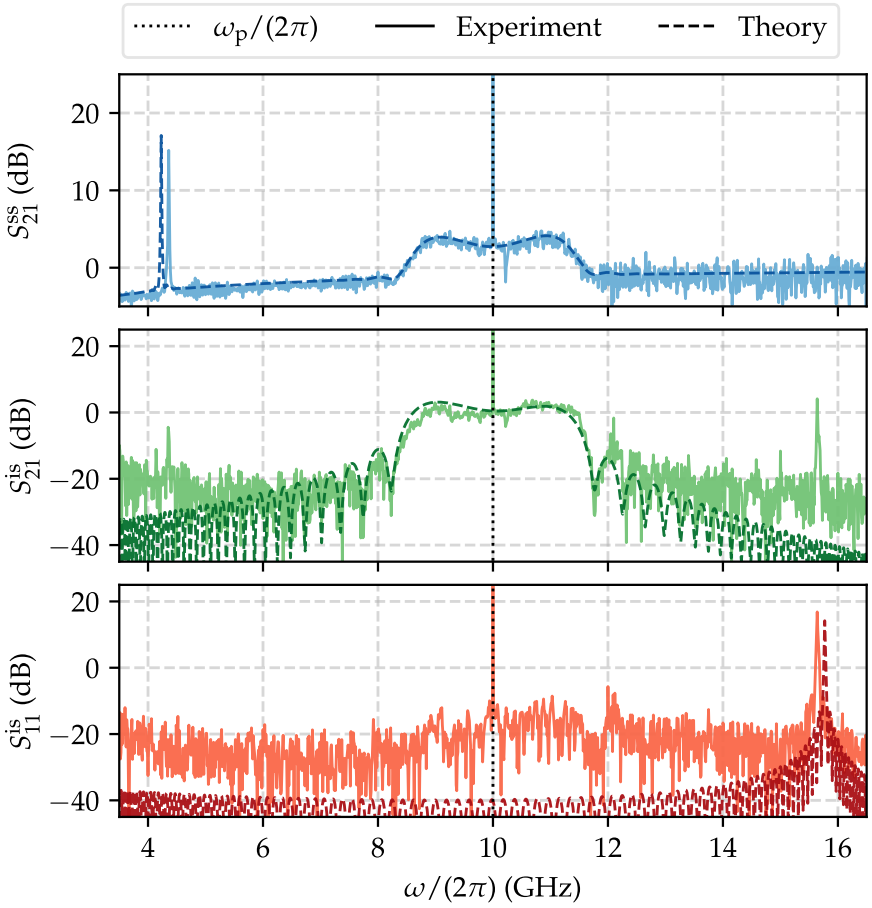

Figure 5.7: Normalized gain of a negative index Josephson waveguide Measurements of the signal gain, in blue, and of the co-propagating, in green, and counter-propagating, in red, idlers conversion gain for a pump frequency $\omega_p/(2\pi) = 10$ GHz and a pump power $P_p = -62.0$ dBm. Note that the frequency axis corresponds to the frequency measured by the VNA which is equal to the generated one, $\omega_s/(2\pi)$, only for the upper panel. While, for the other two it corresponds to the idler one $\omega_s/(2\pi) = (2\omega_p - \omega_s)/(2\pi)$. The dashed lines have been obtained solving numerically the coupled differential equations derived in Section 2.3.1 in Chapter 2 with a a pump frequency $\omega_p/(2\pi) = 10$ GHz and a pump power $P_p = -64.0$ dBm. We stress here that such simulations have been performed without any fitting parameters, but the pump power, which is slightly adjusted.

The transmitted signal wave, in blue, gets amplified whenever the frequency and phase-matching conditions are satisfied. Around the pump frequency, the device shows a double lobe amplification profile with about 4 dB of maximum gain and a 1.5 GHz bandwidth. This gain corresponds to the broadband co-propagating amplification process described in [51]. The double lobe profile results from the fact that the phase-mismatch vanishes on either sides of the pump frequency, as

discussed in Section 2.3.2 in Chapter 2. The low maximum value is can be attributed to the relatively short length of the device. Moreover, the presence of the counter-propagating amplification process may also limit its value. Indeed, the bright and narrow-band peak at low frequency, $\omega_s/(2\pi) = 4.36$ GHz, corresponds to the amplification of signal and idler waves propagating in opposite directions. The latter is schematically described in Figure 5.5 by the red and blue stars. In this case the phase-mismatch crosses zero at only one signal frequency, as described in Section 2.3.2 in Chapter 2.

The measurements of the idlers scattering parameters confirm the origin of the two amplification processes. The counter-propagating idler gain, in red, shows the presence of only one bright and narrow-band peak at the frequency $\omega_i/(2\pi) = 15.64$ GHz. In the same way, the co-propagating idler conversion gain, in green, shows a broadband double lobe amplification around to the pump frequency with the same 1.5 GHz bandwidth of the signal.

The nonlinear behavior of the device can be simulated with the coupled differential equations derived in Section 2.3.1 in Chapter 2 and using the parameters extracted from the linear characterization discussed in Section 5.2. To quantitatively simulate the two amplification processes we include the modes losses in the model via Equation 2.56, derived in Chapter 2. Note that the two amplification processes are simulated separately, meaning that for each of them we are using a minimal three mode model with only a pump, a signal and an idler involved. Moreover, the initial conditions to simulate the two processes are different:

- For the co-propagating amplification we have $a_p(0) = a_{p,0}$, $a_s(0) = a_{s,0}$ and $a_i(0) = 0$.
- While for the counter-propagating one we give $a_p(0) = a_{p,0}$, $a_s(0) = a_{s,0}$ and $a_i(l) = 0$.

The dashed lines in Figure 5.7 are the results of those simulations for an input pump power of -64.0 dBm. At first sight the agreement is quite good. The simulations reproduce the bandwidth, the involved frequencies and the magnitudes of the processes, especially for the broadband co-propagating amplification, while there is a discrepancy, in both amplitude and frequency, for the counter-propagating one. This discrepancy could be caused by a distortion of the dispersion relation given by stray linear inductances and capacitances in the transmission line, which have been neglected, or by an error in the estimation of the values of L_g, C_g, C_s and I_c obtained from the characterization in the linear regime, described in Section 5.2. Such error has an higher influence on the counter-propagating amplification process because its phase-matching condition strongly depends on the curvature of the dispersion relation.

A more detailed description of the system gain and attenuation calibration can be found in Chapter 3

It is worth mentioning that the simulations have been performed using a different value for the input pump power with respect to the experimental one. The difference amounts to 2.0 dB and it can be attributed to several factors. First of all, the reference plane for the experimental value of the pump power is at the switch level, where the two 50 Ω loads are connected, and not at the input of the device. Then, the simulations have been performed with the linear parameters given in Table 5.1, an error in their estimation contributes to the aforementioned discrepancy.

A final consideration has to be made on the presence of a peak at exactly $\omega_i/(2\pi) = 15.64$ GHz in the S_{21}^{is} measurement. Being its magnitude about 15 dB lower than its S_{11}^{is} counterpart, we attribute it to spurious reflections. This hypothesis can be confirmed by looking at the pump power dependence of both S_{jk}^{is} parameters.

COUNTER-PROPAGATING MODES However, before that, let us have a closer look to the counter-propagating amplification process for a pump tone with frequency $\omega_p/(2\pi) = 8.5$ GHz. For this choice of pump frequency such process is phase-matched at the signal-idler pair of frequencies $\omega_s/(2\pi) = 3.59$ GHz and $\omega_i/(2\pi) = 13.41$ GHz. The

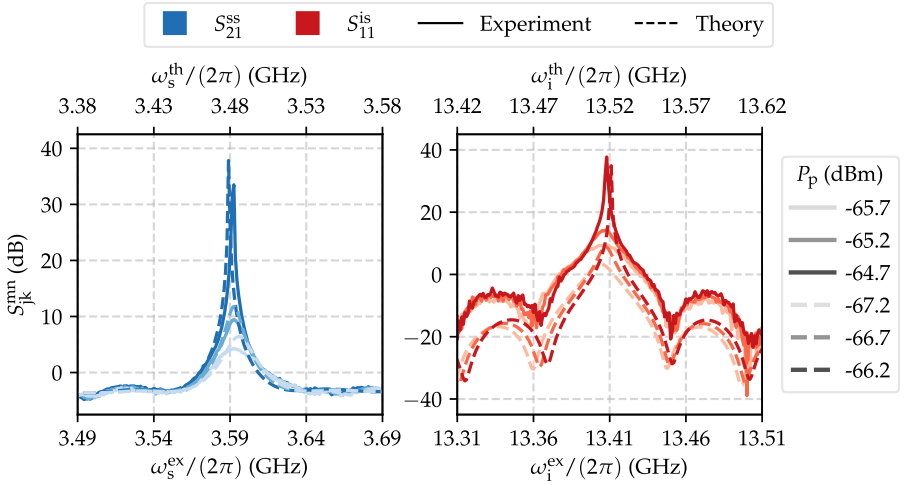

Figure 5.8: Gain profiles of the counter-propagating amplification process The solid lines represent the calibrated signal gain, in blue, and the counter-propagating idler conversion gain, in red, as a function of the signal (idler) frequency (bottom x-axis) for a pump tone with frequency $\omega_p/(2\pi) = 8.5$ GHz. The dashed lines correspond the to result of simulations, performed using the device parameters given in Table 5.1, as a function of the signal (idler) frequency (top x-axis) performed for the same pump frequency. Each color shade represent a different pump power as reported in the legend. Note the difference between the experimental pump powers and the simulation ones.

signal and idler gain profiles around these frequencies ar shown in

Figure 5.8(a) for three different input pump powers, together with the corresponding numerical simulations, performed using the device's parameters given in Table 5.1. As the pump power increases the gain increases with a maximum value approaching 40 dB; while the bandwidth decreases. This behavior is well reproduced by the simulations, besides a discrepancy in the frequencies, of about 100 MHz, and in the pump input powers, which have been previously discussed.

Moreover, it is worth mentioning that at such high power other nonlinear processes or intermodulation terms, that are not taken into account by our three-mode model, can be taking place in the device, leading to complex dynamics. To efficiently model such situation X-PARAMETER [106] or WRSPICE simulations would be needed.

PUMP POWER DEPENDENCE The amplification processes require a strong pump tone, with respect to the signal one, to be activated. The pump power dependence of the signal and idlers gains for a pump frequency of 8.5 GHz is shown in Figure 5.9(a). As expected, the amount of gain increases as the pump power increases, until a critical value $P_{\mathrm{p}}^{\mathrm{c}}$ is reached. At this value, of about -64.6 dBm for this pump frequency, the transmission suddenly drops. A reason for such breakdown can certainly be that the pump current $I_{\mathrm{p}} = \sqrt{P_{\mathrm{p}}/Z_0}$ approaches the critical, or switching, current of the array of junctions I_{c}. This phenomena is not captured by the simulations. However, as shown by the right y-axis of Figure 5.9, it seems that the device can sustain higher pump currents than the junctions' critical one. This might be surprising, but computing the experimental pump to critical currents ratio is not as straightforward as it seems. It strongly depends on the input line calibration and on the estimation of both the characteristic impedance and critical current of the device.

Besides this, from these measurements we can compare the power dependence of the two amplification processes. In Chapter 2 we have seen how the two gains, in the ideal condition of perfect phase-matching, scale in very different ways. The signal gain resulting from the co-propagating amplification should scale exponentially with the pump power in the asymptotic limit; while the one resulting from the counter-propagating process has an periodic $1/\cos(g\ell)$ dependence, where $g\ell$ is the amplification length. This different scaling is clearly visible in Figure 5.9(b). The counter-propagating signal gain diverges very quickly as the pump power increases compared to the standard co-propagating one.

The different scaling are given in Equation 2.64 and Equation 2.69 derived in Section 2.2.2 in Chapter 2

Finally, by comparing the pump power dependence of the idler S_{is}^{mn} parameters at the frequency at which the counter-propagating amplification process is phase-matched, $\omega_{\mathrm{i}}/(2\pi) = 13.41$ GHz, shown in Figure 5.9(c), we can further confirm that the increase in the S_{21}^{is} parameter is due to spurious reflections.

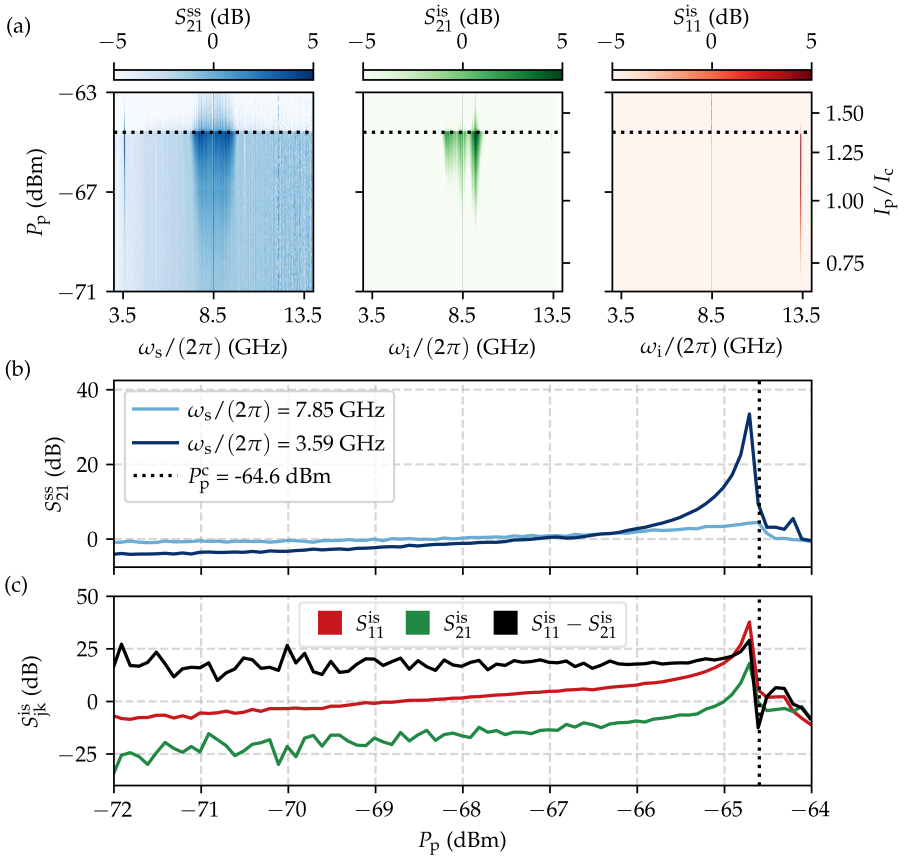

Figure 5.9: Pump power dependent gain of a negative index Josephson waveguide

(a) Measured signal gain, in blue, and co-propagating, in green, and counter-propagating, in red, idler conversion gain for a pump tone with frequency $\omega_p/(2\pi) = 8.5$ GHz as a function of the pump power at the input of the device and of the signal (idler) frequency. The dotted line corresponds to the critical power after transmission drops.

(b) Comparison between the pump power dependence of the co-propagating and counter-propagating amplification processes. The darker blue line corresponds to the signal gain resulting from the counter-propagating amplification process at the phase-matching frequency $\omega_s/(2\pi) = 3.59$ GHz, while the lighter blue line represents the signal gain obtained from the co-propagating amplification process at the phase-matching frequency $\omega_s/(2\pi) = 7.85$ GHz. The dotted line corresponds to the critical power at which the transmission drops.

(c) Comparison between the idler S-parameters, with the same color code as in (a), at the frequency at which the counter-propagating amplification process is phase-matched, *i.e.* $\omega_i/(2\pi) = 13.41$ GHz, as a function of the calibrated input pump power. The black line corresponds to the difference between the two, as reported in the legend.

PUMP FREQUENCY DEPENDENCE As described in Section 2.3.2 in Chapter 2, a key feature of a negative index Josephson waveguide is

that it does not rely on any dispersion [20] or nonlinear engineering [84] and, as for the latter case, the pump frequency is not fixed by design. It can be tuned over a large range of frequencies.

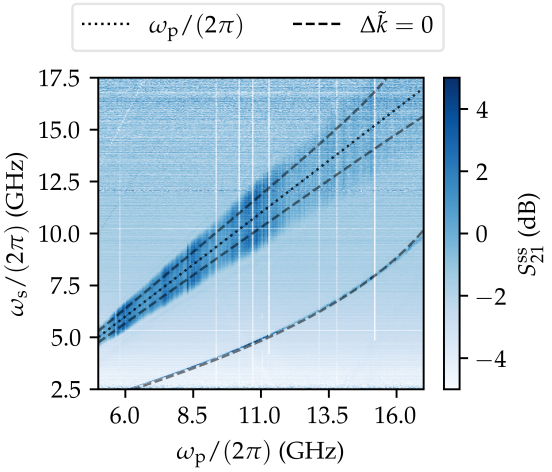

Figure 5.10: Pump frequency dependent gain of a negative index Josephson waveguide
Calibrated signal S_{21}^{ss} parameter as a function of the pump and signal frequencies. For each pump frequency the pump power is not properly optimized to maximize the signal gain. The black dashed lines represent the solution of the analytical formula $\Delta\tilde{k} = 0$ for either the co-propagating amplification process or the counter-propagating one. The dotted line highlights the pump frequency.

The pump frequency dependence of the signal gain is shown in Figure 5.10. For each pump frequency the pump power has not been properly optimized to maximize the gain. Thus, for some frequencies, the computed value was already on the onset of the device breakdown described in the previous section. This explains why there are some frequency independent lines with no transmission.

As we saw at the beginning of the section, in Figure 5.4, both the broadband co-propagating amplification process and the counter-propagating one are visible. The former is always centered around the pump frequency with a double lobe profile; while, the latter basically follows the curvature of the dispersion relation (see Figure 5.5). Both processes can be tuned over a wide range of frequencies. However, the amount of gain lowers as the pump frequency increases. This is expected for a LH TWPA: higher frequencies implies an effectively shorter device, as discussed in Section 5.2.1. The pump frequency dependence of both amplification processes is set by phase-matching condition as highlighted by the dashed lines, which represent the solution of the analytical formula $\Delta\tilde{k} = 0$.

In Figure 5.4, at the beginning of the section, we also discussed the nonreciprocity of the device. Probing it from port 2 to port 1, *i.e.* from

right to left, while sending the pump tone still in the forward direction, results in the amplification of the signal at high frequency and in the generation of a low frequency idler. Besides, sending a signal wave propagating in the opposite direction with respect to the pump one also leads to the phase-matching of the frequency conversion processes described in Section 2.4 in Chapter 2. A preliminary characterization of these processes is given in the next section.

5.3.2 Frequency conversion

In the previous section we have considered a pump wave propagating in the same direction as the signal one. Let us now focus our attention to the case of counter-propagating signal and pump waves.

From Chapter 2 we know that, besides the previously described counter-propagating amplification with inverted signal and idler, two frequency conversion processes can occur, depending on the frequency of the signal tone:

1. Conversion to a wave co-propagating with the signal itself.
2. Conversion to a wave propagating in the opposite direction with respect to the signal.

The frequency and phase-matching conditions for these two processes are schematically shown on the dispersion relation $\omega(k)$, in Figure 5.11, by the green and blue pentagons and by the red and blue stars, respectively. Here we will present a preliminary characterization of the two frequency conversion processes enabled by the LH dispersion relation.

To characterize, these processes we have to use two different input lines for the signal and pump waves, as depicted in the simplified scheme of the setup in Figure 5.12. This configuration with two directional couplers at the coldest stage of the cryostat allows to perform both reflection and transmission measurements, giving access to output waves traveling in the opposite direction with respect to the input ones, and enables to probe the system with signal waves traveling in the opposite direction with respect to the pump one.

Therefore, the following scattering parameters can be measured:

- $S_{12}^{\mathrm{ss}} = \frac{a_1^{\mathrm{out}}(\omega_{\mathrm{s}})}{a_2^{\mathrm{in}}(\omega_{\mathrm{s}})}$, corresponding to the signal attenuation,
- $S_{12}^{\mathrm{us}} = \frac{a_1^{\mathrm{out}}(\omega_{\mathrm{u}})}{a_2^{\mathrm{in}}(\omega_{\mathrm{s}})}$, corresponding to the co-propagating sideband conversion amplitude,
- $S_{22}^{\mathrm{us}} = \frac{a_2^{\mathrm{out}}(\omega_{\mathrm{u}})}{a_2^{\mathrm{in}}(\omega_{\mathrm{s}})}$, corresponding to the counter-propagating sideband conversion amplitude,

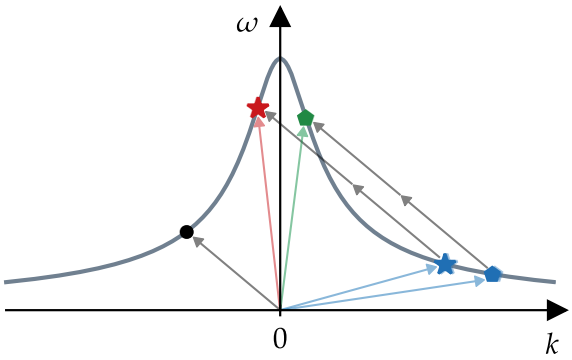

Figure 5.11: Phase-matching conditions for the frequency conversion processes in a negative index Josephson waveguide
LH dispersion relation $\omega(k)$ for both positive and negative wavevectors. As discussed in Chapter 2, the frequency and phase-matching conditions for the conversion processes can be represented as the vector sum of all the waves involved in the process. For a given pump wave, in black, with frequency ω_p, and negative wavevector $-k_p$, two frequency conversion processes can occur depending on the frequency ω_s and wavevector k_s of the signal wave, in blue. In one case, represented by the pentagons, a low frequency signal can be converted to an high frequency wave with frequency ω_{up} and positive wavevector k_{up}. For a signal wave with higher frequency, a second conversion process, represented by the stars, is phase-matched with the generation of a high frequency wave, in red, propagating in the opposite direction with respect to the signal one.

where $\omega_u = 2\omega_p + \omega_s$.

The result of these measurements as a function of the frequency of both the pump and signal tones are shown in Figure 5.13. The signal, in blue, gets up-converted when the energy conservation $2\omega_p + \omega_s = \omega_u$ and the phase-matching condition $2\tilde{k}_p + \tilde{k}_s = \tilde{k}_u$ are satisfied. For a given pump frequency, two signal frequencies satisfy the above mentioned conditions. Hence, the presence of two isolation gaps. As for the amplification processes, the frequency conversion ones do not rely on any particular design feature and are, therefore, frequency tunable. The position of these gaps shifts to higher frequencies, as the pump one increases, until the frequency of the up-converted tone ω_u reaches the plasma frequency ω_j. Here, the two isolation gaps merge and for higher pump frequencies both processes are suppressed. This behavior is well reproduce by the simple analytical formula for the total phase-matching as highlighted by the dashed lines in Figure 5.13. The latter correspond to the solution of $\Delta\tilde{k} = 0$ for the two conversion processes. In one case the process is matched for an up-converted wave traveling in the same direction of the signal, in green in Figure 5.13, while in the other case, in red in Figure 5.13, the up-converted wave travels in the opposite direction with respect to the signal. Indeed, the measurements of the frequency conversion amplitudes show the presence of

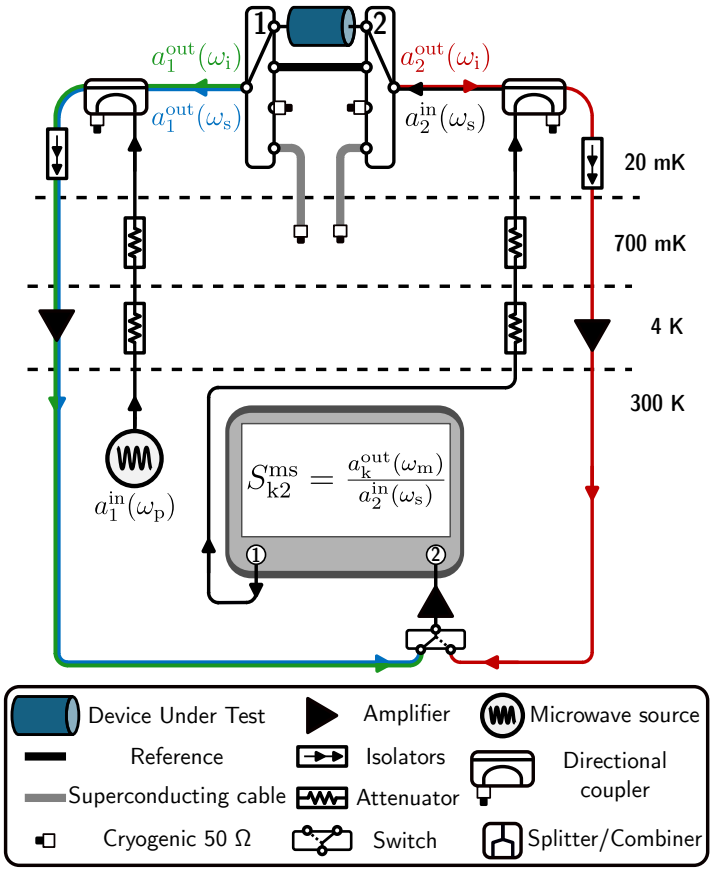

Figure 5.12: Simplified schematic of the experimental setup used for the nonlinear spectroscopy of the frequency conversion processes Only the relevant components and input/output lines used for the characterization of the two frequency conversion processes are shown. A pump tone $a_1^{\mathrm{in}}(\omega_\mathrm{p})$ is generated with a microwave source and sent to the sample in the opposite direction with respect to the VNA probe tone $a_2^{\mathrm{in}}(\omega_\mathrm{s})$. Measuring the response of the sample at the same frequency ω_s through the blue output line gives the signal transmission parameter S_{12}^{ss}. The VNA can also be set to perform frequency conversion measurements, *i.e.* the frequencies of its ports can be configured independently. Thus, by measuring the response of the sample, to the same input waves, at the up-converted frequency $\omega_\mathrm{u} = 2\omega_\mathrm{p} + \omega_\mathrm{s}$ we have access to the frequency conversion amplitude. The directional couplers allow to send the signal and the pump tones in opposite directions and to measure the frequency conversion amplitude at both ports of the sample. A detailed description of the full setup and calibration can be found in Chapter 3.

A better study of the two frequency conversion processes requires a device designed for such purpose

only one up-converted tone in each direction. We could perform such measurements thanks to the extension of the measurement bandwidth of the readout line described in Chapter 3. Unfortunately, the measurement bandwidth of the experimental setup does not allow for a proper

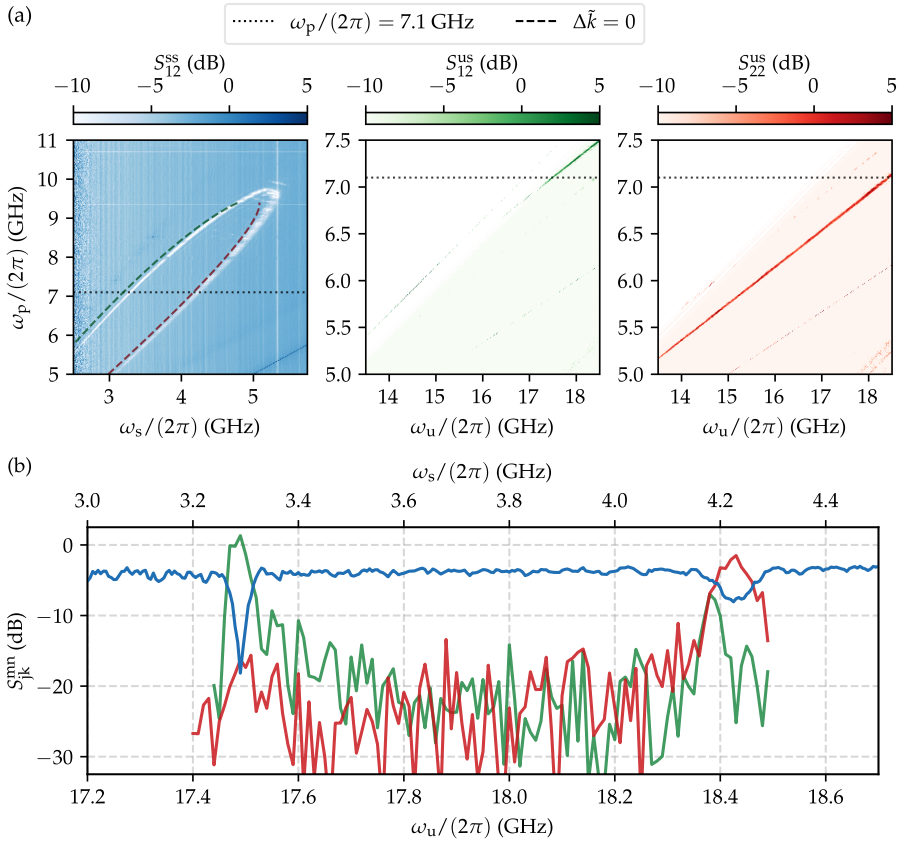

Figure 5.13: Pump frequency dependent isolation of a negative index Josephson waveguide
(a) Normalized signal attenuation, in blue, and co-propagating, in green, and counter-propagating, in red, frequency conversion amplitudes as a function of the pump and signal (sum) frequencies. Note the different scales on the y-axis. The latter and the top left white regions in the frequency conversion amplitude measurements are a consequence of the 3.5 to 18 GHz bandwidth of the experimental setup. The dashed lines corresponds to the phase-matching condition $\Delta\tilde{k} = 0$ for the co-propagating, in green, and counter-propagating, in red, processes. The dotted line correspond to the curves in (b) at $\omega_p/(2\pi) = 7.1$ GHz.
(b) Direct comparison of the normalized S_{jk}^{mn}-parameters, with the same color code as in (a), for a pump frequency of 7.1 GHz.

comparison[8], despite the improvements described in Chapter 3. For only one pump frequency the two conversion gains are measurable and even in this case they are at the edge of the bandwidth, as shown in Figure 5.13(b). However, the directionality of the two conversion processes is already clear from these measurements.

8 Note that the frequency conversion measurements are limited by both the low frequency cut-off of the setup, because they are normalized by the attenuation at the signal frequency, and by the upper one, because they are normalized by the gain at the sum frequency.

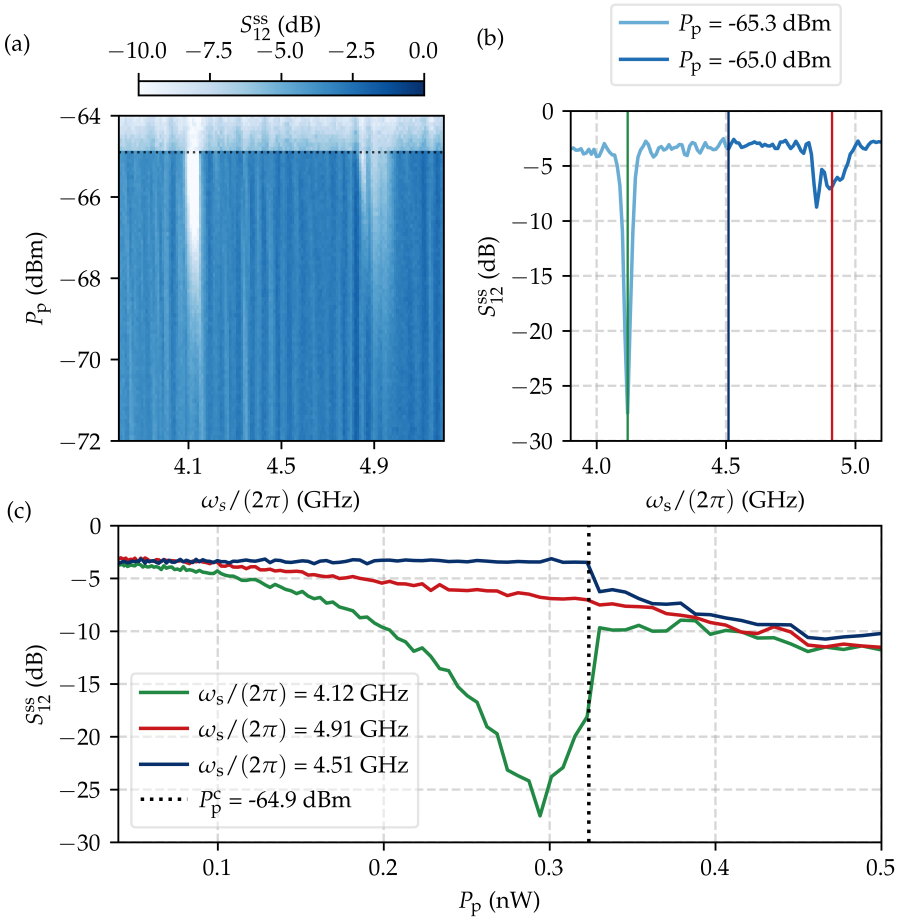

Figure 5.14: Pump power dependent isolation of a negative index Josephson waveguide
(a) Normalized signal attenuation as a function of the pump power and of the signal frequency for a pump tone with frequency $\omega_p = 8.5$ GHz.
(b) Optimal signal attenuation obtained with pump powers of -65.3 dBm for the co-propagating conversion process and of -65.0 dBm for the counter-propagating one as a function of the signal frequency. The vertical lines correspond to the frequencies shown in (c).
(c) Pump power dependence of the co-propagating and counter-propagating amplification processes at the phase-matching frequencies of 4.12 GHz and 4.91 GHz, respectively. The green line corresponds to the signal attenuation resulting from the co-propagating amplification process, while the red line represents the signal attenuation obtained from the counter-propagating one. The dark blue line shows the normalized transmission at a frequency where no process occurs, as reference. The dotted line corresponds to the critical power at which the transmission drops.

As discussed in Section 2.4 in Chapter 2, the propagation direction of the up-converted tone profoundly influences the dynamic of the processes. In particular, a different dependence as a function of the

power of the pump tone is expected. The measurement of the signal attenuation as a function of the pump power and the signal frequency is shown in Figure 5.14(a) for a pump frequency corresponding to 8.5 GHz. As the power of the pump increases two isolation gaps appear. The main differences between the two, besides the frequency, are the bandwidth and the magnitude of the attenuation, as can be easily seen in Figure 5.14(b). The difference in the magnitudes is even clearer from the power dependence of the attenuation at the phase-matching frequencies of the two conversion processes, $\omega_s = 4.12$ GHz and $\omega_s = 4.91$ GHz, shown in Figure 5.14(c). From the latter we can also appreciate the difference between the exponential and cosine scaling discussed in Section 2.4.3 in Chapter 2. The magnitude of the attenuation for the co-propagating case, represented by the green solid line, quickly increases as the product gl, corresponding to the conversion length, approaches $\pi/2$. Above that value full conversion is not achieved anymore and the attenuation lowers, until the pump power reaches the critical value P_p^c, which leads to the previously discussed device breakdown. The latter is highlighted by black dotted line and has been obtained by looking at the normalized transmission at a frequency between the to gaps, where no process occurs, as shown by the solid blue line. On the other hand the amount of attenuation obtained from the counter-propagating process scales exponentially and is limited by the length of the device.

5.4 CONCLUSIONS

This concludes this chapter where we described the experimental characterization of a LH JTL. This is, to the best of our knowledge, the first demonstration of a negative index material showing nonlinear interactions.

Indeed, the linear characterization of the device shows that its electrical length and attenuation decreases as the probe frequency increases. As a consequence, the device presents a low frequency cut-off at about 2.4 GHz. These are direct profs of its LH nature. Moreover, the nonlinear behavior of the device shows all the parametric process described in Chapter 2.

5.4.1 Key results

Exploiting the LH dispersion and the Josephson nonlinearity different parametric processes could be obtained and characterized:

A. First, broadband self-phase-matched amplification, which was theoretically proposed in [51], could be realized. Despite the low value of gain, these results paves the way to the realization

of a new type of Josephson TWPAs which does not rely on any dispersion [20] or nonlinear [84] engineering.

B. Then, we could achieve amplification of signal and idler modes propagating in opposite directions, which opens a new regime of parametric amplification within the superconducting circuits realm. In this case, values of gain as high as 35 dB could be obtained upon a careful tuning of the power of the pump tone. This process is of particular interest for the generation of spatially separated entangled states, which is the subject of the next chapter.

C. Finally, the LH dispersion allows for the phase-matching of two frequency conversion processes, which are of particular interest nowadays for isolation or frequency mixing purposes. A preliminary characterization of these two processes has been performed, with a focus on their different scaling with the power of the pump tone. The two type of frequency conversion, sinusoidal [123] and exponential [28], has been previously realized with RH topologies. The LH architecture greatly simplifies the phase-matching mechanics and offers the possibility to compare them within the same structure offering new opportunities to explore and harness these processes.

5.4.2 Perspectives and open questions

Naturally, being this the first realization of this type of device, it leaves us with a number of open questions and opportunities for further characterization, which, if answered or performed, could increase our understanding of the nonlinear dynamics taking place in this kind of structures.

A. First, the the co-propagating amplification process shows only few dB of gain, far from the requirements for real applications and from the theoretical prediction of C. Kow *et al.* [51]. The relatively short length of the investigated device could explain the observed low amount of achievable gain. However, the presence of other counter-propagating process, which is more efficient in drawing energy from the pump drive, as $g\ell$ approaches $\pi/2$, may limit the available pump power to fuel the co-propagating process. To properly model model such situation a model which takes into account both processes, *i. e.* five modes in total, would be of great help, and is under development. However, it is worth noticing that when probing one of the two processes, only noise is present at the input of the device at the phase-matched frequency of the other one. Therefore, a theoretical description accounting for the amplification of quantum vacuum fluctua-

tions may be required to answer the question if the two processes are limiting each other.

B. Then, a deeper understanding of the high power regime, with corresponding X-PARAMETER [106] or WRSPICE simulations, would be of great help to understand the interplay between the different processes and to answer the question if they are limiting each other.

C. Along the same line, high driving powers may activate other nonlinear processes, such as harmonics generation. A study of the latter, together with a comparison with a RH JTL, could be interesting. Indeed, higher harmonics generating should be suppressed in a LH JTL, as predicted in [51].

D. Moreover, the effect of disorder in the junctions and capacitors parameters could be taken into account and studied.

E. Finally, a characterization of other the device performances such as saturation and added noise has not been done. Indeed, this requires the realization of devices optimized for a given application.

In general, future efforts could point towards the improvement of the design and performances depending of the process of interest, which would strongly benefit from the aforementioned studies.

6 ENTANGLED PHOTON PAIRS GENERATION

Entanglement is one of the most intriguing manifestation of quantum mechanics. It is a property of a composite system in which correlations between its subsystems cannot be explained classically [124]. Nowadays, it is at the core of several quantum technologies with applications ranging from imaging [125], communication [126], information processing [70], computation [127], and metrology [128].

An example of entangled states of light are two-mode squeezed vacuum states, in which quantum correlations are present between the four quadratures describing the system. This is equivalent to the generation of entangled pairs of photons in the two modes. A common experimental tool to realize squeezed vacuum states relies on parametric interactions, where coherent pair superpositions can be generated out of a classical pump [61]. Harnessing the quadratic, $\chi^{(2)}$, or cubic, $\chi^{(3)}$, susceptibilities of nonlinear materials it has been possible to generate entangled photon states, in the optical domain, through spontaneous parametric down-conversion or amplification processes.

In an analogous way, microwave quantum optics experiments can be performed using Josephson metamaterials. In particular, generation of single- and two-mode squeezed microwave radiation has been demonstrated both with resonant [79, 80, 129] and traveling-wave Josephson parametric amplifiers [22–24].

Here, we will first give a brief overview on broadband two-mode squeezing generation with Josephson TWPAs. Then, we will describe the link between 4WM parametric amplification and squeezing generation, and the quantities one needs to look at to characterized such nonclassical state of light. Finally, we will demonstrate the flexibility of JTLs with LH topology as sources of entangled radiation by reporting about the measurements of both co- and counter-propagating signal and idler entangled modes. The latter represent the first experimental investigation, to the best of our knowledge, of the quantum properties of a negative index material.

6.1 QUANTUM OPTICS WITH JOSEPHSON WAVEGUIDES

As described in Chapter 2, Josephson TWPAs are artificial nonlinear materials which are well-established tools for near quantum-limited

broadband amplification of weak microwave signals [20, 83, 84]. Moreover, they have recently attracted a lot of attention in the framework of microwave broadband isolation [26–28]. However, their potential extends beyond these applications. When used as parametric amplifiers, Josephson waveguides can imprint nonclassical correlations between the propagating signal and idler modes. Thus, Josephson TWPAs present themselves as natural sources of broadband two-mode squeezed vacuum states, which are state naturally produced from the parametric amplification of input vacuum fluctuations [32].

Microwave sources of two-mode vacuum squeezed radiation are of primarily interest for a wide range of applications such as quantum sensing and enhanced detection [71, 130, 131], quantum teleportation [132], quantum information with continuous variables [133–135] and for most recently proposed microwave quantum radar and illumination schemes [136–139]. The latter employ two-mode entangled radiation to improve the efficiency of target detection and would greatly benefit from spatial separation of the two signal and idler modes. Moreover, the broadband nature of TWPAs, compared to resonant amplifiers, allows for higher flexibility in the generation of entangled multipartite cluster states, as recently demonstrated [25], which are necessary tools for continuous variables quantum information.

In general, traveling-wave structures offer other advantages, such as larger bandwidth and higher power handling performances, compared to their resonant counterparts. However, there are also some challenges that need to be addressed, starting from loss reduction[1], phase-matching of the desired process, and mitigation of higher harmonics and intermodulation products. All these, will limit the amount of two-mode squeezing, and entanglement, achievable. Indeed, a high amount of two-mode squeezing of about 7 dB below vacuum was obtained with Josephson TWPAs only with a 4WM double-pumped scheme [24]. While, single pump configurations remain limited to 3 dB squeezing below vacuum [22, 23]. These performances are not comparable with what is usually achieved at optical frequencies [140, 141] or with resonant microwave parametric amplifiers [72, 80]. Understanding the current limitations is crucial to design efficient sources of entangled photons in the microwave domain with TWPAs.

In the following we might omit to specify that squeezing and entanglement happens between two modes, but it will always be the considered case

In the following, we will report about the measurements of two-mode vacuum squeezing generated by a LH Josephson waveguide. The main focus will be on the generation of counter-propagating entangled photon states, achieved exploiting the amplification process of signal and idler modes traveling in opposite directions, theoretically and experimentally described in Chapter 2 and in Chapter 5, respectively. However, we will show that the device is also capable of generating co-propagating two-mode squeezing, as in [22–24]. Besides paving the

1 It is worth noticing, that the recent results reported in [93, 98], paved the way to the realization of low-intrinsic-loss Josephson TWPAs.

way for future technological applications, comparing the performances of the two processes gives information which might help in developing a better understanding of squeezing generation in Josephson TWPAs.

Before jumping into the experimental results, let us give a simple and brief theoretical description for the generation of two-mode vacuum squeezed microwave radiation out of a Josephson parametric amplifier. For the sake of simplicity we will make a couple of approximations:

A. Rotating wave approximation, by retaining only the terms at the pump, signal and idler frequencies of interest.

B. Lossless line, which, however, can be included considering a beam splitter model [22].

C. Strong classical pump, by writing the pump operator as a coherent state $\hat{a}_{\mathrm{p}} \mapsto |A_{\mathrm{p}}| e^{i\phi_{\mathrm{p}}}$.

D. Perfect phase-matching, by considering the ideal case in which $\Delta\tilde{k} = 0$.

We refer to [73, 142–145] for a more detailed description of a quantum theory describing the input–output properties of Josephson traveling wave parametric amplifiers.

6.1.1 Two-mode squeezing with a parametric amplifier

The main experimental systems to generate squeezed vacuum states rely on nonlinear systems where coherent pair superpositions can be generated out of a classical pump. These kind of processes can occur in materials with $\chi^{(2)}$ or $\chi^{(3)}$ nonlinearity via parametric down-conversion or amplification [32]. Here we are interested in the latter, where two photons from the pump tone are converted into two photons in the signal and idler modes, whose frequencies are thus symmetric around the pump one.

Such nonlinear interaction can be obtained in Josephson metamaterials thanks to the presence of Josephson junctions and it can be described by an effective Hamiltonian which, in the rotating frame, takes the form [96]:

$$\hat{H}_{4WM} \sim g_4 \left(a_{\mathrm{p}}^2 \hat{a}_{\mathrm{s}}^\dagger \hat{a}_{\mathrm{i}}^\dagger + h.c \right) \sim g_4 \left(|A_{\mathrm{p}}|^2 \hat{a}_{\mathrm{s}}^\dagger \hat{a}_{\mathrm{i}}^\dagger e^{i2\phi_{\mathrm{p}}} + h.c \right), \tag{6.1}$$

where $\hat{a}_{\mathrm{m}}$, with $\mathrm{m} = \{\mathrm{s,i}\}$, represent the signal and idler mode operators, $a_{\mathrm{p}} = |A_{\mathrm{p}}| e^{i\phi_{\mathrm{p}}}$ is the coherent classical pump driving the process, and g_4 is the 4WM nonlinear interaction strength.

The input and outputs relations associated with the above interaction Hamiltonian can be obtained using a squeezing transformation by defining the two-mode squeezing operator:

$$\hat{S}(r, \phi) = \exp \left(\xi \hat{a}_{\mathrm{s}}^\dagger \hat{a}_{\mathrm{i}}^\dagger + h.c \right), \tag{6.2}$$

COEFFICIENT	CO-PROPAGATING	COUNTER-PROPAGATING
s_{ss}	$\cosh(\beta\ell)$	$1/\cos(\beta\ell)$
s_{si}	$e^{i2\phi_p}\sinh(\beta\ell)$	$e^{i2\phi_p}\tan(\beta\ell)$

Table 6.1: Scattering coefficients of the amplification processes
Definition of the scattering coefficients for both co- and counter-propagating amplification processes, obtained from **??** and **??** derived in Chapter 2, respectively. Note that for the sake of simplicity we are neglecting losses and considering the case of perfect phase-matching.

where $\xi = re^{i\phi}$ is the squeezing parameter, with r and ϕ related to the amplitude gain $\sqrt{G}$ of the parametric amplifier[2] and to the phase ϕ_p of the pump tone, respectively. These connections become clear by computing the scattering relations given by $\hat{S}(r,\phi)$:

$$\begin{cases} \hat{a}_{s,out} = \hat{S}^\dagger \hat{a}_{s,in}\hat{S} = \cosh(r)\hat{a}_{s,in} + e^{i\phi}\sinh(r)\hat{a}^\dagger_{i,in}, \\ \hat{a}^\dagger_{i,out} = \hat{S}^\dagger \hat{a}^\dagger_{i,in}\hat{S} = e^{-i\phi}\sinh(r)\hat{a}_{s,in} + \cosh(r)\hat{a}^\dagger_{i,in}, \end{cases} \tag{6.3}$$

Indeed, in Chapter 2 we derived the scattering relations between input and output waves describing the amplification processes in a LH JTL:

$$\begin{cases} a_{s,out} = s_{ss}a_{s,in} + s_{si}a^*_{i,in}, \\ a^*_{i,out} = s_{is}a_{s,in} + s_{ii}a^*_{i,in}, \end{cases} \tag{6.4}$$

where $s_{ss} = s^*_{ii}$ and $s_{is} = s^*_{si}$ are given in Table 6.1 for both the co- and counter-propagating amplification processes[3]. Such relations are the usual ones of a phase-preserving amplifier, where $s_{ss} = \sqrt{G}$ and $s_{si} = e^{i\phi}\sqrt{G-1}$ [30]. Therefore, we can relate r and ϕ to the gain G of our parametric amplifier and to the pump phase ϕ_p through:

$$\cosh(r) = \sqrt{G} = \begin{cases} \cosh(\beta\ell) & \text{if co-propagating,} \\ 1/\cos(\beta\ell) & \text{if counter-propagating,} \end{cases} \tag{6.5}$$
$$\text{and} \quad \phi = 2\phi_p.$$

The state generated by the amplifier can be obtained by applying the two-mode squeezing operator to the signal and idler vacuum state:

$$|TMS\rangle = \hat{S}\,|0\rangle_s\,|0\rangle_i = \frac{1}{\cosh(r)}\sum_{n=0}^{\inf} e^{in\phi}\tanh(r)^n\,|n\rangle_s\,|n\rangle_i\,. \tag{6.6}$$

2 and thus to the power of the pump tone
3 Here, the a_m correspond to the one derived in Section 2.3 in Chapter 2 up to a frequency dependent normalization factor [29, 90].

The latter is a superposition of twin Fock states. Thus, excitations are created coherently from vacuum and the squeezing occurs in the composite system formed by the signal and idler modes, with an average number of photons in each mode given by:

$$\langle TMS|\, \hat{a}^{\dagger}_{\mathrm{s,out}}\hat{a}_{\mathrm{s,out}}\, |TMS\rangle = \langle TMS|\, \hat{a}^{\dagger}_{\mathrm{i,out}}\hat{a}_{\mathrm{i,out}}\, |TMS\rangle = \sinh(r)^2, \quad (6.7)$$

which is equal to $G-1$.

This state is a quantum state of light [69] with correlations between the two modes which cannot be explained classically. Therefore, let us now see how to describe and quantify these correlations.

6.1.2 Quantifying quantum correlations

A quantum state of light can be described through quasi-probability distributions in phase-space, such as the Wigner function [146]. In particular, the two-mode squeezed state introduced above falls into the class of Gaussian states, for which their Wigner function is a gaussian [70]. It is useful to characterized a two-mode squeezed state by studying correlations between the quadratures:

$$\begin{cases} \hat{x}_{\mathrm{s,i}} = \frac{\hat{a}_{\mathrm{s,i}}+\hat{a}^{\dagger}_{\mathrm{s,i}}}{2}, \\ \hat{p_{\mathrm{s,i}}} = \frac{\hat{a}_{\mathrm{s,i}}-\hat{a}^{\dagger}_{\mathrm{s,i}}}{2i}, \end{cases} \quad (6.8)$$

and to define the quadratures vector $\hat{\mathbf{r}}^T = (\hat{x}_{\mathrm{s}}, \hat{p}_{\mathrm{s}}, \hat{x}_{\mathrm{i}}, \hat{p}_{\mathrm{i}})$. Indeed, Gaussian states are completely determined by the first and second order moments of those quadrature operators, *i.e.* by $\langle \mathbf{r} \rangle$ and by the covariance matrix σ. The elements of the latter are given by [22, 147]:

Here we are using the convention that the covariance matrix of the two-mode vacuum is the identity $\mathbb{1}_4$

$$\sigma_{\mathrm{jk}} = 4\left(\frac{1}{2}\langle r_{\mathrm{j}} r_{\mathrm{k}} + r_{\mathrm{k}} r_{\mathrm{j}}\rangle - \langle r_{\mathrm{j}}\rangle\langle r_{\mathrm{k}}\rangle\right), \quad (6.9)$$

One way of quantifying quantum nature of the output state generated by the parametric amplification process consists in comparing its variance to the two-mode vacuum's one. Otherwise, one can perform a quantitative estimation of the entanglement between the two modes by computing the logarithmic negativity $E_{\mathcal{N}}$ [148]. The former method helps us evaluating the squeezed nature of the state, while the latter tells us, for a bipartite system, the amount of entanglement between the two subsystems.

QUANTIFYING SQUEEZING Given that we are dealing with two-mode processes, the correlations appears between the four, previously defined, quadratures. Therefore, to evaluate the amount of squeezing it is useful to define the collective quadratures:

$$\begin{aligned} \hat{x}_{\pm} &= \hat{x}_{\mathrm{s}} \pm \hat{x}_{\mathrm{i}}, \\ \hat{p}_{\pm} &= \hat{p}_{\mathrm{s}} \pm \hat{p}_{\mathrm{i}}, \end{aligned} \quad (6.10)$$

whose variances are given by:

$$\begin{aligned}\langle \hat{x}_{\pm}^2 \rangle &= \frac{1}{2}\left[\cosh(2r) \pm \cos(\phi)\sinh(2r)\right], \\ \langle \hat{p}_{\pm}^2 \rangle &= \frac{1}{2}\left[\cosh(2r) \mp \cos(\phi)\sinh(2r)\right].\end{aligned} \tag{6.11}$$

Comparing their variances to the one of vacuum:

$$\mathrm{Sq}_{\langle \hat{r}_{\pm}^2 \rangle} = 10\log_{10}\left(\frac{\langle \hat{r}_{\pm}^2 \rangle}{0.5}\right) \quad \text{with} \quad \hat{r} = \{\hat{x}, \hat{p}\}, \tag{6.12}$$

we can compute the amount of two-mode squeezing below vacuum in dB.

QUANTIFYING ENTANGLEMENT The second way to quantify the non-classicality of the state relies on a quantitative estimation of the entanglement between the two modes through the logarithmic negativity $E_{\mathcal{N}}$. The positivity of the logarithmic negativity implies that the state is entangled [148, 149].

To compute $E_{\mathcal{N}}$ we can start by writing the covariance matrix in terms of four 2×2 block matrices:

$$\sigma = \begin{pmatrix} A & C \\ C^{\mathrm{T}} & B \end{pmatrix}, \tag{6.13}$$

where the diagonal elements correspond to the single-mode covariance matrices and the off diagonal ones represent the correlations between the two modes. In our case, using Equation 6.9 we have $A = B$ and $C = C^T$, which take the form:

$$\begin{aligned} A &= \begin{pmatrix} \cosh(2r) & 0 \\ 0 & \cosh(2r) \end{pmatrix}, \\ C &= \begin{pmatrix} \cos(\phi)\sinh(2r) & \sin(\phi)\sinh(2r) \\ \sin(\phi)\sinh(2r) & -\cos(\phi)\sinh(2r) \end{pmatrix}, \end{aligned} \tag{6.14}$$

Then, we compute the minimum symplectic eigenvalue of the partially transposed covariance matrix:

$$\nu_- = \sqrt{\frac{\Delta\sigma - \sqrt{(\Delta\sigma)^2 - 4\det\sigma}}{2}}, \tag{6.15}$$

where $\Delta\sigma = \det A + \det B - 2\det C$. Finally, the logarithmic negativity is given by:

$$E_{\mathcal{N}} = \mathrm{Max}[-\ln(\nu_-), 0], \tag{6.16}$$

where, for an ideal two-mode squeezed state, with no loss and perfect phase-matching, we have $\nu_- = e^{-2r}$.

INCLUDING LOSSES Until now, we have consider the ideal lossless case. However, the presence of losses will degrade both the amount of squeezing and entanglement. A simple way to take into account for the modes losses consists in considering the presence of two beam splitters, with transmission coefficients $\eta_{s,i} \leq 1$, acting on the signal and idler fields, independently, after the amplifier [96, 143].

The case $\eta_{s,i} = 1$ correspond to the lossless scenario

6.2 MEASURING TWO-MODE VACUUM SQUEEZING

As described in the previous section the two-mode squeezing state arises from the presence of a strong pump tone, with frequency $\omega_p/(2\pi)$, which leads to the generation of entangled pairs of photons in the signal and idler modes when the parametric amplification process is frequency and phase-matched. We recall here that the LH Josephson waveguide, described in Chapter 5, for a given pump frequency, shows both amplification of co- and counter-propagating signal and idler modes. We will focus on the latter in this section.

This experiment would not have been possible wihout the help of Gwenael Le Gal. He worked on the "squeezing setup" and on the measurements and analysis scripts for the past 2 years making them reliable and "easily" usable. So, kudos to Gwen !

Quantum correlations are present between the components of the quadratures vector $\mathbf{r}$, defined in the previous section. Hence, to measure such entangled state we need to simultaneously record the quadratures $\hat{x}$ and $\hat{p}$ at the signal and idler frequencies of interest $\omega_{s,i}/(2\pi)$, as depicted in Figure 6.1(a). It is worth mentioning that measuring the presence of entanglement between two counter-propagating modes requires two output lines, one connected to the input and one to the output of the device, as schematically shown in Figure 6.1(b). Moreover, the frequencies involved, especially the counter-propagating idler[4], which exceeds 13 GHz, required the development of the "high-frequency" output line, described in Chapter 3.

6.2.1 Experimental setup

To perform these measurements the VNA used for the device linear and nonlinear characterization, described in Chapter 5, has been replaced by a FPGA-based module supported by a up- and down-conversion stage[5], as schematically depicted in Figure 6.1(b). This setup allows, on one side, to generate and up-convert the pump tone and, on the other side, to down-convert, digitized and demodulate the output signals to record the two I and Q quadratures of the electromagnetic field at the frequencies of interest [35]. A more detailed description of

4 We refer to Chapter 5 for a more detailed characterization of the frequency dependence of the counter-propagating amplification process.

5 For this experiment we used a Quantum Machines OPX+ plus Octave system, however previous ones [22] relied on a multi-channel Xilinx RF System-on-Chip (RFSoC) acquisition board as described in [96]

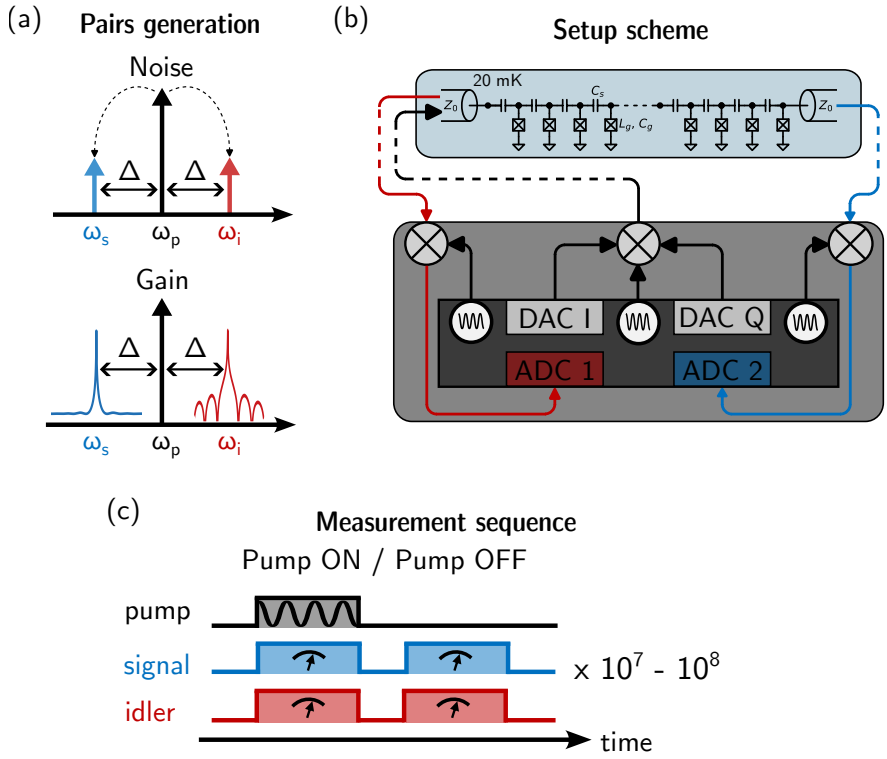

Figure 6.1: Schematic of the generation and detection process for the counter-propagating two-mode vacuum squeezing experiment
(a) Schematic of the spontaneous pairs generation process. We apply a coherent state with a given pump frequency ω_p and signal-idler pairs of entangled photons are generated when the frequency, $2\omega_p = \omega_s + \omega_i$, and phase-matching conditions, $2(k_p + \alpha_p) = k_s + \alpha_s + k_i + \alpha_i$, are satisfied. Driving also the signal mode leads to the amplification processes described in Section 5.3.1.
(b) Simplified schematic of the experimental setup used to detect the entangled microwave radiation. To so so we used a FPGA-based module supported by an up- and down-conversion stage and the radiation emitted at both the input and output of the device is measured simultaneously. A detailed description of the full setup and calibration can be found in Chapter 3.
(c) Measurement sequence for the generation and detection of the entangled pairs of photons. It consists of an ON/OFF cycle depending on the presence of the pump pulse. The OFF measurement gives the noise background. Each cycle is repeated 10^7 or 10^8 times.

the experimental setup and of the generation and acquisition steps is given in Chapter 3.

The on and off measurements are interveled in order to avoid gain drifts

A typical measurement sequence is depicted in Figure 6.1(c). It consists of a pump on/pump off cycle, the interaction is active when the pump in present, while the measurement with the pump off gives the noise background of the detection chain. During each on/off step

the four signal and idler quadratures $X_{s,i}$ and $P_{s,i}$ are recorded using a fast heterodyne detection scheme based on the FPGA module [35]. This sequence is repeated 10^7 or 10^8 times.

Using the same setup it is also possible to measure the gain of the device by adding a weak tone at the signal frequency and measuring its amplitude at the output by using the two-step demodulation described above. Performing the same measurement with the pump off gives the reference to compute the gain.

6.2.2 Quadratures measurements and calibration

Using the heterodyne detection scheme, briefly discussed above, we experimentally measure the four quadratures:

$$\begin{cases} \hat{X}_{s,i} = \frac{1}{2}(\hat{A}_{s,i} + \hat{A}^{\dagger}_{s,i}), \\ \hat{P}_{s,i} = \frac{1}{2i}(\hat{A}_{s,i} - \hat{A}^{\dagger}_{s,i}), \end{cases} \tag{6.17}$$

where $\hat{A}_{s,i}$ are bosonic output field operators given by [22, 35]:

One can neglect the -1 in the square root, considering $G_{s,i} \gg 1$

$$\hat{A}_{s,i} = \sqrt{G^{sys}_{s,i}}\hat{a}_{s,i} + \sqrt{G^{sys}_{s,i} - 1}\hat{h}_{s,i} \tag{6.18}$$

which takes into account the thermal uncorrelated noise added by the amplification chain, through the bosonic operators $\hat{h}_{s,i}$. Note that the indexes s and i means that these quantities are evaluated at the signal or idler frequencies, respectively.

In practice, we pump the device at a frequency $\omega_p/(2\pi)$ and measure the quadratures at the signal and idler frequencies $\omega_{s,i}/(2\pi) = \omega_p/(2\pi) \mp \Delta$. Here, Δ is set by the frequency and phase-matching conditions such that the detection frequencies $\omega_{s,i}/(2\pi)$ fall within the amplification bandwidth of the device, as schematically depicted in Figure 6.1(a). The output signal is down-converted and then digitized using the ADCs, with a typical acquisition time, τ_{acq}, of $6\,\mu s$. Then, the signals are demodulated. Thus, four raw quadratures $X^{raw}_{s,i}$ and $P^{raw}_{s,i}$ are acquired in unit of volts. As stated before, we repeat the quadrature acquisition N_{acq} times, with both the pump off and the pump on. The acquired raw quadratures are expressed in unit of square root of photons at the signal and idler frequencies using the following conversion factor:

$$\gamma_{s,i} = \sqrt{\frac{\tau_{acq}}{Z_0 \hbar \omega_{s,i}}}, \tag{6.19}$$

and normalized by the system gain at the signal and idler frequencies to obtain their value at the output of the sample:

$$r_{s,i} = \gamma_{s,i} \frac{R^{raw}_{s,i}}{\sqrt{G^{sys}_{s,i}}}, \tag{6.20}$$

where $R^{\text{raw}}_{\text{s,i}} = \left\{X^{\text{raw}}_{\text{s,i}}, P^{\text{raw}}_{\text{s,i}}\right\}$. Again, a careful calibration of G_{sys} is necessary for quantitative estimation of the amount of entanglement and squeezing.

Following the above procedure we record 6 two-dimensional quadrature histograms for both the pump on and pump off measurements [79]. By taking the difference between the two we obtained 6 quadratures phase-space distributions. One example of the latter is shown in Figure 6.2 for a pump tone with frequency $\omega_{\text{p}}/(2\pi) = 9$ GHz and power $P_{\text{p}} = -68.9$ dBm. The on/off histograms are obtained with 10^7 acquisitions at the signal and idler frequencies $\omega_{\text{s}}/(2\pi) = 3.834$ GHz and $\omega_{\text{i}}/(2\pi) = 14.166$ GHz, respectively.

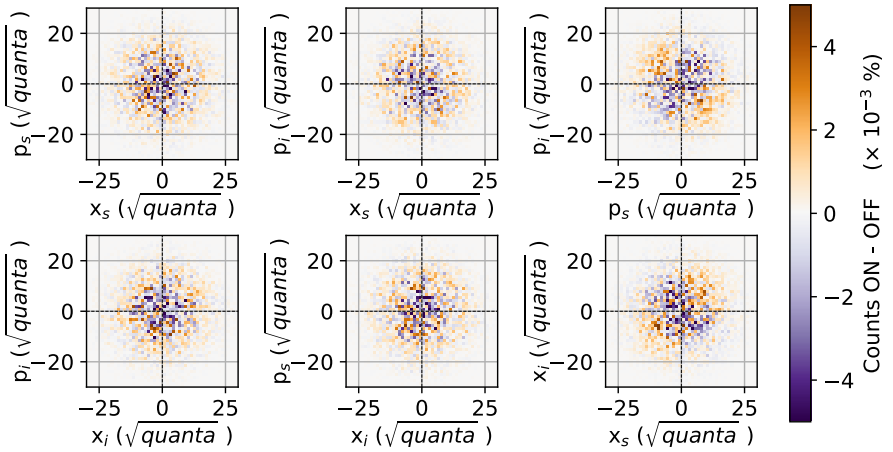

Figure 6.2: Quadratures phase space distribution of two counter-propagating modes
Quadratures phase space distribution given by the difference between the pump on and pump off histograms obtained with 10^7 acquisitions. The pump tone frequency and power are $\omega_{\text{p}}/(2\pi) = 9$ GHz and $P_{\text{p}} = -68.9$ dBm, respectively. The signal and idler modes have been measured at the frequencies $\omega_{\text{s}}/(2\pi) = 3.834$ GHz and $\omega_{\text{i}}/(2\pi) = 14.166$ GHz, respectively. The quadratures corresponding to the idler mode have been measured at the input of the device with respect to the pump, while the signal's ones have been measured at its output.

In the first four panels (x_{s}, p_{s}), (x_{i}, p_{i}), (x_{s}, p_{i}) and (x_{i}, p_{s}) we can observe an isotropic increase of the noise due to amplification, while the last two phase spaces (x_{s}, x_{i}) and (p_{s}, p_{i}) show an anisotropic expansion, which indicates the presence of correlations between the two counter-propagating modes.

From these quadratures distributions, the covariance matrices corresponding to the pump on and pump off measured distributions can be calculated. Assuming that the noise added by the detection chain

is thermal and uncorrelated with the one emitted by the device, the two covariance matrices take the form [22, 147]:

$$\begin{aligned}\sigma_{on} &= \sigma_{TMS} + \sigma_{th} + \mathbb{1}_4,\\ \sigma_{off} &= \sigma_{vac} + \sigma_{th} + \mathbb{1}_4 = \sigma_{th} + 2\mathbb{1}_4,\end{aligned} \tag{6.21}$$

where σ_{th} is the covariance matrix associated to the thermal noise added by the detection chain, σ_{vac} is the covariance matrix of the vacuum state emitted by the amplifier when the pump is off, which is equal to the 4×4 identity matrix $\mathbb{1}_4$. Thus, the covariance matrix representing the two-mode squeezed state can be computed as:

$$\sigma_{TMS} = \sigma_{on} - \sigma_{off} + \mathbb{1}_4. \tag{6.22}$$

The covariance matrix σ_{TMS} inferred from the measured quadratures reported in Figure 6.2 is shown in Figure 6.3. The diagonal elements

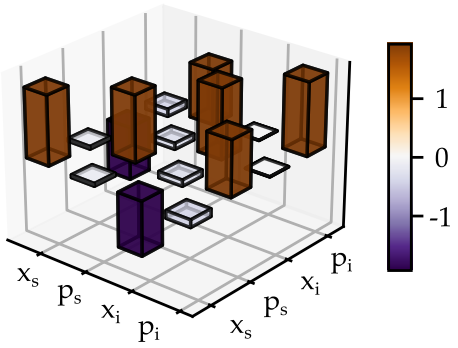

Figure 6.3: Covariance matrix of two counter-propagating modes
Covariance matrix computed from the quadratures shown in Figure 6.2 and following the procedure discussed in the text in Equation 6.22.

represent the variances of the amplified vacuum fluctuations of each single mode, while the off-diagonal elements demonstrate the presence of correlations between the signal and the counter-propagating idler mode. Now, to demonstrate whether these correlations are classical or not further analysis is needed.

6.3 ENTANGLEMENT GENERATION IN A NEGATIVE INDEX JOSEPHSON WAVEGUIDE

The demonstration of broadband two-mode entanglement generation in Josephson waveguides in both 3WM [23] and 4WM [22] devices paved the way towards the generation of more complex multimode entangled states using Josephson TWPAs [25]. All those realizations are based on JTLs with a RH topology.

At first, we will demonstrate that a LH Josephson waveguide can be used for the same purpose, by leveraging the amplification process of co-propagating signal and idler modes. The LH topology greatly simplifies the operation of the device given its self-phase-matching mechanism [51], described in **??** in Chapter 2.

Moreover, we will report about the generation of entanglement between modes that are spatially separated, which is enabled by the parametric amplification process of counter-propagating signal and idler modes, described in Section 2.3 in Chapter 2.

The focus will mainly be on the latter because it represent a novel paradigm for the generation of multimode entanglement with Josephson TWPAs. Note that all these findings have been obtained using the device presented in Chapter 5.

6.3.1 Entanglement between two counter-propagating traveling modes

Exploiting nonlinear waveguides as sources of counter-propagating two-photon states presenting quantum correlations is a longstanding, but still active, field of research within the optical domain [82, 150–152]. Here, we will describe the realization of such source in the microwave range. Although two-mode squeezing of microwave radiation in spatially separated modes has already been demonstrated in non-degenerate resonant amplifiers [80], our implementation relies on a traveling-wave structure, opening new perspectives for the realization of broadband versatile squeezers of microwave radiation.

As discussed in the previous sections, by driving the device with a coherent tone at frequency $\omega_p/(2\pi)$ an entangled state between two signal and idler modes propagating in opposite direction is generated. For a specific pump frequency, the frequencies of the two entangled modes are given by the counter-propagating amplification process frequency and phase-matching conditions. From the characterization with continuous waves, discussed in Section 5.3.1 in Chapter 5, the signal and idler frequencies, at which the process is matched, can be identified.

Here, we will describe measurements obtained for two different pump frequencies: 8.5 GHz and 9 GHz. The corresponding signal and idler ones are given in Table 6.3. We stress that in both cases the two modes, besides being spatially separated, are also detuned in frequency by about 10 GHz, an order of magnitude in energy. Thus, to be able to measure at the idler frequencies of interest we used the "high-frequency" output line described in Chapter 3.

PUMP POWER DEPENDENCE The amount of squeezing and entanglement between the signal and idler modes depends on the parametric gain of the amplifier and, therefore, on the power of the pump tone.

$\omega_p/(2\pi)$ (GHz)	$\omega_s/(2\pi)$ (GHz)	$\omega_i/(2\pi)$ (GHz)	T_s^{sys} (K)	T_i^{sys} (K)	η_s (%)	η_i (%)
8.5	3.59	13.41	17	18	1	1
9.0	3.834	14.166	8	28	0.5	2

Table 6.2: Pump, signal and idler frequencies, measurement efficiencies and system noise temperatures for the counter-propagating squeezing measurements
Values of the pump, signal and idler frequencies, measurement efficiencies and system noise temperatures at which the quadratures distributions, used to evaluate two-mode squeezing and entanglement for the counter-propagating process, have been measured.

Thus, to identify the optimal operating point, the device performances has a function of the pump power have been measured, and are shown in Figure 6.4. For each pump power point we rotate the acquired quadratures and find the optimal phase that minimizes the two-mode squeezing in the x_+ collective quadrature [24].

Each point corresponds to 10^7 acquisitions. For both pump frequencies, we observe squeezing below vacuum and positive logarithmic negativity, demonstrating the nonclassical nature of the generated state. As the gain increase, the values of both quantities grow approximately until the device transmission drops. However, it is hard to quote a number from these measurements because of the high fluctuations. The latter are probably due to the poor measurement efficiency of our detection chain, which is defined as [24]:

$$\eta = \frac{\hbar\omega}{2k_B T_\omega^{sys}}, \tag{6.23}$$

where k_B and $\hbar$ are the Boltzmann and the reduced Planck constants, respectively, and T_ω^{sys} is the system noise temperature at the frequency $\omega/(2\pi)$. The values of $\eta_{s,i}$ at the frequencies of interest are reported in Table 6.3, together with the system noise temperature ones, obtained from the output line calibration, discussed in Chapter 3. Such low values are understandable given that the signal mode is measured at the lower edge of the experimental setup bandwidth, while the idler mode is measured at frequencies above 10 GHz. Moreover, in both cases we are not using a near quantum-limited amplifier, which are not available, at the moment, for frequencies as high as the idler ones[6].

We recall here that we are using two different output lines, one for the signal and one for the idler

PUMP PHASE DEPENDENCE In order to reduce the aforementioned fluctuations and properly evaluate the amount of squeezing below

6 This is one of the reasons which brought us to start the development of a Josephson TWPA operating in the Ku-band, which has been carried out in close collaboration with Silent Waves and whose preliminary results are reported in Chapter 7.

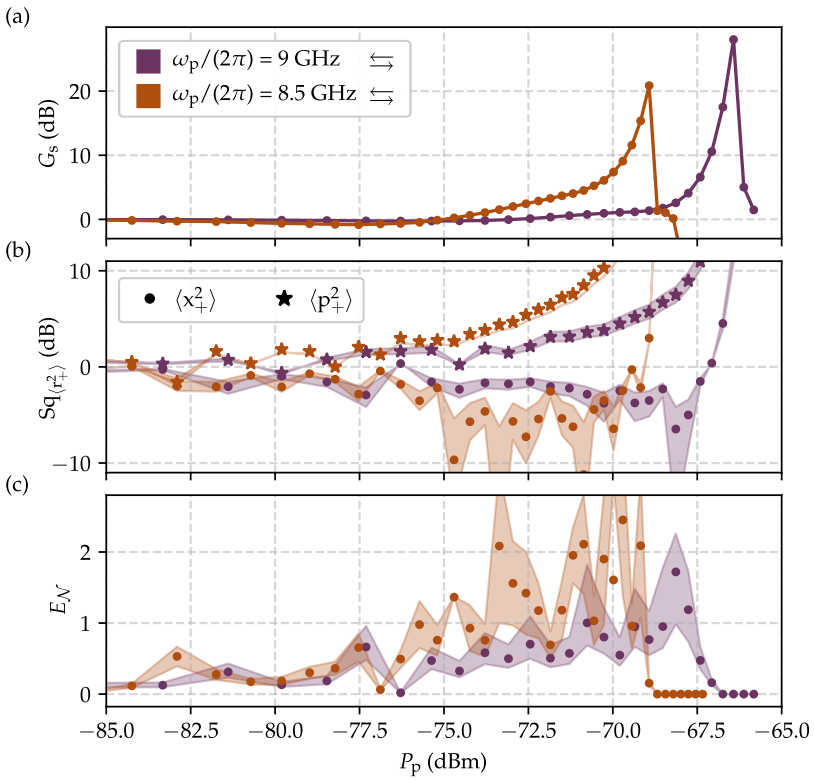

Figure 6.4: Pump power dependence of counter-propagating squeezing and logarithmic negativity
(a) Signal gain, normalized with the pump off measurement, as a function of the pump power for the counter-propagating amplification process, obtained pumping the device at 8.5 GHz, brown data, and 9 GHz, purple ones. The corresponding signal and idler frequencies are given in Table 6.3.
(b) Squeezing, dots, and anti-squeezing, stars, of the collective quadratures obtained from 10^7 acquisitions as a function of pump power for the same configurations as in (a). The shaded area correspond to the systematic error obtained considering and error of ± 1 dB on the system gain.
(c) Logarithmic negativity obtained from 10^7 acquisitions as a function of pump power for the same configurations as in (a). The shaded area correspond to the systematic error obtained considering and error of ± 1 dB on the system gain.

vacuum and entanglement, we measured their dependence has a function of the pump phase performing 10^8 acquisitions per point. Note that to take into account for possible drifts of the system gain we divided the 10^8 acquisitions in 10 sets of 10^7 acquisitions, and performed the output line calibration right before each set.

The pump phase dependence of the collective x_+ quadrature is shown in Figure 6.5(a) for two different pump frequencies. Varying the pump phase allows to control the amount of squeezing below vacuum. We found an optimal value of about -5^{+2}_{-4} dB when driving the device with a pump at 9 GHz with -68.5 dBm of input-referred

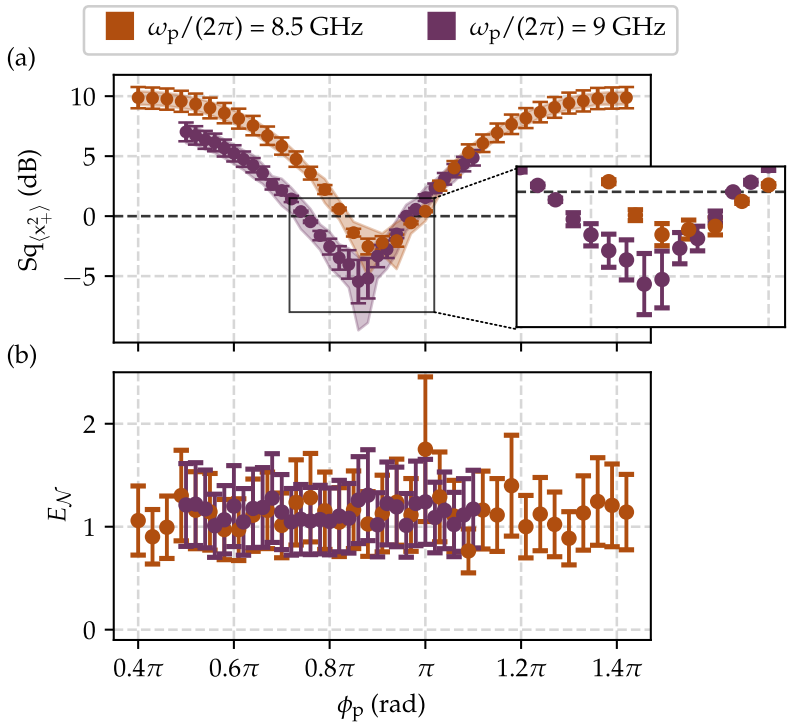

Figure 6.5: Pump phase dependence of squeezing and logarithmic negativity
(a) Squeezing of the collective x_+ quadrature and (b) logarithmic negativity as a function of the pump phase ϕ_p for the pump frequencies $\omega_p/(2\pi) = 8.5$ GHz in brown (with signal and idler pairs measured at $\omega_s/(2\pi) = 3.59$ GHz and $\omega_i/(2\pi) = 13.41$ GHz, respectively) and $\omega_p/(2\pi) = 9$ GHz in purple (with signal and idler pairs measured at $\omega_s/(2\pi) = 3.834$ GHz and $\omega_i/(2\pi) = 14.166$ GHz, respectively) . The pump powers (referenced at the input of the sample) are $P_p = -68.6$ dBm and $P_p = -68.5$ dBm, respectively. The dots indicate the values of squeezing and logarithmic negativity calculated over the 10^8 acquisitions. The errorbars correspond the systematic error from the ± 1 dB uncertainty in the system gain calibration, while the shaded areas correspond to the statistical errors over 10 sets of 10^7 acquisitions.

pump power. On the other hand, the logarithmic negativity has a constant positive value, as can be seen in Figure 6.5(b), witnessing the entanglement between the two counter-propagating modes.

The high degree of squeezing below vacuum reported here is among the highest achieved with a Josephson TWPA [24].

EMISSION BANDWIDTH DEPENDENCE Finally, even if the counter-propagating amplification process is quite narrow-band, we have investigated the dependence of squeezing and entanglement generation over the emission bandwidth of the device. The results of these measurements, as a function of the pump power, for a pump frequency

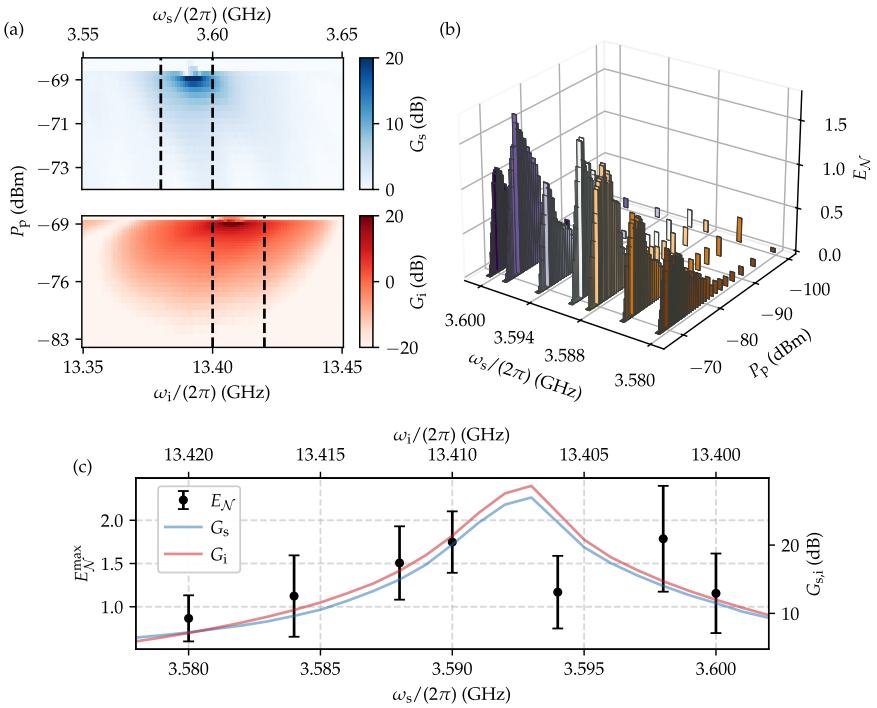

Figure 6.6: Logarithmic negativity dependence on the emission bandwidth
(a) Signal parametric gain, referenced to the pump off signal transmission, in blue, and corresponding backwards propagating idler gain, referred to the input signal power, in red, measured while pumping the device at 8.5 GHz, as a function of signal frequency and pump power. Vertical dashed black lines delimit the frequency span over which the entanglement measurements have been performed.
(b) Logarithmic negativity obtained from 10^7 acquisitions as a function of pump power with the quadratures acquired at seven different signal (and corresponding idler) frequencies within the emission bandwidth. The bars correspond to data after a moving average filter over the 3 nearest-neighbors points.
(c) Average maximum logarithmic negativity measured for the seven different signal (and corresponding idler) frequencies across the emission band shown in (b). The errorbars correspond to systematic errors obtained considering an error on the system gain of ±1 dB.

of 8.5 GHz are reported in Figure 6.6. Seven signal and idler pairs have been measured with frequencies spanning 20 MHz. We observed similar performance and behavior across the measured bandwidth, with logarithmic negativity scaling with the value of parametric gain, except for one point.

6.3.2 Co-propagating modes entanglement generation

The LH dispersion also allows for phase-matching of broadband amplification of co-propagating signal and idler modes. Such parametric

process has been already exploited to demonstrate broadband two-mode vacuum squeezing in Josephson TWPAs [22–24]. A negative index Josephson waveguide, constitutes an alternative platform over which broadband two-mode squeezing generation can be realized and studied. Moreover, it offers the possibility to compare two different squeezing generation processes: the one resulting from sinusoidal amplification, from which entangled signal and idler pairs are generated in opposite directions, and the broadband exponential one.

$\omega_p/(2\pi)$ (GHz)	$\omega_s/(2\pi)$ (GHz)	$\omega_i/(2\pi)$ (GHz)	T_s^{SYS} (K)	T_i^{SYS} (K)	η_s (%)	η_i (%)
8.5	8.747	8.526	6.5	6.9	3	3

Table 6.3: Pump, signal and idler frequencies, measurement efficiencies and system noise temperatures for the co-propagating squeezing measurements
Values of the pump, signal and idler frequencies, measurement efficiencies and system noise temperatures at which the quadratures distributions, used to evaluate two-mode squeezing and entanglement for the co-propagating process, have been measured.

Of particular interest is the pump power dependence of such processes. Indeed, it has been observed [22–24] that entanglement generation is sustained up to few dB of gain, above such value the measured logarithmic negativity drops even if the gain keeps increasing. This behavior is not captured by the theoretical models proposed so far [73, 143]. A similar behavior has been observed in resonant structures as well, but for parametric gains of about 20 dB and it has been explained considering the activation of higher-order couplings and wave-mixing processes [72, 153] because of the high driving powers involved. A proper understanding of this breakdown of squeezing and entanglement in Josephson TWPAs is necessary for the realization of efficient broadband squeezing sources.

Here, by measuring the pump power dependence of gain, squeezing, and logarithmic negativity given by the co-propagating process in a LH TWPA we observe the aforementioned breakdown, as shown in Figure 6.7. These measurements consist of 10^7 acquisitions per point and have been performed at signal and idler frequencies spaced by $\Delta = 26$ MHz from the pump frequency. Note the one order of magnitude difference between this spacing and the one of the counter-propagating measurements, given in Table 6.3. This results in better values of system noise temperatures and measurement efficiencies, as given in **??**. Moreover, now, the two modes have been measured using the same output line, with the experimental setup described in Chapter 3.

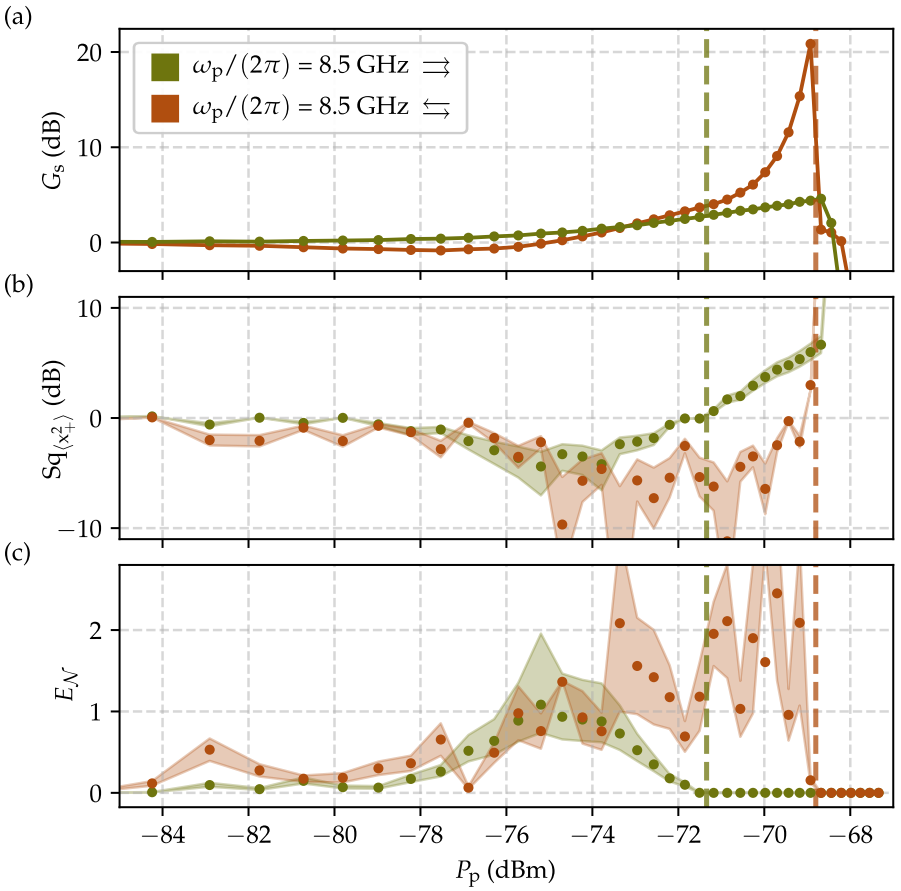

Figure 6.7: Pump power dependence of squeezing and logarithmic negativity

(a) Signal gain (normalized with the pump off measurement) as a function of the pump power for both the co-propagating amplification process, in green, and the counter-propagating one, in brown. The pump frequency is the same for the green and brown data and it corresponds to 8.5 GHz. The signal frequencies are 3.834 GHz for the two counter-propagating case, and 8.474 GHz for the co-propagating one.
(b) Squeezing of the collective quadrature x_+ obtained from 10^7 acquisitions as a function of pump power for the same configurations as in (a). The shaded area correspond to the systematic error obtained considering and error of ± 1 dB on the system gain. The vertical dashed lines correspond to the pump power value at which the logarithmic negativity goes to zero.
(c) Logarithmic negativity obtained from 10^7 acquisitions as a function of pump power for the same configurations as in (a). The shaded area correspond to the systematic error obtained considering and error of ± 1 dB on the system gain. The vertical dashed lines correspond to the pump power value at which the logarithmic negativity goes to zero.

We observe squeezing below vacuum and positive logarithmic negativity between co-propagating signal and idler modes, with optimal

values of $-4.4^{+2.6}_{-1.3}$ dB and $1.1^{+0.9}_{-0.4}$, respectively. This demonstrates the capabilities of the LH JTL to generate co-propagating entangled photon pairs, with performances comparable with the literature [22, 23]. For direct comparison, the results obtained for the counter-propagating pairs generation, for the same pump frequency of 8.5 GHz, are shown in Figure 6.7, as well. It is clear that in the generation of counter-propagating entangled modes is sustained until higher values of gain/pump powers.

The reasons behind the different behaviors are still under investigation, but they probably lie in the different nature of the two processes. In general, several factors can affect the amount of entanglement generated by a Josephson waveguide. For example, from this measurements one can think about attributing the breakdown to non-zero phase-matching[7], which has not been taken into account when modeling two-mode squeezing generation with Josephson TWPAs [73, 143], rather than to higher order processes, as for resonant structures.

6.4 CONCLUSIONS

This brings us to the conclusion of this chapter where we described the generation of nonclassical states of light in a LH waveguide. These results paves the way towards versatile broadband squeezers, vital to continuous variable quantum information processing, and open promising perspectives for performant quantum sensing using highly squeezed light.

6.4.1 Key results

Exploiting the parametric amplification processes, theoretically described in Chapter 2 and experimentally characterized in Chapter 5, we demonstrated the generation of microwave entangled photons in two different configurations:

A. First, the LH TWPA proved itself as an efficient source of counter-propagating entangled photon pairs. Given the high values of parametric gain achievable with the corresponding parametric amplification process, the device showed state-of-the-art performances, compared to previous realizations of two-mode vacuum squeezing sources with Josephson TWPAs [24]. Moreover, we believe this to be the first non-resonant source of counter-propagating entangled photon pairs in the microwave range, opening new possibilities for quantum information [70] and

7 Gwenael Le Gal is currently working on implementing the effect of pump power depended phase mismatches in modeling two-mode squeezing and entanglement generation in RH Josephson TWPAs, in collaboration with Anja Metelmann's group at Karlsruhe Institute of Technology.

quantum illumination [139] applications in the microwave domain.

B. Moreover, exploiting the broadband self-phase-matched amplification, which was theoretically proposed in [51], we could measure the generation of co-propagating two-mode vacuum squeezing with comparable performances with RH Josephson TWPAs [22–24]. However, with respect to the latter, the LH dispersion greatly simplifies the device operation, paving the way for easiest generation of complex multimode entangled states with Josephson metamaterials, which have been recently demonstrated in a 3WM RH structure [25].

6.4.2 Perspectives and open questions

Being this the first realization of this type of device, quite some work has still do be done. Some of which is closely related to gaining a better understanding of the device behavior already from a classical point of view, such as studying the interplay between the two processes to understand if they are limiting each other, as pointed out at the end of Chapter 5. Moreover, a more detailed characterization of the two generation processes could be performed:

A. Regarding the counter-propagating one we have limited ourselves to only two pump frequencies, however, the LH phase-matching mechanics allows for wide tunability, as shown in Chapter 2. A more detailed study of the device performances for several pump frequencies might help understanding the factors limiting the device performances, such as the role played by loss asymmetries between the signal and idler modes [143].

B. On the other hand, for what concern the co-propagating one, the pump phase and the emission bandwidth dependencies have not been measured yet.

C. Finally, these measurements should be corroborated with a quantum theory describing the input-output amplification and noise properties of LH Josephson TWPA. This task is being carried out in collaboration with Archana Kamal's group from Northwestern University.

From a broader point of view, being the generation of nonclassical states of light with Josephson TWPAs still in its infancy, a proper understanding of the effects limiting it, such as losses [73], pump fluctuations [154], phase-mismatches and higher harmonics generation [72], and of their interplay is still missing. The LH device presented here, represents an alternative, to more conventional RH Josephson TWPAs, which can be used to answer such questions.

7 CONCLUSIONS AND PERSPECTIVES

Josephson waveguides represent a prominent platform to study and harness parametric processes in the microwave domain because they allow complete control, at sub-wavelength scale, of wave-dispersion and nonlinear interactions. In this thesis we have seen how several topologies of Josephson waveguides can be realized to achieve near quantum-limited amplification [20, 83, 84], non-reciprocal signal transmission [26–28], and generation of nonclassical radiation [22–25]. In particular, parametric interactions and entanglement generation have been studied in a new Josephson waveguide topology [51], based on an artificial material showing LH wave dispersion, or equivalently negative index of refraction.

Here, we summarize the key results previously discussed and describe some open questions regarding the device behavior. Then, we point out which efforts should be pursued, in our opinion, to improve the device performances. Finally, some long-term perspectives opened by this work are listed.

7.1 CONCLUSIONS

In this work, we have explored the classical and quantum properties of a novel architecture of Josephson waveguide with LH wave dispersion. The latter, combined with the Josephson junctions nonlinearity, allows for native phase-matching of a variety of 4WM nonlinear interactions, such as parametric amplification and frequency conversion, without requiring any complicated dispersion or nonlinear engineering. In particular, LH Josephson waveguides present a unique operating regime, which enables parametric amplification of signal and idler modes propagating in opposite directions, providing natural sources of counter-propagating two-photons entangled states. A traveling-wave implementation of such source was still missing in the microwave domain, to the best of our knowledge, and it is probably the main result of this work.

However, let us go in order, and summarize from the beginning the results reported in this thesis.

7.1.1 Summary of the results

The realization of a negative index material showing nonlinear interactions has been a long journey, which started with the author of this work trying to understand parametric interactions, in particular amplification, in Josephson waveguides. Indeed, the potential of Josephson waveguides lies in the possibility of achieving parametric processes in non-resonant structures, thus removing the bandwidth constraint. However, as seen in this work, embedding a nonlinear medium in a waveguide-based architecture, increases fabrication complexity, and brings further challenges. First of all, the impedance has to be matched to the one of the microwave environment, to allow for traveling modes, and then a phase-matching condition for the targeted process has to be fulfilled. Such challenges can be addressed harnessing different topologies of Josephson waveguides to obtain tailored wave dispersion and nonlinear interactions.

PARAMETRIC INTERACTIONS IN JOSEPHSON WAVEGUIDES In Chapter 2, we have reviewed the main methods to phase-match 4WM parametric processes in these kind of structures. Special focus is given to the amplification processes, the different approaches to phase-match broadband co-propagating amplification, and their ideal gain performant, have been compared, as shown in Figure 7.1.

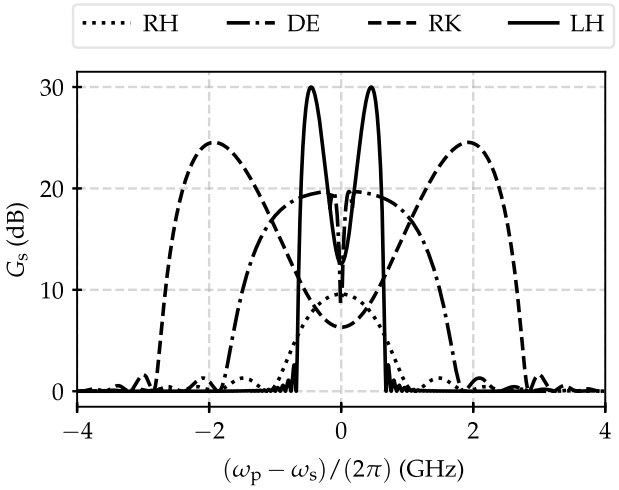

Figure 7.1: Co-propagating gain comparison between different Josephson waveguide
Signal gain G_s of the co-propagating amplification process for the RH, dotted line, DE, dashed-dotted line, RK, dashed line and LH, solid line, JTLs. The gain profiles have been obtained with a pump tone with frequency equal to 6 GHz and a pump to critical currents ratio of 0.4. The parameters of each JTL are given in Table 2.3 in Chapter 2.

The LH topology represent a new modality of Josephson TWPAs for realizing low-noise broadband parametric amplifiers [51], which

do not require any complicated dispersion [20] or nonlinear [84] engineering.

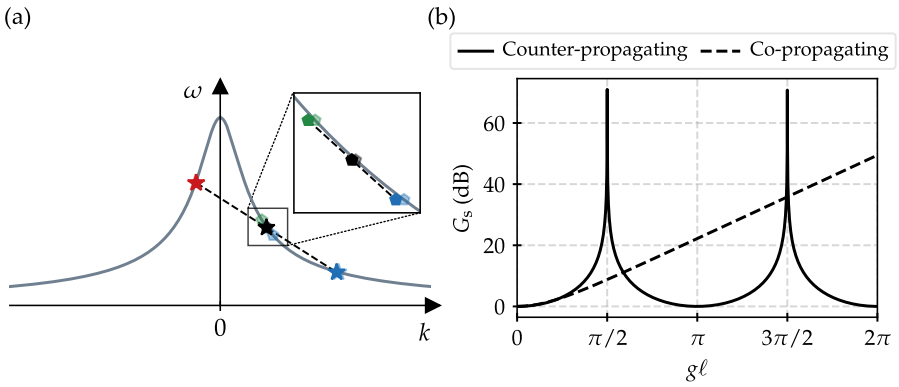

Figure 7.2: Signal gain comparison between co- and counter-propagating amplification in a Left-Handed Josephson waveguide
(a) Phase-matching conditions for the amplification processes in a negative index Josephson waveguide. For a given pump tone, in black, amplification can occur between signal, in blue, and idler, in green or red, modes propagating in the same or in opposite directions, as represented by either the pentagons or the stars, respectively.
(b) Signal gain G_s at the ideal phase-matching condition as a function of the amplification length $g\ell$ for the co-, dashed line, and counter-, solid line, propagating amplification processes. The curves have been obtained with a pump tone with frequency $\omega_p/(2\pi) = 12$ GHz using the parameters given in Table 2.3 in Chapter 2.

Remarkably, the LH dispersion also enables native phase-matching of the amplification process between signal and idler modes propagating in opposite directions, as shown in Figure 7.2(a). In particular, this mode of operation shows a sinusoidal dependence with respect to the amplification length $g\ell$, with the gain diverging when $g\ell$ approaches $(n + \frac{1}{2})\pi$, in contrast to the usual co-propagating amplification case, where the signal gain scales exponentially in the asymptotic limit, as depicted in Figure 7.2(b). Thus, negative index Josephson waveguides allow to reach high values of gain with a relatively short device, opening a new regime of traveling-wave parametric amplification within the superconducting circuits realm.

Finally, we have briefly discussed frequency conversion processes in JTLs and described how to phase-match them, exploiting the LH dispersion, as illustrated in Figure 7.3(a). Again, we found either an exponential or a sinusoidal dependence of the signal attenuation, depending on the relative propagation direction of the signal and up-converted modes involved in the process, as depicted in Figure 7.3(b). Both types of scaling have been already demonstrated using JTLs with RH topologies [28, 123]. However, the LH architecture greatly simplifies the phase-matching mechanics and opens to the possibility of com-

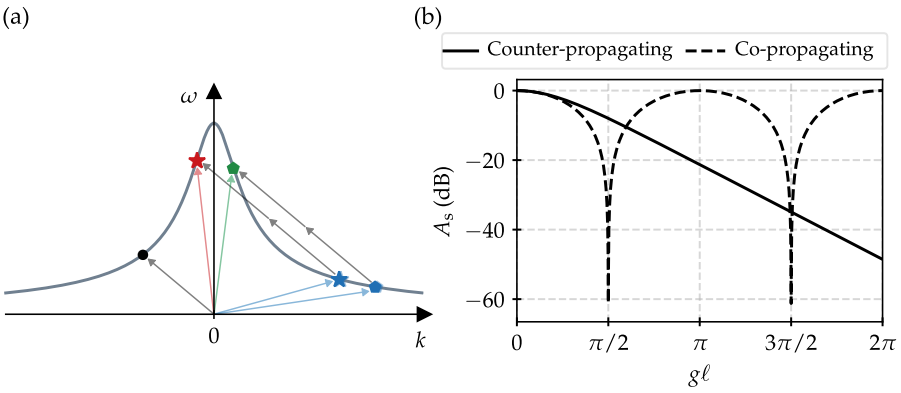

Figure 7.3: Signal attenuation comparison between co- and counter-propagating attenuation in a Left-Handed Josephson waveguide
(a) Phase-matching conditions for the attenuation processes in a negative index Josephson waveguide. For a given pump tone, in black, conversion can occur between a signal, in blue, and an idler, in green or red, modes propagating in the same or in opposite directions, as represented by either the pentagons or the stars, respectively.
(b) Signal attenuation A_s at the ideal phase-matching condition as a function of the conversion length $g\ell$ for the co-, dashed line, and counter-, solid line, propagating conversion processes. The curves have been obtained with a pump tone with frequency $\omega_p/(2\pi) = 7$ GHz using the parameters given in Table 2.4 in Chapter 2.

paring them within the same structure offering new opportunities to realize Traveling Wave Parametric Converters (TWPCs).

HIGH-FREQUENCY READOUT LINE Properly characterizing all the aforementioned processes, in a LH Josephson waveguides, required an extension of the measurement bandwidth of our readout line to the Ku-band, as described in Chapter 3 and shown in Figure 7.4.

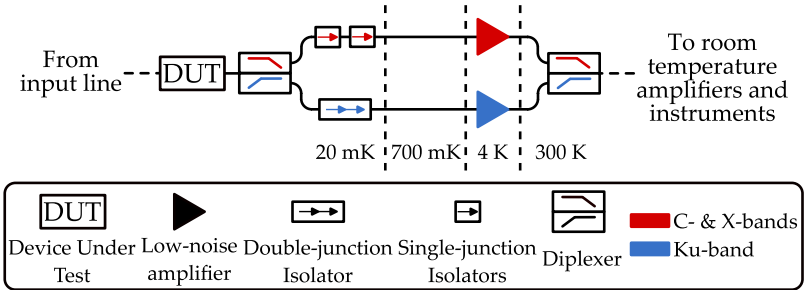

Figure 7.4: Schematic of the high-frequency output line
The output line measurement bandwidth has been extended by splitting it in two path, allowing for isolation and amplification in the C- & X-bands, in red, and in the Ku-band, in blue, and then recombining them at room temperature.

Besides the usefulness for the experiments reported here, the performances of standard TWPAs would greatly benefit from studies of intermodulation product and higher harmonics generation [108], which usually fall in the aforementioned bands. Finally, given the increasing interest in high-frequency qubit read-out [104] and quantum enhanced detection schemes for dark matter and axion searches [102, 103], being able to characterize TWPAs performances above the standard C- & X-bands is particularly desired.

MODULAR FABRICATION OF JOSEPHSON WAVEGUIDES Realizing Josephson waveguides requires to engineer long non-linear mediums composed of thousands of junctions and capacitors, while keeping their losses as low as possible, and their characteristic impedance matched with the typical 50 Ω one of the external microwave environment. Despite such challenges have been already addressed and solved in RH JTLs [20, 83, 93, 98], those implementations are not well suited for the realization of LH JTLs because of either their complexity or their lack of flexibility.

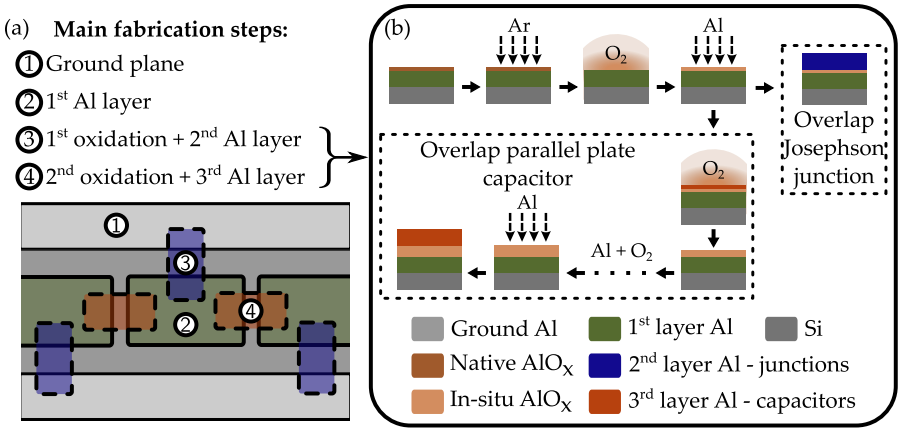

Figure 7.5: Illustration of the fabrication process
(a) Main steps of the fabrication process used for the realization of LH JTLs. The aluminum ground plane is first defined by wet etching. Then, the first aluminum electrode, which is common to both junctions and capacitors is defined. Next, we realize the second electrode of the junctions by cleaning their surface with argon ion milling, forming the tunnel barrier with a controlled oxidation, and depositing a second aluminum layer. Finally, after cleaning the surface of the capacitors first electrodes with argon ion milling, their oxide is deposited by a multi-layer deposition technic, which is followed by the evaporation of a third aluminum layer. To realize a RH JTL, the position of junctions and capacitors can be exchanged.
(b) Schematic of the overlap technic used to realized either the Josephson junctions or the capacitors.

In Chapter 4, we have detailed the fabrication process devised, in collaboration with Alexis Coissard from Silent Wave, to realize

negative index Josephson waveguides. Both junctions and compact capacitors are obtained with the overlap technic [118, 120], allowing for flexibility and high-yield. Given its modularity, the devised process enables the fabrication of both RH and LH Josephson waveguides, with minimal changes, as shown in Figure 7.5. Moreover, it easily allows to go beyond 1D structures and towards two-dimensional lattices [155].

A NEGATIVE-INDEX JOSEPHSON WAVEGUIDE The aforementioned fabrication processes allowed us to realize a Josephson waveguide showing negative index behavior, as described in Chapter 5. Indeed,

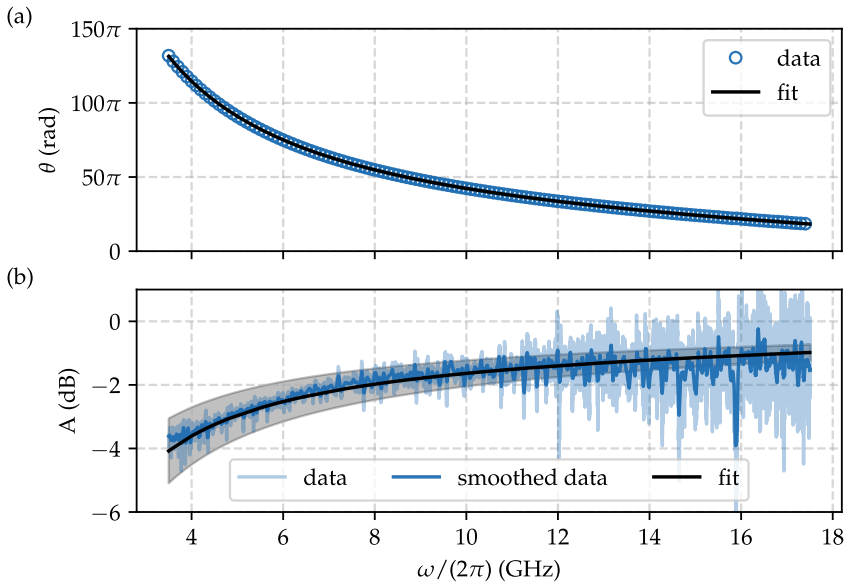

Figure 7.6: Normalized S_{21} parameter of a left-handed transmission line (a) Normalized electrical length (a), and attenuation (b), as a function of frequency, with corresponding fits to the LH dispersion relation and attenuation.

the linear characterization of the device shows a low frequency cut-off at about 2.4 GHz, with electrical length and attenuation increasing as the probe frequency decreases, as shown in Figure 7.6.

More interestingly, thanks to the LH dispersion and to the Josephson nonlinearity, all the parametric processes theoretically described in Chapter 2 could be observed. This is, to the best of our knowledge, the first experimental characterization of a negative index material showing nonlinear interactions. The system presents a nonreciprocal behavior. Sending a signal in the same or opposite direction with respect to the pump tone, leads to different outcomes: the signal can get amplified, attenuated or simply transmitted, as shown in Figure 7.7.

These results paves the way to the realization of broadband fully directional near-quantum limited parametric amplifier without the need for any phase-matching engineering. Moreover, the counter-

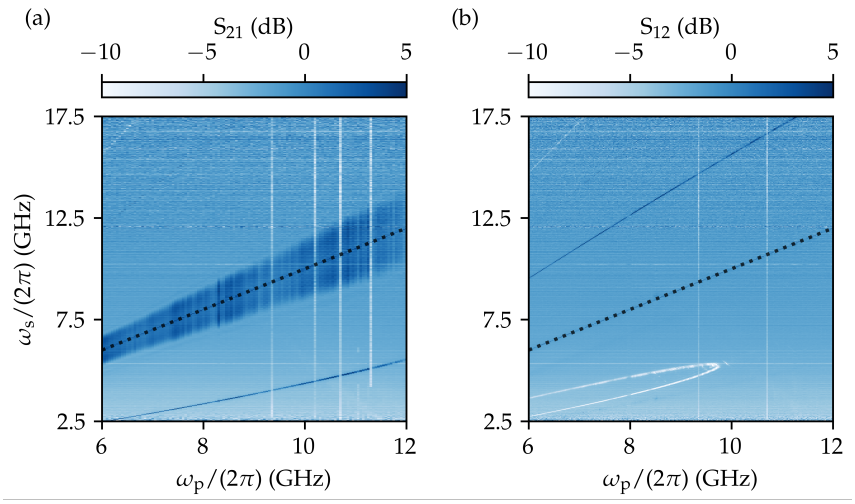

Figure 7.7: S_{21} and S_{12} nonlinear parameters of a negative index Josephson waveguide
Measured (a) S_{21} and (b) S_{12} parameters as a function of the signal and pump frequencies. For both measurements the pump tone, highlighted by the black dots, was sent from port 1 to port 2 of the device.

propagating amplification process allows to realize a source of counter-propagating entangled photons pairs.

GENERATION OF COUNTER-PROPAGATING ENTANGLED PHOTONS

After having characterized the classical behavior, we focused on the study of the quantum properties of the negative-index Josephson waveguide.

Given the high values of parametric gain achievable with the counter-propagating parametric amplification process, we could observe generation of spatially separated two-mode vacuum squeezed states with the realized LH TWPA, as shown in Figure 7.8. We believe this to be the first type of counter-propagating entangled photons pairs source based on a nonlinear waveguide in the microwave range, opening new possibilities for entanglement distribution across distant qubits, recently demonstrated with resonant JPAs [156], and for microwave quantum illumination protocols [139].

Moreover, exploiting the broadband amplification process, we measured the generation of co-propagating two-mode vacuum squeezing, showing comparable performances with respect to previously realized RH Josephson TWPAs [22–24]. However, the LH native phase-matching of the process, greatly simplifies the device design and operation, paving the way for easiest generation of complex multimode entangled states with Josephson metamaterials [25].

These results open promising perspectives for the realization of versatile broadband squeezers, vital for continuous variable quantum information processing, and for performant quantum sensing.

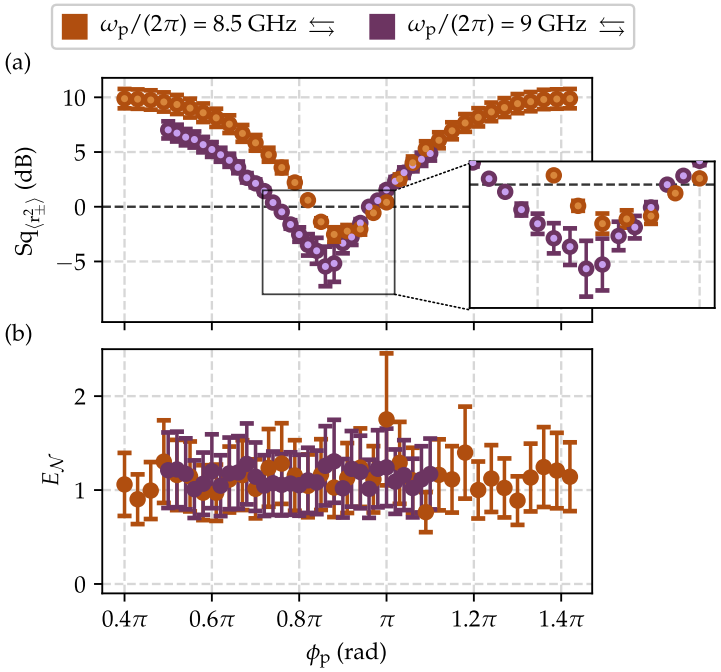

Figure 7.8: Pump phase dependence of squeezing and logarithmic negativity
(a) Squeezing of the collective quadrature and (b) logarithmic negativity as a function of the pump phase ϕ_p for pump drives with frequencies and powers equal to 8.5 GHz and −68.6 dBm, in brown, and 9 GHz and −68.5 dBm, in purple. The errorbars represent the systematic error on the system gain calibration.

7.2 PERSPECTIVES

The previously discussed results highlight the plethora of nonlinear phenomena that can occur in negative-index Josephson waveguides and their potential in the frameworks of quantum computing and quantum optics with superconducting circuits. However, they leave us with a range of open questions and future perspectives. Thus, we shall discuss at least some of them.

7.2.1 Open questions

In this work, we have characterized the nonlinear behavior and performances of a Josephson waveguide showing LH dispersion. In particular, simulating the amplification processes with simple three-mode models, a quantitative agreement with the observed gain profiles has been obtained, as shown in Figure 7.9. However, one may wonder what are the current limitations of the device. Especially, the co-propagating amplification process shows only few dB of gain, far from the requirements for real applications.

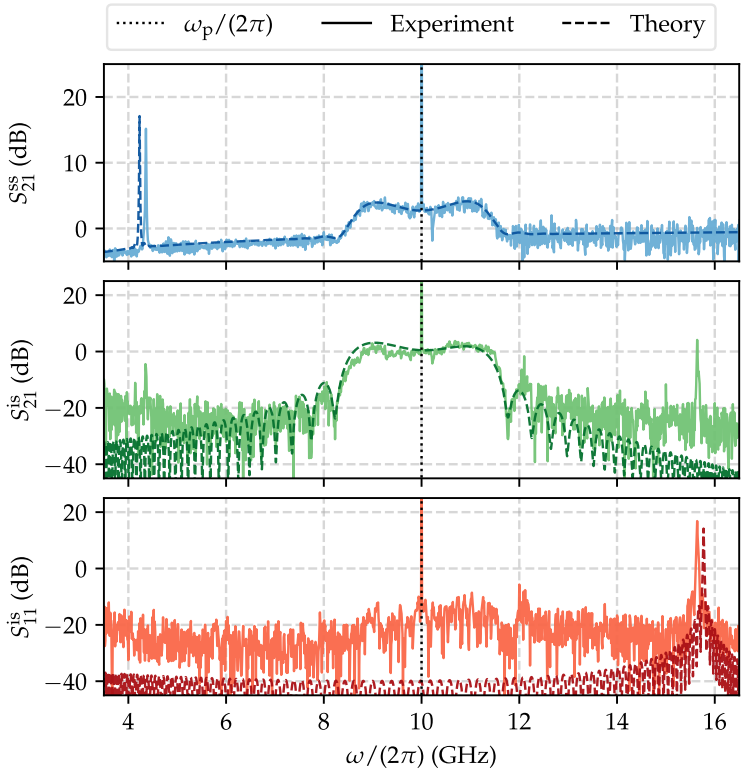

Figure 7.9: Normalized gain of a negative index Josephson waveguide Measurements, solid lines, and simulation, dashed lines, of the signal gain, in blue, and of the co-propagating, in green, and counter-propagating, in red, idlers conversion gain for a pump frequency $\omega_p/(2\pi) = 10$ GHz and a pump power $P_p = -62.0$ dBm. The numerical simulation have been performed with a pump frequency $\omega_p/(2\pi) = 10$ GHz and a pump power $P_p = -64.0$ dBm.

LIMITATIONS OF THE CO-PROPAGATING GAIN As discussed, the parametric amplification of signal and idler modes propagating in the same direction scales exponentially with the amplification length $g\ell$. Hence, a proper engineering of the device length and nonlinear coefficients is required. The relatively short length of the investigated device could explain the observed low amount of achievable gain. However, the presence of other counter-propagating process, which is more efficient in drawing energy from the pump drive, as $g\ell$ approaches $\pi/2$, may limit the available pump power to fuel the co-propagating process. Moreover, the counter-propagating gain divergence at $g\ell = \pi/2$ represents the onset of parametric oscillation, where the system breaks into an unstable regime.

Thus, the question is: will properly engineering the length of a LH TWPA result in good co-propagating amplification, as predicted by C. Kow *et al.* [51]?

Such question can be answered in different ways. First, one could actually realize and measure such device. Then, deriving a model

which takes into account both processes, *i. e.* five modes in total, would be of great help. Although, to efficiently model the complex dynamic of the device and the interplay between the different processes, X-PARAMETER [106] or WRSPICE simulations should be performed. Finally, a theoretical description accounting for the amplification of quantum vacuum fluctuations may be required to answer the question if they are limiting the device performances.

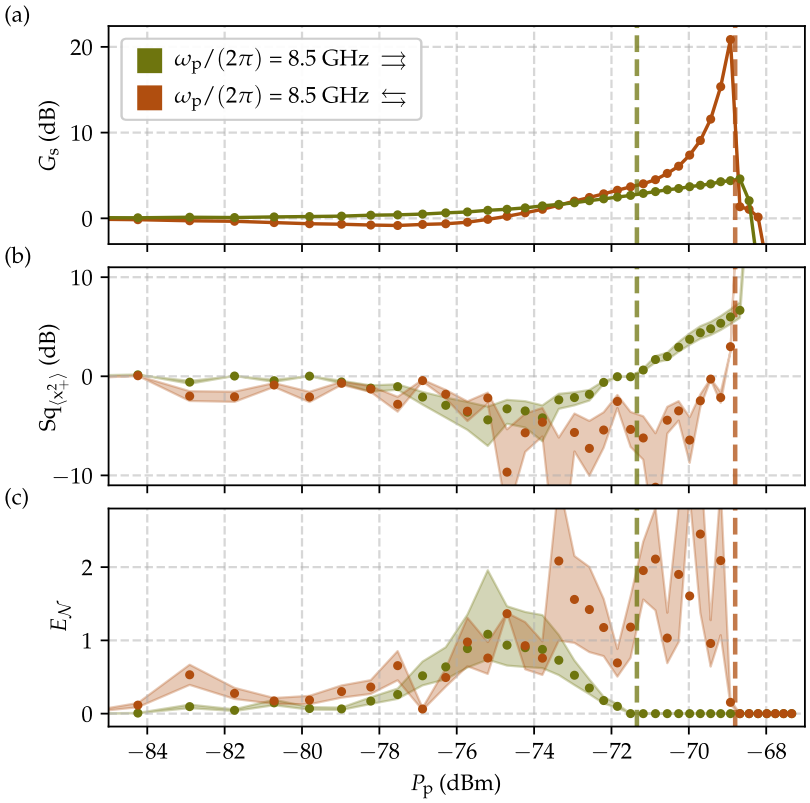

Figure 7.10: Pump power dependence of squeezing and logarithmic negativity
(a) Signal gain (normalized with the pump off measurement), (b) squeezing of the collective quadrature x_+, and (c) logarithmic negativity, as a function of the pump power for both the co-, in green, and counter-, in brown, propagating amplification processes. The pump frequency is equal to 8.5 GHz for both processes. The signal frequencies are 3.834 GHz for the counter-propagating case, and 8.474 GHz for the co-propagating one. The vertical dashed lines correspond to the pump power value at which the logarithmic negativity goes to zero.

SQUEEZING AND ENTANGLEMENT BREAKDOWN Such quantum theory, is also of primary importance to accurately model and improve the generation of entangled microwave radiation in Josephson waveguides.

Along this line, the LH topology represents an alternative platform to study, both experimentally and theoretically, the reasons behind the vanishing of squeezing and entanglement, while the gain still increases, in the co-propagating amplification case. Such behavior has been previously measured in RH Josephson TWPAs [22–24], and observed in our LH device as well. However, we could also observe that the generation of counter-propagating entangled modes is sustained until higher values of gain/pump powers, with respect to the co-propagating one, as shown in Figure 7.10.

The reasons behind the different behaviors are still under investigation, but it is crucial to understand them in order to realize efficient sources of entangled photons in the microwave domain with Josephson TWPAs.

7.2.2 Future possibilities

To conclude, we highlight some efforts, which could be pursued to improve the current device performances, and some ideas on future research projects related to the results presented in this work.

IMPROVING DEVICE PERFORMANCES Whatever the targeted application, being it quantum-limited amplification, non-reciprocal signal transmission, or entanglement generation, the presence of significant dielectric losses will always limit the device performances. The devised fabrication technic, based on the multilayer deposition of aluminum oxide, improved the dielectric loss tangent of about a factor two, with respect to previous realizations [84, 119]. However, it is still far from the recently demonstrated improvements of Josephson TWPAs [93, 98]. Hence, enhancing the quality of the dielectric is still of primarily importance. In the group, a new PhD student, Sébastien Moretti, together with Alexis Coissard and Romain Albert from Silent Wave, is currently investigating the possible different strategies to achieve such goal. Among them, there is improving the multilayer deposition process by optimizing its parameters, such as oxidation pressure and duration, and deposited layers' thickness. A second option is to replace the aluminum oxide with more defect free ones, such as amorphous silicon [157] or silicon nitride [158]. Once a low loss dielectric is obtained, other incremental improvements of the fabrication process could be realized, such as a better cleaning of the silicon surface prior to the ground plane deposition, and a definition of the first superconducting electrodes by etching them together with the ground plane itself.

Then, precisely designing the device for a specific application, *i. e.* as broadband amplifier or frequency converter, will definitely improve the desired performances.

A final, but not negligible improvement, can be obtained by optimizing the impedance environment of the device, starting from the

bonding pads to arrive to the connectors of the chip holder. This is also particularly important for higher-frequencies applications. At Silent Waves, Romain Albert has developed an improved microwave packaging that we have been able to use for the measurements of a Josephson TWPA operating in the Ku-band.

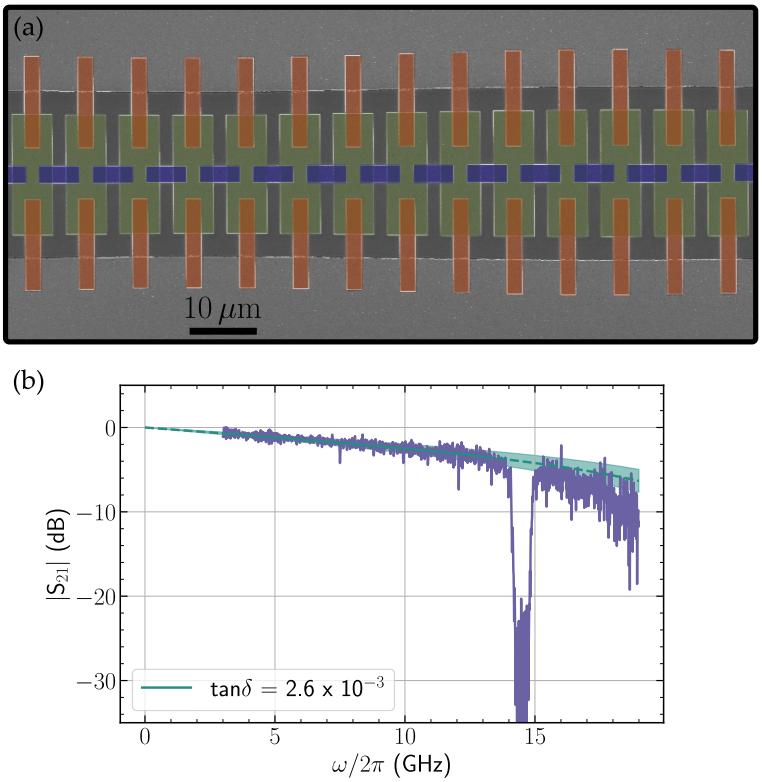

Figure 7.11: Right-Handed Josephson waveguide with dispersion engineering
(a) False colored SEM image of a RH JTL where each unit cells is composed by two junctions in series, in blue and two series capacitor shunted to ground on each side, in red. The green rectangles correspond the first aluminum layer, which is common to both junctions and capacitors.
(b) Normalized $|S_{21}|$ parameter, in purple, as a function of frequency, with corresponding fit, in green. The shaded area corresponds to a $\pm 0.5 \times 10^{-3}$ error on the the obtained value of the dielectric loss tangent $\tan\delta$.

KU-BAND JOSEPHSON TWPA Driven by the necessity to achieve near-quantum limited amplification in the Ku-band for our quantum optics experiments and by the collaborations with the MADMAX [102] and QUAX [97, 103] experiments, for dark matter and axion detection, we started the development, together with Silent Wave, of a Josephson TWPA operating in the Ku-band. The latter is based on a RH JTL with DE phase-matching. The motivations behind this choice have been briefly described in Chapter 2. As previously explained,

the devised fabrication process, easily allows to realize such kind of structure, which is shown in **??**. It presents a periodic modulation of its impedance to open a phase-matching gap in the dispersion relation [83].

A preliminary characterization showed good transmission until 18 GHz, with a gap at about 14.2 GHz, and values of loss tangent comparable with its LH cousin, presented in this work, as shown in Figure 7.11. A detailed analysis of the amplification, noise and saturation performances is under development.

COMPOSITE RIGHT-LEFT-HANDED LINE To conclude, we briefly discuss what, in our opinion, could be the natural extension of this work. Until now, only RH [21, 28] or LH, presented here, JTLs have been demonstrated. The next step would be to combine the two in a composite structure, whose linear properties have been briefly described in Chapter 2. A Composite Right-Left-Handed (CRLH) line presents two frequency bands, with either the RH or LH behavior and, thus with different phase and group velocities in each band. This allows, for example, to realize a two-mode transmission line, as in [28], within a simpler 1D structure. In our group, Ujjawal Singhal is currently working on the development of a CRLH JTL, with the aim of achieving broadband isolation in a simple 4WM architecture.

A second direct application of this type of structure was already proposed in the context of broadband and non-destructive detection of traveling-wave microwave photons [29]. The latter would be a key ingredient for several applications ranging from quantum-information processing to dark matter detection. The idea is to utilize a distributed weakly nonlinear coupling between a transmission line and a resonator, which is continuously probed. Thus, the passage of a photon in the transmission line should induce a displacement in the probe field.

Such scheme could be implemented either by using optimized nonlinear couplers or by embedding a resonant mode inside the transmission line. However, both solutions require careful design of nonlinear interactions and traveling times, and a flexible and low loss fabrication.

BIBLIOGRAPHY

1. Maiman, T. H. Stimulated Optical Radiation in Ruby. *Nature* **187,** 493–494. ISSN: 1476-4687 (Aug. 1960) (cit. on p. 1).
2. Aspect, A., Dalibard, J. & Roger, G. Experimental Test of Bell's Inequalities Using Time-Varying Analyzers. *Physical Review Letters* **49,** 1804–1807 (Dec. 1982) (cit. on p. 1).
3. Tse, M. *et al.* Quantum-Enhanced Advanced LIGO Detectors in the Era of Gravitational-Wave Astronomy. *Physical Review Letters* **123,** 231107 (Dec. 2019) (cit. on pp. 1, 10).
4. Zheludev, N. I. The Road Ahead for Metamaterials. *Science* **328,** 582–583 (Apr. 2010) (cit. on p. 1).
5. Lapine, M., Shadrivov, I. V. & Kivshar, Y. S. Colloquium: Nonlinear Metamaterials. *Reviews of Modern Physics* **86,** 1093–1123 (Sept. 2014) (cit. on pp. 1, 4).
6. Linden, S. *et al.* Photonic Metamaterials: Magnetism at Optical Frequencies. *IEEE Journal of Selected Topics in Quantum Electronics* **12,** 1097–1105. ISSN: 1558-4542 (Nov. 2006) (cit. on p. 1).
7. Pendry, J. B. & Smith, D. R. Reversing Light With Negative Refraction. *Physics Today* **57,** 37–43. ISSN: 0031-9228 (June 2004) (cit. on pp. 1–3, 17, 95).
8. Jung, P., Ustinov, A. V. & Anlage, S. M. Progress in Superconducting Metamaterials. *Superconductor Science and Technology* **27,** 073001. ISSN: 0953-2048 (May 2014) (cit. on pp. 1, 4).
9. Lazarides, N. & Tsironis, G. P. Superconducting Metamaterials. *Physics Reports. Superconducting Metamaterials* **752,** 1–67. ISSN: 0370-1573 (Aug. 2018) (cit. on pp. 1, 4).
10. Carusotto, I. *et al.* Photonic Materials in Circuit Quantum Electrodynamics. *Nature Physics* **16,** 268–279. ISSN: 1745-2481 (Mar. 2020) (cit. on p. 1).
11. Blais, A. *et al.* Circuit Quantum Electrodynamics. *Reviews of Modern Physics* **93,** 025005 (May 2021) (cit. on pp. 1, 2).
12. Acharya, R. *et al.* Quantum Error Correction below the Surface Code Threshold. *Nature* **638,** 920–926. ISSN: 1476-4687 (Feb. 2025) (cit. on p. 1).
13. Bienfait, A. *et al.* Reaching the Quantum Limit of Sensitivity in Electron Spin Resonance. *Nature Nanotechnology* **11,** 253–257. ISSN: 1748-3395 (Mar. 2016) (cit. on p. 1).

14. Storz, S. *et al.* Loophole-Free Bell Inequality Violation with Superconducting Circuits. *Nature* **617,** 265–270. ISSN: 1476-4687 (May 2023) (cit. on p. 1).

15. Egger, D. J. & Wilhelm, F. K. Multimode Circuit Quantum Electrodynamics with Hybrid Metamaterial Transmission Lines. *Physical Review Letters* **111,** 163601 (Oct. 2013) (cit. on pp. 1, 3, 18).

16. Liu, Y. & Houck, A. A. Quantum Electrodynamics near a Photonic Bandgap. *Nature Physics* **13,** 48–52. ISSN: 1745-2481 (Jan. 2017) (cit. on pp. 1, 11).

17. Zhang, X. *et al.* A Superconducting Quantum Simulator Based on a Photonic-Bandgap Metamaterial. *Science* **379,** 278–283 (Jan. 2023) (cit. on p. 1).

18. Ho Eom, B. *et al.* A Wideband, Low-Noise Superconducting Amplifier with High Dynamic Range. *Nature Physics* **8,** 623–627. ISSN: 1745-2473, 1745-2481 (Aug. 2012) (cit. on pp. 1, 4, 34, 35).

19. White, T. C. *et al.* Traveling Wave Parametric Amplifier with Josephson Junctions Using Minimal Resonator Phase Matching. *Applied Physics Letters* **106,** 242601. ISSN: 0003-6951 (June 2015) (cit. on pp. 1, 4, 13, 20, 34).

20. Macklin, C. *et al.* A near–Quantum-Limited Josephson Traveling-Wave Parametric Amplifier. *Science* **350,** 307–310 (Oct. 2015) (cit. on pp. 1, 4, 13, 20, 34, 73, 101, 111, 118, 122, 141, 143, 145).

21. Esposito, M. *et al.* Perspective on Traveling Wave Microwave Parametric Amplifiers. *Applied Physics Letters* **119,** 120501. ISSN: 0003-6951, 1077-3118 (Sept. 2021) (cit. on pp. 1, 2, 8, 153).

22. Esposito, M. *et al.* Observation of Two-Mode Squeezing in a Traveling Wave Parametric Amplifier. *Physical Review Letters* **128,** 153603 (Apr. 2022) (cit. on pp. 1, 11, 13, 45, 64, 68, 70, 121–123, 125, 127, 129, 131, 137, 139–141, 147, 151).

23. Perelshtein, M. *et al.* Broadband Continuous-Variable Entanglement Generation Using a Kerr-Free Josephson Metamaterial. *Physical Review Applied* **18,** 024063 (Aug. 2022) (cit. on pp. 1, 11, 13, 43, 68, 121, 122, 131, 137, 139–141, 147, 151).

24. Qiu, J. Y. *et al.* Broadband Squeezed Microwaves and Amplification with a Josephson Travelling-Wave Parametric Amplifier. *Nature Physics* **19,** 706–713. ISSN: 1745-2481 (May 2023) (cit. on pp. 1, 11, 13, 121, 122, 133, 135, 137, 139–141, 147, 151).

25. Alocco, A. *et al. Programmable Microwave Cluster States via Josephson Metamaterials* July 2025. arXiv: 2507.22823 [quant-ph] (cit. on pp. 1, 122, 131, 140, 141, 147).

26. Ranadive, A. *et al. A Traveling Wave Parametric Amplifier Isolator* June 2024. arXiv: 2406.19752 [cond-mat, physics:quant-ph] (cit. on pp. 1, 13, 47, 52, 95, 122, 141).
27. Malnou, M. *et al.* A Travelling-Wave Parametric Amplifier and Converter. *Nature Electronics*, 1–7. ISSN: 2520-1131 (Aug. 2025) (cit. on pp. 1, 13, 47, 52, 95, 122, 141).
28. Praquin, M. *et al. Mixing of Counterpropagating Signals in a Traveling-Wave Josephson Device* June 2024. arXiv: 2406.19751 [cond-mat, physics:quant-ph] (cit. on pp. 1, 13, 39, 47, 51, 52, 95, 118, 122, 141, 143, 153).
29. Grimsmo, A. L. *et al.* Quantum Metamaterial for Broadband Detection of Single Microwave Photons. *Physical Review Applied* **15,** 034074 (Mar. 2021) (cit. on pp. 1, 13, 18, 23, 124, 153).
30. Caves, C. M. Quantum Limits on Noise in Linear Amplifiers. *Physical Review D* **26,** 1817–1839 (Oct. 1982) (cit. on pp. 2, 7, 60, 124).
31. Clerk, A. A. *et al.* Introduction to Quantum Noise, Measurement, and Amplification. *Reviews of Modern Physics* **82,** 1155–1208 (Apr. 2010) (cit. on pp. 2, 7).
32. Nation, P. D. *et al.* Colloquium: Stimulating Uncertainty: Amplifying the Quantum Vacuum with Superconducting Circuits. *Reviews of Modern Physics* **84,** 1–24 (Jan. 2012) (cit. on pp. 2, 6, 9, 68, 122, 123).
33. Vool, U. & Devoret, M. Introduction to Quantum Electromagnetic Circuits. *International Journal of Circuit Theory and Applications* **45,** 897–934. ISSN: 1097-007X (2017) (cit. on pp. 2, 5, 9).
34. Aumentado, J. Superconducting Parametric Amplifiers: The State of the Art in Josephson Parametric Amplifiers. *IEEE Microwave Magazine* **21,** 45–59. ISSN: 1557-9581 (Aug. 2020) (cit. on pp. 2, 7, 8).
35. Lang, C. *Quantum Microwave Radiation and Its Interference Characterized by Correlation Function Measurements in Circuit Quantum Electrodynamics* Doctoral Thesis (ETH Zurich, 2014) (cit. on pp. 2, 70, 127, 129).
36. Flurin, E. *The Josephson Mixer : A Swiss Army Knife for Microwave Quantum Optics* PhD thesis (Ecole normale supérieure - ENS PARIS, Dec. 2014) (cit. on p. 2).
37. Planat, L. *Resonant and Traveling-Wave Parametric Amplification near the Quantum Limit* PhD thesis (Université Grenoble Alpes, June 2020) (cit. on pp. 2, 9, 27, 35, 41, 46, 79, 96).
38. Veselago, V. G. The electrodynamics of substances with simultaneously negative values of ε and μ. *Soviet Physics Uspekhi* **10,** 509. ISSN: 0038-5670 (Apr. 1968) (cit. on pp. 2, 3, 17, 95).

39. Pendry, J. B. Focus Issue: Negative Refraction and Metamaterials. *Optics Express* **11,** 639–639. ISSN: 1094-4087 (Apr. 2003) (cit. on pp. 2, 3).
40. Pitarke, J. M. *et al.* Theory of Surface Plasmons and Surface-Plasmon Polaritons. *Reports on Progress in Physics* **70,** 1. ISSN: 0034-4885 (Dec. 2006) (cit. on p. 2).
41. Garcia, M. A. Surface Plasmons in Metallic Nanoparticles: Fundamentals and Applications. *Journal of Physics D: Applied Physics* **44,** 283001. ISSN: 0022-3727 (June 2011) (cit. on p. 2).
42. Shelby, R. A., Smith, D. R. & Schultz, S. Experimental Verification of a Negative Index of Refraction. *Science* **292,** 77–79 (Apr. 2001) (cit. on pp. 3, 17, 95).
43. Smith, D. R., Pendry, J. B. & Wiltshire, M. C. K. Metamaterials and Negative Refractive Index. *Science* **305,** 788–792 (Aug. 2004) (cit. on p. 3).
44. Eleftheriades, G., Iyer, A. & Kremer, P. Planar Negative Refractive Index Media Using Periodically L-C Loaded Transmission Lines. *IEEE Transactions on Microwave Theory and Techniques* **50,** 2702–2712 (Dec. 2002) (cit. on pp. 3, 18, 95).
45. Caloz, C. & Itoh, T. Transmission Line Approach of Left-Handed (LH) Materials and Microstrip Implementation of an Artificial LH Transmission Line. *IEEE Transactions on Antennas and Propagation* **52,** 1159–1166. ISSN: 1558-2221 (May 2004) (cit. on pp. 3, 18).
46. Grbic, A. & Eleftheriades, G. V. Overcoming the Diffraction Limit with a Planar Left-Handed Transmission-Line Lens. *Physical Review Letters* **92,** 117403 (Mar. 2004) (cit. on pp. 3, 18).
47. Caloz, C., Sanada, A. & Itoh, T. A Novel Composite Right-/Left-Handed Coupled-Line Directional Coupler with Arbitrary Coupling Level and Broad Bandwidth. *IEEE Transactions on Microwave Theory and Techniques* **52,** 980–992. ISSN: 1557-9670 (Mar. 2004) (cit. on pp. 3, 18, 95).
48. Ovchinnikova, E. A. *et al.* Design and Experimental Study of Superconducting Left-Handed Transmission Lines with Tunable Dispersion. *Superconductor Science and Technology* **26,** 114003. ISSN: 0953-2048 (Oct. 2013) (cit. on pp. 3, 18).
49. Wang, H. *et al.* Mode Structure in Superconducting Metamaterial Transmission-Line Resonators. *Physical Review Applied* **11,** 054062 (May 2019) (cit. on pp. 3, 18, 23, 97).
50. Indrajeet, S. *et al.* Coupling a Superconducting Qubit to a Left-Handed Metamaterial Resonator. *Physical Review Applied* **14,** 064033 (Dec. 2020) (cit. on pp. 3, 18, 95).

51. Kow, C., Podolskiy, V. & Kamal, A. Self-Phase-Matched Broadband Amplification with a Left-Handed Josephson Transmission Line. *Physical Review Applied* **24,** 024026 (Aug. 2025) (cit. on pp. 3, 13, 18, 22, 26, 31, 34, 38, 41, 43, 95, 106, 117–119, 132, 140–142, 149).
52. Popov, A. K. & Shalaev, V. M. Compensating Losses in Negative-Index Metamaterials by Optical Parametric Amplification. *Optics Letters* **31,** 2169–2171. ISSN: 1539-4794 (July 2006) (cit. on p. 4).
53. Malnou, M. *et al.* Three-Wave Mixing Kinetic Inductance Traveling-Wave Amplifier with Near-Quantum-Limited Noise Performance. *PRX Quantum* **2,** 010302. ISSN: 2691-3399 (Jan. 2021) (cit. on pp. 4, 64).
54. Tinkham, M. *Introduction to Superconductivity* ISBN: 978-0-486-13472-7 (Courier Corporation, Jan. 2004) (cit. on p. 4).
55. Likharev, K. K. Superconducting Weak Links. *Reviews of Modern Physics* **51,** 101–159 (Jan. 1979) (cit. on p. 4).
56. Josephson, B. D. Possible New Effects in Superconductive Tunnelling. *Physics Letters* **1,** 251–253. ISSN: 0031-9163 (July 1962) (cit. on p. 4).
57. Golubov, A. A., Kupriyanov, M. Yu. & Il'ichev, E. The Current-Phase Relation in Josephson Junctions. *Reviews of Modern Physics* **76,** 411–469 (Apr. 2004) (cit. on p. 4).
58. Calander, N., Claeson, T. & Rudner, S. Shunted Josephson Tunnel Junctions: High-frequency, Self-pumped Low Noise Amplifiers. *Journal of Applied Physics* **53,** 5093–5103. ISSN: 0021-8979 (July 1982) (cit. on p. 6).
59. Smith, A. *et al.* Low Noise Microwave Parametric Amplifier. *IEEE Transactions on Magnetics* **21,** 1022–1028. ISSN: 1941-0069 (Mar. 1985) (cit. on p. 6).
60. Frattini, N. E. *et al.* 3-Wave Mixing Josephson Dipole Element. *Applied Physics Letters* **110,** 222603. ISSN: 0003-6951, 1077-3118 (May 2017) (cit. on pp. 6, 37).
61. Loudon, R. *The Quantum Theory of Light* ISBN: 978-0-19-850177-0 (Oxford University Press, Sept. 2000) (cit. on pp. 6, 9, 121).
62. Yurke, B. *et al.* Observation of Parametric Amplification and Deamplification in a Josephson Parametric Amplifier. *Physical Review A* **39,** 2519–2533 (Mar. 1989) (cit. on p. 7).
63. Castellanos-Beltran, M. A. & Lehnert, K. W. Widely Tunable Parametric Amplifier Based on a Superconducting Quantum Interference Device Array Resonator. *Applied Physics Letters* **91,** 083509. ISSN: 0003-6951 (Aug. 2007) (cit. on p. 7).

64. Bergeal, N. *et al.* Phase-Preserving Amplification near the Quantum Limit with a Josephson Ring Modulator. *Nature* **465,** 64–68. ISSN: 1476-4687 (May 2010) (cit. on p. 7).

65. Sliwa, K. M. *et al.* Reconfigurable Josephson Circulator/Directional Amplifier. *Physical Review X* **5,** 041020 (Nov. 2015) (cit. on p. 7).

66. Metelmann, A. & Clerk, A. A. Nonreciprocal Photon Transmission and Amplification via Reservoir Engineering. *Physical Review X* **5,** 021025 (June 2015) (cit. on p. 7).

67. Lecocq, F. *et al.* Nonreciprocal Microwave Signal Processing with a Field-Programmable Josephson Amplifier. *Physical Review Applied* **7,** 024028 (Feb. 2017) (cit. on p. 7).

68. Planat, L. *et al.* Understanding the Saturation Power of Josephson Parametric Amplifiers Made from SQUID Arrays. *Physical Review Applied* **11,** 034014 (Mar. 2019) (cit. on pp. 8, 96).

69. Walls, D. F. Squeezed States of Light. *Nature* **306,** 141–146. ISSN: 1476-4687 (Nov. 1983) (cit. on pp. 9, 10, 125).

70. Braunstein, S. L. & van Loock, P. Quantum Information with Continuous Variables. *Reviews of Modern Physics* **77,** 513–577 (June 2005) (cit. on pp. 9, 121, 125, 139).

71. Backes, K. M. *et al.* A Quantum Enhanced Search for Dark Matter Axions. *Nature* **590,** 238–242. ISSN: 0028-0836, 1476-4687 (Feb. 2021) (cit. on pp. 9, 10, 122).

72. Boutin, S. *et al.* Effect of Higher-Order Nonlinearities on Amplification and Squeezing in Josephson Parametric Amplifiers. *Physical Review Applied* **8,** 054030 (Nov. 2017) (cit. on pp. 9, 10, 122, 137, 140).

73. Grimsmo, A. L. & Blais, A. Squeezing and Quantum State Engineering with Josephson Travelling Wave Amplifiers. *npj Quantum Information* **3,** 20. ISSN: 2056-6387 (June 2017) (cit. on pp. 10, 123, 137, 139, 140).

74. Caves, C. M. Quantum-Mechanical Noise in an Interferometer. *Physical Review D* **23,** 1693–1708 (Apr. 1981) (cit. on p. 10).

75. Lloyd, S. & Braunstein, S. L. Quantum Computation over Continuous Variables. *Physical Review Letters* **82,** 1784–1787 (Feb. 1999) (cit. on p. 11).

76. Braunstein, S. L. Squeezing as an Irreducible Resource. *Physical Review A* **71,** 055801 (May 2005) (cit. on p. 11).

77. Movshovich, R. *et al.* Observation of Zero-Point Noise Squeezing via a Josephson-parametric Amplifier. *Physical Review Letters* **65,** 1419–1422 (Sept. 1990) (cit. on p. 11).

78. Castellanos-Beltran, M. A. *et al.* Amplification and Squeezing of Quantum Noise with a Tunable Josephson Metamaterial. *Nature Physics* **4,** 929–931. ISSN: 1745-2481 (Dec. 2008) (cit. on p. 11).

79. Eichler, C. *et al.* Observation of Two-Mode Squeezing in the Microwave Frequency Domain. *Physical Review Letters* **107,** 113601 (Sept. 2011) (cit. on pp. 11, 121, 130).

80. Flurin, E. *et al.* Generating Entangled Microwave Radiation Over Two Transmission Lines. *Physical Review Letters* **109,** 183901 (Oct. 2012) (cit. on pp. 11, 121, 122, 132).

81. Bergeal, N. *et al.* Two-Mode Correlation of Microwave Quantum Noise Generated by Parametric Down-Conversion. *Physical Review Letters* **108,** 123902 (Mar. 2012) (cit. on p. 11).

82. Lu, Z. *et al. Counter-Propagating Entangled Photon Pairs from a Monolayer* Aug. 2025. arXiv: 2508.06860 [quant-ph] (cit. on pp. 11, 132).

83. Planat, L. *et al.* Photonic-Crystal Josephson Traveling-Wave Parametric Amplifier. *Physical Review X* **10,** 021021. ISSN: 2160-3308 (Apr. 2020) (cit. on pp. 13, 35, 41, 73, 101, 122, 141, 145, 153).

84. Ranadive, A. *et al.* Kerr Reversal in Josephson Meta-Material and Traveling Wave Parametric Amplification. *Nature Communications* **13,** 1737. ISSN: 2041-1723 (Apr. 2022) (cit. on pp. 13, 34, 36, 41, 43, 63, 64, 111, 118, 122, 141, 143, 151).

85. Pozar, D. *Microwave Engineering* ISBN: 978-1-118-21363-6 (Wiley, Apr. 2012) (cit. on pp. 13–16, 60, 62, 63, 97, 98, 101).

86. Grbic, A. & Eleftheriades, G. V. Experimental Verification of Backward-Wave Radiation from a Negative Refractive Index Metamaterial. *Journal of Applied Physics* **92,** 5930–5935. ISSN: 0021-8979 (Nov. 2002) (cit. on p. 17).

87. Léger, S. *et al.* Observation of Quantum Many-Body Effects Due to Zero Point Fluctuations in Superconducting Circuits. *Nature Communications* **10,** 5259. ISSN: 2041-1723 (Dec. 2019) (cit. on p. 20).

88. Kuzmin, R. *et al.* Superstrong Coupling in Circuit Quantum Electrodynamics. *npj Quantum Information* **5,** 20. ISSN: 2056-6387 (Feb. 2019) (cit. on p. 20).

89. Manucharyan, V. E. *et al.* Fluxonium: Single Cooper-Pair Circuit Free of Charge Offsets. *Science* **326,** 113–116 (Oct. 2009) (cit. on p. 20).

90. Yaakobi, O. *et al.* Parametric Amplification in Josephson Junction Embedded Transmission Lines. *Physical Review B* **87,** 144301 (Apr. 2013) (cit. on pp. 25, 27, 124).

91. Le Gal, G. *et al.* Gain Compression in Josephson Traveling-Wave Parametric Amplifiers. *Physical Review Applied* **24,** 014022 (July 2025) (cit. on pp. 29, 37, 41, 47, 49, 101).
92. O'Brien, K. *et al.* Resonant Phase Matching of Josephson Junction Traveling Wave Parametric Amplifiers. *Physical Review Letters* **113,** 157001 (Oct. 2014) (cit. on pp. 34, 35).
93. Chang, C. W. S. *et al. Josephson Traveling-Wave Parametric Amplifier Based on Low-Intrinsic-Loss Coplanar Lumped-Element Waveguide* Mar. 2025. arXiv: 2503.07559 [physics] (cit. on pp. 36, 43, 44, 73, 79, 101, 122, 145, 151).
94. Bell, M. T. & Samolov, A. Traveling-Wave Parametric Amplifier Based on a Chain of Coupled Asymmetric SQUIDs. *Physical Review Applied* **4,** 024014 (Aug. 2015) (cit. on p. 36).
95. Zorin, A. B. Josephson Traveling-Wave Parametric Amplifier with Three-Wave Mixing. *Physical Review Applied* **6,** 034006 (Sept. 2016) (cit. on p. 37).
96. Ranadive, A. *Nonlinear Quantum Optics with Josephson Meta-Materials* PhD thesis (Université Grenoble Alpes, Nov. 2022) (cit. on pp. 37, 41, 47, 68, 123, 127).
97. Di Vora, R. *et al.* Search for Galactic Axions with a Traveling Wave Parametric Amplifier. *Physical Review D* **108,** 062005 (Sept. 2023) (cit. on pp. 38, 152).
98. Wang, J. *et al. High-Efficiency, Low-Loss Floquet-mode Traveling Wave Parametric Amplifier* Apr. 2025. arXiv: 2503.11812 [quant-ph] (cit. on pp. 43, 44, 73, 79, 101, 122, 145, 151).
99. Miano, A. & Mukhanov, O. A. Symmetric Traveling Wave Parametric Amplifier. *IEEE Transactions on Applied Superconductivity* **29,** 1–6. ISSN: 1558-2515 (Aug. 2019) (cit. on p. 43).
100. Nilsson, H. R. *et al. A Small Footprint Travelling-Wave Parametric Amplifier with a High Signal-to-Noise Ratio Improvement in a Wide Band* Aug. 2024. arXiv: 2408.16366 (cit. on p. 43).
101. Gaydamachenko, V., Kissling, C. & Grünhaupt, L. Rf-SQUID-based Traveling-Wave Parametric Amplifier with Input Saturation Power of $\ensuremath{-}84$ dBm across More than One Octave in Bandwidth. *Physical Review Applied* **23,** 064053 (June 2025) (cit. on pp. 43, 64).
102. MADMAX Working Group *et al.* Dielectric Haloscopes: A New Way to Detect Axion Dark Matter. *Physical Review Letters* **118,** 091801 (Mar. 2017) (cit. on pp. 43, 59, 145, 152).
103. Braggio, C. *et al.* A Haloscope Amplification Chain Based on a Traveling Wave Parametric Amplifier. *Review of Scientific Instruments* **93,** 094701. ISSN: 0034-6748 (Sept. 2022) (cit. on pp. 43, 145, 152).

104. Anferov, A. *et al.* Superconducting Qubits above 20 GHz Operating over 200 mK. *PRX Quantum* **5,** 030347 (Sept. 2024) (cit. on pp. 43, 59, 145).

105. Eichler, C. & Wallraff, A. Controlling the Dynamic Range of a Josephson Parametric Amplifier. *EPJ Quantum Technology* **1,** 1–19. ISSN: 2196-0763 (Dec. 2014) (cit. on pp. 46, 96).

106. Peng, K. *et al. X-Parameter Based Design and Simulation of Josephson Traveling-Wave Parametric Amplifiers for Quantum Computing Applications* in *2022 IEEE International Conference on Quantum Computing and Engineering (QCE)* (Sept. 2022), 331–340 (cit. on pp. 47, 109, 119, 150).

107. Puertas, J. *Probing Light-Matter Interaction in the Many-Body Regime of Superconducting Quantum Circuits* PhD thesis (Université Grenoble Alpes, June 2018) (cit. on p. 59).

108. Remm, A. *et al.* Intermodulation Distortion in a Josephson Traveling-Wave Parametric Amplifier. *Physical Review Applied* **20,** 034027 (Sept. 2023) (cit. on pp. 60, 145).

109. Ranzani, L. *et al.* Two-Port Microwave Calibration at Millikelvin Temperatures. *Review of Scientific Instruments* **84,** 034704. ISSN: 0034-6748 (Mar. 2013) (cit. on p. 63).

110. Shin, S.-H. *et al.* In-Operando Microwave Scattering-Parameter Calibrated Measurement of a Josephson Traveling Wave Parametric Amplifier. *Applied Physics Letters* **125,** 104001. ISSN: 0003-6951 (Sept. 2024) (cit. on p. 63).

111. Faramarzi, F. *et al.* Near-Quantum-Limited Subgigahertz TiN Kinetic Inductance Traveling-Wave Parametric Amplifier Operating in a Frequency-Translating Mode. *Physical Review Applied* **23,** 024063 (Feb. 2025) (cit. on p. 63).

112. Malnou, M. *et al.* Low-Noise Cryogenic Microwave Amplifier Characterization with a Calibrated Noise Source. *Review of Scientific Instruments* **95,** 034703. ISSN: 0034-6748 (Mar. 2024) (cit. on p. 64).

113. Gurvitch, M., Washington, M. A. & Huggins, H. A. High Quality Refractory Josephson Tunnel Junctions Utilizing Thin Aluminum Layers. *Applied Physics Letters* **42,** 472–474. ISSN: 0003-6951 (Mar. 1983) (cit. on p. 74).

114. Dolan, G. J. Offset Masks for Lift-off Photoprocessing. *Applied Physics Letters* **31,** 337–339. ISSN: 0003-6951 (Sept. 1977) (cit. on p. 74).

115. Lecocq, F. *et al.* Junction Fabrication by Shadow Evaporation without a Suspended Bridge. *Nanotechnology* **22,** 315302. ISSN: 0957-4484 (July 2011) (cit. on p. 74).

116. Wu, X. *et al.* Overlap Junctions for High Coherence Superconducting Qubits. *Applied Physics Letters* **111,** 032602. ISSN: 0003-6951 (July 2017) (cit. on pp. 74, 75).

117. Grünhaupt, L. *et al.* An Argon Ion Beam Milling Process for Native AlOx Layers Enabling Coherent Superconducting Contacts. *Applied Physics Letters* **111,** 072601. ISSN: 0003-6951 (Aug. 2017) (cit. on pp. 74, 87).

118. Bal, M. *et al.* Overlap Junctions for Superconducting Quantum Electronics and Amplifiers. *Applied Physics Letters* **118,** 112601. ISSN: 0003-6951 (Mar. 2021) (cit. on pp. 75, 146).

119. Planat, L. *et al.* Fabrication and Characterization of Aluminum SQUID Transmission Lines. *Physical Review Applied* **12,** 064017 (Dec. 2019) (cit. on pp. 79, 101, 151).

120. Zotova, J. *et al.* Compact Superconducting Microwave Resonators Based on ${\text{Al-AlO}}_{x}$-Al Capacitors. *Physical Review Applied* **19,** 044067 (Apr. 2023) (cit. on pp. 79, 146).

121. Monroe, J. T. *et al.* Optical Direct Write of Dolan–Niemeyer-bridge Junctions for Transmon Qubits. *Applied Physics Letters* **119,** 062601. ISSN: 0003-6951 (Aug. 2021) (cit. on p. 80).

122. Dunsworth, A. *et al.* Characterization and Reduction of Capacitive Loss Induced by Sub-Micron Josephson Junction Fabrication in Superconducting Qubits. *Applied Physics Letters* **111,** 022601. ISSN: 0003-6951, 1077-3118 (July 2017) (cit. on p. 87).

123. Ranzani, L. *et al.* Wideband Isolation by Frequency Conversion in a Josephson-Junction Transmission Line. *Physical Review Applied* **8,** 054035 (Nov. 2017) (cit. on pp. 118, 143).

124. Horodecki, R. *et al.* Quantum Entanglement. *Reviews of Modern Physics* **81,** 865–942 (June 2009) (cit. on p. 121).

125. Shih, Y. Quantum Imaging. *IEEE Journal of Selected Topics in Quantum Electronics* **13,** 1016–1030. ISSN: 1558-4542 (July 2007) (cit. on p. 121).

126. Gisin, N. & Thew, R. Quantum Communication. *Nature Photonics* **1,** 165–171. ISSN: 1749-4893 (Mar. 2007) (cit. on p. 121).

127. Bennett, C. H. & DiVincenzo, D. P. Quantum Information and Computation. *Nature* **404,** 247–255. ISSN: 1476-4687 (Mar. 2000) (cit. on p. 121).

128. Giovannetti, V., Lloyd, S. & Maccone, L. Quantum Metrology. *Physical Review Letters* **96,** 010401 (Jan. 2006) (cit. on p. 121).

129. Menzel, E. P. *et al.* Path Entanglement of Continuous-Variable Quantum Microwaves. *Physical Review Letters* **109,** 250502 (Dec. 2012) (cit. on p. 121).

130. Degen, C. L., Reinhard, F. & Cappellaro, P. Quantum Sensing. *Reviews of Modern Physics* **89,** 035002 (July 2017) (cit. on p. 122).

131. Danilin, S. & Weides, M. *Quantum Sensing with Superconducting Circuits* Mar. 2021. arXiv: 2103.11022 [quant-ph] (cit. on p. 122).

132. Fedorov, K. G. *et al.* Experimental Quantum Teleportation of Propagating Microwaves. *Science Advances* **7,** eabk0891 (Dec. 2021) (cit. on p. 122).

133. Braunstein, S. L. & van Loock, P. Quantum Information with Continuous Variables. *Reviews of Modern Physics* **77,** 513–577 (June 2005) (cit. on p. 122).

134. Weedbrook, C. *et al.* Gaussian Quantum Information. *Reviews of Modern Physics* **84,** 621–669 (May 2012) (cit. on p. 122).

135. Hillmann, T. *et al.* Universal Gate Set for Continuous-Variable Quantum Computation with Microwave Circuits. *Physical Review Letters* **125,** 160501 (Oct. 2020) (cit. on p. 122).

136. Fasolo, L. *et al.* Josephson Traveling Wave Parametric Amplifiers as Non-Classical Light Source for Microwave Quantum Illumination. *Measurement: Sensors* **18,** 100349. ISSN: 2665-9174 (Dec. 2021) (cit. on p. 122).

137. Livreri, P. *et al. Microwave Quantum Radar Using a Josephson Traveling Wave Parametric Amplifier* in *2022 IEEE Radar Conference (RadarConf22)* (Mar. 2022), 1–5 (cit. on p. 122).

138. Assouly, R. *et al.* Quantum Advantage in Microwave Quantum Radar. *Nature Physics* **19,** 1418–1422. ISSN: 1745-2481 (Oct. 2023) (cit. on p. 122).

139. Karsa, A. *et al.* Quantum Illumination and Quantum Radar: A Brief Overview. *Reports on Progress in Physics* **87,** 094001. ISSN: 0034-4885 (Aug. 2024) (cit. on pp. 122, 140, 147).

140. Schnabel, R. Squeezed States of Light and Their Applications in Laser Interferometers. *Physics Reports. Squeezed States of Light and Their Applications in Laser Interferometers* **684,** 1–51. ISSN: 0370-1573 (Apr. 2017) (cit. on p. 122).

141. Aasi, J. *et al.* Enhanced Sensitivity of the LIGO Gravitational Wave Detector by Using Squeezed States of Light. *Nature Photonics* **7,** 613–619. ISSN: 1749-4893 (Aug. 2013) (cit. on p. 122).

142. van der Reep, T. H. A. Mesoscopic Hamiltonian for Josephson Traveling-Wave Parametric Amplifiers. *Physical Review A* **99,** 063838 (June 2019) (cit. on p. 123).

143. Houde, M., Govia, L. & Clerk, A. Loss Asymmetries in Quantum Traveling-Wave Parametric Amplifiers. *Physical Review Applied* **12,** 034054 (Sept. 2019) (cit. on pp. 123, 127, 137, 139, 140).

144. Greco, A. *et al.* Quantum Model for Rf-SQUID-based Metamaterials Enabling Three-Wave Mixing and Four-Wave Mixing Traveling-Wave Parametric Amplification. *Physical Review B* **104,** 184517 (Nov. 2021) (cit. on p. 123).

145. Ferreri, A., Bruschi, D. E. & Wilhelm, F. K. Particle Creation in Left-Handed Metamaterial Transmission Lines. *Physical Review Research* **6,** 033204 (Aug. 2024) (cit. on p. 123).

146. Ferraro, A., Olivares, S. & Paris, M. G. A. *Gaussian States in Continuous Variable Quantum Information* Mar. 2005. arXiv: quant-ph/0503237 (cit. on p. 125).

147. Flurin, E. *et al.* Superconducting Quantum Node for Entanglement and Storage of Microwave Radiation. *Physical Review Letters* **114,** 090503. ISSN: 0031-9007, 1079-7114 (Mar. 2015) (cit. on pp. 125, 131).

148. Adesso, G. & Illuminati, F. Gaussian Measures of Entanglement versus Negativities: Ordering of Two-Mode Gaussian States. *Physical Review A* **72,** 032334 (Sept. 2005) (cit. on pp. 125, 126).

149. Horodecki, P. Separability Criterion and Inseparable Mixed States with Positive Partial Transposition. *Physics Letters A* **232,** 333–339. ISSN: 0375-9601 (Aug. 1997) (cit. on p. 126).

150. Booth, M. C. *et al.* Counterpropagating Entangled Photons from a Waveguide with Periodic Nonlinearity. *Physical Review A* **66,** 023815 (Aug. 2002) (cit. on p. 132).

151. Luo, K.-H. *et al.* Counter-Propagating Photon Pair Generation in a Nonlinear Waveguide. *Optics Express* **28,** 3215–3225. ISSN: 1094-4087 (Feb. 2020) (cit. on p. 132).

152. Liu, Y.-C. *et al.* Observation of Frequency-Uncorrelated Photon Pairs Generated by Counter-Propagating Spontaneous Parametric down-Conversion. *Scientific Reports* **11,** 12628. ISSN: 2045-2322 (June 2021) (cit. on p. 132).

153. Schneider, B. H. *et al.* Observation of Broadband Entanglement in Microwave Radiation from a Single Time-Varying Boundary Condition. *Physical Review Letters* **124,** 140503 (Apr. 2020) (cit. on p. 137).

154. Caves, C. M. & Crouch, D. D. Quantum Wideband Traveling-Wave Analysis of a Degenerate Parametric Amplifier. *JOSA B* **4,** 1535–1545. ISSN: 1520-8540 (Oct. 1987) (cit. on p. 140).

155. Benedetto, E. D. *et al. Emergent Cavity-QED Dynamics along the Edge of a Photonic Lattice* July 2025. arXiv: 2507.13444 [quant-ph] (cit. on p. 146).

156. Andrés-Juanes, A. *et al. Entangling Remote Qubits through a Two-Mode Squeezed Reservoir* Oct. 2025. arXiv: 2510.07139 [quant-ph] (cit. on p. 147).

157. O'Connell, A. D. *et al.* Microwave Dielectric Loss at Single Photon Energies and Millikelvin Temperatures. *Applied Physics Letters* **92,** 112903. ISSN: 0003-6951 (Mar. 2008) (cit. on p. 151).

158. Paik, H. & Osborn, K. D. Reducing Quantum-Regime Dielectric Loss of Silicon Nitride for Superconducting Quantum Circuits. *Applied Physics Letters* **96,** 072505. ISSN: 0003-6951 (Feb. 2010) (cit. on p. 151).